



Arnold Schwarzenegger
Governor

URBAN SURFACE MODIFICATION AS A POTENTIAL OZONE AIR-QUALITY IMPROVEMENT STRATEGY IN CALIFORNIA

PHASE ONE: INITIAL MESOSCALE MODELING

Prepared For:

California Energy Commission
Public Interest Energy Research Program

Prepared By:

Altostratus Inc.

PIER FINAL PROJECT REPORT

July 2005
CEC-500-2005-128



Prepared By:

Altostratus Inc.
Haider Taha
Martinez, California
Contract No. 500-02-013

Prepared For:

California Energy Commission
Public Interest Energy Research (PIER) Program

Marla Mueller,
Contract Manager

Kelly Birkinshaw,
Program Area Team Lead

Ron Kukulka,
Acting Deputy Director
**ENERGY RESEARCH AND DEVELOPMENT
DIVISION**

Robert L. Therkelsen
Executive Director

DISCLAIMER

This report was prepared as the result of work sponsored by the California Energy Commission. It does not necessarily represent the views of the Energy Commission, its employees or the State of California. The Energy Commission, the State of California, its employees, contractors and subcontractors make no warrant, express or implied, and assume no legal liability for the information in this report; nor does any party represent that the uses of this information will not infringe upon privately owned rights. This report has not been approved or disapproved by the California Energy Commission nor has the California Energy Commission passed upon the accuracy or adequacy of the information in this report.

Acknowledgements

This work was supported by the California Energy Commission's Public Interest Energy Research (PIER) Program under contract 500-02-013. Acknowledgements are due project managers Marla Mueller (PIER), Nicole Davis (Global Environmental Research), Kelly Birkinshaw, Program Area Team Lead of the Commission's PIER Energy-Related Environmental Research Program, and California Energy Commissioner Dr. Arthur Rosenfeld. The project advisory committee (PAC) members and others are acknowledged for having provided data or general guidance (see **Disclaimer/Note below**):

- Phil Martien, Saffet Tanrikulu, Michael Rothenberg, David Fairley, Steve Soong, and Jack Colbourn. Bay Area Air Quality Management District (BAAQMD)
- Bruce Katayama, Charles Anderson, Art Smith, and Ron Maertz. Sacramento Metropolitan Air Quality Management District (SMAQMD)
- Zorik Pirveysian, Joe Cassmassi, and Elaine Chang. South Coast Air Quality Management District (SCAQMD)
- James Sweet. San Joaquin Valley Unified Air Pollution Control District (SJVAPCD)
- Dale Quattrochi. National Aeronautics and Space Administration (NASA)
- Eva Wong. U.S. Environmental Protection Agency (EPA)
- Kathy Diehl and Michael Stenburg. Environmental Protection Agency – San Francisco (EPA Region 9)
- Vernon Hughes, Ajith Kaduwela, Bruce Jackson, and Kemal Gurer. California Air Resources Board (ARB)
- Ray Tretheway. Sacramento Tree Foundation
- Jude Lamar. Cleaner Air Partnership
- Ashwani Vasishth. Southern California Association of Governments (SCAG)
- Gary Gero. Los Angeles Department of Water and Power (LADWP)

Environ, Inc. is acknowledged for making the CAMx photochemical model freely available for use by the research community and the National Center for Atmospheric Research (NCAR) is acknowledged for free use of the MM5 modeling system.

Disclaimer/Note: This report does not necessarily represent the views of the PAC members and other listed above or those who provided data or models for this study; nor does it imply their support of this study or its findings.

Please cite this report as follows:

Taha, Haider. 2005. *Urban Surface Modification as a Potential Ozone Air-quality Improvement Strategy in California – Phase One: Initial Mesoscale Modeling*. Altostratus Inc. for the California Energy Commission, PIER Energy-Related Environmental Research. CEC-500-2005-128.

Preface

The Public Interest Energy Research (PIER) Program supports public interest energy research and development that will help improve the quality of life in California by bringing environmentally safe, affordable, and reliable energy services and products to the marketplace.

The PIER Program, managed by the California Energy Commission (Energy Commission), annually awards up to \$62 million to conduct the most promising public interest energy research by partnering with Research, Development, and Demonstration (RD&D) organizations, including individuals, businesses, utilities, and public or private research institutions.

PIER funding efforts are focused on the following RD&D program areas:

- Buildings End-Use Energy Efficiency
- Energy-Related Environmental Research
- Energy Systems Integration
- Environmentally Preferred Advanced Generation
- Industrial/Agricultural/Water End-Use Energy Efficiency
- Renewable Energy Technologies

What follows is the final report for the Urban Heat Island Monitoring project, contract number 500-02-013, conducted by Altostratus Inc. The report is entitled *Urban Surface Modification as a Potential Ozone Air-quality Improvement Strategy in California – Phase One: Initial Mesoscale Modeling*. This project contributes to the Energy-Related Environmental Research program.

For more information on the PIER Program, please visit the Energy Commission's website www.energy.ca.gov/pier/ or contact the Energy Commission at (916) 654-4628.

Table of Contents

Preface	-	-	-	-	-	-	-	-	-	-	ii
Abstract	-	-	-	-	-	-	-	-	-	-	viii
Executive Summary	-	-	-	-	-	-	-	-	-	-	1
1. Introduction and Background	-	-	-	-	-	-	-	-	-	-	6
1.1 Energy Implications of Urban Climates	-	-	-	-	-	-	-	-	-	-	6
1.2 Meteorology and Air Quality	-	-	-	-	-	-	-	-	-	-	9
2. Earlier Studies and Findings on Ozone and Meteorology	-	-	-	-	-	-	-	-	-	-	11
3. Purpose of this Study	-	-	-	-	-	-	-	-	-	-	15
4. Approach	-	-	-	-	-	-	-	-	-	-	16
5. Mesoscale Models	-	-	-	-	-	-	-	-	-	-	18
5.1 Meteorological Model	-	-	-	-	-	-	-	-	-	-	18
5.2 Photochemical Model	-	-	-	-	-	-	-	-	-	-	19
5.3 Model Data	-	-	-	-	-	-	-	-	-	-	21
6. Study Domains and Simulation Grids	-	-	-	-	-	-	-	-	-	-	23
7. Additional Models Configurations	-	-	-	-	-	-	-	-	-	-	26
8. Episodes	-	-	-	-	-	-	-	-	-	-	30
8.1 August 1997 (Southern California)-	-	-	-	-	-	-	-	-	-	-	30
8.2 July–August 2000 (Central California)-	-	-	-	-	-	-	-	-	-	-	31
9. Model Performance Evaluation	-	-	-	-	-	-	-	-	-	-	32
9.1 Model Performance Issues Specific to this Application	-	-	-	-	-	-	-	-	-	-	34
10. Replication of ARB Simulations	-	-	-	-	-	-	-	-	-	-	36
11. Improved Surface Characterization and Input	-	-	-	-	-	-	-	-	-	-	38
12. Base-case Development	-	-	-	-	-	-	-	-	-	-	41
12.1 Southern California (SCOS-1997) Base Case-	-	-	-	-	-	-	-	-	-	-	41
12.2 Central California (CCOS-2000) Base Case-	-	-	-	-	-	-	-	-	-	-	48
13. SCOS and CCOS Model Performance Evaluation	-	-	-	-	-	-	-	-	-	-	56
13.1 Model Performance for the SCOS-97 Domain and Episode	-	-	-	-	-	-	-	-	-	-	56
13.2 Model Performance for the CCOS-00 Domain and Episode	-	-	-	-	-	-	-	-	-	-	65
14. Development of Control Strategy	-	-	-	-	-	-	-	-	-	-	70
14.1 Discussion A: Ultraviolet (UV) Radiation and Albedo Increase	-	-	-	-	-	-	-	-	-	-	78
14.2 Discussion B: Increasing Vegetative Cover and Biogenic Hydrocarbon Emissions	-	-	-	-	-	-	-	-	-	-	82
14.3 Impacts on Biogenic Hydrocarbon Emissions	-	-	-	-	-	-	-	-	-	-	83
15. Meteorological and Air-quality Impacts of Surface-Modification Strategies	-	-	-	-	-	-	-	-	-	-	84
15.1 Southern California	-	-	-	-	-	-	-	-	-	-	84
15.2 Central California	-	-	-	-	-	-	-	-	-	-	99
16. Energy and Emission Equivalents	-	-	-	-	-	-	-	-	-	-	114
16.1 Energy Equivalents: Los Angeles Example-	-	-	-	-	-	-	-	-	-	-	114
16.2 Emission Equivalents: South Coast Air Basin Example	-	-	-	-	-	-	-	-	-	-	116
17. Conclusion	-	-	-	-	-	-	-	-	-	-	118
17.1 Recap	-	-	-	-	-	-	-	-	-	-	118
17.2 Results Summary-	-	-	-	-	-	-	-	-	-	-	119
17.3 Recap of Next/Future Steps and Research Needs	-	-	-	-	-	-	-	-	-	-	122
18. References	-	-	-	-	-	-	-	-	-	-	124
Glossary	-	-	-	-	-	-	-	-	-	-	131

Appendix A: Brief Aspects of Meteorology and Photochemistry and Relevance to California	-	-	-	-	-	-	A-1
Appendix B: Meteorological and Air Quality Stations and Monitors in Southern and Central California	-	-	-	-	-	-	B-1
Appendix C: Highlights of Selected Meteorological Models	-	-	-	-	-	-	C-1
Appendix D: Highlights of Selected Photochemical Models	-	-	-	-	-	-	D-1
Appendix E: Some Surface Characterization Data Sources	-	-	-	-	-	-	E-1

List of Tables

Table 1	Impacts of urban areas on annual HDD and CDD	-	-	-	-	-	9
Table 2	T-O ₃ correlations for selected regions in the U.S	-	-	-	-	-	12
Table 3	Historical August 1997 emission inventories for the South Coast Air Basin	-	-	-	-	-	22
Table 4	Historical 2000 CCOS emission inventory for selected regions	-	-	-	-	-	22
Table 5	Vertical configuration of MM5	-	-	-	-	-	24
Table 6	MM5 and CAMx vertical levels correspondence	-	-	-	-	-	25
Table 7	Assumed EPA/ARB clean boundary conditions used in the study	-	-	-	-	-	29
Table 8	Observed peak ozone in the Southern California domain	-	-	-	-	-	31
Table 9	Observed peak ozone in the Central California domain	-	-	-	-	-	31
Table 10	Base-case values of LULC-related physical parameters (for summer)	-	-	-	-	-	40
Table 11	Air temperature bias (MRE) and error (MURE) averaged for three days-	-	-	-	-	-	57
Table 12	Air temperature bias (MRE) and error (MURE) for each day	-	-	-	-	-	58
Table 13	Wind speed bias (MRE) and error (MURE) averaged for three days-	-	-	-	-	-	58
Table 14	Wind speed bias (MRE) and error (MURE) for each day	-	-	-	-	-	59
Table 15	Wind speed gross error	-	-	-	-	-	59
Table 16	Nested grid model performance for entire domain (Southern California)	-	-	-	-	-	64
Table 17	Nested grid model performance for sub-domains (zones) 3, 4 and 5-	-	-	-	-	-	64
Table 18	Standalone grid model performance for entire domain (Southern California)	-	-	-	-	-	64
Table 19	Standalone grid model performance for sub-domains (zones) 3, 4 and 5-	-	-	-	-	-	64
Table 20	Bias (MRE) and gross error (MURE) for selected regions in the CCOS domain	-	-	-	-	-	66
Table 21	Observed peak concentrations in the CCOS domain	-	-	-	-	-	66
Table 22	MRE, MURE, and UA metrics compared to ARB model performance	-	-	-	-	-	67
Table 23	MRE, MURE, and UA metrics compared to model performance	-	-	-	-	-	68
Table 24	MRE, MURE, and UA metrics compared to ARB model performance for the CCOS domain and episode	-	-	-	-	-	69
Table 25	MRE, MURE, and UA metrics compared to model performance benchmarks (for the CCOS <i>standalone</i> grid)	-	-	-	-	-	69
Table 26	Assumed percentages of built-up surface types for USGS LULC	-	-	-	-	-	70
Table 27	Assumed levels of albedo increase per surface type	-	-	-	-	-	71
Table 28	Scenarios for albedo change at 200-m resolution	-	-	-	-	-	71
Table 29	Scenarios for vegetation cover increase (as % of 200-m cells)	-	-	-	-	-	72
Table 30	Base case and scenarios for soil moisture changes	-	-	-	-	-	72
Table 31	Total ROOF area to be modified (km ²)	-	-	-	-	-	75
Table 32	Total PAVED-surface area (parking, roads, sidewalks) to be modified (km ²)	-	-	-	-	-	76
Table 33	Number of buildings needed for modification	-	-	-	-	-	76
Table 34	Number of trees needed for modification	-	-	-	-	-	76
Table 35	Albedo of selected materials	-	-	-	-	-	82
Table 36	Changes in domain-wide unpaired peak (averaged over two days; 8/5 and 8/6) for the Southern California Domain	-	-	-	-	-	97
Table 37	Changes in region-averaged peaks (CCOS)	-	-	-	-	-	113
Table 38	Potential reduction in LADWP peak demand for three scenarios	-	-	-	-	-	115

List of Figures

Figure 1	Quantities of interest to this modeling study - - - -	16
Figure 2	Model simulation sequence - - - -	17
Figure 3	LULC processing step- - - -	17
Figure 4	Southern California modeling domain and nested grids - -	23
Figure 5	Central California modeling domain and nested grids - -	24
Figure 6a	An example of vertical variation in nudging coefficients - -	28
Figure 6b	Example scaling of vertical diffusivity in SCOS simulations -	28
Figure 7	Model performance and signal/noise - - - -	35
Figure 8	Replication of the ARB SCOS-97 simulations with the CAMx 3.10	36
Figure 9	Replication of the ARB CCOS-00 simulations with the CAMx 3.10	37
Figure 10	Tiles of 200-m resolution USGS LULC for Central to Southern California	39
Figure 11	Simulated base-case wind and temperature fields for Southern California	41
Figure 12	Simulated ozone concentrations on August 5 and 6, Southern California.	46
Figure 13a	Simulated base-case ozone concentrations for the Southern California domain at 1500 LST on August 5, 1997 - - -	47
Figure 13b	Simulated base-case ozone concentrations for the Southern California domain at 1500 LST on August 6, 1997 - - -	47
Figure 14	Simulated base-case wind and temperature fields for Central California	48
Figure 15(a)	Simulated 10-m streamlines at 1600 LST July 31 - - -	51
Figure 15(b)	Simulated 10-m streamlines at 1600 LST August 1 - - -	51
Figure 16	Simulated base case ozone concentrations on July 31 and August 1, 2000 for Central California - - -	52
Figure 17a	Peak ozone concentrations at each grid cell on July 31 - - -	55
Figure 17b	Peak ozone concentrations at each grid cell on August 1 - - -	55
Figure 18	SoCAB Model performance evaluation zones - - -	57
Figure 19	Predicted vs. observed 2-m air temperature (K) - - -	60
Figure 20	Air temperature σ/σ_0 ratios - - - -	62
Figure 21	Air temperature E/σ_0 ratios for 4 days - - - -	62
Figure 22	Air temperature E'/σ_0 ratio for 4 days - - - -	63
Figure 23	Model performance evaluation sub-regions for the CCOS - -	65
Figure 24	Distributions of changes in surface albedo and soil moisture in the SCOS domain - - - -	73
Figure 25	Distributions of changes in surface albedo and soil moisture in the CCOS domain - - - -	74
Figure 26	Modification potential in Southern California - - -	77
Figure 27	Modification potential in Central California - - -	77
Figure 28	Example changes in soil moisture for Southern and Central California	78
Figure 29	Measured spectral reflectance of selected materials - - -	80
Figure 30	Spectral reflectivity characteristics of selected roofing materials -	81
Figure 31	Changes in 2-m air temperature and 10-m wind speed for four Southern California regions and for 5 surface-modification scenarios	85
Figure 32	Air temperature difference (from the base case) for scenario 22 -	88

Figure 33	Maximum hourly decreases in ozone concentration at each grid cell for several scenarios - - - - -	93
Figure 34	RRF for four strategies (South Coast) for August 5 - -	96
Figure 35	Changes in selected ozone indices for the Southern California domain	99
Figure 36	Changes in 2-m air temperature and 10-m wind speed for four Central California regions and for 3 surface-modification scenarios -	101
Figure 37	Air temperature difference (from base case) for case 20 in the CCOS modeling domain - - - - -	104
Figure 38	Differences in ozone concentrations (case 20 minus base case) for July 31 - - - - -	108
Figure 39	Maximum hourly decreases in ozone concentration at each grid cell for several scenarios - - - - -	111
Figure 40	Changes in the 1-hr peak for case 10 and case 20 for four CCOS regions and three days - - - - -	112
Figure 41	Daily peak load (LADWP) vs. daily maximum air temperature (1999-2004) in Los Angeles - - - - -	115
Figure 42	Domain-peak ozone concentration (averaged over August 5 and 6) as a function of NO _x and VOC emissions (%) for Southern California - - - - -	117

Abstract

While the micrometeorological and energy impacts of certain surface modification strategies can be demonstrated and evaluated in the field, the potential large-scale effects from such surface modifications are relatively unknown and can currently be assessed only via numerical modeling. Increased built-up surface albedo and vegetative cover, for example, have been shown to reduce cooling electricity use in summer in the United States, but their regional environmental impacts are more difficult to ascertain, because of uncertainties in meteorological and photochemical models and input data. Thus more up-to-date modeling is necessary if more accurate estimates of such impacts are sought.

This study consists of two phases, the first of which is summarized in this report. This first phase involved modification, update, improvement, and application of state-of-science mesoscale meteorological and photochemical models (MM5 and CAMx) and related emission models in evaluating the potential impacts of these strategies in California during two episodes. The findings suggest both positive and negative impacts depending on location, time, and level of modifications. Peak ozone concentrations in southern California can increase during certain times of the episode; whereas, in central California the peaks decrease considerably. In terms of area-averaged indices, all regions experience reductions in ozone levels. In the future, multi-episodic and seasonal evaluations may be needed.

In the second phase of the study, a new generation of mesoscale (urbanized) meteorological models will be used in further evaluating these positive and negative air-quality impacts to determine the dominant and overall effects.

Keywords: Mesoscale meteorological modeling, photochemical modeling, ozone air quality, surface modifications, MM5, CAMx, urban meteorology

Executive Summary

Introduction

Air quality management plans, such as state implementation plans (SIPs), directly or indirectly provide region-specific estimates of the reductions in precursor emissions needed to reach and/or maintain the carrying capacity of the atmosphere below a certain threshold, so as to meet the standards for criteria pollutants. For ozone, such estimates suggest that a significant level of emissions reduction may be needed in urbanized areas—especially in terms of NO_x.

As emission control strategies become relatively more expensive, and therefore more difficult to implement when regions approach their attainment targets (both in time and level of control), it is desirable to explore additional strategies that can supplement those planned or already in place. It is hoped that such alternative strategies would also be cost effective, so that they could efficiently complement the mix of other emission controls. One of several such strategies that have been discussed and evaluated at least qualitatively (but perhaps inconsistently) is the so-called “urban heat island control” strategy or, more accurately, “urban surface modification.” The proposed strategies of increased surface albedo and vegetative cover will produce effects, both positive and negative, regardless of whether heat islands exist and/or their timing (i.e., the classical heat island peaks at night).

Increased surface albedo and vegetative cover have been shown in field measurements, experiments, and theoretical modeling work to produce significant, measurable, verifiable, and repeatable savings in energy used for summer cooling. The savings have been evaluated and quantified at both the regional (utility) and building scales.

However, in terms of meteorology and air quality, the potential impacts of large-scale surface modifications can presently be demonstrated only via numerical (e.g., mesoscale meteorological and photochemical) modeling. The potential air-quality impacts of these strategies have been evaluated sporadically by several research entities, with mixed results. All studies show positive and negative impacts, but differ in characterizing the dominant effect in each region—that is, whether these strategies represent an overall benefit or a liability.

Because of the nature of the proposed strategies, and the many issues involved in modeling and quantifying their potential impacts, the U.S. Environmental Protection Agency (EPA) and air pollution control districts have considered these proposed strategies only informally/qualitatively and have not yet considered them seriously in a regulatory framework. This is partly because of the lack of conclusive results from modeling studies and partly because the current regulatory framework does not easily allow for “unconventional” strategies to be readily included in the SIP process. Thus, new or updated modeling efforts are needed to further improve upon past studies, develop more reliable and credible results, and resolve some issues with earlier modeling work—as well as to assemble modeling systems that are more acceptable to and can be adopted by regulatory agencies in their planning and modeling processes.

Purpose

The purpose of this study was to explore and evaluate the potential of surface modifications in improving ozone air quality *in addition to their energy savings*.

Objectives

This study's first objective was to ensure that, at least, no significant *adverse air-quality* impacts would result from increasing urban albedo and vegetative cover for the purpose of *reducing electricity use*. The study also sought to discern whether such strategies have potential additional benefits, such as improving air quality, to provide a basis for considering them separately on their own merit.

As with some other strategies, the modification of surface properties in urban areas can cause both net decreases and increases in ozone concentrations. The task, then, is to tailor strategies to regions of interest so that they produce overall beneficial impacts while minimizing negative impacts. The optimal mix of such strategies (to maximize the net ozone reductions) will differ among regions and will depend on factors such as local emissions, meteorology, and episodic conditions. Thus, ideally, the variability in all forcings should be considered, and specific modeling studies should be designed to quantify local potential impacts. For the first phase of this study, the photochemical episodes used were those of August 3 through 7, 1997, for Southern California (SCOS-97), and July 29 through August 4, 2000, for Central California (CCOS-2000).

Outcomes

The present study was designed as an initial step towards developing region-specific impact assessments for California. Future follow-up studies could then be undertaken to provide more in-depth analysis and modeling detail for region-specific *implementation* plans or scenarios. In this initial phase of the project (Phase 2 of this study is currently underway), the modeling was performed in a fashion compatible with work done at the California regulatory agencies for the episodes identified earlier. However, the study introduced several improvements to the modeling methodology as well as to input data to improve the simulation of specific surface modification strategies. A relatively more detailed surface characterization system was also implemented to override the default and relatively coarse characterization of urban areas in mesoscale models.

Results to date (Phase 1 of study) suggest a host of meteorological changes in response to such surface modifications—most notably in relatively lower surface and air temperatures. These changes are the main effects of interest sought in this application, because decreased air temperatures help reduce cooling electricity use, emissions of ozone precursors (that are temperature dependent), and photochemical reaction rates in dominant mechanisms increasing tropospheric ozone, such as peroxyacetyl nitrate (PAN) chemistry. The spatial distribution of perturbations in meteorological fields (e.g., temperature, wind, and PBL depth) follows closely the geographical distribution of surface modifications. Where surface modifications are larger, the impacts on air temperature in the affected areas and immediately downwind of them are greater. For example, **Figures ES-1 and ES-2** depict changes in 2-m air temperatures (relative to the base case) for Southern and Central California at 1300 on August 4 and at 1200 on July 31,

respectively. The base-case wind vector field (at 10m) is superimposed on the temperature-change field in each domain.

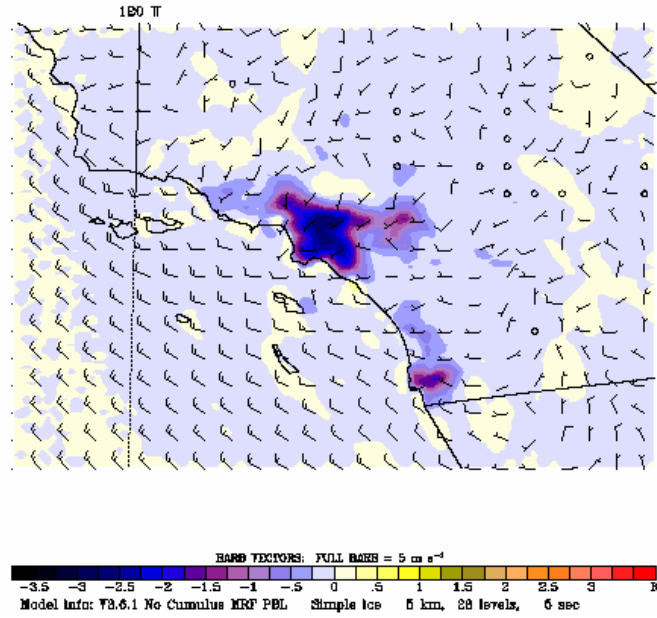


Figure ES-1. Change in air temperature in Southern California as a result of increased urban albedo and vegetative cover (1300 on August 4).

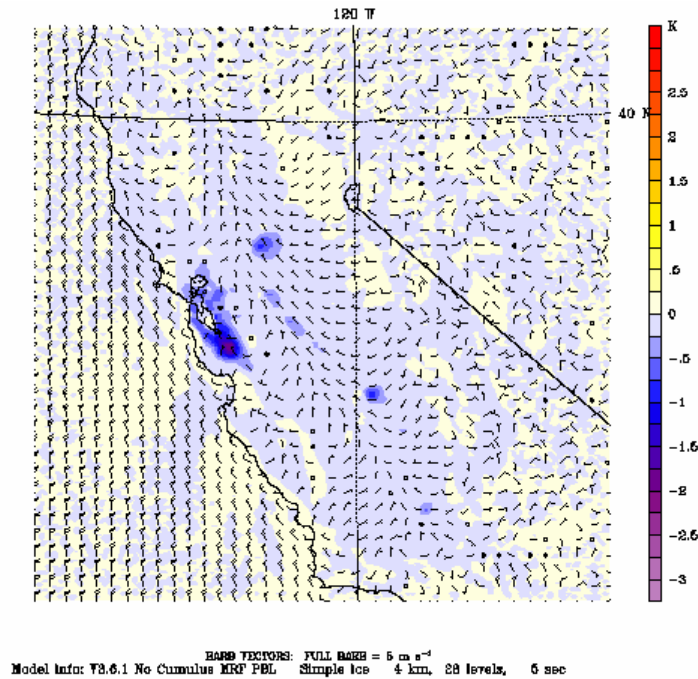


Figure ES-2. Change in air temperature in Central California as a result of increased urban albedo and vegetative cover (1200 on July 31).

Conclusions

Overall, the simulations suggest that there is a large spatiotemporal variability in the impacts of meteorological perturbations on ozone concentrations. The sub-regional peaks in Central California (Sacramento, San Francisco Bay Area, Highway 99 corridor, Fresno, and Bakersfield) decrease as a result of implementing surface modification strategies. In Southern California, the domain peak can increase or decrease on August 5, depending on assumed surface modification scenarios but always decreases on August 6. In central California, 3-day averaged decreases in the regional peaks are in the range of 2 to 13 ppb, depending on the region, whereas in Southern California, the 2-day averaged reductions in the peak range from about 0.5 to 3 ppb.

The report provides additional metrics other than peak-related ones (e.g., area-averaged indices with respect to the 8-hour standard, 1-hour standard, 24-hour averages, daytime changes). In addition, some changes were converted into emission reduction “equivalents” to provide an alternate means of qualitatively evaluating the usefulness of the proposed strategies.

Recommendations

To achieve the levels of ozone changes detailed in the report, a significant surface modification effort is needed. Crude calculations suggest that, for the assumptions made in the study, about half of the modifiable built-up surface area (e.g., roofs, paved surfaces, driveways, parking lots) in each urbanized region need to be modified—for example, with application of high-albedo materials. In terms of vegetative cover increase, the calculations suggest that some 200,000 trees need to be added to the smaller urbanized regions in California (e.g., Bakersfield), and up to some 8 million trees need to be added in very large regions such as Southern California (which also includes the Los Angeles Basin, San Diego, and all surrounding areas).

Of course, implementation-specific simulations and calculations will have to be made in detailed follow-up studies to determine more accurately the level of modifications needed. Ultimately, there may be smaller or larger modification levels needed than suggested in this report. In particular, Phase 2 of this study will address these modeling issues in more detail with a new generation of modified and urbanized meteorological models and corresponding photochemical simulations.

For each region, the relative levels of benefits and adverse effects also depend on the level of surface modifications. Qualitatively speaking, there appears to be region-specific thresholds or ranges for such modifications beyond which further increases in surface modifications do not produce much additional net benefits and in some cases tend to produce net disbenefits. Because of such issues and the existence of competing non-linear effects, region-by-region and multi-episodic assessments and modeling may be needed to identify the optimal mix of surface modification strategies. And because the benefits and adverse effects also change from one location to another (or one level of surface modifications to another, etc.) region-by-region analysis and modeling are needed to evaluate the local usefulness and effectiveness of a range of scenarios and strategies before the appropriate policy action or recommendation can be developed.

Benefits to California

From a regulatory perspective, photochemical air-quality modeling is an important tool and a cornerstone component in the planning process that ultimately leads to implementing effective strategies for air-quality improvements. The Clean Air Act requires that non-attainment areas, especially those designated as *serious* or higher (for ozone), use a photochemical grid model to study the potential impacts of proposed control strategies and/or demonstrate attainment, using designated field-intensive periods or historical air-quality episodes, such as those with high observed ozone concentrations. To facilitate the usefulness of these results, the modeling episodes selected in this study were chosen to be compatible with those used by California regulatory agencies.

The ultimate goal of urban-surface modification strategies is to help lower ozone concentrations in California cities directly (by reducing the use of electricity for cooling) and indirectly (by affecting meteorology-dependent emission and photochemical-reaction rates). The anticipated effects from surface modifications such as increased albedo and vegetative cover arise because of the relatively lower surface temperatures (slower rates of warming) of the modified surfaces. These lower surface temperatures in turn cause changes in air temperatures, area-emission rates of ozone precursors (including biogenic emissions), electricity use for cooling and related emissions from power plants, and rates of photochemical production of ozone.

1. Introduction and Background

In accordance with the California Energy Commission's (Energy Commission) mission of fostering energy efficiency and environment-friendly energy policies, this study was funded under the Energy Commission's Public Interest Energy Research, Energy-Related Environmental (PIER-EA) program to evaluate and analyze the potential air-quality impacts of modifications in urban surface properties, such as built-up surface albedo and soil moisture/vegetation cover. These strategies have well-known and well-documented benefits in terms of reducing the amount of energy (electricity) needed for cooling. The purpose of this study was to assess the potential benefits that these strategies may have in terms of ozone air quality. In the past, the Energy Commission has supported "urban heat island" studies, research into cool materials, and evaluation of reforestation programs. In this study, the ultimate goal was to create interest in the regulatory environment for possible consideration of these strategies.

Currently, there is interest at several other organizations and institutions in the United States (e.g., the Department of Energy (DOE) and the U.S. Environmental Protection Agency (EPA)) in evaluating the potential benefits of these urban surface modification strategies. For example, in 1997, the EPA initiated the Urban Heat Island Pilot Project (UHIPP) to investigate the potential impacts and possible benefits of high-albedo urban materials and increased vegetative cover in improving air quality in urban areas. More recently, the EPA supported a number of modeling studies to assess these potential impacts and issues related to "heat island reduction strategies" in the Houston-Galveston area in Texas.

The purpose of this study and any related follow-up work is to ultimately provide a basis for consideration of surface-modification strategies in a regulatory framework. The EPA requires that certain demonstration episodes be simulated to show potential benefits from any proposed air-quality improvement strategy. In this study, two demonstration episodes (August 1997 and July–August 2000, for Southern and Central California, respectively) were used as a basis for evaluating the effectiveness of surface-modification strategies in improving ozone air quality. The study is based on mesoscale meteorological and air-quality (photochemical) modeling and evaluation of potential impacts in California's major airsheds under these episodic conditions.

The first part of this section discusses some energy and demand aspects of this work, and the second part (and the rest of the report) focuses on meteorological and air quality issues. Energy implications will also be revisited in Section 16.1.

1.1 Energy Implications of Urban Climates

Urban climates and energy are interrelated in two ways. First, energy conversion and use can contribute to creating specific urban-climate phenomena, such as heat islands, via increased anthropogenic heating of ambient air by equipment, air conditioners, cooling towers, motor vehicles, and other sources of heat, such as combustion. Although energy conversion and use are only a couple of many heat-island causative factors, they can be significant in areas where such sources are highly concentrated. Energy use and conversion also result in increased emissions of air pollutants such as carbon dioxide (CO₂), nitrogen oxides (NO_x), volatile organic compounds (VOC), and water vapor (from motor vehicle exhausts, refineries, chimneys, electricity generators, and other sources), which can enhance local pollution and greenhouse effects.

Increased emissions of particulate matter or formation of aerosols can also affect the concentration of condensation nuclei and possibly the local formation of convective clouds. Increased local cloud cover can in turn reduce the actinic flux and air temperature in the boundary layer.

The second of the energy-urban climate interactions is that urban climate directly affects energy use e.g., heating, ventilating, and air conditioning (HVAC) energy use, systems and equipment, motor vehicles, industrial processes, and so on. In buildings, for example, more cooling and less heating is generally needed when heat islands are present. In addition, HVAC system efficiencies are to a certain extent functions of ambient air temperature and thus are affected by urban climates, even if only by small amounts.

The physical effects of the proposed control strategies (i.e., the desirable reductions in surface and air temperatures and related meteorological and photochemical changes resulting from increasing surface albedo and vegetative cover) will occur regardless of whether a local heat island exists. These proposed strategies will produce both positive and negative effects, and the prior existence of heat islands and their timing (i.e., typically, heat islands peak at night) are irrelevant in this respect. Nevertheless, a heat island can occur in an urban area, so the following discussion provides some background information related to this phenomenon. Briefly, some of the causative factors that can help create a heat island (Taha 1997a, 1997b) are:

- **Higher thermal capacity.** The abundance of high thermal-capacity materials such as concrete, brick, stone, pavement, asphalt, and steel in urban areas causes built-up surfaces and structures to store relatively more heat than in rural surrounds. Many of these materials also have high thermal conductivities, thus further increasing heat fluxes and storage in them. Urban regions also typically have a larger total surface area exposed to the sun per horizontal area than do rural regions (due to a higher surface-to-area ratio (SAR) and plan-area density). Rural areas tend to have a SAR close to 1. In residential neighborhoods, the SAR is in the order of 2–3, whereas in urban cores, it reaches about 5 or higher. In areas like Manhattan, the SAR can easily reach 10 or more. As a result of the combination of these two factors (increased thermal capacity and increased SAR), solar radiation is captured and stored more efficiently in urban areas.
- **Reduced view factor.** The smaller sky-view factor (SVF) in urban areas, relative to that in open surrounds, helps create a canopy-layer heat island, especially during nighttime. This heat island arises because radiative cooling of urban surfaces (and canopy-layer air) to the sky is hindered by the obstructions in urban areas, such as walls and structures). As a result, a heat island can be created due to the differential in cooling rates between urban areas and rural surrounds. The SVF mechanism is at work during daytime, but its relative contribution is smaller than at night. In addition, the reverse effect can also occur, e.g., shading in urban canyons and the competing effect of decreased effective albedo, discussed next.
- **Lower effective albedo.** The albedo of building materials, pavements, and other urban structures is generally similar to or lower than that of vegetation or barren land (which is abundant in rural areas). But in some cases, the reverse is true—that is, albedo of urban

surfaces can be higher than that of the rural surrounds. For example, low-altitude aircraft measurements over the Los Angeles Basin (Taha 1997b) showed that urban albedo in some parts can reach up to 0.20 when the rural, more-vegetated surroundings have an albedo of 0.15. In general, a heat island can arise when *effective* urban albedo (i.e., the overall albedo resulting from combined effects of surfaces' albedo and urban geometry) is lower than that of the rural surrounding areas. Thus, not only can many urban surfaces such as roofs, walls, pavements, streets, and structures have low albedos, urban areas also create a lower *effective* albedo, compared to that of rural or surrounding areas. The geometry of urban canyons increases multiple reflections of incident solar radiation, and therefore increases the probability that photons be absorbed by canyon surfaces (instead of escaping back), thus resulting in lower effective albedo.

- **Reduced latent heat fluxes.** As a result of relatively smaller vegetative cover in urban areas, the partitioning of incoming solar radiation into sensible and latent heat fluxes is altered. Thus in urban areas, the Bowen ratio (β) (which is the ratio of sensible to latent heat fluxes) is larger, and this ultimately results in higher air temperatures. In rural areas or suburbs where there is typically more vegetation, evaporation, and evaporative cooling, β is smaller, and that can help keep air temperatures relatively lower. Typical values for β are around 4 or 5 in urban areas and about 0.8 to 1.5 in vegetative canopies. By comparison, β is in the neighborhood of 0.1 for oceans and in the tropical forests it is about 0.2.
- **Anthropogenic heating.** Urban areas also alter the energy balance “actively” via injection of heat directly into the air and, to a smaller extent, into the surfaces. Typical sources of urban anthropogenic heat include motor vehicles; stacks and chimneys; heating, ventilating, and air-conditioning (HVAC) in motor vehicles and buildings; industrial machinery and processes; refineries and processing plants; and power plants. Typical values of anthropogenic heat flux density in residential areas are in the order of 10–20 watts per square meter (W m^{-2}) and in dense urban cores in the range of 50–100 W m^{-2} (Taha 1997a). Flux densities larger than 100 W m^{-2} are thought to occur at certain times in extremely dense urban cores, such as Lower Manhattan (about 120–150 W m^{-2}). In Japan, flux densities of up to 500 W m^{-2} have been reported, although this is highly uncommon. By comparison, the maximum incoming solar radiation flux density at street level on a cloudless summer day can range from 800 to 1000 W m^{-2} around solar noon. Outside of the atmosphere, the incoming solar radiation flux density (solar constant) is at about 1350 W m^{-2} .

In terms of energy use, a typical impact of heat islands is to increase cooling loads in summer and decrease heating loads in winter. The net effect, of course, will depend on the characteristics of a region's climate (summer-, winter-dominated, or none) and general meteorological features, such as wind patterns, available sunshine, precipitation, topographically induced flows and phenomena, and other factors. It will also depend on local energy-specific aspects, such as population density, dominant sectors of energy consumption, types of buildings, age, distribution, general building envelope characteristics, saturation of HVAC equipment, and local cost of fuel and electricity rates. For example, most urban areas in the United States would see a typical increase in cooling degree-days (CDD) of between 15% and 35% as a result of urban heat

island (UHI), with some extremes as high as around 90%. A typical decrease in heating degree-days (HDD) would be about 5% to 14%, with extremes as high as about 30%. In general, a decrease in HDD can translate into a decrease in winter-time heating needs (although relatively small compared to the increase in summertime cooling electricity needs). **Table 1** shows example impacts on HDD and CDD in selected regions.

Table 1. Impacts of urban areas on annual HDD and CDD (base 18.3°C, or 65°F)

	Impact on HDD	Impact on CDD
Los Angeles	-30%	+90%
Washington D.C.	-5%	+20%
St. Louis	-5%	+10%
New York	-5%	+25%
Baltimore	-15%	+35%
Seattle	-15%	+55%
Detroit	-5%	+15%
Chicago	-5%	+25%
Denver	-10%	+20%

Source: (Taha 1997a)

The differences in CDD and HDD shown in Table 1 are those “seen” by the atmosphere. However, one CDD is not equivalent to one HDD when converted to energy costs—for example, if cooling is achieved with electricity and heating mainly with natural gas. Electricity and gas costs are different, and the HDD/CDD equivalence also depends on how cooling and heating are achieved locally, taking into account differences in HVAC systems, primary and secondary systems, power plants, and overall system efficiencies. Thus the conversion from HDD/CDD to energy use and costs depends on local factors and energy rates. In the United States, the average electricity cost is about \$0.08/ kilowatthour (kWh) and the average gas cost is about \$0.65/therm (1 therm = 10⁵ Btu), but deviations from these averages (by geographical location and time/season) can be quite significant. Thus the HDD/CDD data given in **Table 1** are for qualitative comparison purposes. Section 16.1 also gives some correlations between peak demand and temperature, to provide a qualitative assessment of the potential reduction in energy use (load/demand at utility scale) from implementing urban surface modification strategies.

1.2 Meteorology and Air Quality

Several modeling studies have suggested that urban environmental control strategies such as surface albedo and vegetative cover increases can reduce surface and air temperatures (e.g., Taha 1999; Taha et al. 1999; Sailor 1993; Taha 1996, 1997b) in areas where such surface modifications are most concentrated. The main local impacts of interest from relatively lower ambient temperatures include, in descending order: (1) a reduction in temperature-dependent rates of certain photochemical reactions; (2) a decrease in temperature-dependent biogenic hydrocarbon emissions from existing vegetation; (3) a decrease in evaporative losses of organic compounds from mobile and stationary sources; (4) a decreased need for cooling energy, generating capacity, and, ultimately, emissions from power plants; and (5) decreases from on-road and off-road mobile source emissions. Thus, generally speaking, increased urban surface albedo and vegetative cover have the potential to reduce ozone formation. However, cooling an urban area via such strategies can also cause adverse effects on ozone air quality because inhibited mixing and changes in the wind field can increase ozone concentrations in certain areas and times. Because of these competing and nonlinear effects, evaluation of such urban

environmental control strategies relies mainly on use of prognostic meteorological and air quality models.

Gabersek and Taha (1996) and Taha (1996, 1997b) show that these strategies may be an effective way of reducing urban air temperatures in various regions in the United States (by up to 5°C (41°F) in summer in areas such as the Los Angeles Basin, for example), thus helping reduce exposure to ozone. Taha et al. (2000) show that the effects in three U.S. regions tend to be generally positive but that negative, unwanted effects still occur. That study showed that Sacramento, California, would benefit more from these strategies than Salt Lake City, Utah, or Baton Rouge, Louisiana. In the latter two regions, the peak ozone concentration did not change as a result of surface modification; whereas, in Sacramento, a peak of 139 parts per billion (ppb) was decreased by 9 ppb. Area-wide indices in all three regions decreased in general. Taha (2003c) performed an extensive meteorological-photochemical modeling study of the Houston-Galveston, Texas, region to assess the potential impacts of surface modifications. Although that study was inconclusive because of outstanding issues with model performance and quantification of the resulting signal, it showed that the impacts can be significant (both positive and negative) and that further work must be done to improve model performance and more accurately quantify the potential benefits of these strategies. One can expect perturbations in all meteorological fields to follow as a result of implementing surface modifications; however, the main interest in this and other studies is the change in air temperature and its potential impact on ozone air quality.

2. Earlier Studies and Findings on Ozone and Meteorology

A number of studies have examined the role of meteorology in tropospheric and ground-level ozone formation, scavenging, transport, and accumulation; however, the parameter of most interest to this study is ambient air temperature. Air quality studies in general show a positive correlation between ozone concentrations and temperature. A warmer environment is generally more conducive to ozone formation and accumulation, mainly because of temperature impact on peroxyacetyl nitrate (PAN) chemistry (increased breakup of PAN), accompanying stagnation (reduced venting and transport), increased solar radiation (actinic flux), and other factors, but it is the mix of meteorology and emissions that determines the ultimate outcome in a specific region under specific conditions.

The relationship between changes in meteorological variables and photochemical production of ozone can be demonstrated relatively easily in controlled environments such as smog chambers, and with a relatively straightforward pinpointing of causative factors. An outdoor smog chamber can be used to show a direct relationship between maximum daily temperature and maximum ozone concentrations, holding all other variables constant, such as solar radiation intensity, initial mix of precursors, and water vapor mixing ratio. Kelly and Gunst (1990) found a very linear relationship and little scatter along a regression fit between maximum ozone and temperature in an outdoor chamber filled with “Los Angeles” air. Such correlations between temperature and ozone concentrations have also been shown in outdoor smog chambers and ambient measurements by the EPA (EPA 1996).

However, in the real, highly dynamic atmosphere, finding a direct cause-and-effect relationship may be difficult because of the complex and nonlinear interactions between meteorological, chemical, emissions, and other processes in a three-dimensional time-varying fashion. But in general, several studies have found that increased temperature, stagnation, and solar radiation produce conditions conducive to high ozone formation (Deuel et al. 1999). Temperature can also be thought of as a surrogate to and inclusive of these other factors, and is often used in correlations with ozone levels because other parameters of stagnation, such as wind or solar radiation, do not correlate well with ozone concentrations. The relationship between atmospheric ozone formation and temperature has been documented in a number of studies (Kuntasal and Chang 1987; Atwater 1984; Wackter and Bayly 1988; Clark and Karl 1982, and others). For example, the Kuntasal study used temperature at 850 millibars (mb) over Southern California as a predictor to ozone concentrations. In the U.S. Northeast, Zhang et al. (1998) found that summertime ozone concentrations increase during periods of high temperatures (heat waves) and attending environmental conditions. Flaum et al. (1996) found that in summer, the correlation between ozone and temperature is strongest, e.g., when temperature is above 21°C (70°F), and Samson (1988) showed that the incidence of ozone concentration exceedances above 120 ppb increases almost linearly with the increase in mean maximum temperature, based on ambient data from Michigan.

In their analysis of observational data from the Southeast, McNider et al. (1995) show that maximum surface air temperature is the meteorological variable with the highest correlation with ozone concentrations. The EPA (1996) shows that above 30°C (86°F), the temperature-ozone relationship is statistically significant at all sites that were monitored for the analysis. For illustration, **Table 2** gives the rates of increase in peak ozone concentrations with daily

maximum temperature. Although these correlations were observed in the U.S. locations selected in this table, this type of relationship between peak ozone (O₃) and temperature has been observed elsewhere as well. For example, a study by Wunderli and Gehrig (1991) in Switzerland reports rates of 3–5 ppb/°C between 10°C and 25°C (50°F and 77°F) but little change below 10°C (50°F). Other studies, e.g., Morris et al. (1989) and Penner et al. (1989) also found that ozone concentrations increase as a result of temperature increases under a number of climate change scenarios. Such correlations were also reported in Sillman and Samson (1995).

Table 2. O₃-T correlation (change in daily maximum ozone with maximum daily temperature) for selected regions in the U.S. (Near-surface air temperatures used).

	T < 27°C	T > 27°C
	ΔO ₃ /ΔT (ppb/°C)	ΔO ₃ /ΔT (ppb/°C)
<i>Urban</i>		
New York region*	1.5	8.8
Detroit	1.4	4.4
Atlanta	3.2	7.1
Phoenix	**	1.4
Southern California	11.3	**
<i>Non-urban</i>		
Pennsylvania (Williamsport)	1.2	4.0
Michigan (Saline)	0.8	3.1
Oregon (Medford)	0.5	3.3
Kentucky (Mammoth Cave)	0.1	4.4
North Dakota (Williston)	0.2	0.8

Sources: (EPA 1996; Sillman and Samson 1995)

* Includes New York, New Jersey, and Connecticut. ** No data

Of course, in **Table 2**, the given ozone-temperature changes are regional (not necessarily urban) and the correlations for Southern California are further complicated by geographical factors relative to those of other regions. As Sillman and Samson (1995) point out, the latter is due mainly because of significantly varying microclimates across the Los Angeles Basin. But when a threshold of 17°C (63°F) was used instead of > 27°C (81°F) as above, a strong correlation between ozone and temperature was still obtained, which indicates that the correlation may hold equally well across different regions of the Basin.

Several other studies also provide correlations between some measures of air temperature and ozone concentrations. For example, Jones et al. (1989) correlated the number of days with ozone exceedances above 120 ppb against near-surface air temperature above 30°C (86°F) in selected urban areas. Wakim (1989) developed such correlations for Houston, Washington D.C., and New York. In Atlanta, Georgia, Cardelino and Chameides (1990) showed a significant correlation between temperature and ozone levels, based on ambient data. They suggest, as is discussed in this report, that temperature is not the only factor in smog production (higher air temperatures are not always a guarantee that ozone concentrations will be higher than during days with relatively lower temperatures). Using the carbon bond (CB-IV) mechanism as implemented in the Ozone Isopleth Plotting with Optional Mechanisms-IV (OZIPM4) model, Hogo and Gery (1988) show

that the effect of increased air temperature on maximum ozone concentrations is significant, whether only chemistry effects are accounted for or both chemistry and emission effects are included. The chemistry effect (mainly the effect of PAN chemistry) alone would increase maximum ozone concentrations by 2.8 ppb/°C (1.56 ppb/°F) whereas the combined chemistry and emission effects would increase it by 5.3 ppb/°C (2.94 ppb/°F) (correlations valid in the temperature range of 18°C to 34°C) (64°F to 93°F).

Some indirect effects related to temperature variations have also been documented. For example, in a modeling study of the Atlanta region, Cardelino et al. (1995) show that converting a forest into urban land use increases the rate of biogenic emissions from remaining vegetation because of the resulting temperature rise. The effect of an increase of 8°C (46°F) in air temperature in a forested area causes isoprene emissions to roughly double. An increase in isoprene emissions can be one factor in accelerating production of ozone, depending on a number of other variables and conditions. In a regional modeling study of the U.S. Northeast, Olerud et al. (1995) found that if temperature increases uniformly across the region by 2°C (36°F), the peak ozone concentrations in New York increase by 13 ppb over its base value. A decrease of 14 ppb in the peak was seen as a result of decreasing temperature by 2°C (36°F). Morris et al. (1991) evaluated the role of temperature on ozone air quality and found that VOC control (to reach O₃ attainment) must be increased as temperature increased.

Using a zero-dimensional model with a reaction mechanism of Stockwell et al. (1990), Walcek and Yuan (1994) show that increasing temperature, water vapor content, and sunlight intensity all increase ozone formation. They also suggest that ozone formation increases almost linearly with solar radiation but relatively less-linearly with temperature and moisture content. Under controlled conditions, an increase of 5°C (41°F) (temperature alone) results in 10%–20% increase in ozone production rates. An increase of 10% in relative humidity increases ozone formation by 5%–10%. The roles of water vapor, sunlight, and temperature are also discussed in Appendix A for some aspects of photochemistry.

The EPA estimates that an increase in air temperature of 4°C (39°F) in the New York region could cause an increase of 4% in ozone concentrations (Smith and Tirpak 1989). A study by Morris et al. (1989) found that in California, ozone concentrations could increase by 20% or 30 ppb (150 to 180 ppb) during high-ozone days in August as a result of a 4°C (39°F) increase in air temperature and that the number of days in August with ozone higher than 120 ppb could increase by 30%. There can also be a decrease in ozone concentrations under certain conditions (e.g., up to 2.5%). In the San Joaquin Valley (Fresno and Bakersfield), the increase reached about 5 ppb in daily maximum ozone. In areas farther away from anthropogenic emission sources, such as near the Sierra-Nevada, only little changes in ozone occurred.

In preliminary studies, Gery et al. (1987) found that, with all other parameters constant (including stratospheric ozone concentrations), a 2°C (36°F) temperature increase caused an increase of 2%–4% in ground-level ozone, and that an increase of 5°C (41°F) caused ozone to increase by 5%–10%. Morris et al. (1991) found that if air temperature was increased uniformly by 4°C (39°F) over the U.S. Northeast, ozone concentrations increased throughout the region and that the largest concentrations were typically in the order of 28 ppb higher (compared to a baseline of 145 ppb). In studying the Michigan region, Sillman and Samson (1995) found that

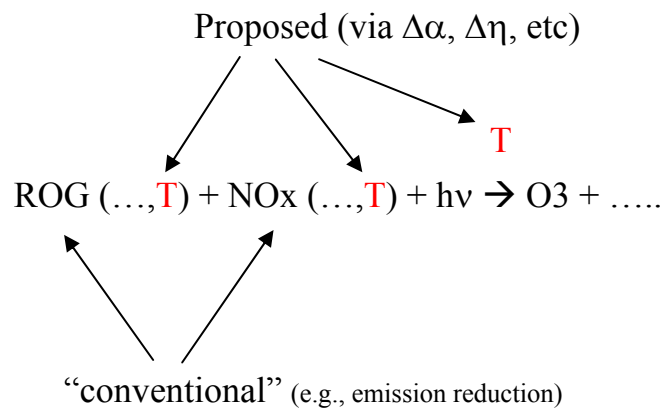
both urban and rural ozone concentrations increase with temperature above 10°C (50°F). Below 10°C (50°F) ozone levels remained near the background concentrations. Based on their simulation results for days in July and August (1988), the rate of change in peak ozone with respect to maximum temperature is 2 ppb/°C (1.1 ppb/°F) (as an average between urban and rural boundary layers) for a change in temperature between 15°C and 35°C (95°F). While ozone increased with temperature in both regions, the urban rate varied more quickly with temperature than the rural rate. For example, the simulations showed that between 15°C and 35°C (59°F and 95°F), the rural rate of ozone production increased from 2.5 to 5 ppb/day, whereas the urban production increased from 0 to about 5 ppb/day (that is, at 15°C (59°F) and below, the urban atmosphere was overall a net sink for ozone).

The foregoing discussion focused on temperature and ozone formation, since this is the main aspect of interest here; however, the appendix provides additional information on meteorology and its impacts on photochemistry.

3. Purpose of this Study

The ultimate objective of undertaking this study and possible future similar follow-ups was to bring strategies of urban surface modifications into possible regulatory consideration by air pollution control and management districts, the California Air Resources Board, and the EPA. The immediate objectives of this study were to evaluate these strategies using more recent observational field data, surface information, models, emission inventories, as well as an improved modeling methodology. Another goal was to begin addressing some of the unresolved items from past modeling studies, such as model performance and signal/noise aspects and translation of results into EPA-recommended metrics and indices.

As seen in the diagram below, the proposed strategy shifts the attainment test from quantifying emission reductions to quantifying other parameters, such as meteorological changes (e.g., temperature, as shown in the diagram). Thus while emission reduction is a “conventional” strategy that forms the basis of most regulatory plans and state implementation plans (SIPs), urban surface modification is “unconventional” in that it impacts—and hopefully improves—air quality via meteorological changes which must then be translated into emission reduction *equivalents*. Of course, other factors beyond just temperature (e.g., winds, mixing/PBL height, boundary layer fluxes) are also affected by these strategies, and in combination, can increase or decrease ozone concentrations.



The effects of such strategies on ozone concentrations can be both negative and positive, because the land-atmosphere-meteorology-chemistry system is highly non-linear; therefore, the aim is to maximize the desirable effects and minimize the inadvertent ones.

Beyond this study’s specific objectives, the modeling system and results generated by this project can have other useful applications, such as:

- Quantifying energy use at utility and building scales (and potential savings)
- Quantifying and modeling emissions of anthropogenic and biogenic precursors (and possible reductions)
- Modeling the impacts of thermal environmental changes and effects of heat waves (including the potential to offset heat-related mortality or health effects)
- Modeling and quantifying the potential impacts from a climate-change perspective (e.g., reduction in GHG emissions) as well as local effects.

As seen in **Figure 2**, two example scenarios (e.g., a base case and a modified scenario) can be compared against each other by running each through the process and using, for example, results from the photochemical model to evaluate potential benefits, differences, or any changes in air quality that would result from the modified scenario. For each case, the process begins with LULC and meteorological modeling, through a number of processors, then through emission modeling and finally through photochemical simulations. The results are compared across each step (between the base and modified scenarios), but perhaps most importantly, the final step—air quality modeling results—is where most of the impact (of interest to this study) is assessed.

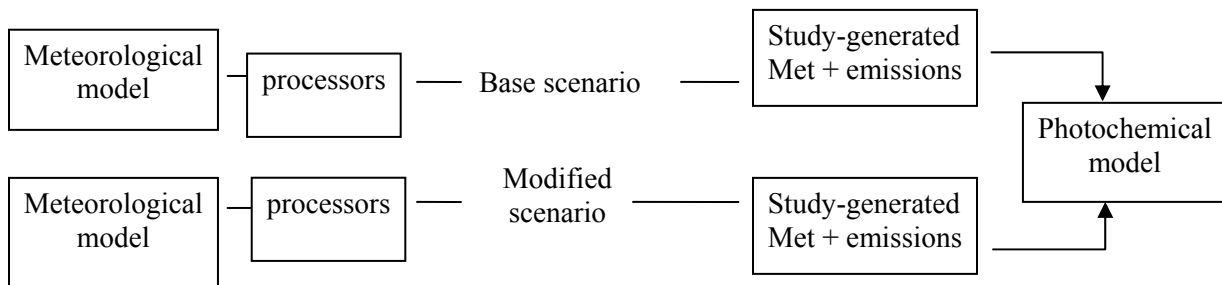


Figure 2. Model simulation sequence

Prior to the meteorological simulation step, calculations are carried out to compute certain surface characteristics of interest (e.g., albedo, roughness length, soil moisture, thermal inertia, emissivity, and so on) to prepare gridded surface input to the meteorological model. The flowchart in **Figure 3** shows the main steps in this process. The default input to the mesoscale model (e.g., MM5) is thus overridden with newly updated parameters corresponding to each scenario. The purpose of this process is to increase the resolution of the surface characterization based on more resolved data (such as the 200-m United States Geological Survey (USGS) LULC scheme, other fine-resolution and more recent characterizations, or directly observable values such as those from satellite or airborne sensing platforms), to make the input and simulations more region-specific, which is particularly important for fine-resolution modeling. The steps shown in **Figure 3** are performed before and during meteorological model initialization.

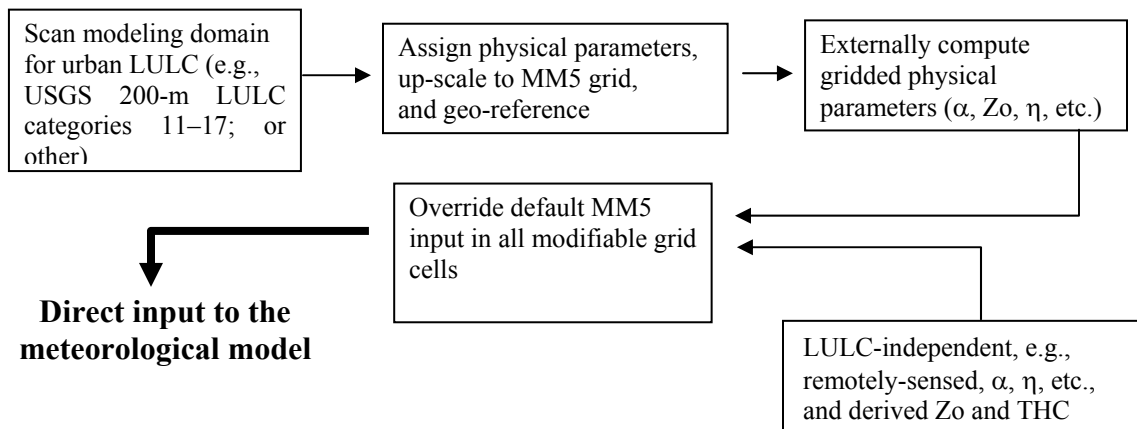


Figure 3. LULC processing step

5. Mesoscale Models

This study modifies and uses version 3.5 of the Pennsylvania State University and the National Center for Atmospheric Research (PSU/NCAR) mesoscale model MM5 (Dudhia 1993) and version 3.10 of the Comprehensive Air Quality Model with Extensions (CAMx) (Yarwood et al. 1996) models for meteorological and photochemical (air quality) modeling, respectively. A number of modifications were made in this study to increase suitability to the goals of this study.

The MM5 and CAMx models have been widely used and evaluated by the scientific and regulatory communities over the years and over a range of studies, and have been used in meteorological and air-quality modeling for regulatory applications—as well as for academic and scientific research. And although these models do not necessarily perform consistently better than others, there is sufficient accumulated experience with them to justify their use in this study. In addition, these models are also used by the air pollution control and management districts in California, such as the South Coast Air Quality Management District (SCAQMD), the Bay Area Air Quality Management District (BAAQMD), the Sacramento Metropolitan Air Quality Management District (SMAQMD), and the ARB.

5.1 Meteorological Model

The meteorological model used in this study is the PSU/NCAR MM5 (Dudhia 1993; Grell et al. 1994). The model is in the public domain and has been under continuous development at PSU, NCAR, other universities, as well as by private sector researchers and modelers. The MM5 is one of the more widely used mesoscale models in conjunction with photochemical regulatory modeling (e.g., Tesche et al. 2001; Seaman and Stauffer 1996; and Seaman et al. 1997). The MM5 was used by Taha (2003a, 2003b, 2003c) for simulating the potential impacts of urban surface modification strategies.

The MM5 is an Eulerian, three-dimensional grid, non-hydrostatic, primitive-equation prognostic model. The basis of the model are the three-dimensional prognostic equations for wind (u, v, w), temperature, perturbation pressure, and water vapor mixing ratio. The model uses a sigma-altitude (σ - z) terrain-following vertical coordinate system and allows for multiple and flexi-nesting in the horizontal. The sigma levels are defined according to a hydrostatic reference state and are time-independent (invariant) during the course of the simulation. The model allows for moving nests as well as for turning on and off selected nests during the simulation. There can be one-way nesting or two-way feedback and various smoothing methods.

In terms of numerics, the MM5 uses a leapfrog scheme in time with time-splitting, and a second-order scheme in space. For sub-grid scale parameterizations of turbulent fluxes, the model allows for a number of different (local and non-local) PBL schemes such as Eta and Gayno-Seaman, and MRF (Hong and Pan 1996), fine-resolution Blackadar (Zhang and Anthes 1982), and Mellor-Yamada (Burk and Thompson 1989). The model has a number of physics, microphysics, and convection options. Microphysics options include stable precipitation parameterizations, such as warm rain (Hsie and Anthes 1984), ice physics (Dudhia 1993), ice and graupel (Tao and Simpson 1993), and the Schultz and Reisner schemes (Schultz 1995; Reisner et al. 1998).

The model also has a number of cumulus parameterization schemes (e.g., Anthes 1977; Grell et al. 1994; Kain and Fritsch 1993; Arakawa-Schubert (Grell et al. 1991); and Betts and Miller 1986). It allows for coupling with land-surface models (e.g., PM and OSU/NOAH (Pan and

Mahrt 1987)). The MM5 has Four-Dimensional Data Assimilation (FDDA) capabilities (Stauffer and Seaman 1990) for both analyses and observational (station, point) nudging. Use of FDDA can in certain cases improve the model performance, especially over longer simulation time frames, depending on the actual conditions being simulated.

The model's grid is based on the Arakawa-B stagger configuration, where scalars are defined at the center of the grid and velocity variables are allocated at the corners. In the vertical, all variables are defined at half-sigma levels except for the vertical component of velocity, which is defined at the full sigma levels. Minimum horizontal grid resolution is on the order of 500 meters (although in theory, the model can be run at smaller grid spacing). In the vertical, resolution is variable and stretched (for example: a few meters thick near the ground to hundreds of meters thick near model top). Of course, both horizontal and vertical resolutions can be significantly improved if sub-grid-scale parameterization is modified to accommodate such.

Initialization of the model is based on integrated divergence removal. Initial and boundary-condition data are typically specified from large-scale (synoptic) three-dimensional analyses and usually applied at the outermost grids of the coarse domains. Example analyses are those from the NCAR NCEP Reanalysis Project (NNRP) and Global Data Assimilation System (GDAS) and are available from the NCAR archives. The model's top boundary conditions are those of a radiative or rigid layer and at the surface, those of prognostic surface temperature, constant or varying water surface temperature, and a constant-flux surface layer (fluxes based on similarity theory). At the lateral boundaries, time-dependent in/outflow (relaxation) conditions are assumed. The model produces comprehensive forecast variables (e.g., wind field, temperature, water vapor, cloud rain and ice, boundary-layer fluxes and variables, perturbation pressure), and host of derived quantities.

5.2 Photochemical Model

This study used version 3.10 of the CAMx model (Yarwood et al. 1996). The CAMx is an Eulerian, three-dimensional grid, photochemical model that allows simulation and assessment of "one atmosphere", i.e., ozone (gaseous) and particulate matter (PM) air pollution. This state-of-science model is highly modular in structure, which facilitates updates, modifications, and integration of user-developed algorithms and routines. In addition, the model allows for a number of coordinate systems (map projections) and for nested configurations to provide detail and efficiency in simulating larger domains. More recent versions (e.g., version 4.11s) incorporate additional improvements in treatment of ozone and PM. At its core, CAMx uses a continuity equation (advection-diffusion equation) closed by k-theory for both horizontal and vertical advection, transport, and diffusion. As with other similar photochemical models (such as the Urban Airshed Models (UAM-IV, UAM-V), and Community Multiscale Air Quality (CMAQ) model, for example), CAMx solves the advection-diffusion equation and accounts for emissions (sources), dispersion/transport, chemical transformations, and removal (sinks). The typical pollutant continuity equation for a species "i" is:

$$\frac{\partial C_i}{\partial t} = -\nabla_h \cdot \vec{V}_h C_i + \left[\frac{\partial C_i e}{\partial z} - C_i \frac{\partial}{\partial z} \left(\frac{\partial h}{\partial t} \right) \right] + \nabla \cdot \rho K \nabla \left(\frac{C_i}{\rho} \right) + \left\langle \frac{\partial C_i}{\partial t} \right\rangle_{emi} + \left\langle \frac{\partial C_i}{\partial t} \right\rangle_{rem} + \left\langle \frac{\partial C_i}{\partial t} \right\rangle_{chem}$$

where C is concentration, V is wind vector (the subscript “h” indicates horizontal component), e is vertical entrainment rate, z is height, h is layer-interface height, K is diffusivity, ρ is density, and the subscript for the last three terms indicate emission (source), removal (sink), and chemistry (e.g., reactions, transformations). In CAMx, this equation is solved numerically, using a time-splitting (operator splitting) method to evaluate the various terms separately and then to evaluate their combined contributions. Advection solution is split into vertical, N-S, and E-W in a mass consistent fashion. The chemistry term of the above equation can be solved with different chemical and lumping mechanisms, e.g., CB-IV or the Statewide Air Pollution Research Center model (SAPRC-99). Both dry and wet deposition (scavenging) can be accounted for in CAMx.

The model grid is based on a staggered Arakawa-C configuration. In the horizontal, scalars and concentrations are located at cell center to represent cell-averaged conditions, whereas wind vector is carried at the edges (cell interfaces) and the u - and v - components are staggered with respect to each other. The meteorological fields are passed from the meteorological model (e.g., MM5) to CAMx into this grid configuration. In the vertical, scalars are situated at cell center (halfway between layer interfaces), except for vertical entrainment rate and vertical diffusivities, which are at the layer interfaces.

CAMx also has useful features, such as: (1) a flexible two-way nesting and feedback structure, and the ability to turn on or off selected nested grids during the course of the simulation, which allows computing resources to be used more efficiently, (2) the availability of versions of the CB-IV chemical mechanism as well as the SAPRC99, which provides alternate methods of VOC lumping in surrogate species, (3) options for standard or fast chemical kinetics solvers which can provide significant model speedup where needed, (4) plume-in grid simulation capabilities (inorganic chemistry) to handle the details of point-source plumes (e.g., NO_x plumes) within the grid until the plume has dispersed well enough for accurate representation within the model grid structure, (5) ozone source apportionment technology (OSAT) which is a CAMx feature that enables users to track the source regions and/or source categories contributing to resulting ozone concentrations at specific (user-selected) grid cells, (6) process analysis (PA) capabilities, whereby the results can be evaluated in terms of model formulation and the relative role of various terms and processes (e.g., process rates for advection, diffusion, chemistry, deposition) in the conservation relations, or provide reaction rate data for all chemical mechanisms in selected grid cells, (7) an advanced photolysis model (NCAR’s Tropospheric Ultraviolet and Visible (TUV) radiative transfer and photolysis model) that allows modification of photolysis rates to account for changes in albedo, ozone column, zenith angle, elevation, etc., and an option to adjust these rates for the impacts of clouds based on the Regional Acid Deposition Model (RADM).

Environ Inc. has recently added new capabilities to CAMx, including: (1) three modules for improved treatment of particulate matter, (2) reactive tracer tracking, and (3) wet deposition of particulate matter and gases. For dry deposition, there are separate resistance models for gases and aerosols. Similarly, it has separate wet deposition models for gases and aerosols.

5.3 Model Data

Input data used in the land-use, meteorological, and photochemical modeling and processing steps consist of the following:

1. **USGS 200-m resolution, 38-category LULC.** These data are used in deriving themophysical input to override the default surface characterization in the meteorological and photochemical models. The urban part of this LULC classification scheme is resolved into seven sub-categories, which are discussed in Section 11.
2. **Historical/episodic analyses and large-scale observational surface and upper-air data (for input to the meteorological model) to characterize base-case episodic conditions.** In this study, the National Centers for Environmental Protection/(NCEP)/NCAR analyses (NNRP) were used to provide initial and boundary conditions for the MM5 simulations. In addition, field-intensive aerometric/pollutant species observational data from the Southern California Ozone Study of 1997 (SCOS-97) and the Central California Ozone Study of 2000 (CCOS-00) were used to supplement the model input (e.g., in FDDA), as well as for evaluating base model performance.
3. **Episodic local air-quality data and emission inventories (for input to the photochemical model).** In this study, the CAMx input data were obtained from the California Air Resources Board, the South Coast Air Quality Management District (AQMD), and the Bay Area AQMD, specifically for the SCOS-97 and CCOS-00 field campaign episodes. These inventories were corrected in this study (e.g., updating biogenic hydrocarbon emissions), for changing meteorological conditions across a number of scenarios and for different base cases. It is beyond the scope of this study to completely re-generate emission inventories (from the bottom up), other than correcting or updating the emissions as described above. It is to be noted that the base emission inventories, especially for CCOS 2000 episodes, are still undergoing evaluation, quality checks, and updates/modifications by the ARB and the air districts.

5.3.1 Emission inventories

This study uses historical emission inventories for the modeling episodes and domains defined in this report. **Tables 3 and 4** give the overall total emissions for the SCOS-1997 and CCOS-2000 episodes, respectively. These may be different from the day-specific emissions used in the photochemical modeling. Air quality management plans, such as those developed by the SCAQMD and the BAAQMD, also identify two types of future emission inventories. “Future-year baseline emissions” include no additional emission controls beyond currently installed options, but account for increases in emissions as the result of increases in population, vehicle miles traveled, and other factors. On the other hand, “future-year controlled emission inventories” is a type of scenario developed for a future year where the Air Quality Management Plan (AQMP) emission controls are applied onto the future-year baseline emissions. In this phase of the study and the simulation results discussed in this report, only historical emissions were used. In **Table 3**, two regions are given: one corresponding to the South Coast Air Basin, and the other corresponding to the entire modeling domain (discussed in Section 6), including the South Coast Air Basin. The entries in **Table 3** do not include biogenic emissions. Biogenic VOC emissions for Southern California during this episode were in the order of 800 TPD on August 5 and 680 TPD on August 6. In this modeling work, of course, these will change from one meteorological scenario to another, as correction is done for the effects of temperature changes

and other factors. Also, no values were given for biogenic NO_x emissions, but are presumably small.

Table 3. Historical August 1997 emission inventory for the South Coast Air Basin

	South Coast Air Basin (TPD)				Modeling Region (TPD)**		
	VOC	NO _x	CO		VOC	NO _x	CO
<i>on-road</i>	580	822	5634		887	1244	8691
<i>off-road</i>	218	341	1246		301	521	677
<i>stationary</i>	464	120	56		759	351	300
TOTAL	1262	1283	6936		1947	2116	9668

** This does not include emissions from Mexico.

Source: SCAQMD AQMP 2003

Similarly, **Table 4** summarizes the historical emission inventory for Central California. Three regions are given as well as a remainder for other regions in the CCOS-2000 domain. The emissions given in Table 4 are averages over three days of the episode, i.e., July 30, July 31, and August 1, 2000. There is large variability in emissions between July 30, a Sunday, and July 31 and August 1, a Monday and Tuesday, respectively.

Table 4. Historical 2000 CCOS emission inventory (TPD) for selected regions

	CO	NO _x	SO _x	TOG
SF Bay Area				
<i>On-Road</i>	1960	312	3	217
<i>Off-Road</i>	730	181	2	127
<i>Stationary + ship</i>	151	126	76	808
<i>Biogenics</i>	--	10	--	397
Sacramento				
<i>On-Road</i>	655	95	1	74
<i>Off-Road</i>	277	63	1	42
<i>Stationary + ship</i>	36	24	1	185
<i>Biogenics</i>	--	12	--	430
San Joaquin Valley				
<i>On-Road</i>	1396	195	2	142
<i>Off-Road</i>	487	184	4	81
<i>Stationary + ship</i>	64	180	31	1247
<i>Biogenics</i>	--	65	--	842
Domain remainder				
<i>On-Road</i>	1861	260	2	206
<i>Off-Road</i>	636	186	5	156
<i>Stationary + ship</i>	574	173	31	949
<i>Biogenics</i>	--	75	--	4149

Source: (Environ 2002)

6. Study Domains and Simulation Grids

The modeling domains for Southern and Central California are shown in **Figure 4** and **Figure 5**, respectively. The horizontal grid description is as follows:

- For the Southern California meteorological modeling domain, the innermost grid (in MM5) is: $82 \times 118 \times 5 \text{ km}$, shown as D03 in the figure. Two additional grids, $82 \times 118 \times 15 \text{ km}$ and $68 \times 80 \times 45 \text{ km}$, are added to the outside of this nest. In the vertical, 28 half-sigma levels were used in most scenarios. In some cases, not reported here, up to 48 levels were used to test the model performance with improved resolution near the ground. For the CAMx simulations, the grid is: $80 \times 116 \times 5 \text{ km}$, corresponding roughly to the innermost domain (D03) shown in **Figure 4**. In the vertical, 16 levels were used.
- For the Central California (CCOS) domain, the MM5 is setup with an innermost grid of $187 \times 187 \times 4 \text{ km}$ (D02 in figure). The outer coarse grid, shown in **Figure 5** is $187 \times 187 \times 12 \text{ km}$. In the vertical, 28 to 48 half-sigma levels were tested. For the photochemical simulation (CAMx), the grid is $185 \times 185 \times 4 \text{ km}$ with 16 vertical levels (corresponding roughly to the inner domain shown in the figure).

Some additional information on the vertical structure of the MM5 as configured for the simulations in this study is given in **Table 5** and the mapping of vertical layers from MM5 to CAMx is shown in **Table 6**. The top level in the meteorological simulations (K=1) corresponds to pressure level 50 mb which, as seen in Table 6, corresponds roughly to 18.8 km above mean sea level.

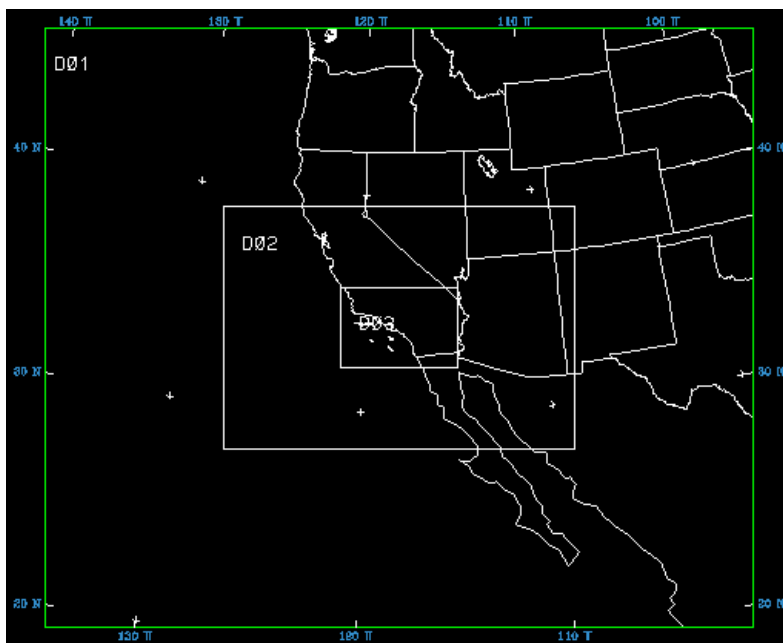


Figure 4. Southern California modeling domain and nested grids. In some final simulations, only D02 and D03 were used. In addition, D03 is re-run via NESTDOWN and used to provide meteorological fields to the photochemical model and simulations.

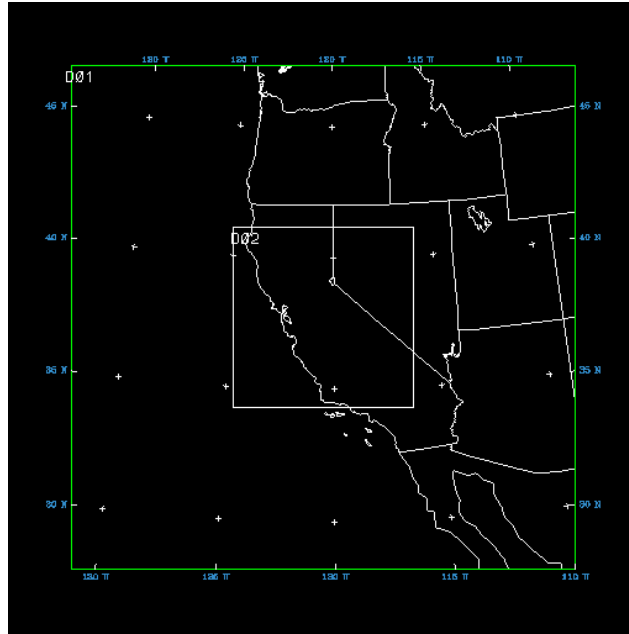


Figure 5. Central California modeling domain and nested grids. Nest D02 is re-run via NESTDOWN and used to provide meteorological fields to the photochemical model and simulations.

Table 5. Vertical configuration of MM5
(for simulations discussed in the report)

K	σ (K)	$\frac{1}{2}\sigma$ (K)	$\Delta\sigma$ (K)
1	0.0000	0.0125	0.0250
2	0.0250	0.0375	0.0250
3	0.0500	0.0750	0.0500
4	0.1000	0.1250	0.0500
5	0.1500	0.1750	0.0500
6	0.2000	0.2250	0.0500
7	0.2500	0.2750	0.0500
8	0.3000	0.3250	0.0500
9	0.3500	0.3750	0.0500
10	0.4000	0.4250	0.0500
11	0.4500	0.4750	0.0500
12	0.5000	0.5250	0.0500
13	0.5500	0.5750	0.0500
14	0.6000	0.6250	0.0500
15	0.6500	0.6750	0.0500
16	0.7000	0.7250	0.0500
17	0.7500	0.7750	0.0500
18	0.8000	0.8200	0.0400
19	0.8400	0.8550	0.0300
20	0.8700	0.8850	0.0300
21	0.9000	0.9150	0.0300
22	0.9300	0.9400	0.0200
23	0.9500	0.9600	0.0200
24	0.9700	0.9750	0.0100
25	0.9800	0.9840	0.0080
26	0.9880	0.9915	0.0070
27	0.9950	0.9963	0.0025
28	0.9975	0.9987	0.0025
29	1.0000		

Table 6. MM5 and CAMx vertical levels correspondence

K	σ	~AGL (m)	CAMx Layers
1	0.0000	18870	
2	0.0250	17170	
3	0.0500	15800	
4	0.1000	13670	
5	0.1500	12010	
6	0.2000	10630	
7	0.2500	9450	
8	0.3000	8410	
9	0.3500	7490	
10	0.4000	6650	
11	0.4500	5880	
12	0.5000	5170	
13	0.5500	4510	16
14	0.6000	3890	15
15	0.6500	3310	14
16	0.7000	2770	13
17	0.7500	2250	12
18	0.8000	1760	11
19	0.8400	1380	10
20	0.8700	1100	9
21	0.9000	840	8
22	0.9300	580	7
23	0.9500	410	6
24	0.9700	245	5
25	0.9800	160	4
26	0.9880	100	3
27	0.9950	40	2
28	0.9975	20	1
29	1.0000	0	Surface

7. Additional Model Configurations and Options

In addition to the grid and domain information provided in the foregoing discussion, the following summarizes a number of options and configurations used in the present simulations:

- A. The 24-category USGS LULC system was used in the coarse grids, as well as in some non-modifiable areas in the finest grid. This is a coarse classification scheme that does not allow much detail in urban areas (only one urban category is recognized), and thus is overridden in modifiable grid cells.
- B. The default gridded surface characterization (24-category LULC discussed in A, above) input to the MM5 is overridden (using calculations discussed in Section 4, Approach) in 1291 modifiable grid cells (5 by 5 km each) in the Southern California domain and 1944 grid cells (4 by 4 km each) in the Central California domain. The modifiable grid cells were identified based on LULC analysis of California and are those that contain at least a certain amount of urban land use.
- C. The NCEP/NCAR (NNRP) 6-hourly reanalysis data were used for initializing and providing boundary conditions for the MM5 in simulating the selected episodes. As discussed elsewhere in this report, in some SCOS scenarios (and in results presented here for the SCOS component of this study) the NNRP analyses were modified to generate “warmer” boundary conditions (e.g., +2°C (or +3.6°F) to compensate for systematic under-prediction of temperature (temperature bias is discussed later in the section on model performance).
- D. The MM5 is run with 29 sigma levels (for both SCOS and CCOS domains) with the top of the domain at 50 mb.
- E. *Analysis* nudging was used in different manners depending on nest level (see F below). Point (station, observational) nudging was used initially in a number of scenarios for both SCOS and CCOS domains/episodes but did not improve model performance (and thus only analysis nudging was used).
- F. Four-dimensional *analysis* nudging was done everywhere in the coarse grids (in the vertical and horizontal directions). In the finest grid, nudging was done only above the boundary layer and in a manner such that the nudging coefficients increase gradually with height away from the PBL top (as seen, for example, in **Figure 6a**).
- G. In addition to space-varying the weight of nudging, the coefficients were also varied to test any impact on model performance but were generally kept as small as possible to not interfere with the signal while improving model performance.
- H. Where nudging was done, all meteorological variables (temperature, wind, and water vapor mixing ratio) were nudged.
- I. Two-way feedback was used in all nests including the finest grid. When a full episode is completed with this configuration, the simulated fields are re-downscaled (via NESTDOWN) from the coarser grids to the innermost, finest one, which is then re-run (simulated again) as a standalone grid for each scenario. The output from the standalone grid is then used in emissions calculations and in driving the photochemical model.
- J. For microphysics, the “simple-ice” scheme (Dudhia 1993) was used. In this scheme, cloud, rainwater, and ice fields are predicted explicitly using microphysical processes.
- K. For sub-grid scale parameterizations, the MRF PBL scheme (Hong and Pan 1996) was used. This option is also appropriate for fine-resolution PBL. Turbulent kinetic energy (TKE) schemes such as the ETA and the Gayno-Seaman PBL were also used and

- evaluated during the earlier stages of this study, but model performance (especially the signal), was deemed more suitable and less noisy with the MRF PBL option.
- L. Observational mesoscale forcings and circulation details were assimilated into the simulations (via MM5 pre-processors, i.e., the LITTLE_R and RAWINS programs for objective analysis of direct observations). In some cases, runs were performed with no mesoscale forcing included to evaluate impact on model performance; it was observed that the inclusion of mesoscale detail for this study's configuration and episodes slightly improved model performance.
 - M. The diagnosis of vertical diffusivity profiles (from MM5 to CAMx) was based on a profile method (O'Brien 1970). Based on initial results, the vertical diffusivities in the Southern California simulations were scaled down to offset over-prediction of mixing height by the MRF PBL scheme in the MM5. It is known that the MRF scheme often overestimates mixing heights/PBL depth (due to a number of reasons, including the way convective velocity (w^*) is parameterized and the use of Bulk Richardson number along with a critical value to determine PBL height). Two methods are suggested for countering this overestimation: (1) decrease the value of the critical Richardson number (Ri_c), and (2) adjust (scale down) vertical diffusivity, K_v , as was done in this study. **Figure 6b** shows, for example, how K_v was scaled down (for SCOS simulations) beginning at level 5 and in increasing weight.
 - N. The photochemical model (CAMx) is run with 16 vertical layers (as shown earlier in **Table 6**). The first 16 levels in MM5 are mapped into the 16 layers of CAMx.
 - O. Biogenic hydrocarbon emissions from *existing* vegetation are updated (corrected) for each scenario, including the base case, to account for the effects of varying meteorology (temperature, solar radiation, water vapor) and CO_2 concentrations on emissions. The corrections are done using a relation by Guenther et al. (1993, 1999).
 - P. The chemical reaction simulations in this study were performed using the CB-IV mechanism (Gery et al. 1988). The SAPRC (99) mechanism was not used.
 - Q. Dry deposition processes were accounted for, where applicable.
 - R. The plume-in grid model (in CAMx) was used to simulate the dispersion of plumes (mainly NO_x) until the plume concentrations became resolvable at the grid resolution.
 - S. Cloud and rainfall processes were accounted for in the photochemical simulations.
 - T. The boundary concentrations for chemical species are those of "EPA/ARB-clean" conditions (see next paragraph and **Table 7** for more information)

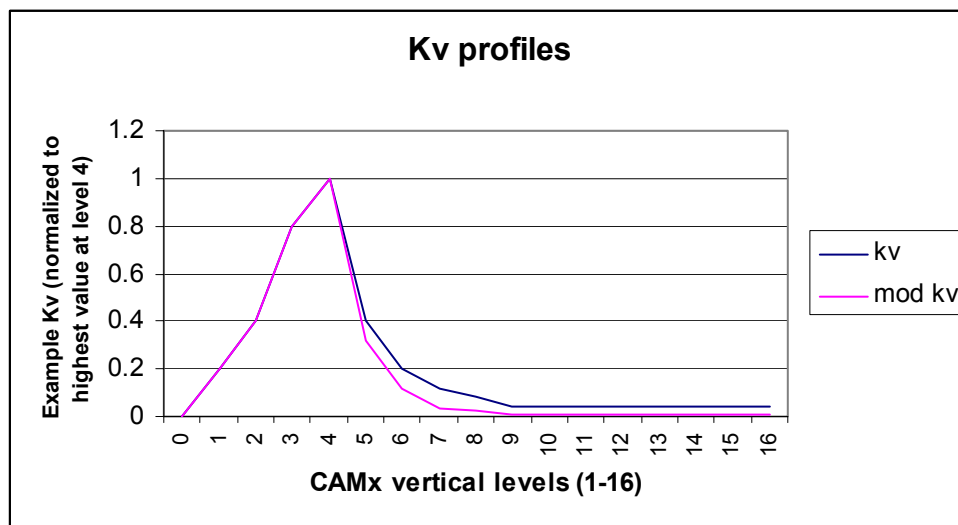
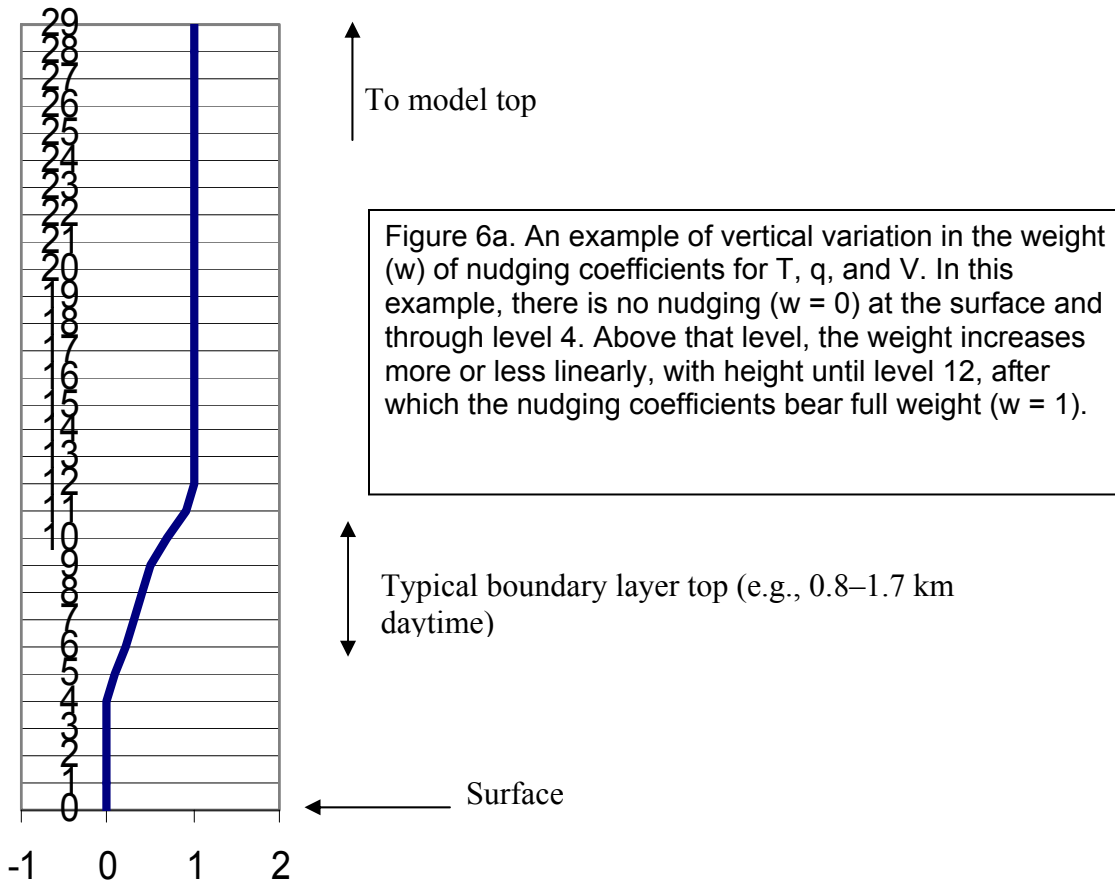


Figure 6b. Example scaling of vertical diffusivity in SCOS simulations

The species-concentrations boundary conditions used in this study are based on the ARB clean boundary and top concentrations. These conditions are slight modifications to the recommended “EPA continental average” boundary conditions for gaseous pollutants. For the following species, the concentrations used in the present simulations are given in **Table 7**. Where there are two numbers, this indicates different concentrations for north-south compared to east-west boundaries. Except for two entries, there is essentially no difference between the assumed boundary concentrations for the SCOS or CCOS episodes.

Table 7. EPA/ARB clean boundary conditions used in this study
(last digit rounded)

	SCOS-1997		CCOS-2000	
	Lateral (ppm)	Top (ppm)	Lateral (ppm)	Top (ppm)
O ₃	0.04	0.06	0.04	0.07
NO	0.000001	0.001	0.000001	0.000
NO ₂	0.000001	0.002	0.000001	0.002
CO	0.35 / 0.20	0.2	0.35 / 0.20	0.2
PAR	0.0149 / 0.041	0.0149	0.0149 / 0.041	0.0149
ETH	0.002 / 0.001	0.0005	0.002 / 0.001	0.0005
OLE	0.0003 / 0.0008	0.0003	0.0003 / 0.0008	0.0003
TOL	0.0002 / 0.0005	0.0002	0.0002 / 0.0005	0.0002
XYL	0.00009 / 0.0002	0.0001	0.00009 / 0.0002	0.0001
FORM	0.002 / 0.005	0.002	0.002 / 0.005	0.002
ALD2	0.0005 / 0.001	0.0006	0.0005 / 0.001	0.0006
ISOP	0.000009	0.0000	0.000009	0.0000

O₃=ozone; NO=nitric oxide; NO₂=nitrogen dioxide; CO=carbon monoxide; PAR=photosynthetically active radiation; ETH=ethene; OLE=olefin; TOL=toluene; XYL=xylene; FORM=formaldehyde; ALD2=higher aldehydes; ISOP=isoprene.

8. Episodes

The episodes used in this modeling study were chosen to be compatible with those used by regulatory agencies in California. The photochemical episodes correspond to August 3 through 7, 1997 for Southern California (SCOS-97) and July 29 through August 4, 2000 for Central California (CCOS-2000). The meteorological modeling episodes are longer, to allow for two spin-up days before the start of the photochemical episode, and in some cases the meteorological modeling also lasts one or two days longer.

8.1 August 1997 (Southern California)

According to a CART-based (classification and regression tree) scheme (South Coast Air Quality Management District; AQMP 1989), all days in the August 1997 episode of Southern California were of Type-1 severity, which is the highest of the 5 levels included in that classification system. Type-1 has accounted for over 50% of all days exceeding the 1-hour federal standard, averaged over the period 1996–2002 (SCAQMD AQMP 2003). Because of this, there is great interest in modeling and studying this episode. In this study, August 5 and 6 are considered the primary days and the episode is described in the SCAQMD's 2003 Air Quality Management Plan (www.aqmd.gov/aqmp/AQMD03AQMP.htm). This episode resulted in the Los Angeles Basin's second highest annual maximum observed ozone concentration of 187 ppb at Riverside-Rubidoux in the eastern part of the Basin. The episode occurred during typical ozone-conducive conditions (e.g., stagnation, small pressure gradients across the region, high temperatures, large solar radiation input, and low-level inversions). Wind transport during the episode was moderate and onshore flow was generally weak as a result of the above conditions. Beginning late on August 6, a coastal eddy formed, and became well-developed on August 7. This caused a southerly transport of pollutants into the Santa-Clarita and Antelope Valley regions, where near-peak concentrations were also observed on August 6.

Peak inland temperatures were consistently higher than 38°C (100°F) during the episode, and the highest temperature of 45°C (113°F) in the Los Angeles Basin was observed in Riverside on August 5. The mesoscale temperature, wind, and pressure gradients were relatively consistent from August 3 through most of August 6, but later changed because of the eddy development on that day and on August 7. As a result of the weak pressure gradient, the sea breeze flow on August 5 was disorganized and did not reach the farther inland parts of the Basin or the northern and eastern mountain passes. However, the so-called "Southern Transport Route," which occurred on August 5, caused the transport of coastal emissions through the Santa Ana Pass and into the eastern part of the Los Angeles Basin (e.g., Corona, Riverside, Moreno Valley, Perris). On August 6, when the coastal eddy developed and southerly flow began to strengthen and continued through August 7, the sea-breeze front was pushed further inland, and the flow continued onto the northern mountain passes such as Newhall Pass and into Santa Clarita.

Table 8 summarizes the peak observed ozone concentrations in the Basin during that episode. For further information on that episode, refer to the South Coast AQMD's 2003 Air Quality Management Plan.

Table 8. Observed peak ozone in Southern California

Date in 1997	Observed peak	Location of observed peak
August 4	140 ppb	Central San Bernardino Mountains
August 5	187 ppb	Rubidoux
August 6	170 ppb	Central San Bernardino Mountains
August 7	150 ppb	Central San Bernardino Mountains

8.2 July–August 2000 (Central California)

This Central California episode, especially on the primary day of interest in this study (July 31, 2000), was characterized by strong inversion layers, as evidenced by a high 500-mb geopotential height and a high 850-mb temperature (indicating subsidence motion). It is also typical of the California conditions conducive to ozone build up, e.g., a high-pressure system (Pacific High) and its extension over California, which prevents cyclonic systems from passing through the area. The result is a stagnant air mass that is poorly mixed (Lehrman et al. 2001). In all days of the episode, high ozone was observed in Livermore and its transport from the San Francisco Bay Area was strong. Flow through the Bay Area affected the regions of Fresno and Bakersfield, but had no direct impact on Sacramento on July 31. The flow arriving at Sacramento on that day passed further north of the Bay Area.

Table 9 shows peak observed ozone concentrations in areas of Central California. For further information on this episode, refer to the Bay Area AQMD’s 2003 air quality management plan (www.baaqmd.gov/pln/plans/ozone/2003_modeling/index.htm).

Table 9. Observed peak ozone in the Central California domain

Date in 2000	Observed peak	Location of observed peak
July 31	126 ppb	Livermore
August 1	133 ppb	Sacramento
August 2	151 ppb	San Joaquin (Edison)

9. Model Performance Evaluation

This project evaluated meteorological and photochemical base case model performances for a number of scenarios (i.e., a number of model configurations, data sources, and parameterizations); performing both qualitative and quantitative evaluations. The meteorological model's general performance attributes and its skills in reproducing upper-air and near surface flow and temperature fields were evaluated qualitatively. For *surface and near-surface* meteorological and species concentrations fields, relatively more quantitative evaluations were performed, since this is a region of interest in this study (e.g., impacts of near-surface changes caused by surface modifications).

A number of indices have been used in the scientific and regulatory communities to evaluate meteorological and photochemical model performance, e.g., those recommended by the EPA (1991). Some of these indices are defined next, along with their recommended tolerances or desirable ranges.

A. Accuracy of peak prediction, unpaired (UA):

$$UA = \frac{V_p - V_o}{V_o}$$

Where V_p and V_o are the predicted and observed values of the peak concentration, respectively. This applies to the highest concentration across all hours and monitors. The EPA-recommended value for UA is within $\pm 20\%$.

B. Normalized bias (mean relative error, MRE):

$$MRE = \frac{1}{N} \sum_{i=1}^M \sum_{j=1}^H \frac{V_p(i, j) - V_o(i, j)}{V_o(i, j)}$$

Where, M is the total number of monitors, H is total number of hours (of available observations) at each monitor, and N is the total number of monitor-hours considered in this test (metric), $N=M \times H$. The EPA-recommended value for MRE is to be within $\pm 15\%$. Because low observed concentrations (e.g., of ozone) can be erroneous, it is a common practice to ignore in MRE calculations those observation-simulation data pairs in which the observations are smaller than a certain threshold, e.g., 60 ppb ozone (as will be used in this report).

C. Gross error (mean unbiased relative error, MURE):

$$MURE = \frac{1}{N} \sum_{i=1}^M \sum_{j=1}^H \frac{|V_p(i, j) - V_o(i, j)|}{V_o(i, j)}$$

The EPA-recommended value for MURE is 35% or smaller. The same threshold (for example 60 ppb) for rejecting observation-simulation data pairs also applies in calculating MURE.

D. Root mean square error (RMSE) (E):

$$E = \left\{ \frac{1}{N} \sum_{j=1}^H \sum_{i=1}^M (V_p(i, j) - V_o(i, j))^2 \right\}^{1/2}$$

E. Unbiased RMSE (E'):

$$E' = \left\{ \frac{1}{N} \sum_{j=1}^H \sum_{i=1}^M \left[(V_p(i, j) - \bar{V}_p) - (V_o(i, j) - \bar{V}_o) \right]^2 \right\}^{1/2}$$

which is RMSE after removal of systematic bias.

F. Standard deviations of observations and predictions (σ and σ_o):

$$\sigma_o = \left\{ \frac{1}{N} \sum_{j=1}^H \sum_{i=1}^M (V_o(i, j) - \bar{V}_o)^2 \right\}^{1/2} \quad \text{and} \quad \sigma = \left\{ \frac{1}{N} \sum_{j=1}^H \sum_{i=1}^M (V_p(i, j) - \bar{V}_p)^2 \right\}^{1/2}$$

where E is RMSE, E' is unbiased RMSE (i.e., after removal of constant bias), and σ and σ_o are the standard deviations of the simulated and observed parameters. Of course, any of the above indices can also be evaluated at any one location ($i=1$), time interval ($j=1$), or subdomain.

Pielke (1984, 2002) recommends the following model skills:

1. $\sigma \sim \sigma_o$
2. $E < \sigma_o$
3. $E' < \sigma_o$
4. $E' / \sigma_o \leq 0.6$

Thus criteria A through F above provide some means to evaluate the base model performance for both meteorology and photochemistry.

For California, DaMassa et al. (1992) and Tesche (1988) provide three classes of photochemical model performance:

Class A represents an ideal performance by a photochemical model. This is based on a successful multi-species evaluation. For ozone, the criteria for the entire modeling domain are:

- Unpaired peak accuracy: $UA \leq \pm 10\%$
- Bias: $B \leq \pm 5\%$
- Gross error: $E \leq 25\%$

For each modeling domain sub-region, the criteria are:

- Bias: $B \leq \pm 30\%$
- Gross error: $E \leq 40\%$

Class B represents a typical performance. As with Class A, this also is based on a successful multi-species evaluation. For ozone, the criteria for the entire modeling domain are:

- Unpaired peak accuracy: $UA \leq \pm 20\%$
- Bias: $B \leq \pm 15\%$
- Gross error: $E \leq 35\%$

For each modeling domain sub-region, the criteria are:

- Bias: $B \leq \pm 30\%$
- Gross error: $E \leq 40\%$

Class C is marginal performance. For ozone, the ranges for the entire modeling domain are:

- Unpaired peak accuracy: $UA > \pm 20\%$
- Bias: $B > \pm 15\%$
- Gross error: $E > 35\%$

Unlike the situation for photochemical model performance (e.g., EPA 1991), there is relatively less quantitative agreement on what constitutes a good meteorological model performance in terms of indices like MRE and MURE. However, upon a general evaluation and review of a number of modeling studies (e.g., Tesche et al. 2001; Environ 2001) there appears to be an informal consensus, for example, that a good meteorological model performance would embody the following:

Air temperature MRE (bias)	$\leq \pm 0.5 \text{ K}$
Air temperature MURE (error)	$\leq 2.0 \text{ K}$
Wind speed MRE (bias)	$\leq \pm 0.5 \text{ m s}^{-1}$
Wind speed MURE (error)	$\leq 2.0 \text{ m s}^{-1}$ (proposed)
Wind direction MURE (error)	$\leq 30^\circ$

9.1 Model Performance Issues Specific to this Application

Modeling the meteorological and air quality impacts of surface modification strategies adds another issue to model performance evaluation that is related to the signal and noise (versus performance). Of course, any modeling work will involve some issues and aspects related to model performance, noise, and signal, but with this strategy, surface modifications affect both meteorology and emissions/photochemistry, unlike other control strategies that typically affect only emissions. As a result, each surface modification scenario (e.g., various levels of increased surface albedo and vegetative cover) has the potential to alter the quality of model performance (both meteorological and photochemical), as illustrated in **Figure 7**. Thus, some issues must be considered in this study and type of applications, for example:

- Evaluate the appropriate extent of using FDDA and the strength of nudging to yield good model performance without affecting the clarity of the signal (too strong FDDA can cause noisy signals or damp them)
- If point (station) nudging FDDA is used, evaluate the impact of avoiding nudging near and in modifiable urban areas of the domain
- Evaluate the impacts of assimilating mesoscale analyses in the meteorological model. Although this is generally a good practice for improving model performance and adding regional/episodic detail, it may also interfere with the signal in certain cases
- Evaluate the impacts of modified surface input and other parameters

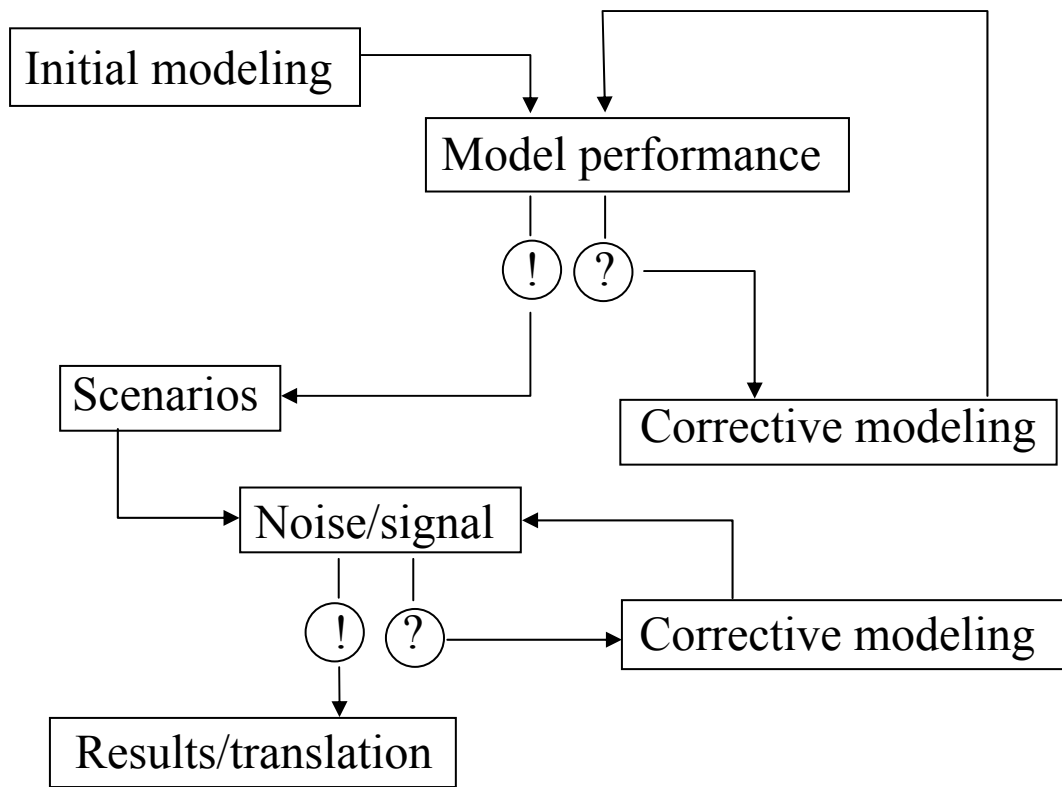


Figure 7. Model performance and signal/noise

10. Replication of ARB Simulations

During the early stages of this study, one of the first tasks after obtaining emission inventories from the ARB and air districts (for the CCOS-2000 and SCOS-1997) was to locally replicate their simulation results. The purpose of this exercise was simply to ensure that the emission data obtained and the modeling systems set up and used in this project were relatively consistent with those of regulatory agencies and that there were no major errors, omissions, or data quality issues. It was straightforward to replicate both domains and episodes. No detailed analysis was performed at that stage beyond qualitative examination and comparison of the original and replicated ozone concentrations fields and related input/output data. **Figure 8** shows an example snapshot output from this study's initial replication of the ARB simulations of the SCOS-97 domain and episode. It shows the simulated peak concentrations at 1500 on August 5, 1997, which was within 3 ppb of the ARB's simulated peak. Similarly, **Figure 9** depicts a snapshot example of the CCOS replication. In this case, the hour at 1300 LST on July 31, 2000 is shown, and the peak concentration is 1 ppb lower than that of the ARB's simulations (235 ppb at this hour).

Significant improvements beyond these simulations were completed before a final base case was established (for each of CCOS and SCOS) and used as a baseline for studying the potential air quality benefits of surface modification strategies. The base cases, for each of the SCOS and CCOS episodes and domains, as well as corresponding model performance improvements, are discussed in Section 12.

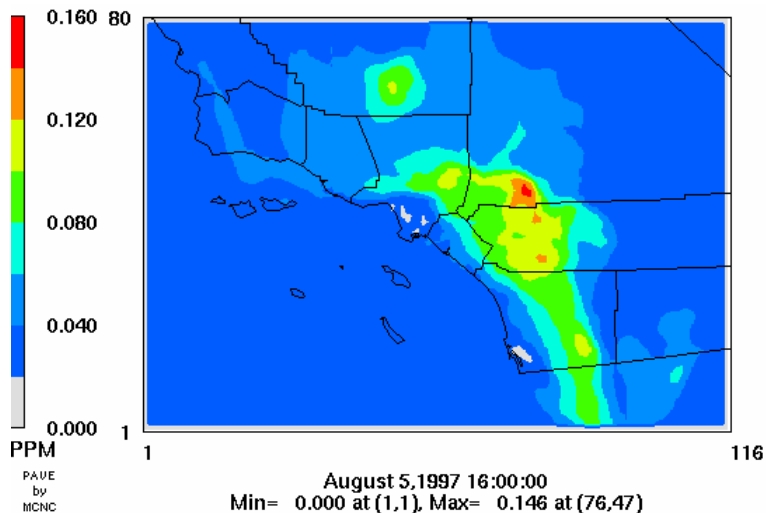


Figure 8. Replication of the ARB SCOS-97 simulations with the CAMx 3.10. The date and hour shown in this figure correspond 8/5/1997 at 1600 LST. The observed peak on that day was 187 ppb about 35 km southwest of the simulated peak's location.

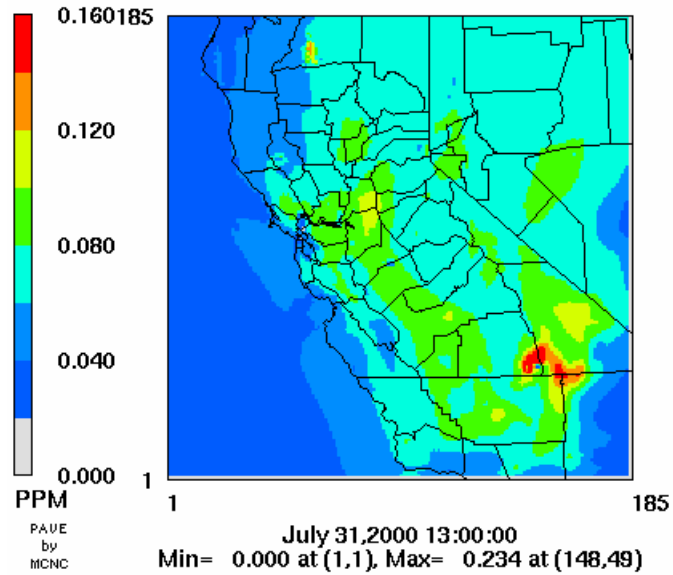


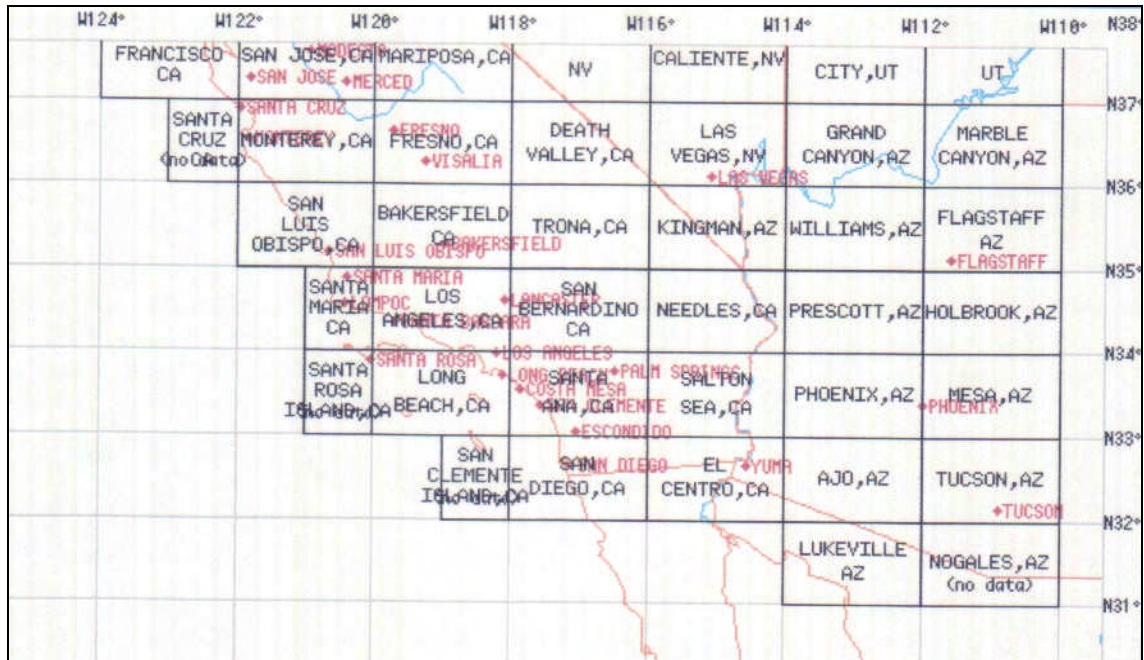
Figure 9. Replication of the ARB CCOS-00 simulations with the CAMx 3.10. The date and hour shown in this figure correspond July 31, 2000 at 1300 LST. There are various regional peaks (e.g., SF Bay Area, Sacramento, North and South San Joaquin Valley). The highest concentration in this figure is due to fires in the southeastern part of the domain.

11. Improved Surface Characterization and Input

Prior to developing and establishing a meteorological and photochemical base case in *this* study, the surface characterization input to the meteorological model (MM5) was improved by use of more resolved land-use categories (e.g., based on 200-m, 37-category USGS LULC). This scheme provides seven *urban* categories instead of the single category typically used in the MM5. The relatively increased level of detail allows for specification of various surface properties (e.g., albedo, emissivity, soil moisture) in a more resolved manner for each surface or cover type. The gridded surface properties are then computed after assigning physical parameter values to each surface type based on previously measured and derived values, and the input in MM5 is directly overridden in the modifiable areas.

The 200-m LULC data was obtained for areas of interest in quadrants (or tiles), from the USGS. For example, to characterize the surface (base case scenario) and to develop control scenarios (surface modification strategies) in Southern California, 200-m LULC data from the following tiles were used: (1) Los Angeles, (2) San Bernardino, (3) Long Beach, (4) Santa Ana, and (5) San Diego (see **Figure 10**). Although surface modifications are expected to occur mainly in the more built-up areas, all regions in the state classified as urban (i.e., having any small amount of urban land use) are also considered for modification in this study. Of course, the levels of modifications that are possible in areas with small urban land use are also small and can be negligible at times.

For each 200-m “pixel” of USGS LULC, various parameter values were assigned to develop a basis for the characterization of the lower boundary in the meteorological model. This is done for base and modified scenarios alike. **Table 10** lists land use and land cover categories and the corresponding values assigned to each for the base case scenario. These values are derived from a combination of sources (e.g., Pielke 2002; Taha et al. 2000; and Taha 1996, 1997a,b) and described in Taha (2003a, 2003b, 2003c). It should be noted that these values are for summer conditions when vegetation is in full bloom. The basis for some of the calculations in this table (e.g., surface albedo) will be explained further in this report.



Source: USGS

Figure 10. Tiles of 200-m resolution USGS LULC for Central and Southern California. Each tile is 2° by 1°.

Table 10. *Base-case* values of LULC-related physical parameters (for summer conditions). (These values are used to develop new input and override the default input to the MM5.)

USGS LULC		α	Z_o (cm)	η	THC ($\text{cal cm}^{-2} \text{K}^{-1} \text{s}^{-0.5}$)
Urban					
11	Residential	0.157	35	0.10	0.03
12	Commercial/Services	0.139	150	0.05	0.03
13	Industrial	0.152	150	0.05	0.03
14	Transportation/Communication	0.117	35	0.02	0.03
15	Industrial and commercial	0.145	150	0.05	0.03
16	Mixed urban or built up	0.134	50	0.05	0.03
17	Other urban or built up	0.142	50	0.05	0.03
Agriculture					
21	Cropland and pasture	0.18	15	0.25	0.04
22	Orchards, groves, Vineyards	0.16	20	0.25	0.04
23	Confined feeding operations	0.12	15	0.12	0.03
24	Other agricultural	0.15	12	0.20	0.03
Rangeland					
31	Herbaceous rangeland	0.18	12	0.15	0.04
32	Shrub and brush rangeland	0.18	20	0.15	0.03
33	Mixed rangeland	0.18	15	0.15	0.03
Forest					
41	Deciduous forest	0.15	100	0.20	0.04
42	Evergreen forest	0.18	150	0.30	0.05
43	Mixed forest	0.16	125	0.25	0.04
Water					
51	Streams and canals	0.08	2	1.0	0.06
52	Lakes	0.06	1	1.0	0.06
53	Reservoirs	0.08	1	1.0	0.06
54	Bays and estuaries	0.06	2	1.0	0.06
Wetland					
61	Forested wetlands	0.16	40	0.35	0.05
62	Non-forested wetlands	0.12	20	0.45	0.06
Barren land					
71	Dry salt flats	0.40	5	0.02	0.02
72	Beaches	0.40	5	0.06	0.03
73	Sandy areas (not beaches)	0.30	5	0.02	0.02
74	Bare rock	0.28	15	0.01	0.01
75	Strip mines and quarries	0.20	15	0.01	0.01
76	Transitional areas	0.18	10	0.02	0.02
77	Mixed barren land	0.18	10	0.02	0.02
Tundra					
81	Shrub and brush tundra	0.18	20	0.25	0.04
82	Herbaceous tundra	0.18	15	0.20	0.05
83	Bare ground	0.16	5	0.05	0.02
84	Wet tundra	0.10	10	0.40	0.05
85	Mixed tundra	0.12	15	0.20	0.04
Snow/Ice					
91	Perennial snowfields	0.80	2	0.95	0.05
92	Glaciers	0.35	5	0.90	0.05

12. Base-Case Development

Following the approach and model configurations discussed earlier, base-case meteorological and photochemical scenarios were developed for each of the Southern and Central California domains and their corresponding episodes. Surface characterization was conducted as discussed in Section 11. The purpose of this section (and the following figures) is to qualitatively summarize the base case meteorological and photochemical simulation results. Relatively more quantitative model performance evaluation will be given in Section 13. During the initial stages of this study, a number of base cases were developed for each domain, and model performance was evaluated after each cycle. The base cases presented in this section are those that produced an optimal and reasonable model performance, taking into consideration the need for clarity in the control-strategy signal, as discussed earlier.

In the next two sections, results are presented for the innermost nests only, i.e., the *finest* grid of each simulation domain, as defined earlier.

12.1 Southern California (SCOS 97) Base Case

In **Figure 11 (a through x)**, the simulated base-case air temperature and wind vector fields (at $\sigma = 0.999$) are given at intervals of two hours on August 5 and 6 of 1997 (primary days of the photochemical episode). The focus here is to qualitatively evaluate: (1) the temperature field, and (2) the wind flow pattern, general direction, and the development of a coastal eddy on August 6 (discussed earlier in the episode description). **Figures a through l** are for August 5, and **Figures m through x** are for August 6.

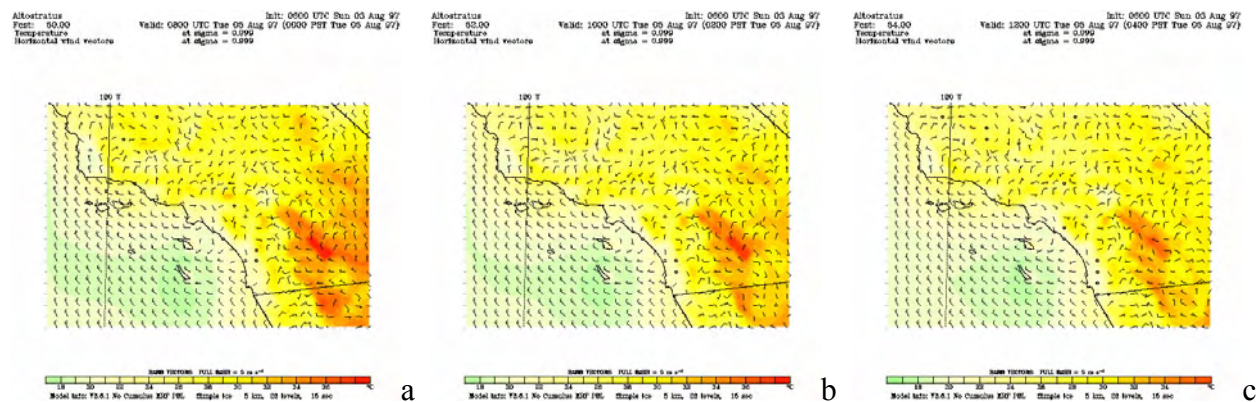
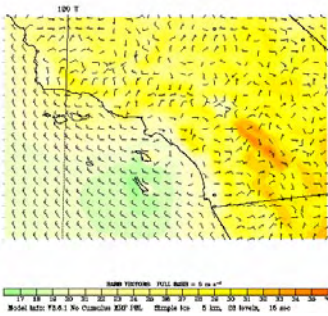


Figure 11 (a-x). Simulated base-case wind and temperature fields for Southern California. Figures with thick border (h and t) are enlarged below to show more detail.

Altostratus
 Post: 66.00
 Temperature
 Horizontal wind vectors

Valid: 1400 UTC Tue 05 Aug 97
 at sigma = 0.999

Valid: 0000 UTC Sun 05 Aug 97
 at sigma = 0.999

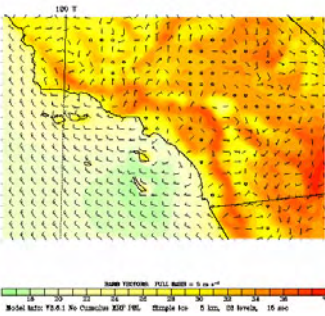


d

Altostratus
 Post: 66.00
 Temperature
 Horizontal wind vectors

Valid: 1600 UTC Tue 05 Aug 97
 at sigma = 0.999

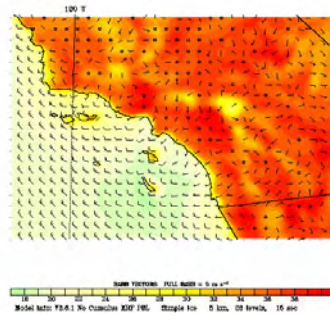
Valid: 0000 UTC Sun 05 Aug 97
 at sigma = 0.999



e

Altostratus
 Post: 60.00
 Temperature
 Horizontal wind vectors

Valid: 1800 UTC Tue 05 Aug 97
 at sigma = 0.999

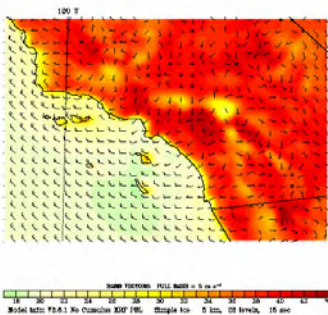


f

Altostratus
 Post: 62.00
 Temperature
 Horizontal wind vectors

Valid: 2000 UTC Tue 05 Aug 97
 at sigma = 0.999

Valid: 0000 UTC Sun 05 Aug 97
 at sigma = 0.999

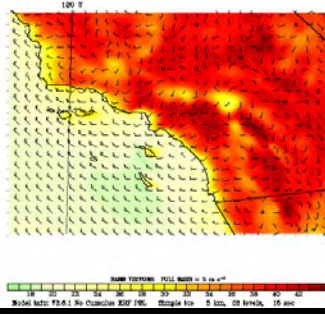


g

Altostratus
 Post: 64.00
 Temperature
 Horizontal wind vectors

Valid: 2200 UTC Tue 05 Aug 97
 at sigma = 0.999

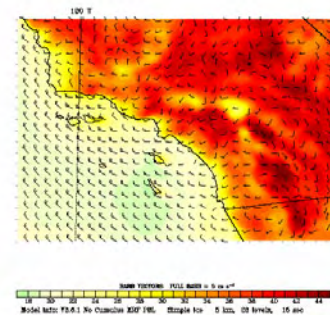
Valid: 0000 UTC Wed 05 Aug 97
 at sigma = 0.999



h

Altostratus
 Post: 66.00
 Temperature
 Horizontal wind vectors

Valid: 0000 UTC Wed 05 Aug 97
 at sigma = 0.999

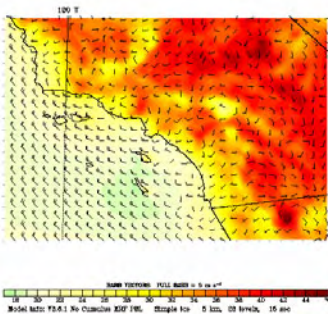


i

Altostratus
 Post: 66.00
 Temperature
 Horizontal wind vectors

Valid: 0000 UTC Sun 05 Aug 97
 at sigma = 0.999

Valid: 0400 UTC Wed 05 Aug 97
 at sigma = 0.999

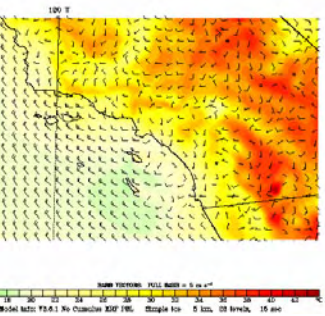


j

Altostratus
 Post: 70.00
 Temperature
 Horizontal wind vectors

Valid: 0600 UTC Wed 05 Aug 97
 at sigma = 0.999

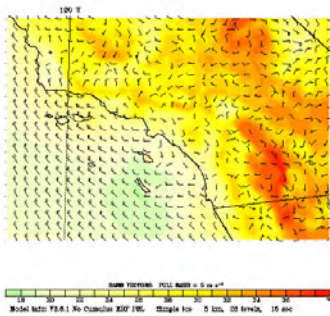
Valid: 0600 UTC Sun 05 Aug 97
 at sigma = 0.999



k

Altostratus
 Post: 72.00
 Temperature
 Horizontal wind vectors

Valid: 0800 UTC Wed 05 Aug 97
 at sigma = 0.999

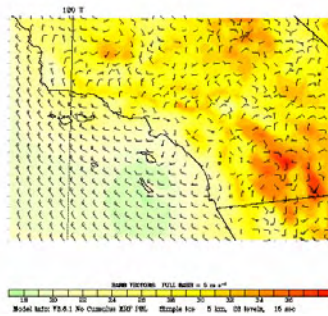


l

Altostratus
 Post: 74.00
 Temperature
 Horizontal wind vectors

Valid: 0800 UTC Sun 05 Aug 97
 at sigma = 0.999

Valid: 1000 UTC Wed 05 Aug 97
 at sigma = 0.999

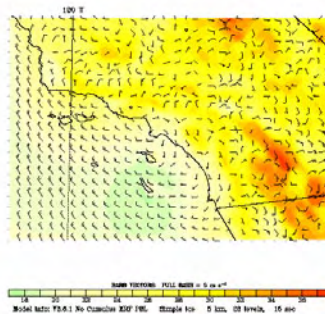


m

Altostratus
 Post: 76.00
 Temperature
 Horizontal wind vectors

Valid: 1000 UTC Wed 05 Aug 97
 at sigma = 0.999

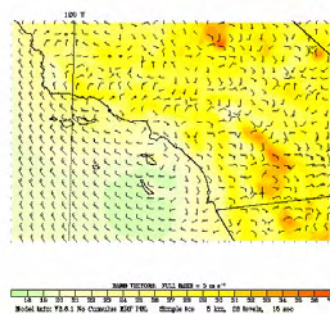
Valid: 1200 UTC Wed 05 Aug 97
 at sigma = 0.999



n

Altostratus
 Post: 76.00
 Temperature
 Horizontal wind vectors

Valid: 1200 UTC Sun 05 Aug 97
 at sigma = 0.999



o

Figure 11 (continued).

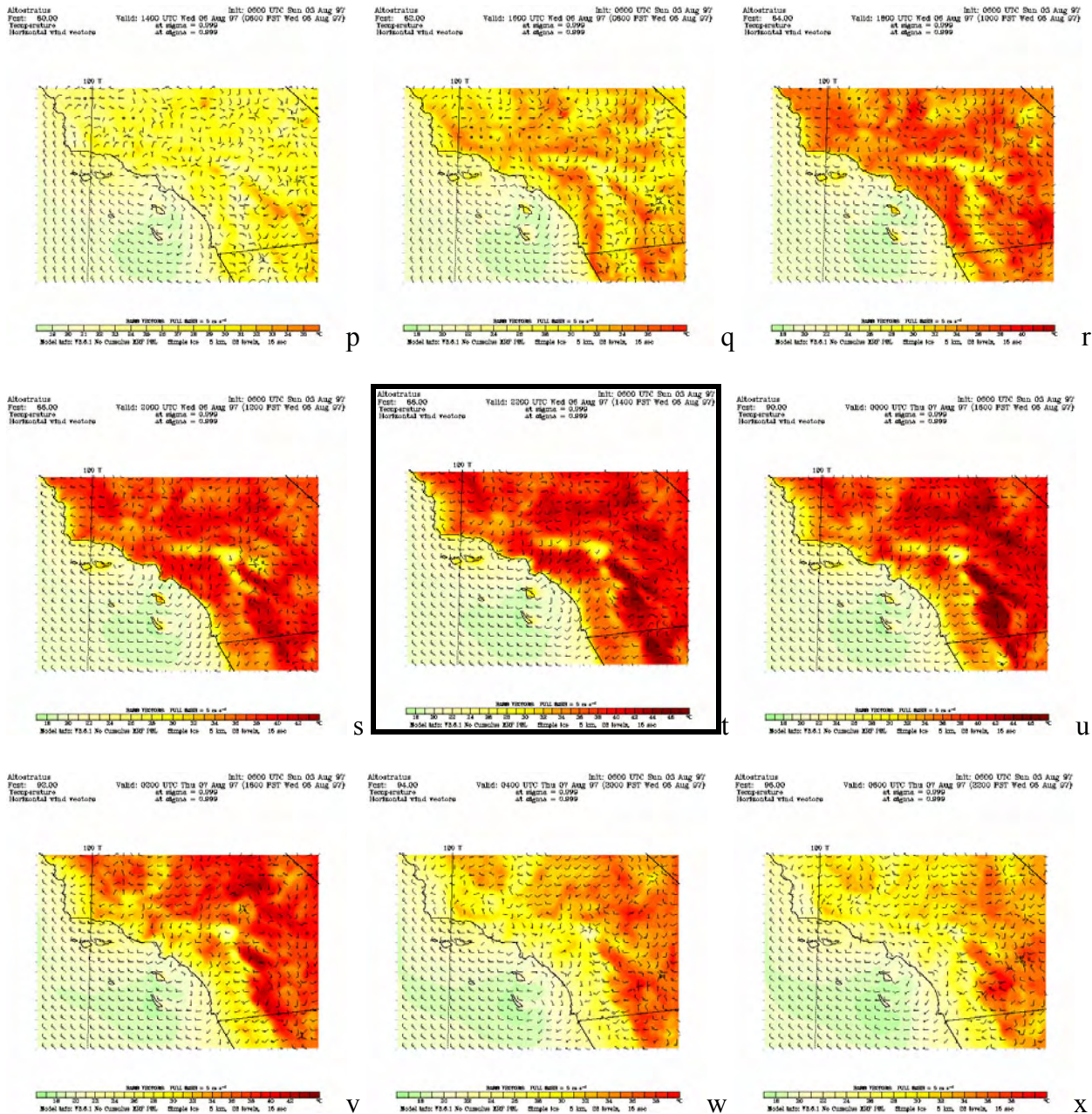


Figure 11 (continued).

Figures 11h and 11t (in bold frames above) are enlarged below, to show relatively more detail.

In general, the simulations produce the observed temperature field reasonably well, including spatial characteristics. The model also captures the observed peak temperature of 45°C (113°F) in Riverside on August 5 (Figure 11h). Compared to its immediate surroundings, the Los Angeles basin appears to be generally warmer. For example, on August 5 at 1500 PST (Figure 11h), downtown Los Angeles appears to be 6°C (43°F) warmer than the coastal area upwind of it (e.g., Santa Monica) and further inland (e.g., in Ontario, San Bernardino, and Riverside the

temperature is about 7°C (45°F) higher than in the coastal areas). Compared to their *immediate* surroundings, these areas (Downtown, Ontario, San Bernardino, and Riverside) are about 3°C–4°C (5.4°F–7.2°F) warmer. Obviously, some of this effect may be caused by an urban heat island, but it is difficult to determine how much of that temperature difference is actually caused by that mechanism.

The simulated flow field also seems to be reasonably comparable to the observations, including the development of a coastal eddy on August 6. The eddy can be qualitatively seen in the figures (e.g., compare **Figures 11h and 11t** below). This eddy causes a southerly flow through most of the Los Angeles Basin and all the way south to the San Diego region. Some of this type of circulation is also simulated on the August 5, but not as strong as on the August 6. In inland areas, the flow is somewhat disorganized, which again is expected because the area is under the influence of a high pressure system with small local gradients.

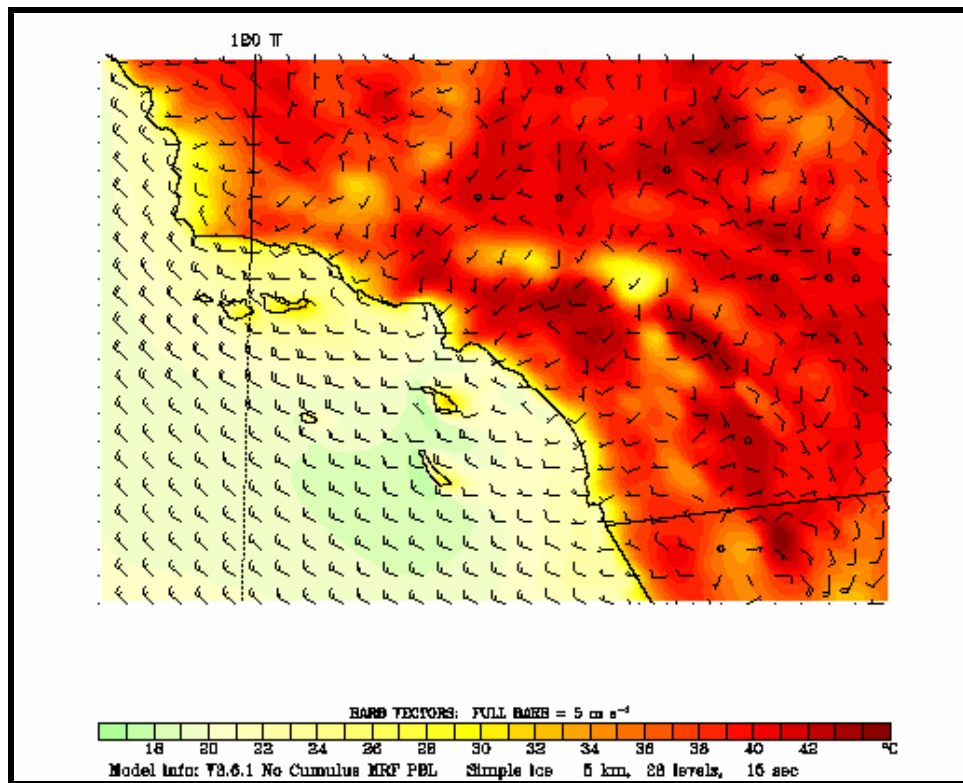


Figure 11h (detail). Simulated temperature and winds at 1400 PST on August 5, 1997 at $\sigma = 0.999$

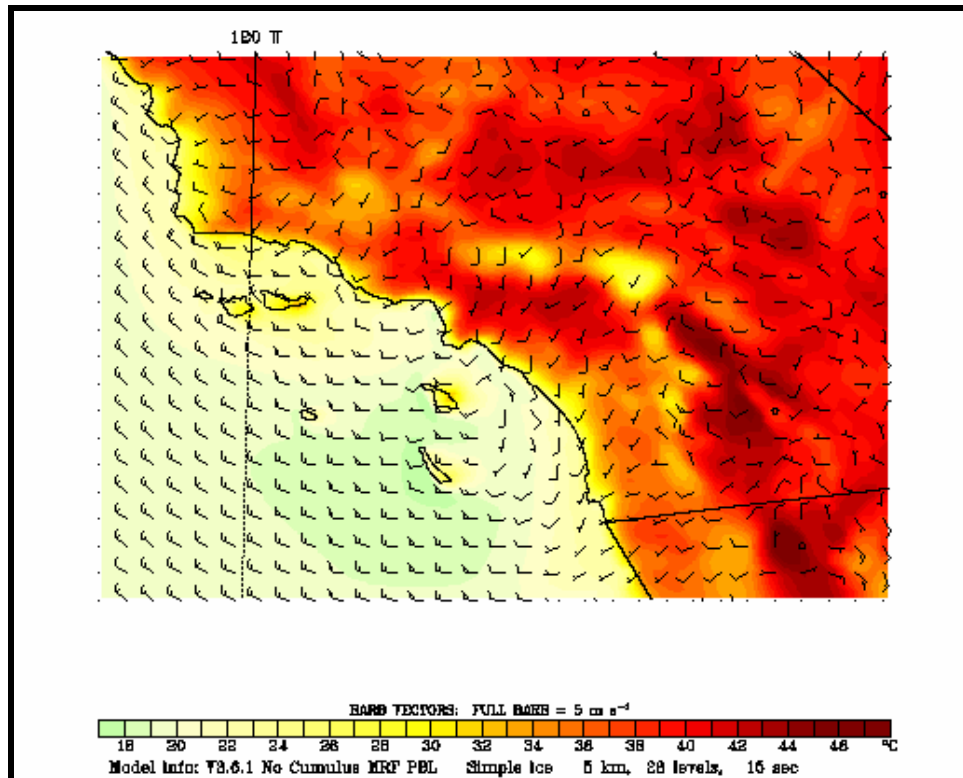


Figure 11t (detail). Simulated temperature and winds at 1400 PST on August 6, 1997 at $\sigma = 0.999$

Figure 12 (a through l) provides a qualitative description of the simulated ozone concentration fields at about 10 m above ground level and at two-hour intervals over the two primary days of the episode. In general, the model correctly captures the locations of the highest concentrations, including the peak on August 5 (figures d and e). The model also captures, on August 6, the general displacement of the peak to the west and north of its location on the August 5 (figures j and k). The difference in location of the peak (the shift to the west and north, into Santa Clarita and Antelope Valley) is a result of the flow associated with the coastal eddy, discussed earlier.

In addition to these snapshots on August 5 and 6, the hour at 1500 PST on both days (not shown in Figure 12) are enlarged in **Figures 13 a and b**, to show further detail. These are concentrations during the time of the basin peaks on those days. As seen in the figures, the peak concentrations on August 5 are just southwest of Rubidoux-Riverside (where the observed peak was) and on August 6, the peaks occur over the central San Gabriel/San Bernardino mountains as well as in Santa Clarita/Antelope Valley areas. Photochemical model performance evaluation for this base case is discussed later in this report.

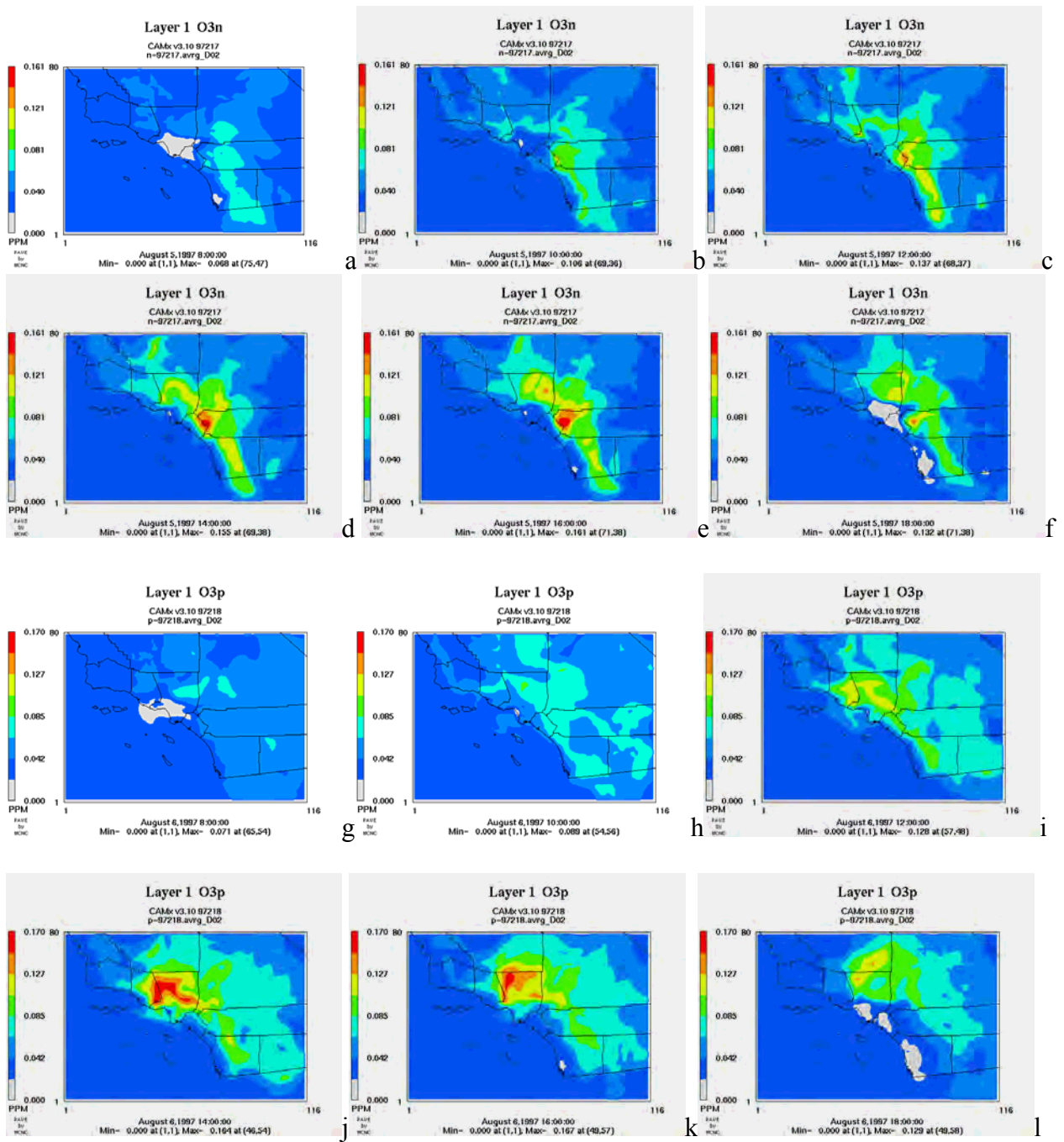


Figure 12 (a-l). Simulated ozone concentrations on August 5 and 6, Southern California

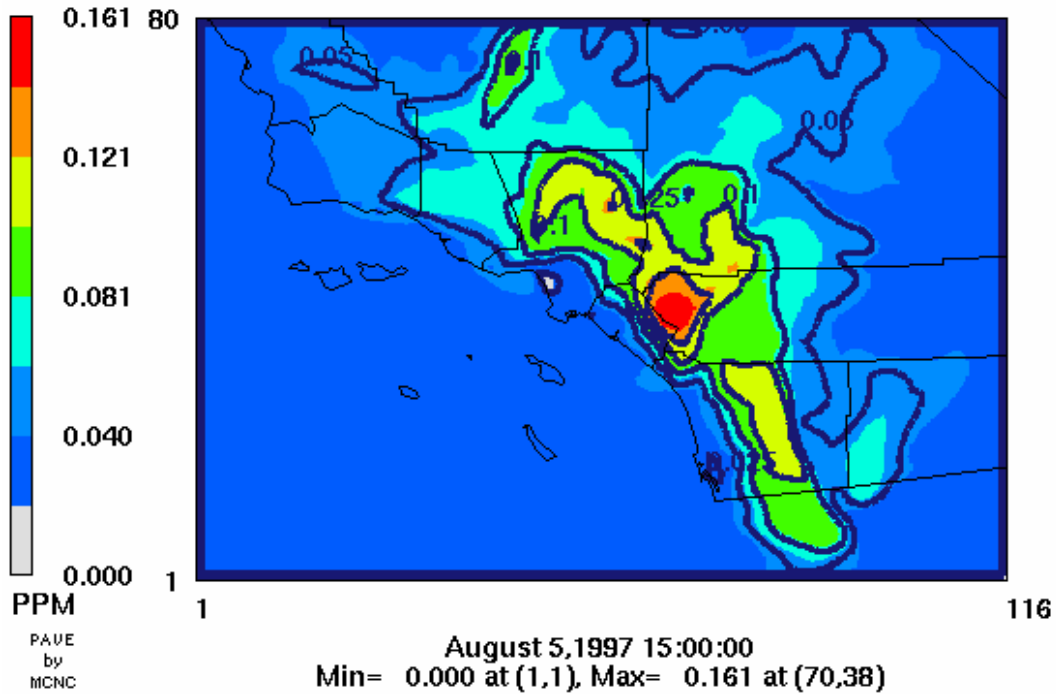


Figure 13a. Simulated base-case ozone concentrations for Southern California at 1500 LST on August 5, 1997. The simulated peak is 161 ppb, slightly southwest of Rubidoux-Riverside.

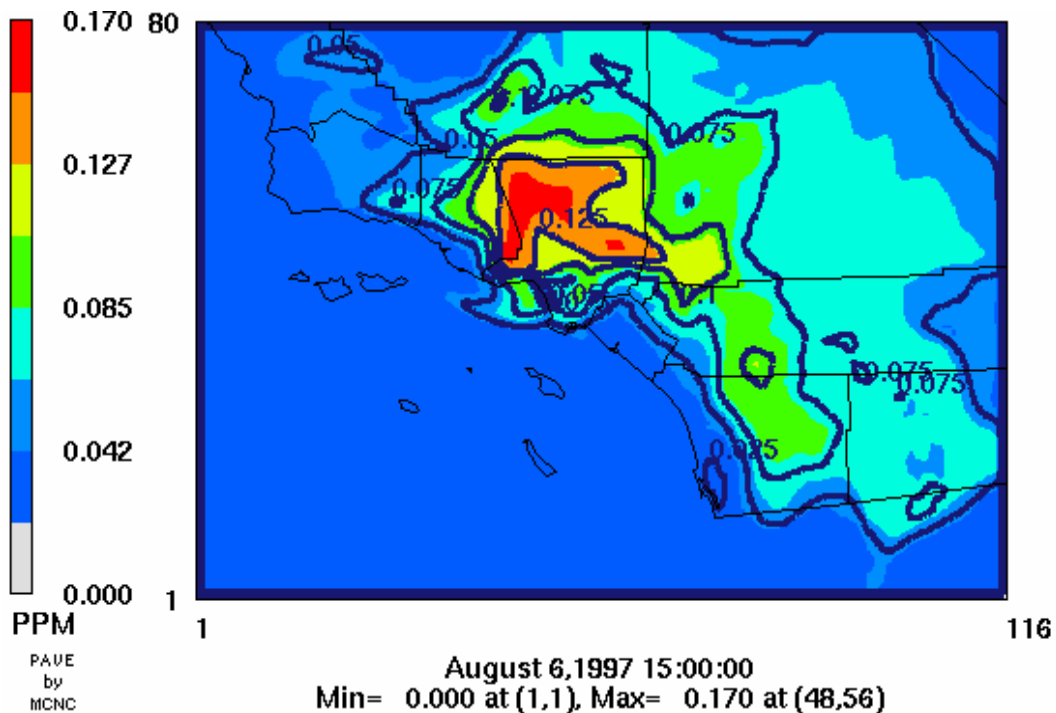


Figure 13b. Simulated base-case ozone concentrations for Southern California at 1500 LST on August 6, 1997. The simulated peak is 170 ppb, North of Santa Clarita. Another area of peak concentrations is seen over the Central San Gabriel Mountains.

12.2 Central California (CCOS 2000) Base Case

Figure 14 (a through x) shows the simulated air-temperature and wind vector fields (at $\sigma = 0.999$) at intervals of 2 hours from 1800 on July 30 through 1600 on August 1, 2000, for the Central California domain. As with the above figures for Southern California, the purpose here is to provide a qualitative summary of the evolution of temperature and wind fields over those two days.

One aspect of interest, for example, is the coupling between the San Francisco Bay Area (SFBA) and the Sacramento Valley. When there is strong transport from the SFBA to Sacramento, the peak ozone in the latter tends to be higher than on those days without such transport. **Figure 15** shows streamlines for the simulated 10-m winds at 1600 LST on July 31 and August 1, respectively. Qualitatively, it can be seen that the flow from the SFBA to Sacramento is relatively blocked on July 31 (**Figure 15a**) compared to the flow on August 1 (**Figure 15b**). In the former case, flow in the Central Valley (including Sacramento) is northerly and any trajectory arriving Sacramento from the west originates further north of the SFBA, e.g., north of Santa Rosa. The flow through the SFBA, as well as from Sacramento, on that day causes southbound transport into San Joaquin Valley thus causing some of the higher ozone peaks in that region as well. On August 1, however, the simulated flow arriving Sacramento goes directly through the SFBA and on to the northeast. On that day, there is also southerly transport and thus the peak concentrations in SJV are relatively smaller. As will be discussed later, these conditions have impacts on the simulated peak times in Sacramento.

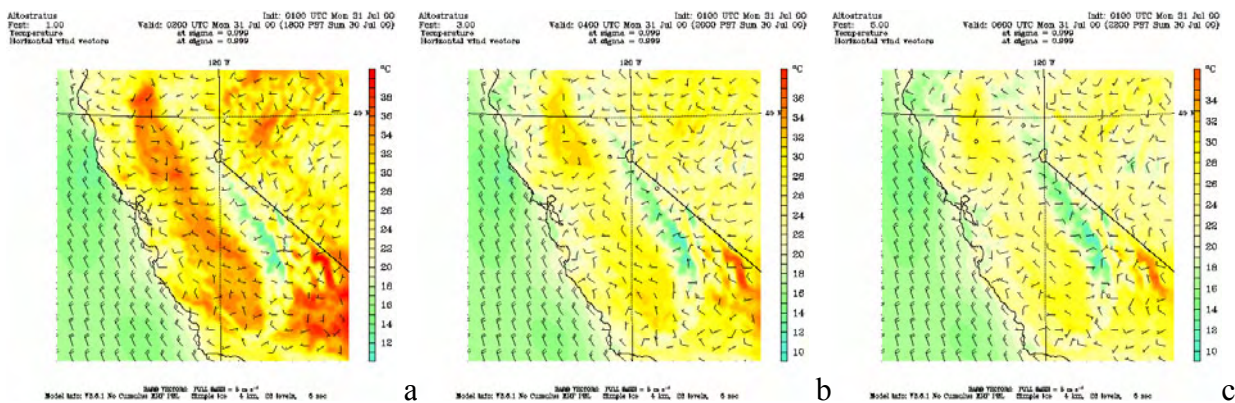


Figure 14 (a-x). Simulated base-case wind and temperature fields for Central California

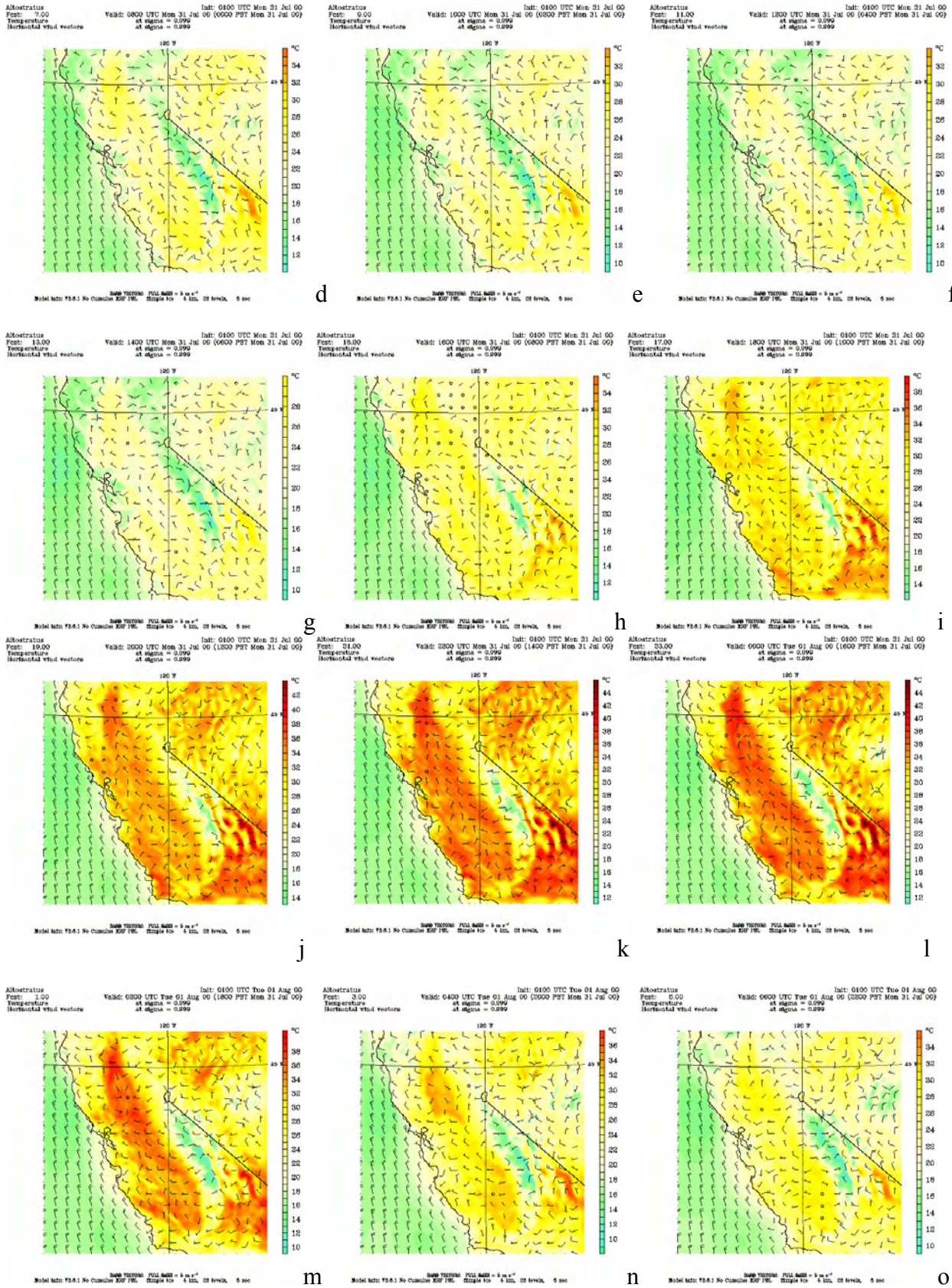


Figure 14 (continued)

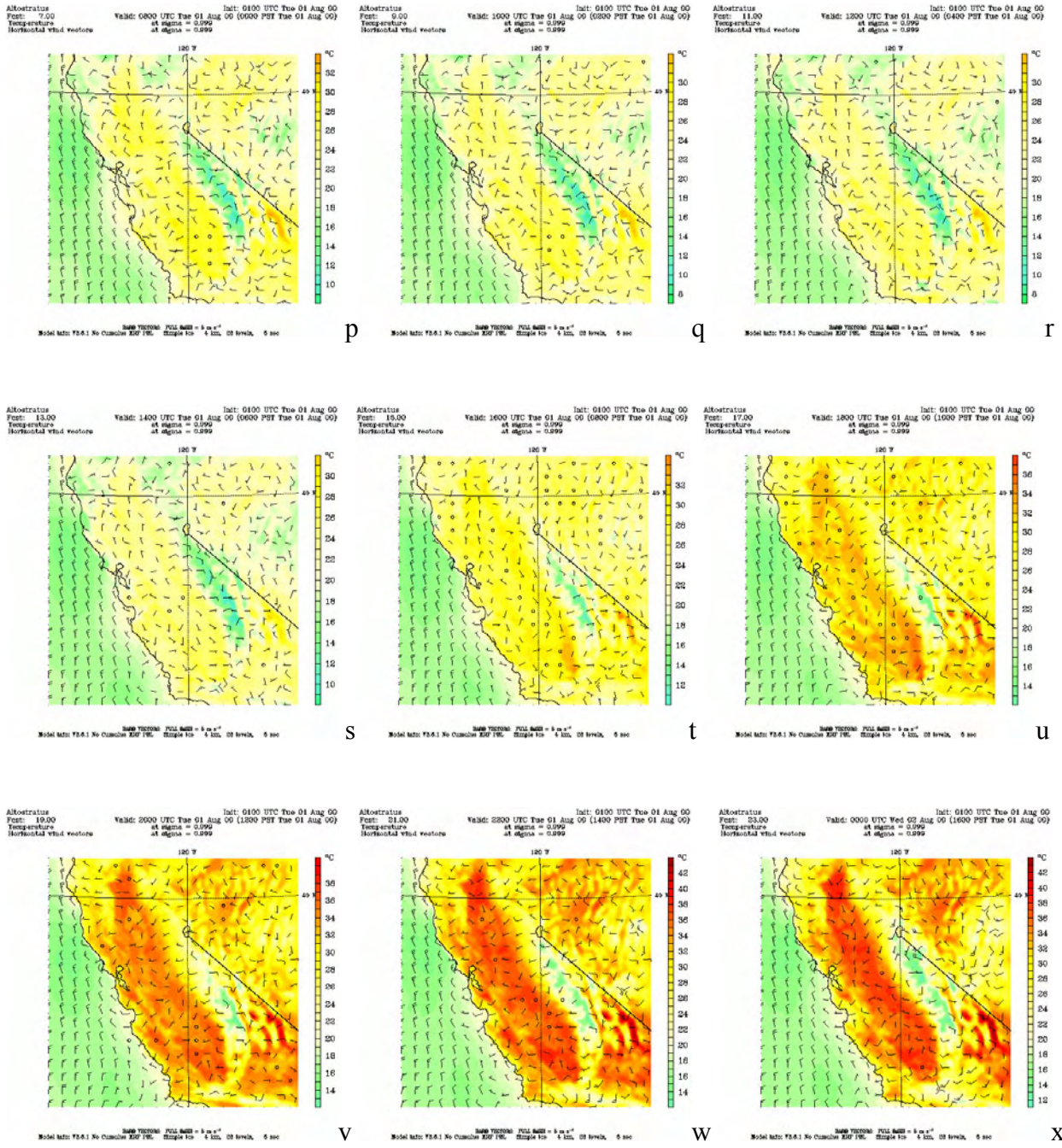
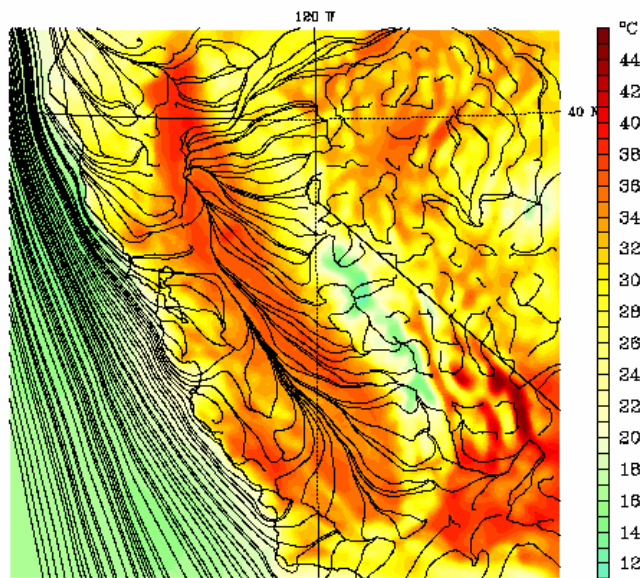


Figure 14 (continued)

Altostratus
 Fcst: 23.00
 Temperature
 Horizontal wind streamlines

Valid: 0000 UTC Tue 01 Aug 00 (1600 PST Mon 31 Jul 00)
 at sigma = 0.999
 at sigma = 0.999

Init: 0100 UTC Mon 31 Jul 00



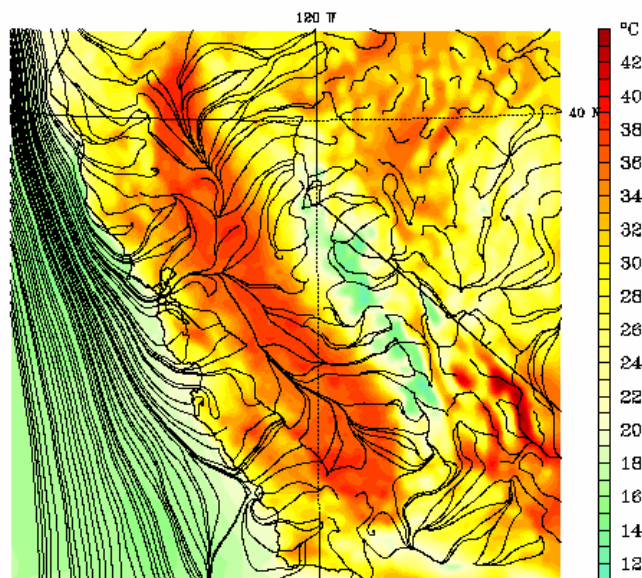
Model Info: Y8.6.1 No Cumulus MRF PBL Simple Ice 4 km, 28 levels, 6 sec

Figure 15(a). Simulated 10-m streamlines at 1600 LST July 31

Altostratus
 Fcst: 23.00
 Temperature
 Horizontal wind streamlines

Valid: 0000 UTC Wed 02 Aug 00 (1600 PST Tue 01 Aug 00)
 at sigma = 0.999
 at sigma = 0.999

Init: 0100 UTC Tue 01 Aug 00



Model Info: Y8.6.1 No Cumulus MRF PBL Simple Ice 4 km, 28 levels, 6 sec

Figure 15(b). Simulated 10-m streamlines at 1600 LST August 1

Figure 16 (a–x) depicts the simulated base-case ozone concentrations field for the Central California domain at two-hour intervals for July 31 and August 1, 2000 (primary days of the episode in this study). In general, the simulations show that on July 31, most domain peaks occur in the SFBA, Fresno, Bakersfield, and south of Porterville (**Figure 16 h,i,j**). Per observations, July 31 is a day when most peaks occur in the SFBA and SJV (relative to Sacramento conditions) and the model appears to capture this general feature. The model also captures the peaking in SFBA and Sacramento on August 1 (when north and south SJV have relatively smaller ozone concentrations), as seen **Figure 16 t,u,v**. On August 1, the largest simulated (as well as observed) peaks are in the Sacramento-Folsom-Roseville area.

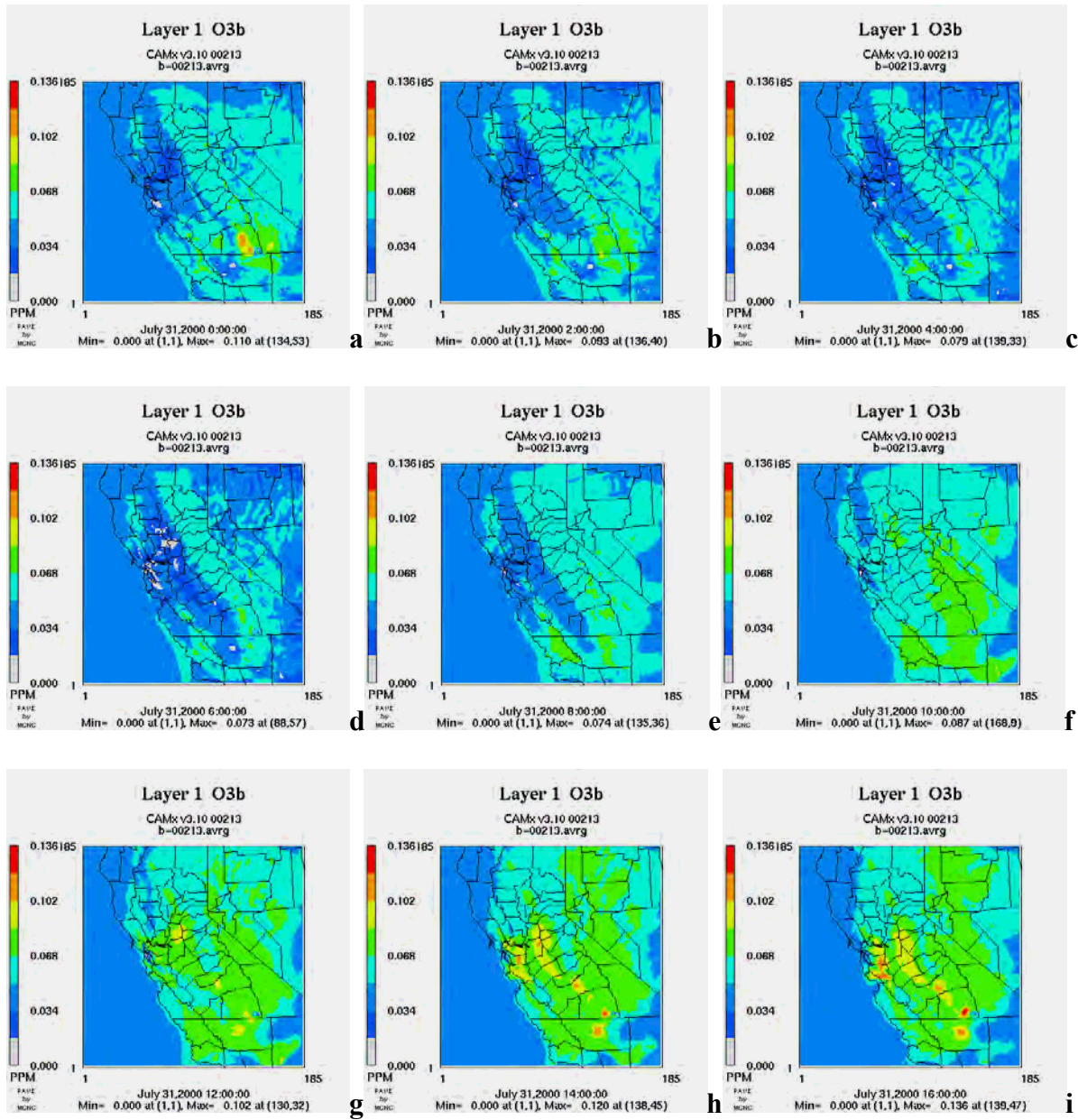


Figure 16 (a-x). Simulated base case ozone concentrations on July 31 and August 1, 2000 for Central California

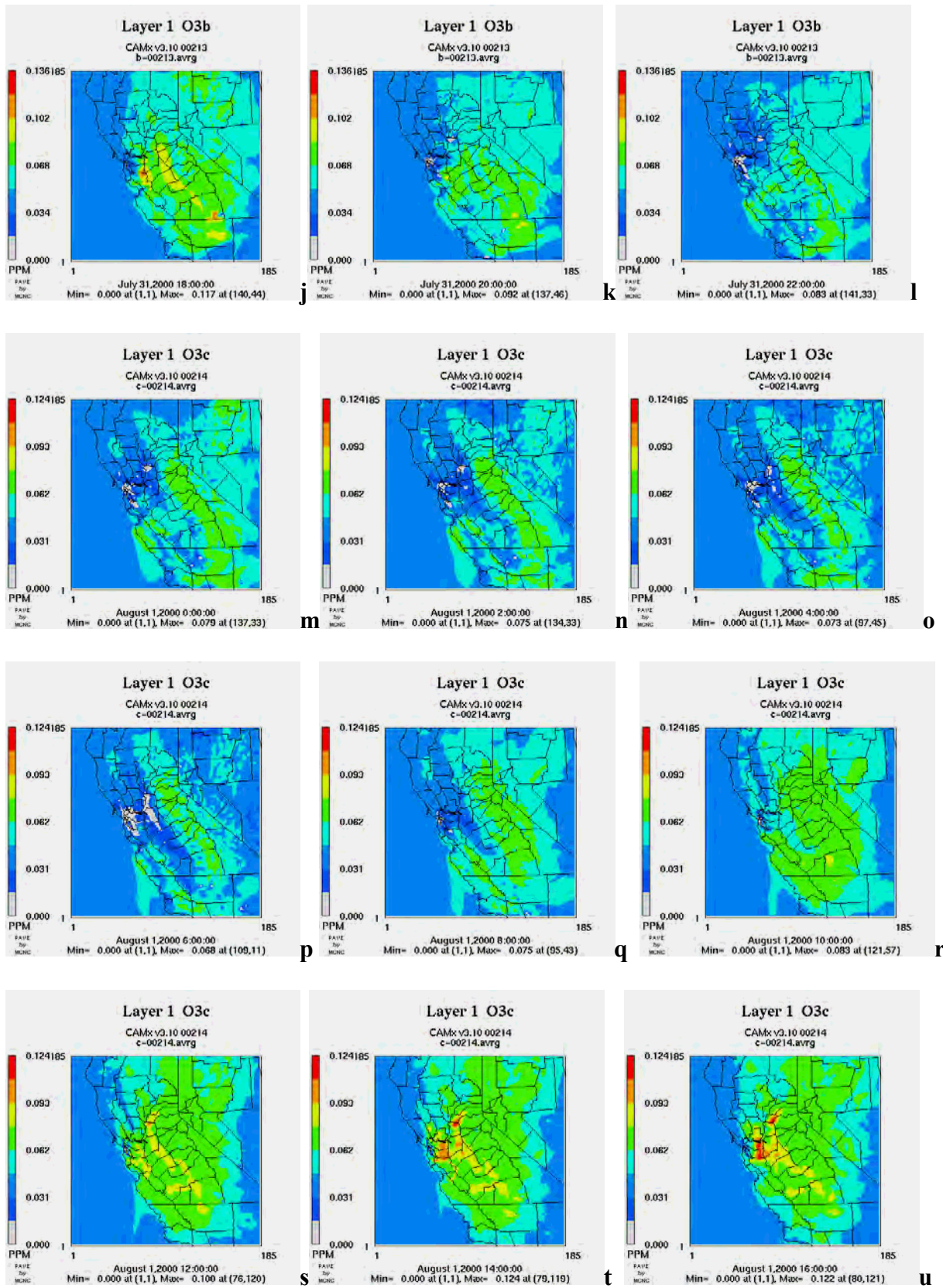


Figure 16 (continued)

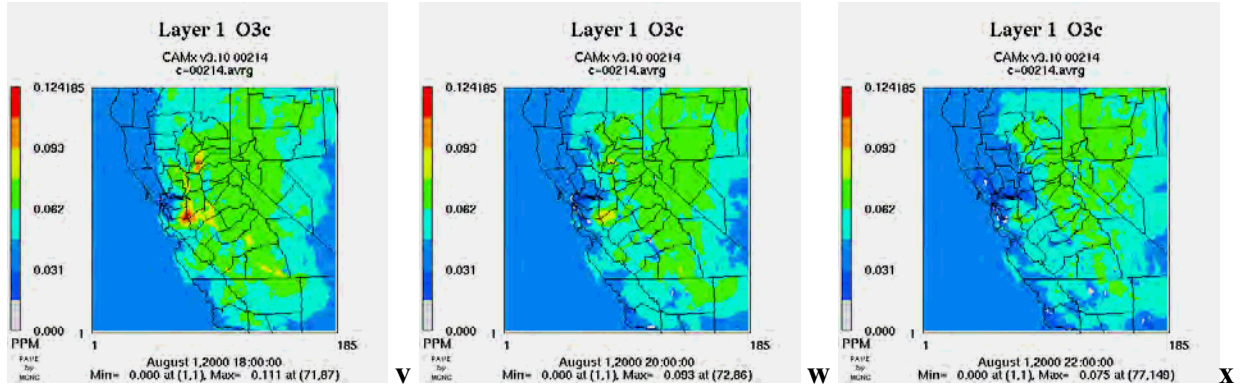


Figure 16 (continued)

Figure 17 (a,b) represents another way to qualitatively summarize the simulated high ozone concentrations in Central California on July 31 and August 1, 2000. These figures show the peak concentration (peak 1-hour average) at each grid cell, regardless of the actual hour when it occurred. Thus the plots can be temporally inconsistent across the domain (but in general, most of the peaks occur within a relatively narrow time window relative to each other (i.e., most occur between 1300 and 1600 LST). In both figures, the scale is capped at 120 ppb for clarity, even though simulated concentrations as high as 158 ppb occur on July 31.

In **Figure 17a**, the simulations suggest peak ozone concentrations in the neighborhoods of 113 ppb in Bakersfield, 158 ppb in the Porterville region, 110 ppb in Fresno, 115 in the Livermore/Fremont area, and 117 in South San Jose to Gilroy. The Sacramento region has lower peaks, on the order of 85–95 ppb. In the Lodi-Stockton-Modesto-Turlock area, the peaks are on the order of 95–100 ppb. On August 1 (**Figure 17b**), the simulated high concentrations are on the order of 118 ppb in the Sacramento region, 115 ppb in the Livermore and east San Jose regions, and 108 in the Porterville region. Finally, in the Manteca-Modesto-Turlock area, the highs are in the order of 97–100 ppb.

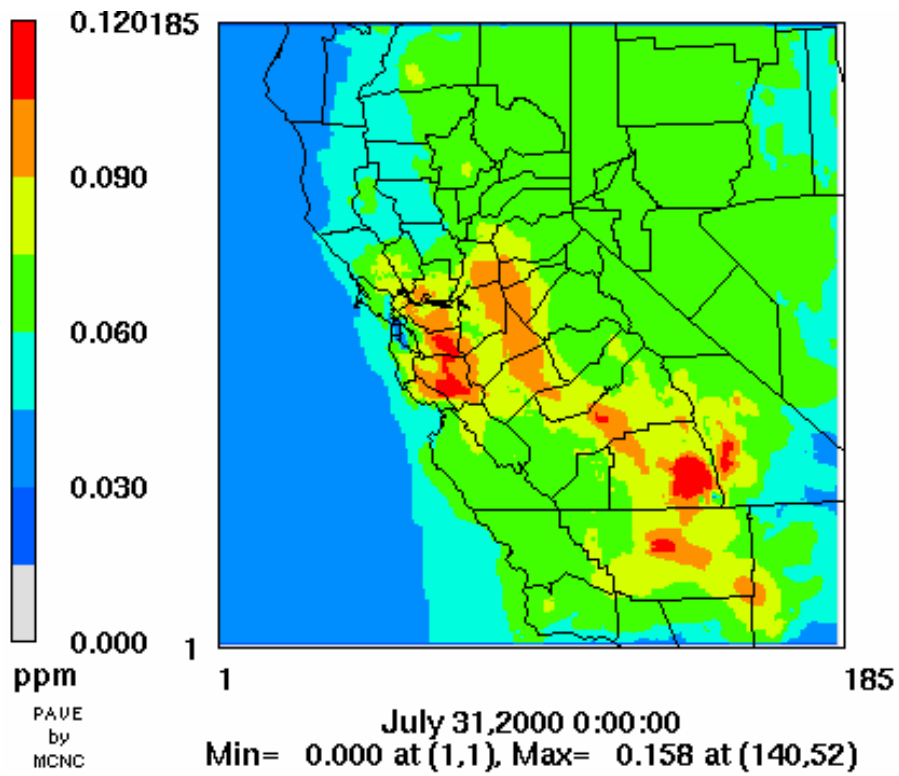


Figure 17a. Peak ozone concentrations at each grid cell on July 31

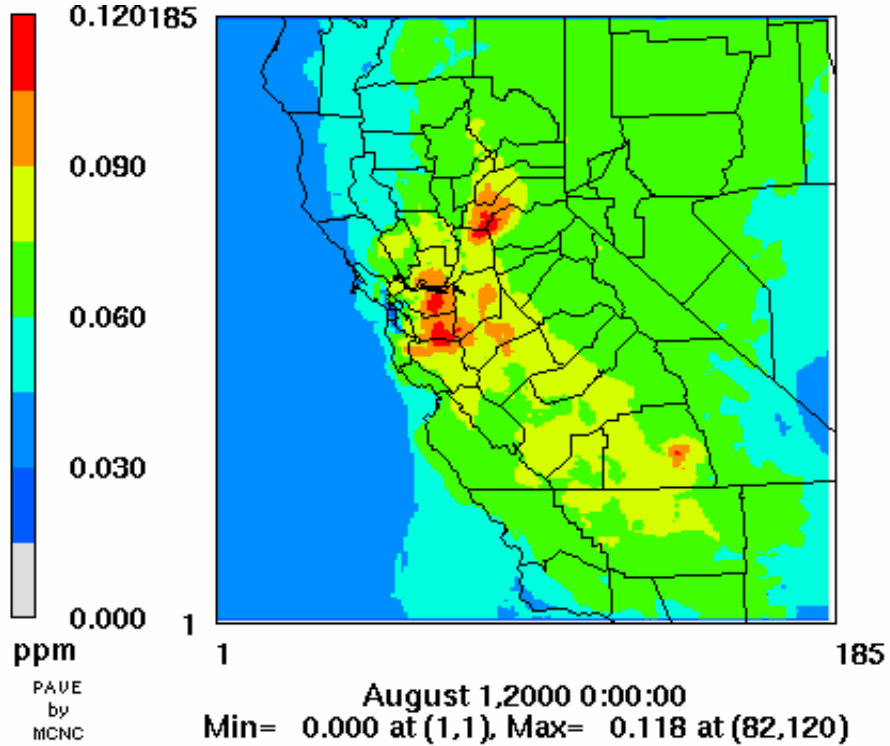


Figure 17b. Peak ozone concentrations at each grid cell on August 1

13. SCOS and CCOS Model Performance Evaluation

Following the above qualitative analysis of near-surface meteorological fields (temperature and wind) and ozone concentrations, a relatively more quantitative analysis is provided in this section. For this purpose, the benchmark metrics defined earlier (in Section 9) will be used to evaluate both meteorological and photochemical model performance domain-wide and in sub-domain regions in each of Central and Southern California and for the episodes defined earlier. Of interest in this performance evaluation exercise are those fields near the surface (e.g., 2-m air temperature and 10 m wind velocity). The reason for focusing on these near-surface fields, besides relative data availability, is that the objective of this study is to evaluate boundary-layer processes and the impacts of surface modification on near-surface meteorological and air-quality conditions (in the canopy layer and at street level)—a zone where model performance is most important. Also, photochemical model performance evaluation (from a regulatory perspective) focuses relatively more on ground-level ozone concentrations.

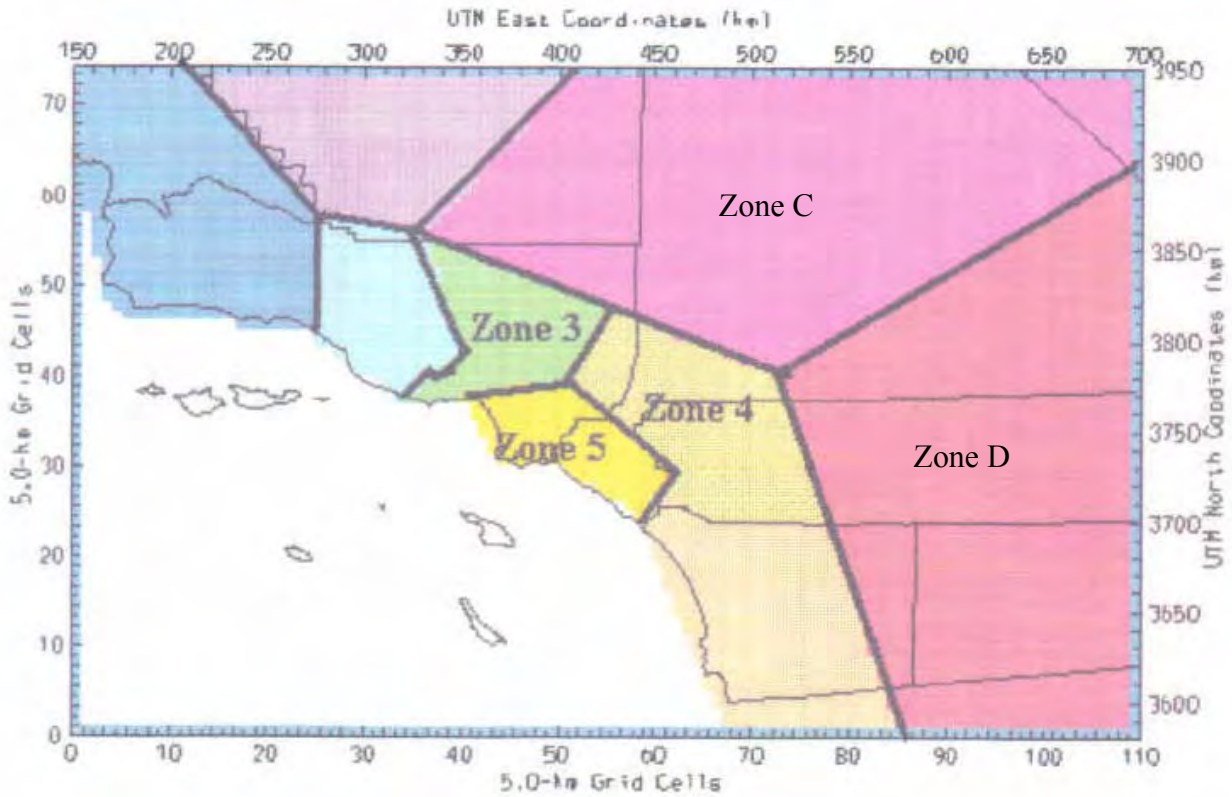
Appendix B provides a listing of meteorological/air quality stations or monitor locations from which observational data were extracted and used in model performance evaluation in this study. However, not all of these stations were used for evaluation purposes; only a subset was used. For example, in the SCOS domain, the meteorological stations used here are those used by the ARB in evaluating the CALMET model performance; whereas, for photochemical model evaluation, the data are those used by the ARB/SCAQMD in evaluating the UAM model performance. For the CCOS, data used by the ARB, Environ, and Alpine Geophysics in evaluating meteorological model performance (in progress) and by the ARB in evaluating photochemical model performance were used in this study.

13.1 Model Performance for the SCOS-97 Domain and Episode

The South Coast Air Quality Management District's air quality management plan (www.aqmd.gov/aqmp/AQMD03AQMP.htm) identifies nine regions (sub-domains) in the Southern California modeling domain for evaluation of photochemical model performance (see **Figure 18**). Of particular interest are zones 3, 4, and 5 (AQMP 2003). Zone 3 includes the San Fernando Valley; Zone 4 includes eastern San Gabriel, San Bernardino, and Riverside; and Zone 5 includes the City of Los Angeles and Orange County. Zone 4 represents an area of typically higher ozone concentrations and is also the where the domain peak occurred on August 5 (primary day). Zone 4 is also an important area for analysis because it is a region for primary downwind impact. As a result, the South Coast AQMD recommends that Zone 4 be a priority in evaluating model performance.

Monitors included in Zone 3 are: Burbank, Reseda, Calabasas, Van Nuys, Santa Clarita, and Mount Wilson. Those in Zone 4 include: Lake Arrowhead, Azusa, Banning, Fontana, Glendora, Lake Elsinore, Lake Gregory, Perris, Phelan, Pomona, Redlands, Rubidoux, San Bernardino (2 stations), Upland, Cajon Pass, Cajun, Azusa, and Temecula; whereas those in Region 5 include: Anaheim, Costa Mesa, El Toro, Hawthorne, La Habra, Lynwood, Long Beach, Pasadena, Los Angeles VAH (Veterans Administration Hospital), Pico Rivera, and Palos Verdes. Refer to Appendix B for more information.

Although these regions were designated mainly for photochemical model performance evaluation, they are used in this study to evaluate the meteorological model performance as well.



Source: SCAQMD AQMP, 2003

Figure 18. Model performance evaluation zones

Table 11 shows MRE (mean bias) and MURE (mean gross error) computed for air temperature as an average over three days of the episode (August 4, 5, and 6) and for four zones where sufficient observational data were available. **Table 12** provides separate mean bias and error by day for the three days analyzed here and for the same four regions given in **Table 11**. When comparing these computed values with the proposed benchmarks discussed earlier, results suggest that model performance is generally acceptable. Overall, temperature bias is close the proposed range of $\pm 0.5K$, except for Zone C on the first two of the three days analyzed here. The model does better in zones 3 and 4 (the Los Angeles Basin) than in the other two zones in the desert. Temperature gross error is generally close to the proposed benchmark value of $\leq 2.0K$, but mostly higher than it.

Table 11. Air temperature bias (MRE) and error (MURE) averaged for three days. Domain: Southern California

	Temperature Bias (K) all days*	Temperature Gross Error (K) all days*
Zone c	1.16	2.4
Zone d	-0.38	2.5
Zone 3	-0.18	1.9
Zone 4	0.06	2.8

*August 4, 5, and 6

Table 12. Air temperature bias (MRE) and error (MURE) for each day.
Domain: Southern California

	Temperature Bias, K (8/4)	Gross error, K, (8/4)
Zone c	1.41	2.43
Zone d	0.58	2.85
Zone 3	-0.31	1.50
Zone 4	0.36	2.66

	Temperature Bias, K, (8/5)	Gross error, K, (8/5)
Zone c	1.49	2.42
Zone d	-0.90	2.75
Zone 3	-0.17	1.80
Zone 4	-0.39	2.75

	Temperature Bias, K, (8/6)	Gross error, K, (8/6)
Zone c	0.65	2.64
Zone d	-0.71	2.22
Zone 3	-0.52	2.40
Zone 4	0.05	2.73

Table 13 shows MRE (mean bias) and MURE (mean gross error) computed for wind speed and averaged over three days of the episode (August 4, 5, and 6). **Table 14** separates the mean bias and error by day. Comparing these computed values with the proposed benchmarks discussed earlier suggests that model performance is generally reasonable. Overall, wind-speed bias is often larger than the desired benchmark but not significantly higher. Gross error is somewhat larger than proposed benchmark limits discussed earlier.

Table 13. Wind speed bias (MRE) and error (MURE) averaged for three days.
Domain: Southern California.

	Wind speed Bias, m/s (all days)*	Wind speed Gross error, m/s (all days)*
Zone c	-0.23	1.76
Zone d	1.13	2.20
Zone 3	0.63	2.05
Zone 4	1.20	1.90

*August 4, 5, and 6.

Table 14. Wind speed bias (MRE) and error (MURE) for each day.
Domain: Southern California.

	Wind Speed Bias, m/s (8/4)	Wind Speed Gross Error, m/s (8/4)
Zone c	-0.37	1.48
Zone d	1.12	2.15
Zone 3	0.72	1.81
Zone 4	1.02	1.55

	Wind Speed Bias, m/s (8/5)	Wind Speed Gross Error, m/s (8/5)
Zone c	-0.48	1.70
Zone d	0.69	1.82
Zone 3	0.41	2.36
Zone 4	0.85	1.91

	Wind Speed Bias, m/s (8/6)	Wind Speed Gross Error, m/s (8/6)
Zone c	0.11	2.05
Zone d	1.53	2.60
Zone 3	0.73	2.00
Zone 4	1.66	2.21

Finally, **Table 15** summarizes gross error (MURE) for wind direction on each day and for each of the four zones discussed above. Compared to the proposed benchmark of $\leq 30^\circ$ the model clearly is not within the recommended performance (it has about double the allowed error on the average). However, because the error is smaller than 90° (except for one entry in the table), the model's reproduction of the general flow direction can be deemed still reasonable, meaning that it is producing the general pattern and direction and the expected reversal in the flow, as well as other features. No wind direction bias is discussed here, because it does not carry much meaning in this case.

Table 15. Wind direction gross error. Domain: Southern California.

	Wind Direction ($^\circ$) Gross Error (8/4)	Wind Direction ($^\circ$) Gross Error (8/5)	Wind Direction ($^\circ$) Gross Error (8/6)
Zone c	70	76	74
Zone d	82	99	62
Zone 3	56	57	64
Zone 4	51	47	62

The scatter graphs in **Figure 19** (A,B,C, and D) are another example in evaluating model performance (here in terms of predicted air temperature). The predicted (y-axis) and observed (x-axis) 2-m air temperature are plotted for each evaluation zone listed in tables 11 and 12. Here, N is the number of available station-hours for *observations* (all simulation hours are available but cannot be used if observations are missing). Also given are the coefficients of correlations (r^2) and the linear equation describing the best fit (the fit is not shown in the figures). All three days are included in these plots (for time periods when data is available).

As seen in these figures, there is an over-prediction trend at the lower range of air temperature in zones C (< 295K) and D (< 300K) with an average over-prediction of 3K in Zone C and 2K in Zone D. There is some under-prediction at the higher range of temperature in Zone D (> 305K) with an average under-prediction of 2K. In zones 3 and 4, there is no strong bias towards under- or over-prediction.

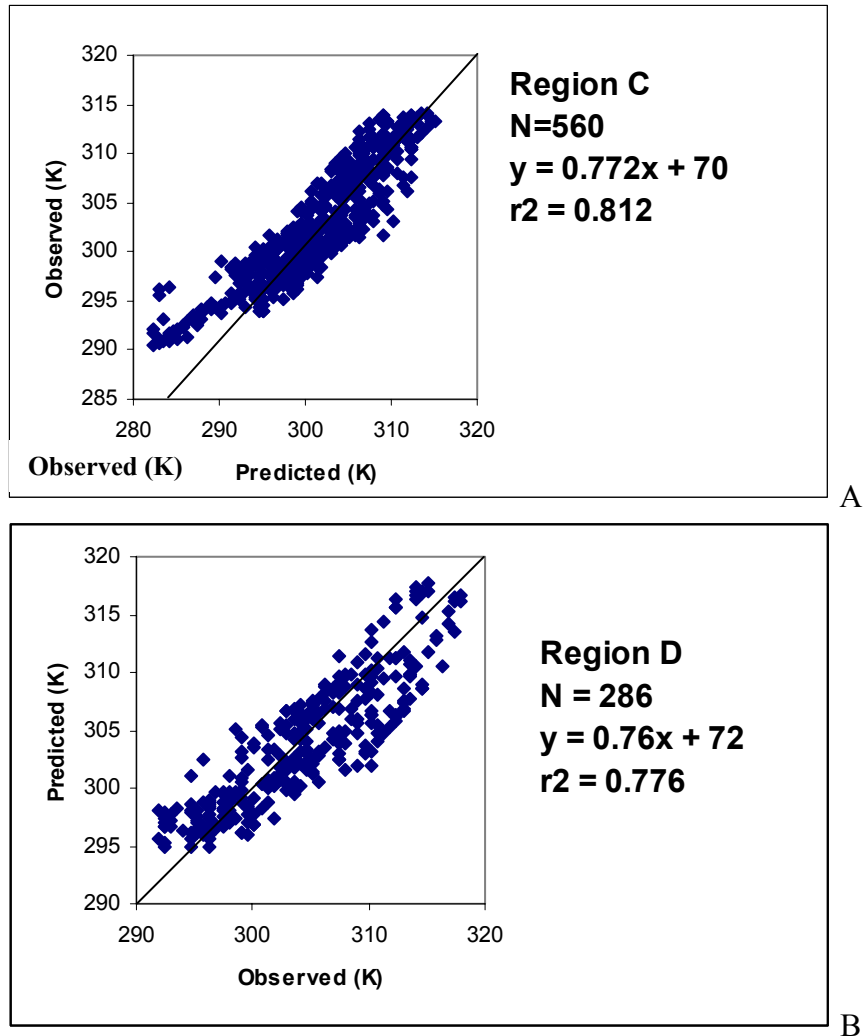
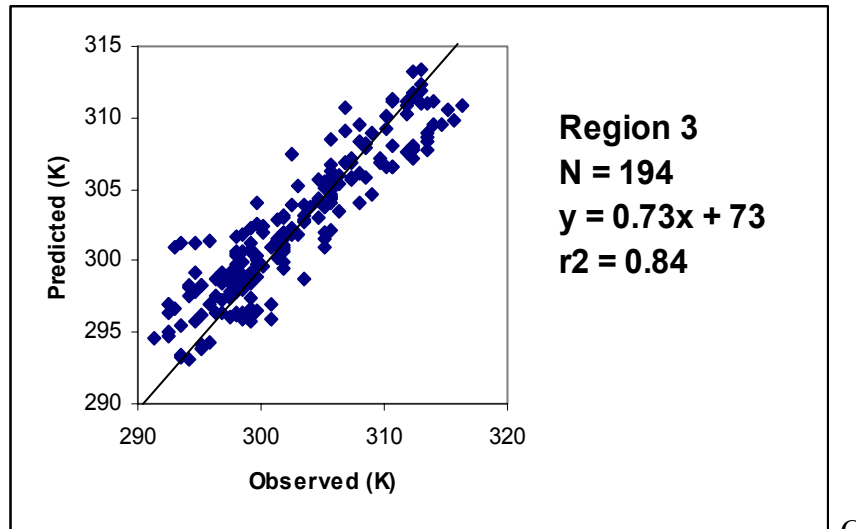
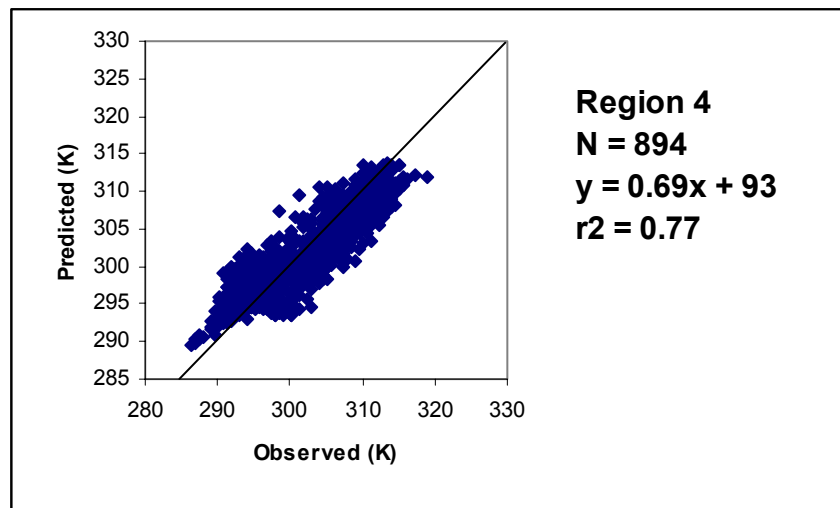


Figure 19. (a ,b, c, d). Predicted vs. observed 2-m air temperature (K).



C



D

Figure 19. (continued).

As described earlier in the discussion of model configuration, each base-case scenario (including the final base case) was run in two stages. The first involved a nested run with two-way feedback (i.e., feedback between the finest grid and its mother domains), whereas the second involved downscaling to and running the finest-resolution nest as a single, standalone grid. The standalone grid is then used in subsequent emission and photochemical modeling and in evaluating the impacts of surface modification strategies. In **Figures 20, 21, and 22**, model performance for the finest grid is given for both nested and standalone configurations from one example run, for comparative purposes. These figures show air temperature and some of the metrics discussed earlier. It is clear from these figures that while both nested and standalone grids perform reasonably well, the nested grid performs slightly better than the standalone one, for example between hours 61 and 67.

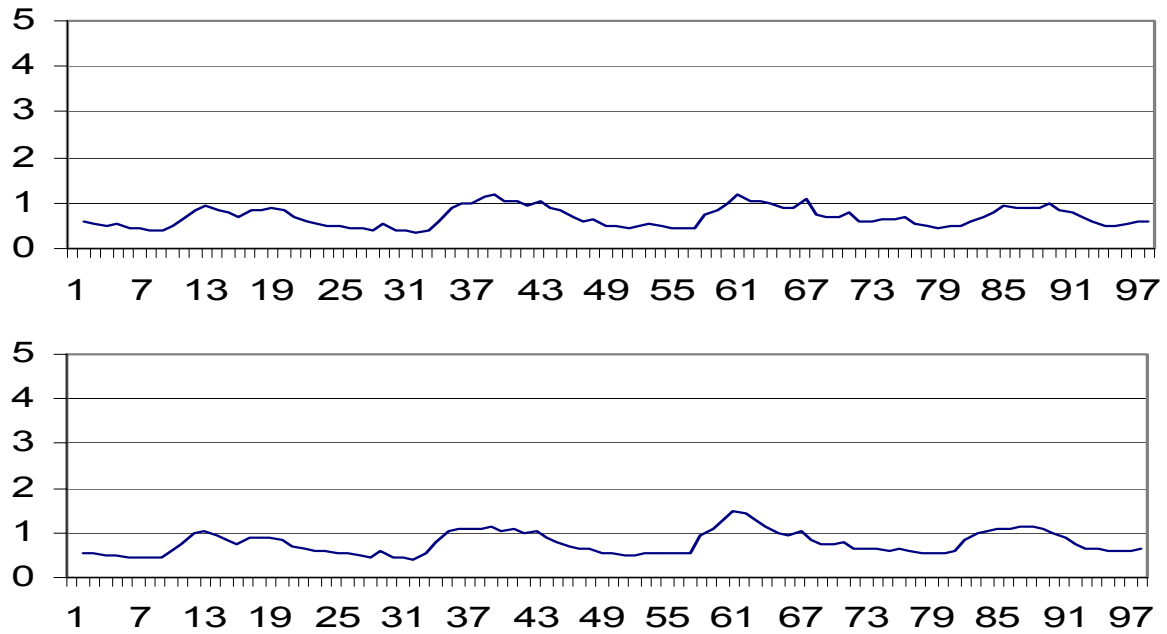


Figure 20. Air temperature σ/σ_0 ratio for 4 days for nested run (top) and downscaled, standalone grid run (bottom). Suggested skill criterion is $\sigma/\sigma_0 \sim 1$.

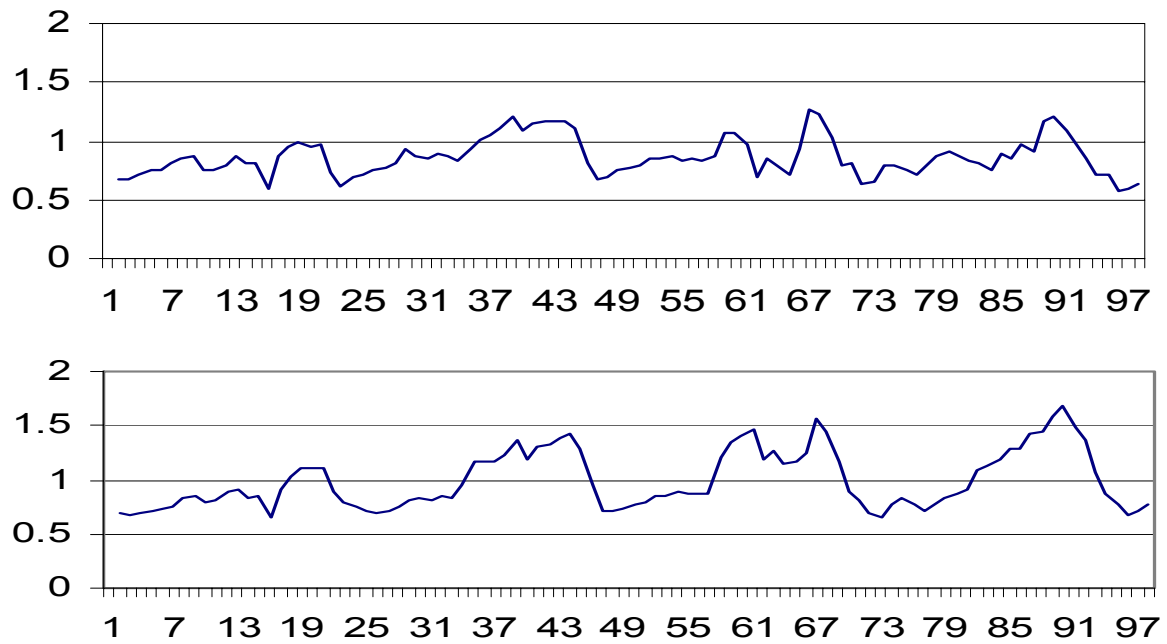


Figure 21. Air temperature E/σ_0 ratio for 4 days for the nested run (top) and downscaled standalone grid run (bottom). Suggested skill criterion is $E < \sigma_0$.

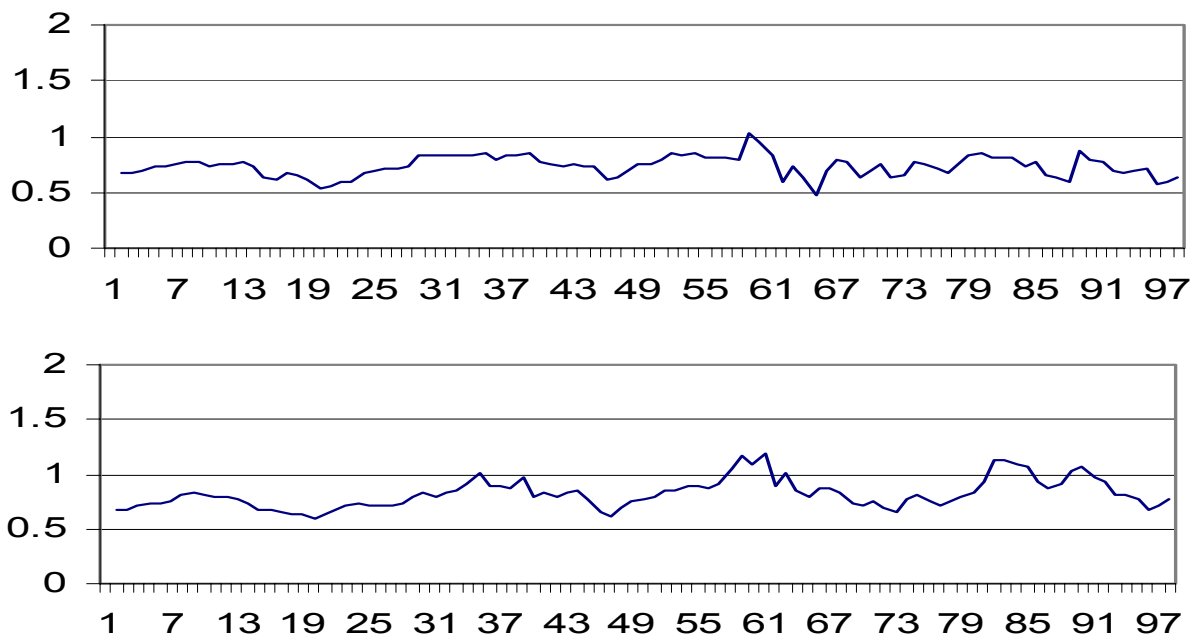


Figure 22. Air temperature E'/σ_0 ratio for 4 days for the nested run (top) and downscaled, standalone grid run (bottom). Suggested skill criterion is $E' < \sigma_0$.

A concluding note to the foregoing evaluation of meteorological simulations is that the performance of the meteorological model, as in this application, is an aspect that will need further evaluation and possible improvement in the future. However, the potential for possible further improvements may not be large because of the specific constraints on performance that this type of application imposes.

In the remainder of this sub-section, photochemical model (CAMx) performance for the Southern California domain is discussed using the benchmarks defined earlier. Here, model performance for the finest grid is given for both nested and standalone runs (see above discussion), for comparative purposes. **Tables 16 and 17** summarize the nested grid run performance, and **Tables 18 and 19** summarize the “standalone” grid’s model performance.

In **Table 16** (and in following tables), yellow-shaded entries indicate results from this study. In the left part of the table, the urban airshed from this study is compared to that from UAM and CALGRID modeling results, both of which are listed in the South Coast AQMD’s 2003 AQMP. For a number of reasons, the UAM was the preferred model selected by the South Coast AQMD. In **Table 16**, normalized MRE and MURE are as defined earlier, and UA is the accuracy of the predicted peak (unpaired), all given on a domain-wide basis. The observed peak on August 5 was 187 ppb, and the simulated peak in this study was 161 ppb. On August 6, both observed and simulated peaks were 170 ppb. Model performance in this study (in yellow) for the entire domain (**Table 16**) meets all recommended benchmarks, and is comparable to UAM and CALGRID model performance (it is also better than those models on August 6).

For sub-domain (regional) evaluation (**Table 17**), model performance varies by day and zone, but for the most important region (Zone 4), model performance in this study is consistently better

than the performance attained by the UAM or CALGRID models. It also meets all recommended benchmarks in that zone. In Zone 3, the model meets the benchmarks and is generally comparable to the UAM performance. The model performance is poorest in Zone 5 (which is also true for UAM and CALGRID results) and is worse than that of UAM or CALGRID, except for MRE on 8/6.

Table 16. Nested grid model performance for the entire domain (Southern California)

Day	UA Domain-wide			Domain-wide	
	UAM	CALGRID	MRE	MURE	
8/5	0.86	0.98	0.88	-0.085	0.26
8/6	1.00	1.20	0.90	-0.005	0.25

Table 17. Nested grid model performance for sub-domains (zones) 3, 4, and 5 (Southern California)

	Day	Zone 3			Zone 4			Zone 5		
		UAM	CALGRID	MRE	UAM	CALGRID	MRE	UAM	CALGRID	MRE
MRE	8/5	-0.16	-0.20	0.05	-0.01	-0.04	0.11	-0.32	0.25	-0.05
	8/6	0.13	-0.09	0.25	-0.03	0.17	0.09	-0.18	0.46	-0.03
MURE	8/5	0.32	0.32	0.29	0.22	0.25	0.35	0.37	0.14	0.23
	8/6	0.35	0.31	0.35	0.19	0.36	0.37	0.76	0.58	0.62

In **Tables 18 and 19**, the same metrics are provided but this time for the *standalone* grid run. The performance of the peak is slightly worse relative to that in the nested run (the simulated peaks are now 158 ppb instead of 161 ppb for August 5, and 164 ppb instead of 170 ppb for August 6) but the area-wide metrics improve, except for MRE on August 6. However, the model still meets all the recommended benchmarks. For sub-domain model performance (**Table 19**), there is a general improvement over the nested simulation results above, although some metrics do get worse. Again, model performance in Zone 4 is better than that of UAM and CALGRID. The MRE in Zone 5 is now better than that of UAM, but the MURE in Zone 5, although it improves slightly, is still an area of poor performance.

Table 18. Standalone grid model performance for entire domain (Southern California)

Day	UA Domain-wide			Domain-wide	
	UAM	CALGRID	MRE	MURE	
8/5	0.84	0.98	0.88	-0.04	0.26
8/6	0.96	1.20	0.90	-0.04	0.22

Table 19. Standalone grid model performance for sub-domains (zones) 3, 4, and 5 (Southern California)

	Day	Zone 3			Zone 4			Zone 5		
		UAM	CALGRID	MRE	UAM	CALGRID	MRE	UAM	CALGRID	MRE
MRE	8/5	-0.22	-0.20	0.05	0.03	-0.04	0.11	0.16	0.25	-0.05
	8/6	0.11	-0.09	0.25	-0.07	0.17	0.09	-0.12	0.46	-0.03
MURE	8/5	0.35	0.32	0.29	0.22	0.25	0.35	0.35	0.14	0.23
	8/6	0.29	0.31	0.35	0.17	0.36	0.37	0.70	0.58	0.62

13.2 Model Performance Evaluation for the CCOS-00 Domain and Episode

Following the general sequence of model performance evaluation discussion above for the SCOS domain and episode, this section gives the meteorological and photochemical modeling statistics for the CCOS domain/episode. For the purpose of evaluating the sub-domain performance of these models, the ARB and the air districts involved with studying the CCOS have proposed nine regions, as seen in **Figure 23**. Of interest for model performance evaluation are zones **3** (SFBA), **6** (Sacramento Valley), **7** (North SJV), and **8** (south SJV). These zones will also be used in comparing certain model performance metrics from this study with those obtained by the ARB.

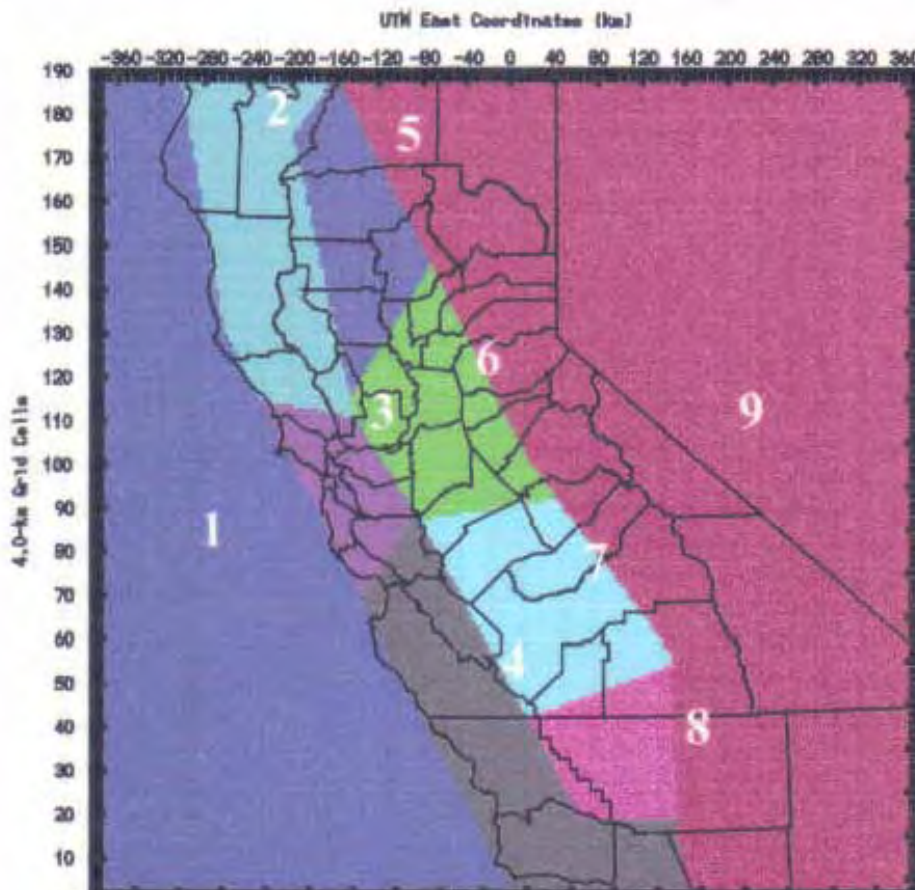


Figure 23. Model performance evaluation sub-regions proposed by the California Air Resources Board and air districts for the CCOS domain and episode. The numbers are to the right of the zones they represent.

Table 20 summarizes some of the temperature and wind MRE and MURE metrics, as defined earlier. Focus is on the regions of interest discussed above and on two days of the episode (July 30 and 31) that are considered primary days in this study. As above, the statistics are for the finest grid of the modeling domain. Compared to the proposed benchmarks for air temperature, the table shows that the performance is relatively worse than for the Southern California simulations, with only about one-third of the metrics meeting the benchmarks for air temperature. However, compared to other modeling efforts *to date* in studying this CCOS domain and episode, e.g., those reviewed by the Modeling Advisory Committee (MAC), the

metrics below are relatively acceptable. The wind speed MRE and MURE suggest good model performance (better than those for the SCOS simulations) and meet or are close to meeting the suggested benchmarks. In terms of wind direction gross error, the model does not meet the suggested benchmarks, but the simulated wind direction is better than that in the SCOS simulations discussed above.

Table 20. Bias (MRE) and gross error (MURE) for selected regions in the CCOS domain

	Date in 2000	Tair bias (K)	Tair error (K)	WSP bias (m/s)	WSP error (m/s)	WDR error (°)
North Sacramento Valley	7/30	-0.85	1.72	-0.53	1.53	61.29
	7/31	-2.24	3.75	0.85	1.91	45.94
South Sacramento Valley	7/30	-1.58	2.07	-0.05	1.45	61.35
	7/31	N/A	N/A	-0.21	1.29	54.11
San Francisco Bay Area	7/30	2.17	3.37	-0.86	1.36	57.90
	7/31	2.96	4.51	-0.72	1.44	60.66
Central SJV	7/30	-1.24	1.91	-0.25	1.19	24.94
	7/31	0.41	2.16	0.45	1.43	50.35
South SJV	7/30	-1.41	1.65	-1.19	1.38	40.63
	7/31	0.36	2.06	-1.06	1.43	66.27

(Tair=air temperature, WSP=wind speed, WDR=wind direction)

Next, the photochemical model performance for the CCOS domain and episode is presented. A brief summary of observed peaks is provided in **Table 21** for days 7/30 through 8/01, 2000 (although 8/1 is not used in subsequent analysis or model performance evaluation) for the zones defined earlier in **Figure 23**. In Table 21, peaks that are equal to or greater than 120 ppb are highlighted. For the three days shown in the table, the observed peaks suggest a sequence where SJV peaks first on July 30, the SFBA peaks second on July 31, and Sacramento peaks third, on August 1 (other days, e.g., later peaking days in SJV, were not examined in this discussion).

Table 21. Observed peak concentrations in the CCOS domain

CCOS region	Observed peak (ppb) and time of occurrence (PST)		
	7/30	7/31	8/01
2	70 (1600)	NA	NA
3 SFBA	82 (1500)	126 (1800)	109 (1600)
4	86 (1700)	109 (1600)	91 (2000)
5	85 (1200)	82 (1600)	105 (1500)
6 Sacramento	121 (1600)	110 (1500)	134 (1900)
7 North SJV	129 (1500)	118 (1500)	118 (1500)
8 South SJV	128 (1500)	115 (1400)	116 (1500)
9	131 (1500)	120 (1500)	104 (1600)

Source: California Air Resources Board 2003

As with model evaluation for the SCOS domain and episode, two base-case configurations are evaluated here for the CCOS episode. One corresponds to the nested grid (where the finest grid has feedback from and to the coarser grids) and the second corresponds to the standalone grid.

Tables 22 and 23 summarize model performance metrics for the *nested* grid. In **Table 22**, columns highlighted with an orange header represent results from this study. These are compared with model performance metrics reported by the ARB, shown in columns labeled “ARB MRE,” “ARB MURE,” and “ARB UA.” Note that the CCOS modeling effort by ARB and AQMDs is still in progress and thus the ARB model performance metrics listed below (which were obtained in spring of 2004) may have changed and improved further since the writing of this report. Instances where the modeling in this study performs better than that of the ARB is highlighted in blue, instances where model performance is inferior to the ARB’s but still acceptable per EPA benchmarks is highlighted in green, and instances where it fails to meet the recommended benchmarks is highlighted in yellow.

Table 22. Normalized MRE, MURE, and UA metrics compared to ARB model performance for the CCOS domain and episode. This is for *nested* grid.

7/30					Peak				
Zone	MRE	MURE	ARB MRE	ARB MURE	Predicted	Observed	UA	ARB UA	
3 SFBA	-0.09	0.14	0.13	0.24	99.6	82	1.21	1.31	
6 Sacramento	0.00	0.11	0.09	0.19	98.2	121	0.81	1.07	
7 North SJV	-0.11	0.16	-0.08	0.18	90.4	129	0.70	1.01	
8 South SJV	-0.22	0.23	-0.12	0.2	102.9	128	0.80	0.96	

7/31					Peak				
Zone	MRE	MURE	ARB MRE	ARB MURE	Predicted	Observed	Ratio (UA)	ARB ratio (UA)	
3 SFBA	-0.16	0.21	0.01	0.22	111.8	126	0.88	0.93	
6 Sacramento	-0.09	0.12	0.05	0.16	92.8	110	0.84	1.25	
7 North SJV	-0.11	0.15	0.03	0.17	101.5	118	0.86	1.09	
8 South SJV	-0.15	0.16	-0.12	0.18	106.6	115	0.92	1.04	

In **Table 23**, model performance is evaluated with respect to the recommended benchmarks. Other regions are also included. As above, those metrics that do not meet the recommended benchmarks are highlighted in yellow. Note, for example, that the second UA value (UA=1.21) in **Table 23** is highlighted in yellow because it exceeds the benchmark, but is shown in blue in **Table 22** above because it is still relatively more acceptable than the ARB-reported value of 1.31.

Table 23. Normalized MRE and MURE, and UA metrics compared to model performance benchmarks (for the CCOS domain and episode; for *nested* grid)

7/30			Peak		
	MRE	MURE	Predicted	Observed	Ratio (UA)
2	-0.02	0.02	73.6	70	1.05
3 SFBA	-0.09	0.14	99.6	82	1.21
4	-0.14	0.18	102.9	86	1.19
5	-0.07	0.11	80.8	85	0.95
6 Sacramento	0.00	0.11	98.20	121	0.81
7 North SJV	-0.11	0.16	90.4	129	0.70
8 South SJV	-0.22	0.23	102.9	128	0.80
9	-0.17	0.19	102.9	131	0.78

7/31			Peak		
	MRE	MURE	Predicted	Observed	Ratio (UA)
2	NA	NA	76.1	NA	NA
3 SFBA	-0.16	0.21	111.8	126	0.88
4	-0.22	0.25	106.6	109	0.97
5	-0.13	0.15	74.8	82	0.91
6 Sacramento	-0.09	0.12	92.80	110	0.84
7 North SJV	-0.11	0.15	101.5	118	0.86
8 South SJV	-0.15	0.16	106.6	115	0.92
9	-0.18	0.20	106.6	120	0.88

In **Table 24**, MRE, MURE, and UA metrics are summarized again; but this time for the *standalone* grid run. The color coding is similar to that defined for **Table 22**. With the exception of the peak on 7/31 and MRE in Zone 8 on 7/30, other metrics have either improved or remained unchanged with respect to the nested case shown in Table 22. But overall, model performance for the standalone scenario is an improvement over the nested case.

Finally, **Table 25**, which summarizes model performance with respect to the recommended benchmarks, also shows that the standalone run generally improved the performance of the model, compared to the nested case (compare to Table 23).

Table 24. MRE, MURE, and UA metrics compared to ARB model performance for the CCOS domain and episode. This is for *standalone* grid.

7/30					Peak			
Zone	MRE	MURE	ARB MRE	ARB MURE	Predicted	Observed	Ratio (UA)	ARB ratio (UA)
3	0.04	0.06	0.13	0.24	107.8	82	1.31	1.31
6	0.00	0.11	0.09	0.19	123.5	121	1.02	1.07
7	-0.11	0.16	-0.08	0.18	103.2	129	0.80	1.01
8	-0.22	0.23	-0.12	0.2	106	128	0.82	0.96

7/31					Peak			
Zone	MRE	MURE	ARB MRE	ARB MURE	Predicted	Observed	Ratio (UA)	ARB ratio (UA)
3	-0.15	0.19	0.01	0.22	118.9	126	0.94	0.93
6	-0.09	0.12	0.05	0.16	102.6	110	0.93	1.25
7	-0.11	0.15	0.03	0.17	113.1	118	0.95	1.09
8	-0.14	0.15	-0.12	0.18	112.1	115	0.97	1.04

Table 25. Normalized MRE and MURE, and UA metrics compared to model performance benchmarks (for the CCOS domain and episode; for *standalone* grid)

7/30			Peak		
	MRE	MURE	Predicted	Observed	UA
2	0.01	0.01	85	70	1.21
3 SFBA	0.04	0.06	107.8	82	1.31
4	-0.15	0.17	107.3	86	1.24
5	-0.08	0.11	82.8	85	0.97
6 Sacramento	0.00	0.11	123.5	121	1.02
7 North SJV	-0.11	0.16	103.2	129	0.80
8 South SJV	-0.22	0.23	106	128	0.82
9	-0.14	0.17	268.3	131	2.04

7/31			Peak		
	MRE	MURE	Predicted	Observed	UA
2	NA	NA	79.4	0	NA
3 SFBA	0.00	0.13	118.9	126	0.94
4	-0.15	0.19	113.1	109	1.03
5	-0.14	0.15	75.9	82	0.92
6 Sacramento	-0.09	0.12	102.6	110	0.93
7 North SJV	-0.11	0.15	113.1	118	0.95
8 South SJV	-0.14	0.15	112.1	115	0.97
9	-0.13	0.16	135.7	120	1.13

14. Development of Control Strategy

The main premise of the surface-modification strategies being evaluated in this report is to cool urban areas and, thus, achieve the potential air-quality benefits resulting from their implementation. More accurately, the goal is to prevent urban areas from warming up as much as they would if the control strategies (urban surface modifications) were not in place. As summarized earlier in **Figure 1**, such control strategies can include increased urban vegetative cover, increased urban surface albedo, specific urban design and planning strategies, geometrical and solar access considerations, and so on. The main focus of this study and report is on the potential impacts of increased urban surface albedo and vegetative cover on the local meteorology, precursor emissions, and ozone air quality.

This section summarizes the basis for developing surface modification scenarios. **Table 10** summarizes the assumed surface properties (at 200 m resolution) for each base-case scenario. Once a base case has been established and the corresponding model performance has been evaluated the modeling work proceeds to evaluating the impacts of surface modifications (e.g., increases in albedo and vegetative cover). A first step in establishing such control scenarios is to define the makeup of representative urban land-use categories. **Table 26** identifies the area makeup of the seven urban USGS LULC categories identified earlier (Table 10) as assumed in this study, based on previous surface characterization work (e.g., Taha 1996, 1997; Akbari et al. 1999; and Rose et al. 2003). Of course the numbers given in Table 26 are not city-specific—that is, it cannot be claimed that they are Sacramento-specific or Los-Angeles-specific, but they are generally representative of U.S. urban regions. Obviously, the site-specificity of such characterizations can be improved upon in the future, in a follow-up to this study.

Table 26. Assumed percentages of built-up surface types for urban USGS LULC

USGS LULC		% roof	% road	% parking	% sidewalk or driveway	% remainder
Urban categories						
11	Residential	20	13	4	9	54
12	Commercial/Services	21	15	40	3	21
13	Industrial	20	11	28	1	40
14	Transportation/Communication	20	40	30	1	9
15	Industrial and Commercial	20	13	34	2	31
16	Mixed urban or built up	21	21	11	2	45
17	Other urban or built up	21	21	11	2	45

The next step is to assign a level of albedo increase for each of the most common urban surface types. **Table 27** presents two levels of albedo increase, representing moderate and high changes that also account for the effects of albedo reduction due to such factors as weathering, dust accumulation, debris, and soiling. The table also identifies scenarios (cases 10, 11, 20, and 22) that represent some of the cases to be discussed in the results sections later in the report.

Table 27. Assumed levels of albedo increase per surface type

Surface type	Increase in albedo		Typical <u>base</u> albedo value
	Moderate <u>increase</u> (cases 10 and 11)	Large <u>increase</u> (case 20 and 22)	
Residential roofs	0.10	0.30	0.15
Commercial roofs	0.20	0.40	0.20
Roads	0.15	0.25	0.10
Sidewalks/Driveways	0.10	0.20	0.15
Parking lots	0.15	0.25	0.10

Based on the above assumed per-surface changes and the aerial makeup of various surface types, the base-case albedo values and their changes per 200 m USGS LULC category can now be computed. **Table 28** shows the results for the cases identified above. These new 200 m albedo values are then georeferenced in the modeling domain and averaged/up-scaled to match the model resolution of the finest grids in each of the SCOS and CCOS domains. For the SCOS domain, the 200 m data is up-scaled to 5km, and for the CCOS domain, up to 4 km.

Table 28. Scenarios for albedo (α) change at 200-m resolution for the base case and scenarios 10, 11, 20, and 22

USGS LULC		Base α	New value for scenarios 10 and 11	New Value for scenarios 20 and 22
Urban categories				
11	Residential	0.157	0.217	0.278
12	Commercial/Services	0.139	0.252	0.366
13	Industrial	0.152	0.242	0.332
14	Transportation/Communication	0.117	0.245	0.374
15	Industrial and Commercial	0.145	0.242	0.349
16	Mixed urban or built up	0.134	0.207	0.281
17	Other urban or built up	0.142	0.180	0.199

The foregoing discussion summarized the development of albedo modification scenarios; urban reforestation scenarios are discussed next. The approach is generally similar to that for albedo calculations discussed above. The main difference is in the assignment of vegetation change to each surface type or land use. The basic assumption here is that approximately 2 trees are added per unit in the moderate scenario (cases 01 and 11) and approximately 4 trees per unit in the high scenario (scenario 02 and 22). A “unit” is defined here as a standalone residential, commercial, or industrial unit (or combinations). More accurately, these assumptions are translated into percent increase in vegetation cover per 200-m grid cell (that is, percentage of 200 m grid cell area), as shown in **Table 29**.

Table 29. Scenarios for vegetation cover increase (as % of 200-m cells)

USGS LULC		% Change for scenarios 01 and 11	% Change for scenarios 02 and 22
Urban categories			
11	Residential	9	18
12	Commercial/Services	9	18
13	Industrial	4	8
14	Transportation/Communication	2	4
15	Industrial and Commercial	6	12
16	Mixed urban or built up	5.5	11
17	Other urban or built up	5.5	11

Upon translation of these increases in vegetative cover into corresponding changes in soil moisture content, the following base and modified scenarios are obtained for each 200 m USGS LULC (**Table 30**). The basis for this derivation is simply a linear interpolation that assumes that if a grid cell were totally revegetated, its soil moisture content will increase by 0.3. That is:

$$\eta' = \eta + 0.3\Delta$$

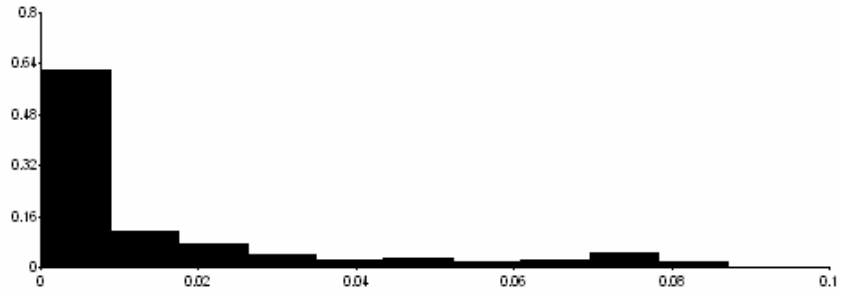
where η' and η are respectively the new and base-case soil moisture content of a 200 m grid cell, and Δ is the fractional change in vegetative cover.

Table 30. Base case and scenarios for soil moisture (η) changes

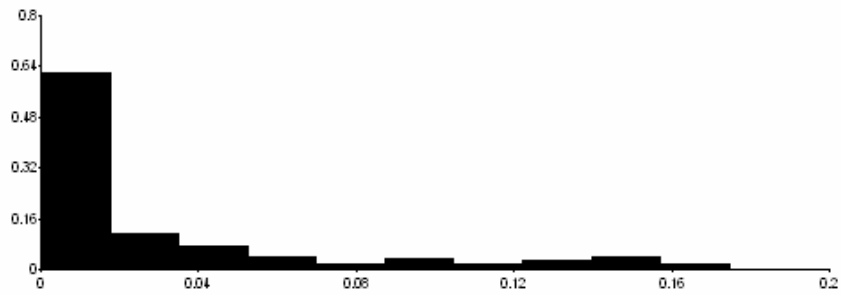
USGS LULC		base η	New value for scenarios 01/11	New value for scenarios 02/22
Urban categories				
11	Residential	0.10	0.127	0.154
12	Commercial/Services	0.05	0.086	0.122
13	Industrial	0.05	0.062	0.074
14	Transportation/Communication	0.02	0.026	0.032
15	Industrial and Commercial	0.05	0.074	0.098
16	Mixed urban or built up	0.05	0.067	0.083
17	Other urban or built up	0.05	0.077	0.104

To provide a picture of the spatial distribution of these changes in surface albedo and soil moisture, **Figures 24 and 25** provide relative distributions of changes in the SCOS (Figure 24) and CCOS (Figure 25) domains. The given percentages are relative to a total of 1291 modifiable grid cells in the SCOS domain and 1944 modifiable grid cells in the CCOS domain. Note that the distribution shapes for the moderate and high scenarios are similar; only the level of change (as seen on the x-axis) differs from one case to another. From this analysis, it is clear that:

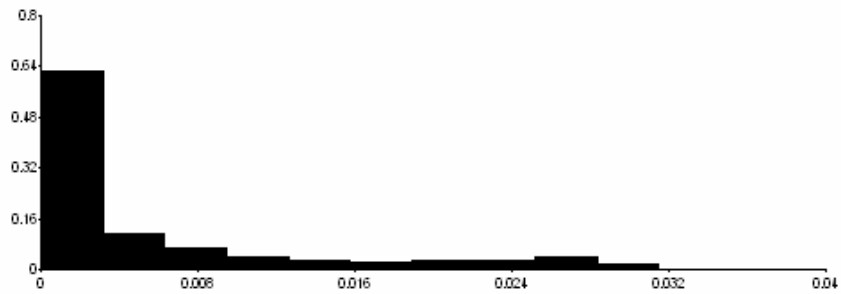
- About 80% of the modifiable area is affected by increases of smaller than 0.02 in albedo for the moderate scenario and smaller than 0.04 for the high scenario (at model-grid resolution).
- About 80% of the modified area is affected by increases < 0.008 in soil moisture (for the moderate-increase scenarios) and < 0.016 in the high scenarios (at model-grid resolution).



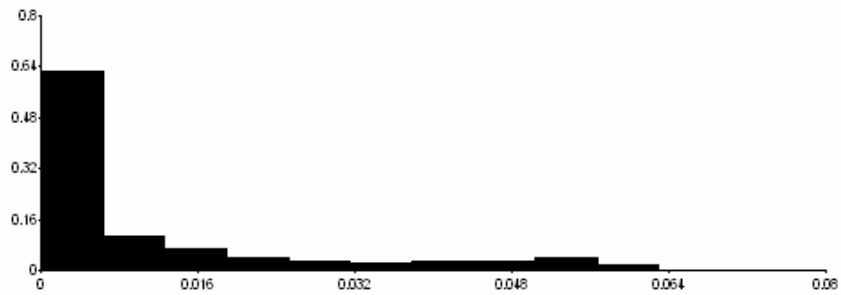
(A) SCOS albedo increase distribution for the moderate-increase case (10 and 11)



(B) SCOS albedo increase distribution for the high-increase case (20 and 22)

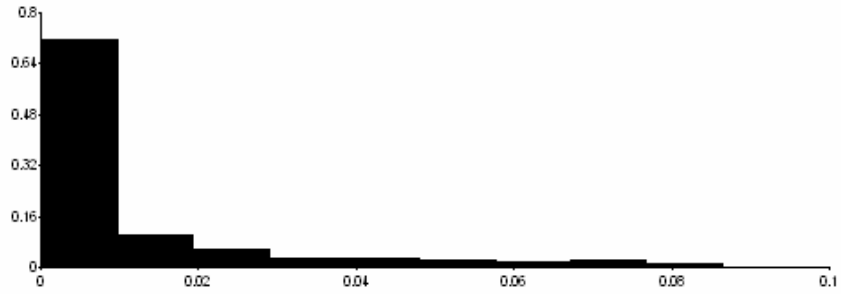


(C) SCOS soil moisture increase distribution for the moderate-increase case (01 and 11)

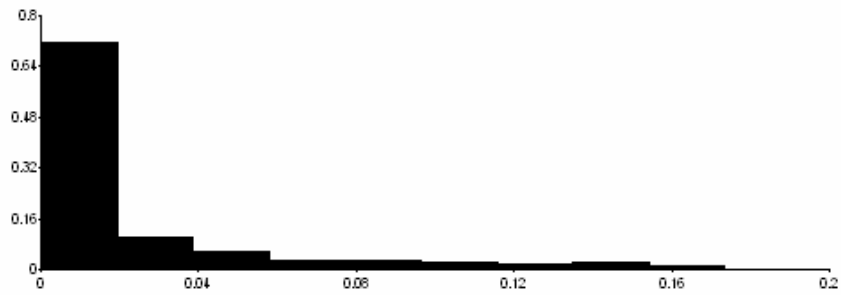


(D) SCOS soil moisture increase distribution for the high-increase case (02 and 22)

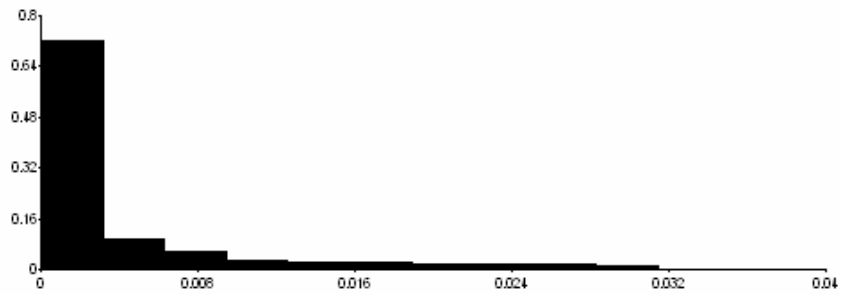
Figure 24. (A–D): Distributions of changes in surface albedo and soil moisture in the SCOS domain. Total number of modifiable cells = 1291.



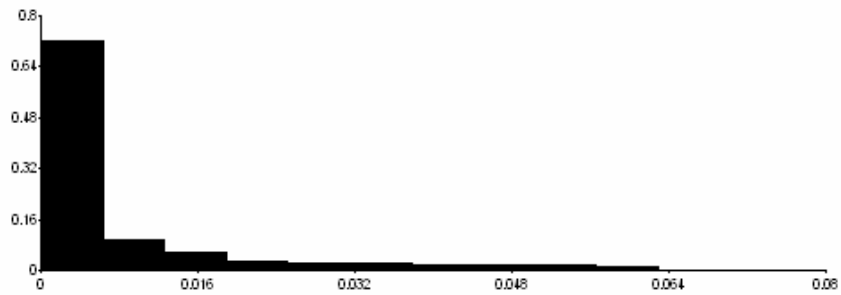
(A) CCOS albedo increase distribution for the moderate-increase case (10 and 11)



(B) CCOS albedo increase distribution for the high-increase case (20 and 22)



(C) CCOS soil moisture increase distribution for the moderate-increase case (01 and 11)



(D) CCOS soil moisture increase distribution for the high-increase case (02 and 22)

Figure 25 (A–D): Distributions of changes in surface albedo and soil moisture in the CCOS domain. Total number of modifiable cells = 1944.

The following discussion provides some information that can be used to arrive at a crude estimate of what surface modifications may be needed to achieve the above changes in regional albedo and soil moisture (and the resulting meteorological and air quality changes discussed later in this report). Note that the estimates given in the tables below are based on simple and very crude assumptions, and are by no means exact or accurate.

Based on the LULC characterization discussed earlier in this report, **Tables 31 and 32** provide some crude estimates of the total area (in square kilometers, or km²) of roofs and paved surfaces that need to be modified in each USGS LULC category in some urban regions in California. As will be shown later in the discussions of results, those regions with the largest modification areas are also those with the largest meteorological and air-quality changes. In the tables below, the first row gives an estimate of the total urban area (km²) in each region, based on 200 m USGS LULC analysis (note that this LULC classification scheme can be outdated in some cases by 10 years or more, and thus may not correspond exactly to an urban region's present extent).

When the sum of all modified surfaces in each region (i.e., sum of areas of roofs, streets, sidewalks, parking lots, etc., to be modified) is calculated, it is found to represent about 55%–58% of the total urban area in each region. In other words, about 55% to 58% of the urban surface area in each region must be modified in order to attain the meteorological and air quality effects discussed later in the results. Of course this is a hypothetical situation developed for the purpose of evaluating the potential effects in this study; many other scenarios are possible, such as increasing the level of surface modification while decreasing modified area. Also, any actual implementation plan would require more specific modifications and modeling that would be tailored for the detailed specifics and conditions of each region of interest, and the amount of change may thus be larger or smaller than what is assumed here.

Table 31. Total ROOF area to be modified (km²)

	Bakersfield	Fresno	Sacramento	SF Bay Area	Los Angeles Basin	San Diego
Urban area** →	174	283	553	2540	5404	652
LULC ↓						
11	16.0	35.3	60.5	296.1	671.9	78.5
12	3.8	10.8	18.6	84.0	187.5	26.1
13	7.3	3.8	7.0	61.9	86.5	6.0
14	4.2	3.4	9.2	27.9	55.0	9.6
15	0.05	0	0.38	6.8	4.6	0.08
16	0.9	1.3	5.5	5.7	10.4	0.3
17	2.8	2.5	11.0	31.1	77.7	11.3
TOTAL→	35	57	112	513	1093	132

** Total area (km²) as used in this study.

Table 32. Total PAVED surface area (parking, roads, sidewalks) to be modified (km²)

	Bakersfield	Fresno	Sacramento	SF Bay Area	Los Angeles Basin	San Diego
Urban area** →	174	283	553	2540	5404	652
LULC ↓						
11	20.8	45.9	78.7	384.9	873.5	102.1
12	10.5	29.8	51.4	232.0	518.0	72.2
13	14.6	7.6	14.0	123.8	173.0	12.0
14	15.0	12.3	32.7	99.3	195.5	34.3
15	0.13	0	0.94	16.8	11.3	0.19
16	1.6	2.2	8.9	9.3	16.9	0.61
17	4.6	4.0	17.8	50.4	125.8	18.3
TOTAL→	67	102	204	916	1914	239

** Total area (km²) as used in this study.

If additional simplifying assumptions are made about the representative roof areas of residential, commercial, industrial, and other types of buildings, and of representative tree canopies, then the following rough estimates can also be derived. Again, a warning is appropriate here that these are simply crude estimates and are not based on any specific analysis. Thus **Tables 33 and 34** show, respectively, the number of buildings (roofs) that need to be modified and the number of trees that need to be added to achieve the surface modification levels mentioned above and the effects discussed in Section 15.

Table 33. Number of buildings needed for modification (includes all types)

Region	Total number of roofs (buildings) to modify (×1000)
Bakersfield	137
Fresno	244
Greater Sacramento Valley	486
Greater San Francisco Bay Area	2090
Los Angeles Basin/Southern California	4640
Greater San Diego region	571

Table 34. Number of trees needed for modification (average of cases 01 and 02)

Region	Total number of trees to add (×1000), assuming 50 m ² per tree
Bakersfield	235
Fresno	453
Greater Sacramento Valley	840
Greater San Francisco Bay Area	3923
Los Angeles Basin/Southern California	8601
Greater San Diego region	1036

Finally, **Figures 26 and 27** show the potential of surface modification as computed for the Southern and Central California domains, respectively. In the figures, higher relief means greater potential for modification (i.e., potential for increasing surface albedo and/or vegetation fraction). This potential was computed based on the LULC analysis discussed earlier along with the assumed distribution of surface types and availability for modification. In **Figure 28**, an example is shown for the corresponding increases in soil moisture for the two domains. Changes in albedo would have the same spatial pattern, only different values.

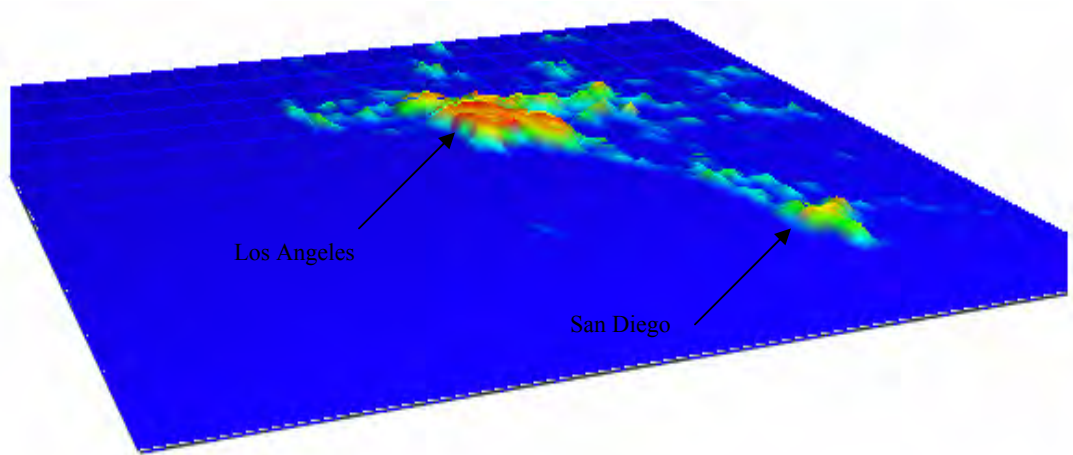


Figure 26. Surface modification potential in Southern California (not to scale)

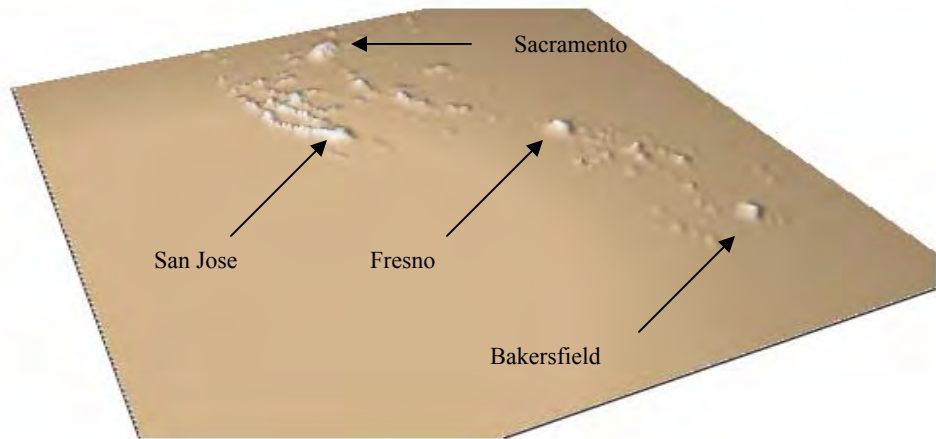


Figure 27. Surface modification potential in Central California (not to scale)

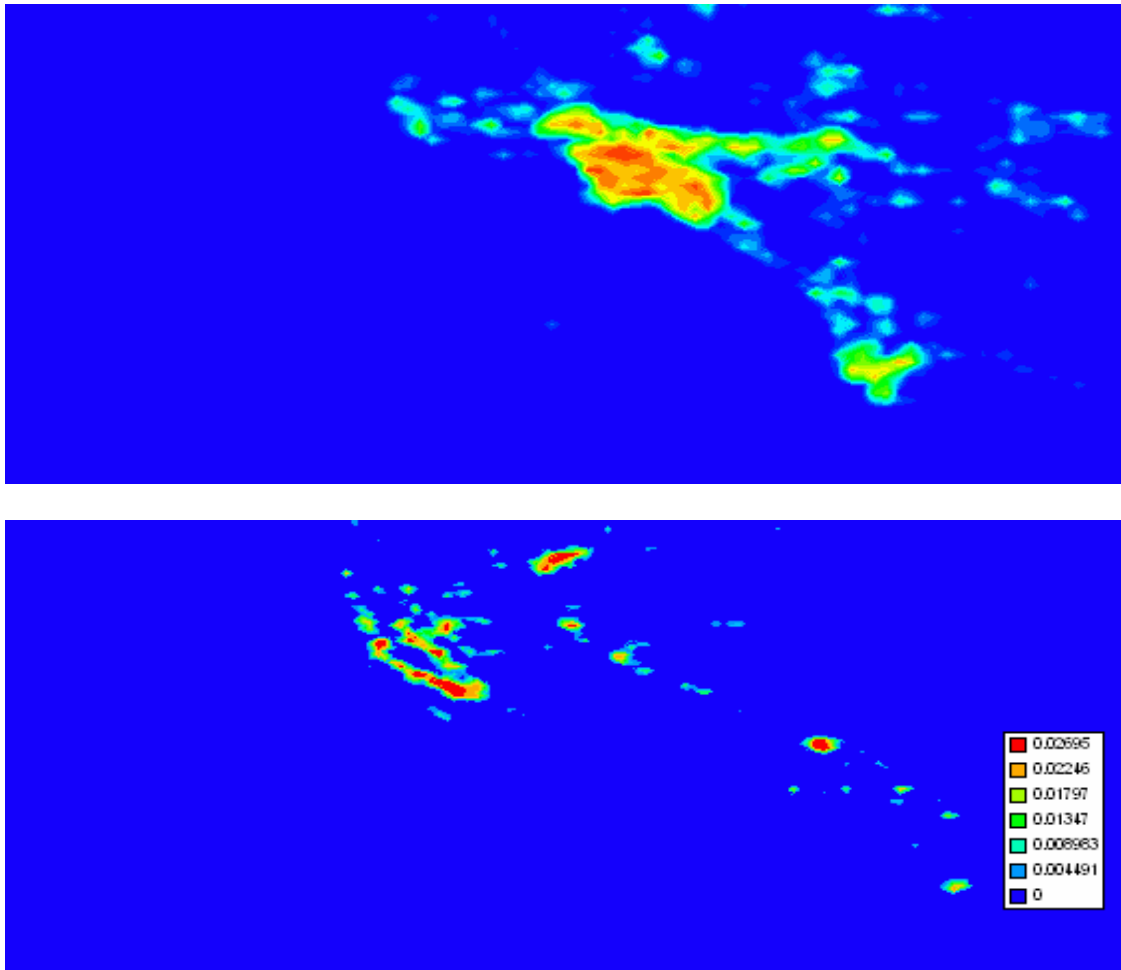


Figure 28. Example changes in soil moisture for Southern California (top) and Central California (bottom). Figures are not in similar in scale.

14.1 Discussion A: Ultraviolet (UV) Radiation and Albedo Increase

In terms of the strategy discussed in this report, albedo is bound by the range of 0.28 to 2.8 μm , i.e., *solar* albedo. By definition, this includes tropospheric radiation in the general regions of UV, visible, and near infrared (NIR) spectra. In addition to the main effect of changing visible and NIR albedo, there is interest in the potential effects of possible changes in UV albedo as a result of implementing this strategy. This is so because the energies in the UV wavelength range drive most of the important photodissociation reactions (e.g., those of NO_2 , O_3 , and PAN, which can have potential implications on ozone formation, leading to negative impacts). However, in reality, the proposed changes in urban surface albedo may have small or no effect at all on UV albedo. As discussed in this section, most reflective materials incur no increase in UV albedo and some high-albedo materials actually have lower UV albedos than conventional materials.

Regardless of whether or not high-albedo materials actually change UV albedo, the effects of UV radiation changes (e.g., UV-B) on ozone formation are not easy to discern. Increased UV-B in areas with high NO_x emissions (e.g., urban and industrial areas) can increase ozone formation

(Gery et al. 1988; Thompson 1992) and the opposite can be true in areas with low NO_x emissions, such as suburban or rural regions (Liu and Trainer 1988).

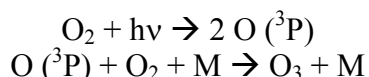
In terms of spectral energy distribution, the UV range contains about 5%, the visible about 46%, and the NIR about 49% of the energy. Thus when increasing albedo for cooling purposes, changes in UV albedo (if they occur at all) have very small overall impacts. But changes in the visible and NIR are roughly equal and very important and thus the main target of this strategy.

The purpose of this discussion is to briefly address the issue of potential UV albedo changes related to increasing overall urban albedo. The issue actually involves more than just the changes in albedo (i.e., how much UV radiation is available); it also involves actinic irradiance and species-specific characteristics such as quantum yield and absorption cross sections (which all together determine the rates of photodissociation for a particular species). But the focus here is on albedo because it is the one parameter that is changing from one surface-modification scenario to another.

Generally, the UV spectrum is defined as follows:

- UV-A: 0.315–0.400 μm
- UV-B: 0.280–0.315 μm
- UV-C: 0.100–0.280 μm

Stratospheric oxygen absorbs UV radiation in the range 0.17–0.24 μm and photodissociates to produce ozone:



where M = air = N₂, O₂, for example. This leaves only UV-B and UV-A radiation to reach the troposphere because the ozone produced in the above process absorbs UV at and below 0.29 μm. Thus in the troposphere, wavelengths of relevance to photochemical reactions are those 0.30 μm and longer (Seinfeld and Pandis 1998) but still short enough to contain the high energy spectrum. Of the smog-related photochemical reactions in the polluted boundary layer, photodissociations of importance to the strategy of increasing albedo are mainly those of NO₂, O₃, and PAN. Nitrogen dioxide absorbs at wavelengths of 0.45 μm or shorter, but because there is little UV radiation reaching the troposphere at or shorter than 0.29 μm, the theoretical critical UV range of interest for NO₂ is thus between 0.30 and 0.45 μm (Cooper and Alley 1994).

Further narrowing this range is the fact that 90% of the NO₂ molecules absorb UV energy below 0.4 μm (Stern et al. 1984) and as a result, the practical range of importance for NO₂ photodissociation is 0.3 to 0.37 μm (Seinfeld 1975). For O₃, the critical UV wavelength range is 0.315 μm or shorter (Harrison 1990) and for PAN, the cutoff is 0.35 μm or shorter (Seinfeld and Pandis 1998). Thus the inclusive range of 0.3 to 0.37 μm is the overall “envelope” that needs to be considered when modifying surface albedo. This envelope is shown by the area to the left of the vertical *red* line (and red arrow) in **Figure 29**.

As seen in **Figure 29**, it is possible to select materials that increase overall albedo without increasing UV albedo—e.g., compare curves B, D, and E that show increase in overall albedo without much changing (if not decreasing) UV albedo. The fact that some high-albedo materials reflect less UV than their low-albedo counterparts can be seen in **Figure 30**. For example, if a cedar shake roof is replaced by either a titanium dioxide (TiO₂)-painted roof or a limestone-based product to increase albedo, the UV albedo decreases, while the overall albedo increases significantly. In the first case, the UV albedo decreases from about 0.58 to 0.15, while the overall albedo increases from about 0.35 to 0.7. However, except for new construction, the given example of replacing a cedar-shake roof with a TiO₂-painted roof is not a common practice, as in most cases a roof will likely be replaced with one of similar material, construction, texture, and appearance. As will be discussed later, there exist materials that are similar in these ways, but with different solar albedos and relatively unchanged UV albedos.

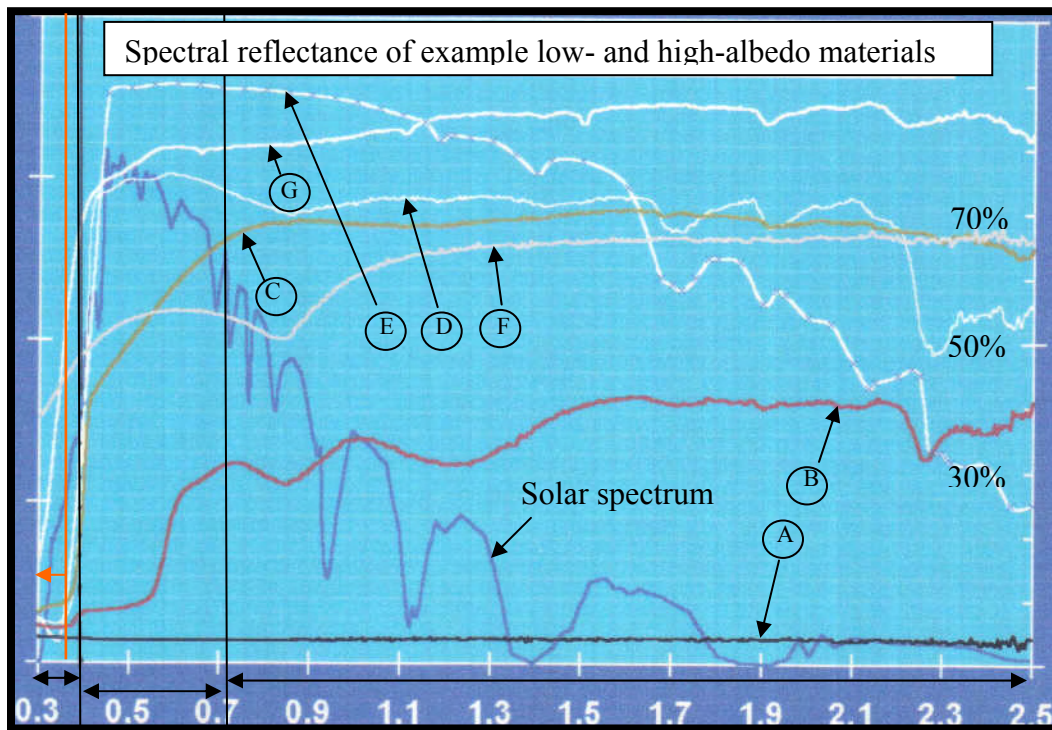


Figure 29. Measured spectral reflectance of selected materials based on measurements by Berdahl et al. (2002) and Berdahl and Bretz (1997). The vertical black lines overlaid on the figure depict the UV, visible, and NIR ranges, respectively shown with two-headed arrows at the bottom of the figure. The vertical red line and arrow show the UV range of practical relevance to photodissociation (in terms of albedo modifications). The blue line shows the solar spectrum (solar energy intensity). Other labels are discussed in the text.

In **Figure 29**, consider, for example, material A, which has a very low albedo (~ 0.05). By moving to material B or C, the overall albedo increases to about 0.25 and 0.60, respectively, whereas the changes in UV albedo are relatively smaller, e.g., from 0.05 to 0.06 (A \rightarrow B) and to about 0.09 (A \rightarrow C). However, materials D and E have much higher solar albedos (e.g., 0.7 and 0.82, respectively), but their UV albedos are similar to (unchanged from) that of material B, for example. In fact, the UV albedo of D or E can be lower than that of B. Of course there are also

high-albedo materials such as F and G (about 0.7) that also have high UV albedo (e.g., up to about 0.4). From an ozone photochemistry perspective, one needs to avoid this latter type of materials, unless they are used to replace similar ones, i.e., with originally high UV albedo.

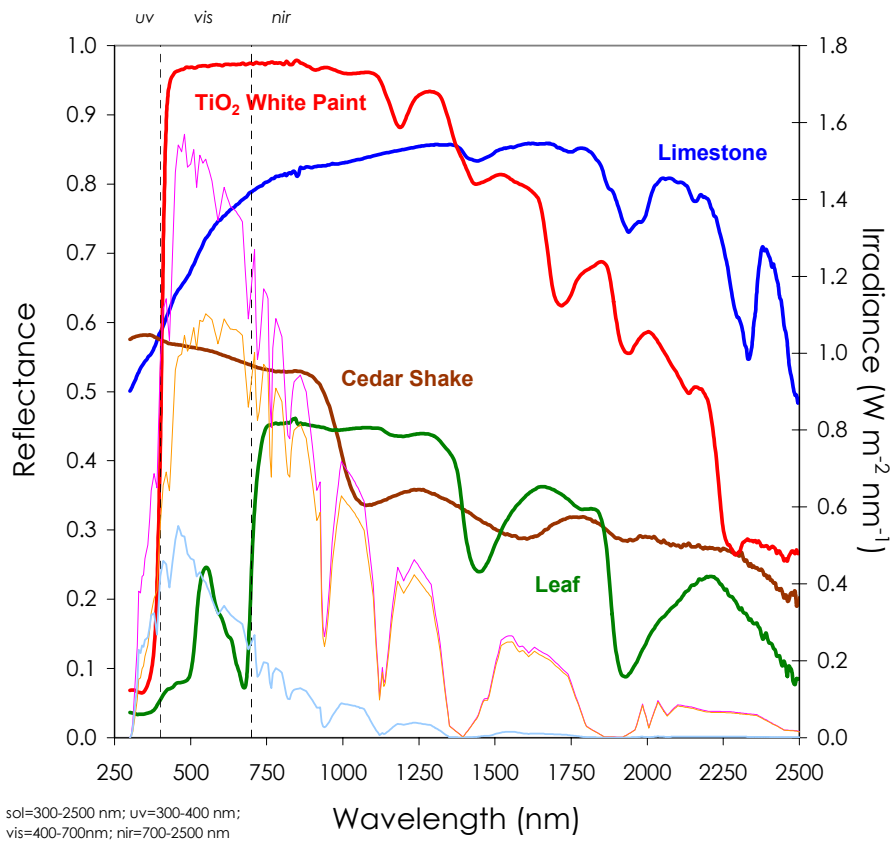


Figure courtesy of Ronnen Levinson (2004), Lawrence Berkeley National Laboratory, Berkeley, California. Also: Akbari et al. (2003).

Figure 30. Spectral reflectivity characteristics of selected roofing materials. A leaf is also included for comparison.

Berdahl and Bretz (1997) provide reflectance measurements and albedo values for a variety of materials (some examples shown in **Table 35**). The materials selected in Table 35 are of similar structure, construction, and material, but of different albedos. As seen in the table, it is possible to increase solar albedo in the visible and NIR ranges without changing the UV albedo by any significant amount. In some cases, such as the *single-ply* example in **Table 35**, UV albedo actually decreases while visible and NIR albedos increase. For asphalt shingles, there is no change in UV albedo at all, while overall albedo increases from 0.08 to 0.21.

Table 35. Albedo of selected materials

<i>Example materials</i>	<i>Albedo</i>			
	<i>Solar</i>	<i>UV</i>	<i>VIS</i>	<i>NIR</i>
Coatings (in order of increasing solar albedo)				
<i>Product 1</i>	0.74	0.10	0.79	0.76
<i>Product 2</i>	0.83	0.11	0.89	0.85
<i>Product 3</i>	0.85	0.12	0.90	0.87
Single-ply membranes (in order of increasing solar albedo)				
<i>Product 1</i>	0.77	0.25	0.80	0.79
<i>Product 2</i>	0.80	0.19	0.87	0.79
<i>Product 3</i>	0.83	0.14	0.91	0.82
Asphalt shingles (in order of increasing solar albedo)				
<i>Product 1</i>	0.08	0.05	0.08	0.09
<i>Product 2</i>	0.08	0.06	0.08	0.09
<i>Product 3</i>	0.12	0.06	0.12	0.12
<i>Product 4</i>	0.20	0.06	0.22	0.19
<i>Product 5</i>	0.21	0.06	0.24	0.21

Source: Based on Berdahl and Bretz 1997

In summary, the purpose of the above discussion is to show that it is possible to increase visible and NIR albedo without increasing UV albedo. Thus it is possible to maximize the expected benefits from lower air temperatures without the inadvertent effects that might be associated with changes in UV albedo. This is an implicit assumption made in developing scenarios of albedo increases in this modeling study. Thus in the meteorological simulations of modified scenarios, solar albedo is increased, whereas UV albedo is assumed unchanged in the photochemical simulations.

In the CAMx-implemented CB-V mechanism used in this study, the UV albedo is space-varying, depending on land use. The minimum value is 0.044 and the highest 0.076. Over most of the urban areas, such as the major urban zones in the CCOS and SCOS modeling domains, the UV albedo is at the higher end of the range, e.g., between 0.06 and 0.07. These values are unchanged in the simulations of various surface modification scenarios, as explained above.

14.2 Discussion B: Increasing Vegetative Cover and Biogenic Hydrocarbon Emissions

Another issue of relevance to photochemical production of ozone is the increase in vegetative cover, e.g., the selection of tree species or other vegetation. Of importance here is the rate of biogenic hydrocarbons emissions, such as those of isoprene and monoterpenes. The target in implementing any urban reforestation strategy is thus to use non- or low-emitting vegetation species. In an earlier modeling study, for example, Taha (1996) showed that for the Los Angeles Basin, tree species emitting at a rate of more than 2 micrograms per gram per hour ($\mu\text{g/g/hr}$) of isoprene and/or monoterpenes could bring adverse effects on air quality when introduced in large numbers (e.g., thousands or millions of trees). That study also pointed out that numerous species of zero-emitting vegetation exist that could be used for such an application (Bloch and Winer 1994). Thus in actual implementation schemes of urban reforestation strategies, careful selection of tree species is an important issue. In this modeling study, and as discussed in this report, the additional vegetation introduced in urban areas is assumed to be non-emitting.

14.3 Impacts on biogenic hydrocarbon emissions

The changes in meteorology, e.g., temperature, solar radiation, and water vapor mixing ratios (as well as CO₂ concentrations) have an impact on the rates of emissions of hydrocarbons (isoprene and monoterpenes) from vegetation. Thus even though it is assumed here that the *additional* vegetation introduced in urban areas is non emitting, the effects of reduced air temperature (from increased urban albedo and vegetation) on emission from *existing* vegetation still must be quantified. To account for this effect, this modeling study uses a function developed by Guenther et al. (1993), given below. A newer form of this function exists (Guenther et al. 1999), which also requires knowledge of longer-term changes in meteorological parameters. In this episodic study, it is assumed that solar radiation does not change from one control scenario to another and that changes in water vapor are small, so that the main corrections performed here are those for air temperature change, as follows:

$$C_T = \left\{ \exp \frac{\gamma(T - T_s)}{RT_s T} \right\} / \left\{ 1 + \exp \frac{\eta(T - T_m)}{RT_s T} \right\}$$
$$M_T = M_s \exp[\theta(T - T_s)]$$

where C_T is a *correction factor* for the effect of temperature on emission rate of isoprene at temperature T , and M_T is the monoterpene *emission rate* at temperature T . In the equations above, γ , η , and θ are constants, T is actual air temperature (for which the emission rate is being calculated), T_s is standard air temperature, R is the gas constant, T_m is a constant (314K), and M_s is the emission rate at standard air temperature.

It should be noted that changes in biogenic emissions can have different impacts on ozone formation. The directionality of that effect depends on several factors, notably the local NO_x/VOC concentration ratio. In addition, decreasing air temperature does not always decrease biogenic emissions; according to above equation, if temperature is in the range of 38°C–42°C (100°F–108°F), decreasing it can actually *increase* emissions. The sensitivity of emission rates to temperature is highest in the range of about 25°C to 37°C (77°F–99°F).

In this study, these adjustment and corrections to biogenic emissions were performed for each scenario, including the base case.

15. Meteorological and Air-quality Impacts of Surface-modification Strategies

This section discusses the modeled impacts of increased urban albedo and reforestation on meteorology and ozone air quality. The changes in meteorology are discussed first, focusing on air temperature and wind speed changes. The ozone changes are then discussed. It is understood that all meteorological parameters change as a result of surface modifications. The focus on air temperature here is simply to keep the discussion relatively compact and because it is the parameter of most relevance to the issues of urban heat islands mitigation and urban surface modification. On the other hand, the changes in ozone concentrations account for all those meteorological perturbations (e.g., temperature, moisture, winds, mixing height), as well as changes in emissions and photochemistry.

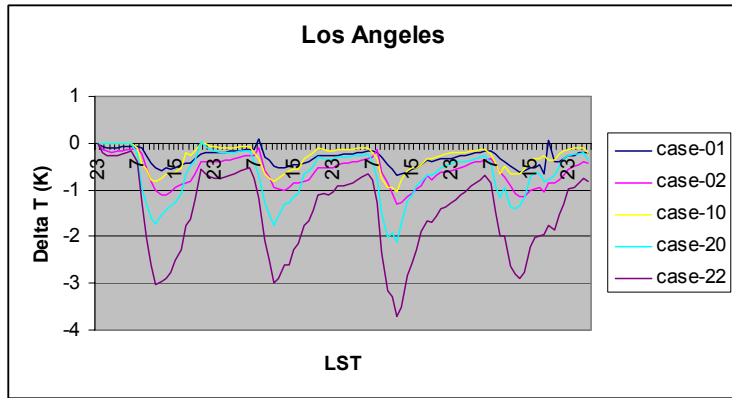
Results are provided for a number of scenarios, as appropriate for each case. As a shorthand notation, the following case designations are used (not all cases are shown in the results section):

00	Base case
01	Moderate increases in vegetation cover
02	Large increases in vegetation cover
10	Moderate increases in albedo
20	Large increases in albedo
11	Combined moderate increases in albedo and vegetation cover
22	Combined large increases in albedo and vegetation cover

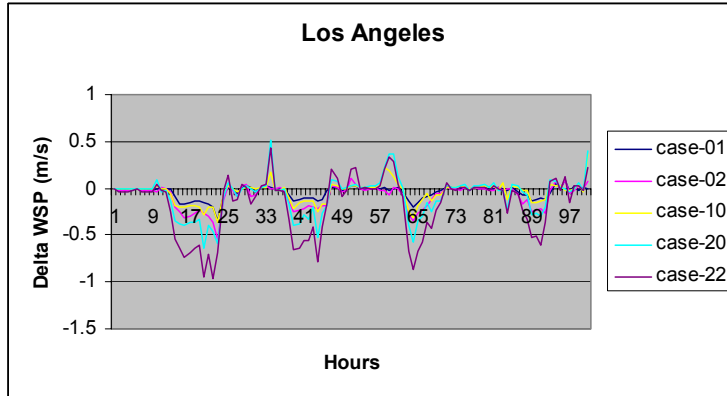
15.1 Southern California

This section presents two types of analyses. First, time series of air temperature and wind-speed changes are given for a number of scenarios simulated in this study. In the second part, two-dimensional changes in air temperature are shown for one scenario (case 22) and one day as an example. The time-series of changes are given for four regions: (1) Los Angeles (Downtown area), (2) San Fernando Valley (Burbank area), (3) Pomona (and nearby inland areas), and (4) San Diego. These also are regions that experience some of the largest changes in surface properties, meteorology, and air-quality as a result of “implementing” the strategies defined earlier in this report.

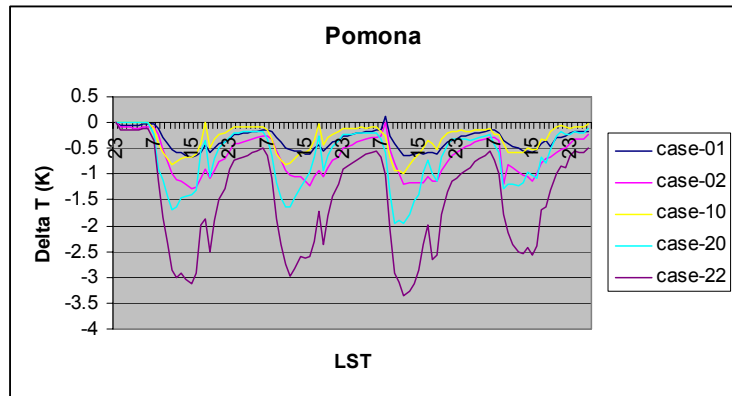
Figure 31 (A–H) summarizes changes in 2 m air temperature and 10 m wind speed for these four regions and five scenarios. The time-series are for four days (August 3, 4, 5 and 6). As can be seen for all four regions, a typical temperature-change pattern is a decrease during the daylight hours and smaller (or near-zero) decrease during the night. The amount of temperature decrease gets larger as the level of surface modification increases. For example in figure A (Los Angeles), cases 20 and 22 have the highest impacts, with decreases in air temperature of as much as 3°C (5.4°F) and up to 3.5°C (6.3°F) on one occasion. The other three cases (with relatively smaller surface modifications), produce smaller impacts on air temperature, e.g., decreases of up to 1°C (1.8°F). Overall, the effectiveness of the strategies at reducing air temperature is in the following increasing order of scenarios: 01, 10, 02, 20, and 22.



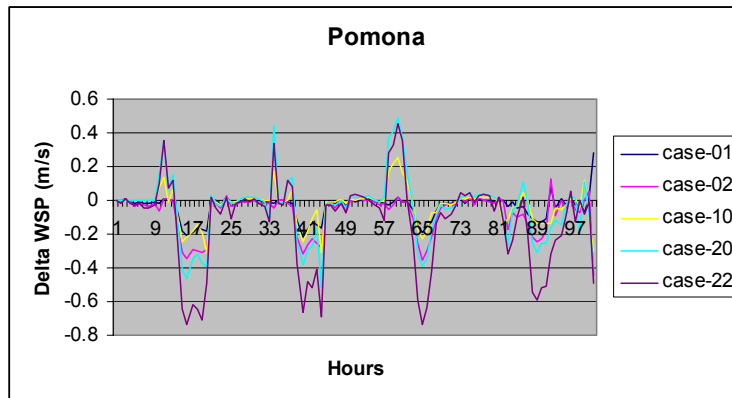
A



B

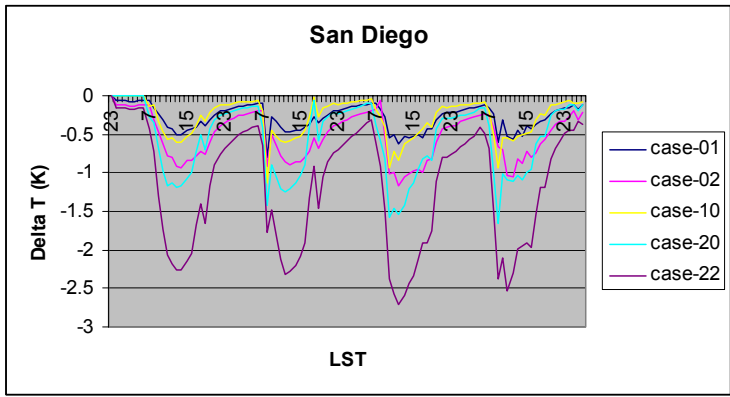


C

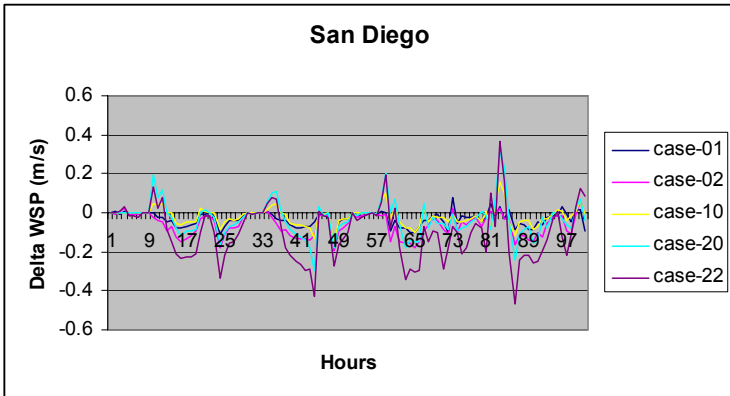


D

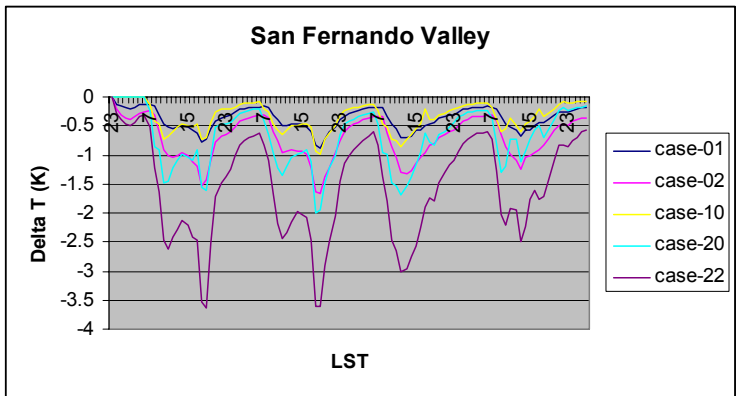
Figure 31. (A–H). Changes in 2-m air temperature and 10-m wind speed in four Southern California areas and for 5 surface-modification scenarios (August 3–6). Data are from a representative grid cell in each defined region.



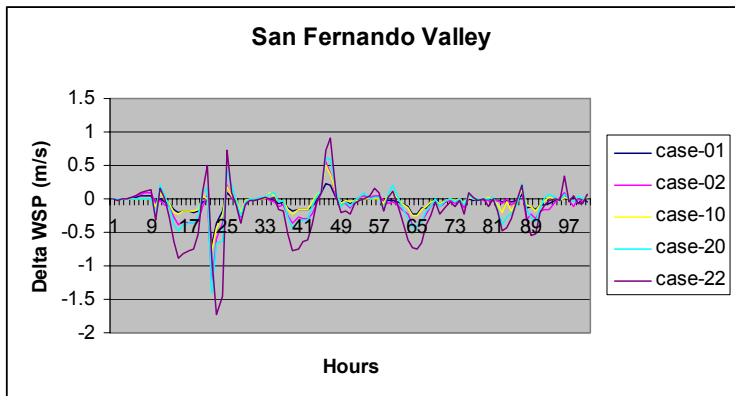
E



F



G



H

Figure 31. (continued).

In Figure 31 C (Pomona), the same change pattern is seen but with slightly smaller magnitudes (e.g., smaller than Los Angeles by about 0.5°C (0.9°F) in some cases and at certain times). However, overall, the effect is about the same as it is in Los Angeles. In San Diego (Figure 31 E), where surface modifications are relatively smaller, the impacts on air temperature are likewise reduced. Although the order of scenarios (effectiveness) is the same as in the other areas, the changes in temperature are about 1°C (1.8°F) smaller than in Los Angeles, overall. Finally, in the San Fernando Valley (Figure 31 G), the changes are of the same order of magnitude as in Los Angeles and Pomona, with a slight difference in the timing of the largest decrease (e.g., on the first two days), which seems to occur later during the day rather than earlier, as in the other cases. In almost all cases, the decrease in air temperature starts at 0900 LST (local standard time) and tapers off around 2100 LST, although at different magnitudes.

Note that the largest temperature decreases occur on August 5 (the primary day of the episode) except for the San Fernando Valley, where slightly more cooling occurs earlier in the episode.

In terms of wind speed, there is likewise a general diurnal pattern in changes relative to the base case conditions. The decrease in wind speed is also generally proportional to the level of surface modification. As seen in Figure 31 B (Los Angeles), for example, there is a somewhat detectable diurnal cycle where wind slows (by up to about 0.7 to 1 meters per second (m s^{-1}) between 1500 and 0300 LST. On two of the episode days, there is also a slight acceleration between 0800 and 1000 LST (of about 0.3 to 0.5 m s^{-1}). In Pomona (Figure 31 D), there is a cyclic reduction of up to about 0.6 m s^{-1} between 1200 and 2000 LST, i.e., with onset slightly delayed relative to Los Angeles and also of a shorter duration. The increases in speed occur between 0700 and 1200 LST and up to about 0.4 m s^{-1} . In San Diego (Figure 31 F), the changes seem to be less organized than in the Los Angeles and Pomona regions, but still display a pattern of decrease between 0900 and 2000 and then between 2200 and 0200 LST almost daily. The acceleration is somewhat more random. The changes are also smaller, generally about up to 0.4 m s^{-1} .

Finally, in the Burbank region and the San Fernando Valley (Figure 31 H), the changes in wind speed appear to have a periodic decrease between 1000 to 1600 LST (of up to about 0.3 m s^{-1}). However, the pattern is not as clear as in the other regions.

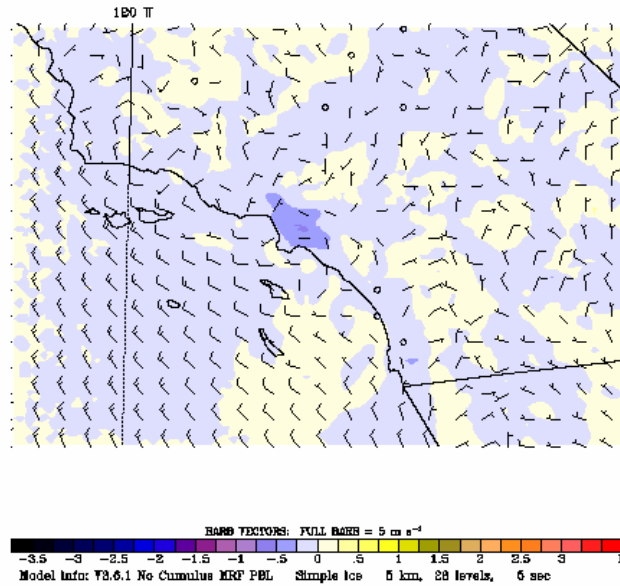
Next, one case is arbitrarily selected for two-dimensional graphical analysis. The scenario presented in **Figure 32** corresponds to case 22 (large increases in urban albedo and forest) and shows some of the largest potential impacts on air temperature resulting from surface modifications.

Figure 32 shows the change in air temperature (case 22 minus case 00) superimposed on the base-case wind vector field (of case 00). A number of hours (at two-hour intervals) are shown for an earlier day of the episode (August 4) from 0700 to 2100 LST. The temperature difference and its evolution throughout the day, shown here for case 22, are typical across all other scenarios (not shown) and other episode days as well. Of course, the magnitude of change is different. At night, there is no difference in air temperature in all cases. As seen in the time series above, the temperature difference starts at early morning hours, grows larger, then tapers off towards evening time and disappears by about 22 LST. This is seen again in the figures below.

The spatial distribution of temperature change matches very closely the level of surface modifications in the modifiable areas, e.g., compare **Figure 32** (changes in air temperature) with **Figure 26** (potential for surface modifications). Figure 32 also shows how the temperature difference can be advected downwind (at the end of the day), for example, through the northern and eastern passes of the basin and into the Mojave Desert.

```

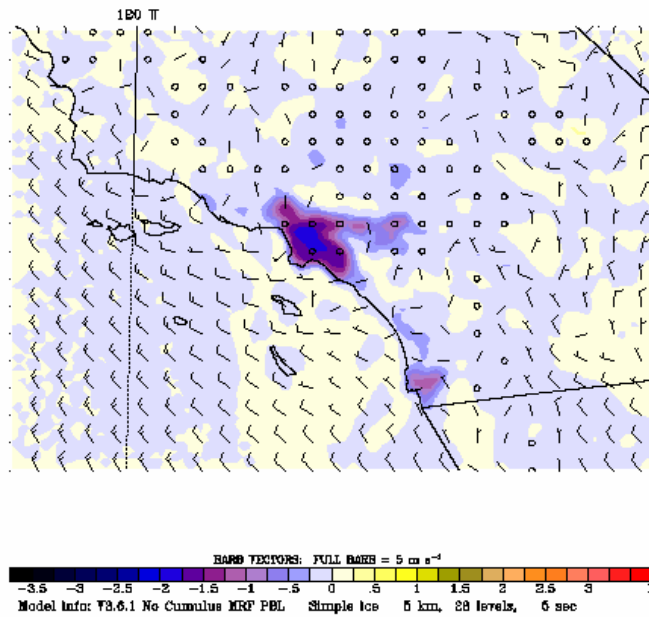
Dataset: case22 RIP: ripexecute.diff.SCOS Init: 0600 UTC Sun 03 Aug 97
Fcst: 32.00 Valid: 1400 UTC Mon 04 Aug 97 (0700 PDT Mon 04 Aug 97)
Temperature at sigma = 0.999
(diff. from case=case00, time= 32.00)
Horizontal wind vectors at sigma = 0.999
  
```



A

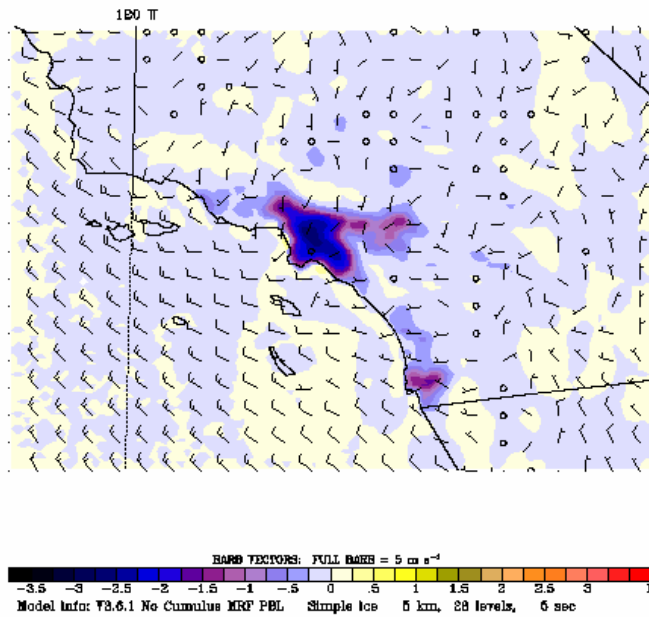
Figure 32. (A–H). Air temperature difference (from the base case) for scenario 22. Temperature difference is superimposed over the base-case wind vector field.

Dataset: case22 RIP: riperecute.diff.SCOS Init: 0600 UTC Sun 03 Aug 97
 Fcst: 34.00 Valid: 1600 UTC Mon 04 Aug 97 (0900 PDT Mon 04 Aug 97)
 Temperature at sigma = 0.999
 (diff. from case=case00, time= 34.00)
 Horizontal wind vectors at sigma = 0.999



B

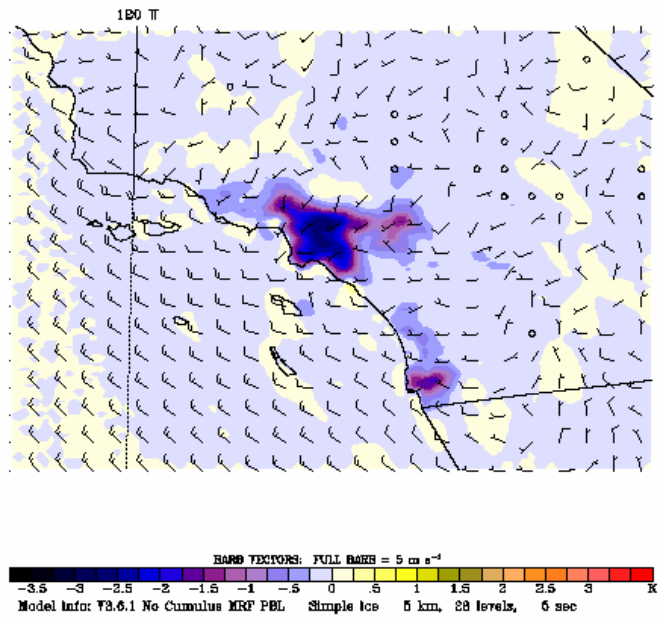
Dataset: case22 RIP: riperecute.diff.SCOS Init: 0600 UTC Sun 03 Aug 97
 Fcst: 36.00 Valid: 1600 UTC Mon 04 Aug 97 (1100 PDT Mon 04 Aug 97)
 Temperature at sigma = 0.999
 (diff. from case=case00, time= 36.00)
 Horizontal wind vectors at sigma = 0.999



C

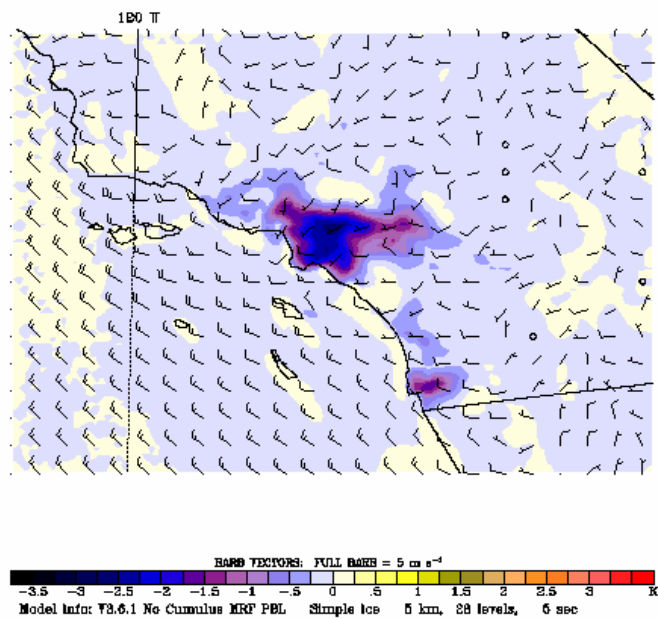
Figure 32. (continued).

Dataset: case22 RIP: ripexecute.diff.SCOS Init: 0600 UTC Sun 03 Aug 97
 Fcst: 36.00 Valid: 2000 UTC Mon 04 Aug 97 (1300 PDT Mon 04 Aug 97)
 Temperature at sigma = 0.999
 (diff. from case=case00, time= 36.00)
 Horizontal wind vectors at sigma = 0.999



D

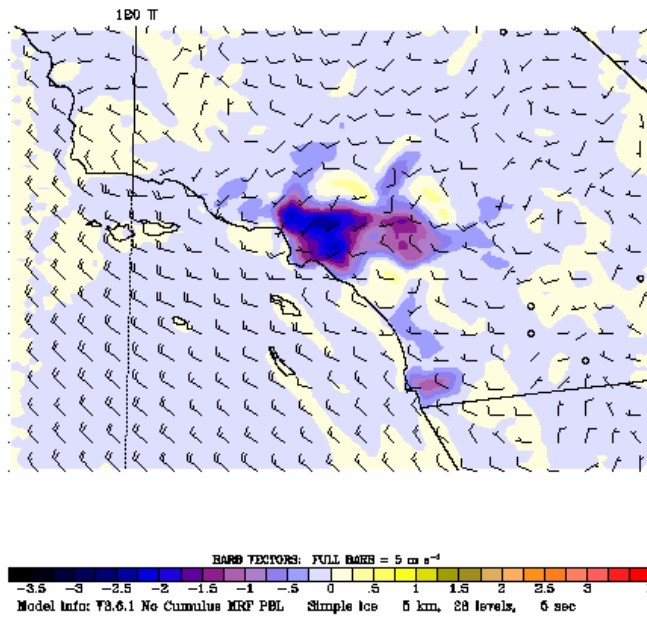
Dataset: case22 RIP: ripexecute.diff.SCOS Init: 0600 UTC Sun 03 Aug 97
 Fcst: 40.00 Valid: 2200 UTC Mon 04 Aug 97 (1500 PDT Mon 04 Aug 97)
 Temperature at sigma = 0.999
 (diff. from case=case00, time= 40.00)
 Horizontal wind vectors at sigma = 0.999



E

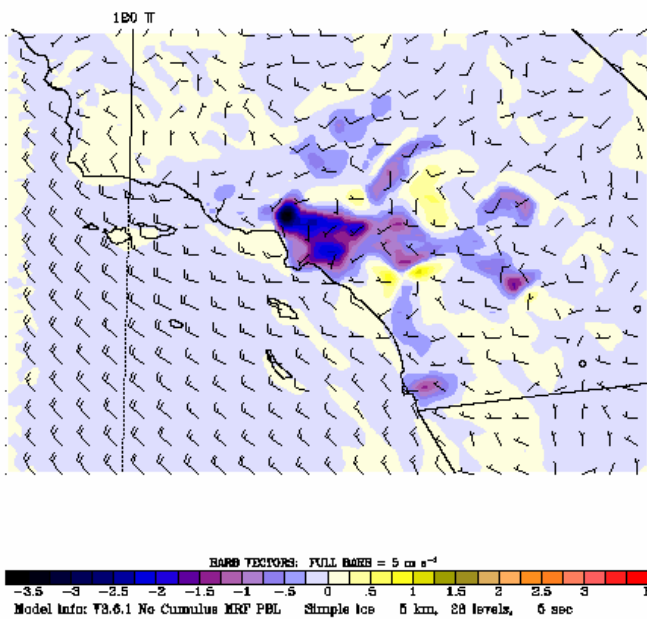
Figure 32. (continued).

Dataset: case22 RIP: ripexecute.diff.SCOS Init: 0600 UTC Sun 03 Aug 97
 Fcst: 42.00 Valid: 0000 UTC Tue 05 Aug 97 (1700 PDT Mon 04 Aug 97)
 Temperature at sigma = 0.999
 (diff. from case=case00, time= 42.00)
 Horizontal wind vectors at sigma = 0.999



F

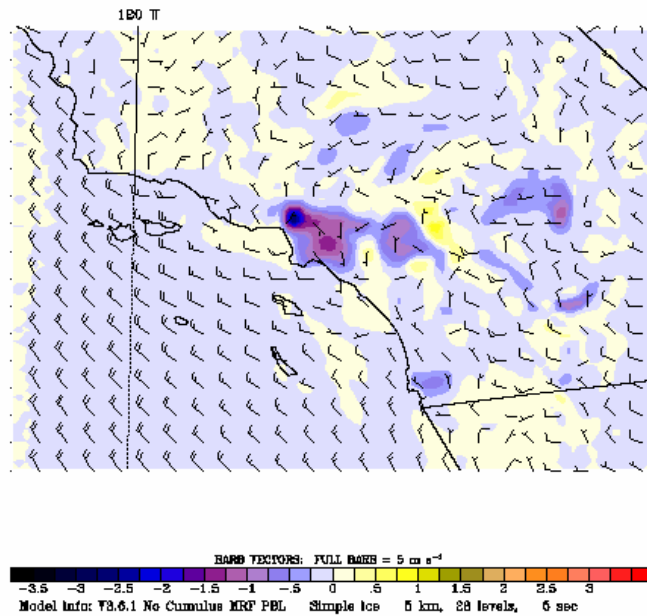
Dataset: case22 RIP: ripexecute.diff.SCOS Init: 0600 UTC Sun 03 Aug 97
 Fcst: 44.00 Valid: 0200 UTC Tue 05 Aug 97 (1900 PDT Mon 04 Aug 97)
 Temperature at sigma = 0.999
 (diff. from case=case00, time= 44.00)
 Horizontal wind vectors at sigma = 0.999



G

Figure 32. (continued).

Dataset: case22 RIP: ripexecute.diff.SCOS Init: 0600 UTC Sun 03 Aug 97
 Fcst: 46.00 Valid: 0400 UTC Tue 05 Aug 97 (2100 PDT Mon 04 Aug 97)
 Temperature at sigma = 0.999
 (diff. from case=case00, time= 46.00)
 Horizontal wind vectors at sigma = 0.999



H

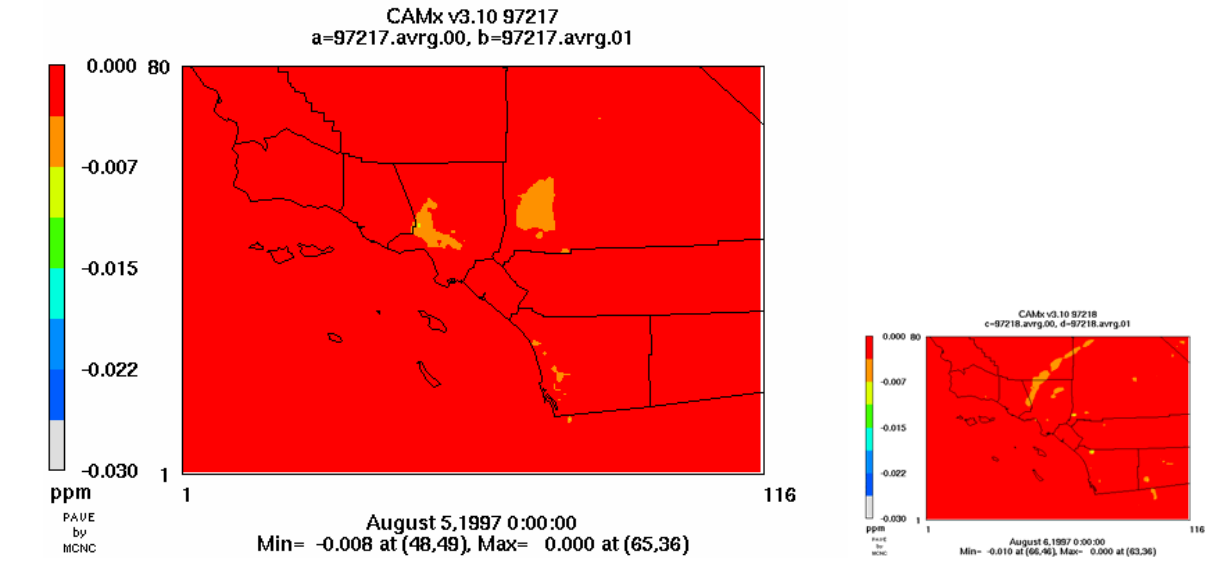
Figure 32. (continued).

Following the above discussion of meteorological changes (e.g., temperature and wind speed), the rest of this section focuses on the corresponding changes in ozone concentrations. The focus here is on the primary day of the episode (August 5) but August 6 is also discussed and shown in some of the figures.

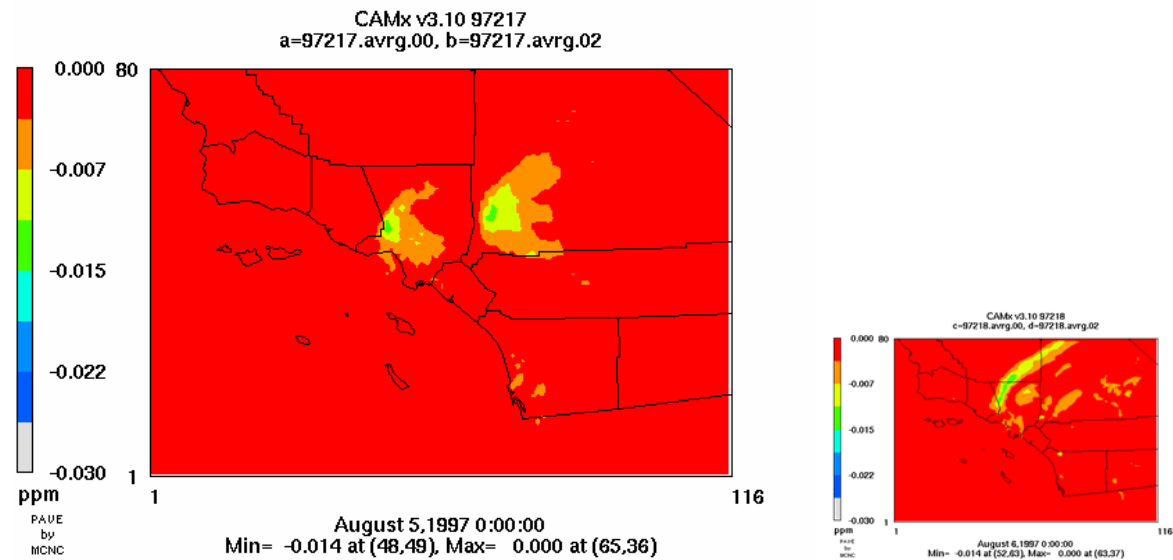
First a qualitative analysis is provided by examining, for example, the largest hourly change in concentrations at each grid cell in the domain. As discussed previously in this report, and further explained in Appendix A, the nonlinear nature of the photochemical reactions system producing ozone can cause both increases and decreases in concentrations when surface modifications are “implemented” and meteorological fields are perturbed. **Figure 33** shows only the decreases in concentrations (note that this simply is the largest change throughout the domain and is not spatiotemporally consistent, nor is it related to the changes in the peaks discussed later or the timing of these changes). Following **Figure 33**, a number of metrics will be provided that accounts for both decreases and increases in ozone concentrations, and diurnal effects (e.g., relative reduction factor (RRF) analysis), as well as analysis of 1-hour, 8-hour, and 24-hour averages.

Figure 33 shows qualitatively where the changes (e.g., decreases) tend to occur, rather than provide a specific quantitative analysis. The results suggest that the changes increase as the level or amount of surface modifications becomes larger. On August 6, the plume-like pattern in the figures shows that ozone decreases are also advected downwind on that day, into the Mojave Desert. It can also be seen that the largest decreases on August 5 do not occur near the location

of the peak (smaller decreases occur there), whereas, on August 6, most of the larger decreases occur near the peak's locations.

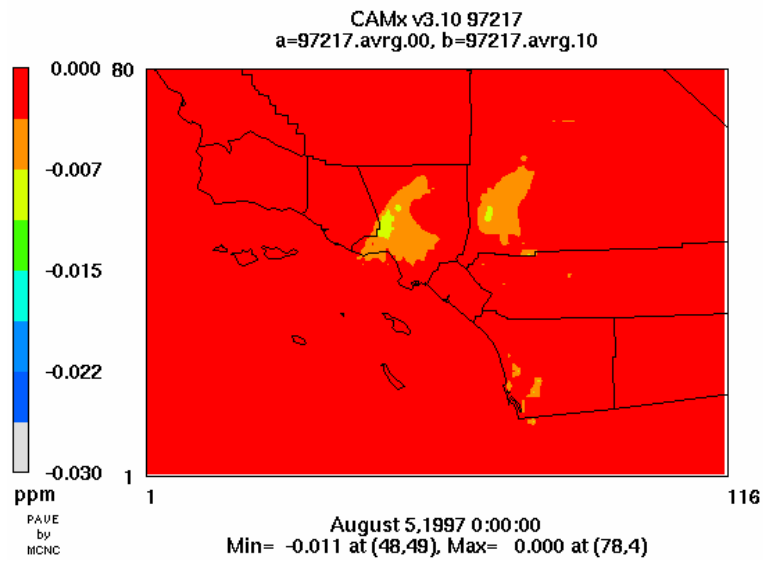


Above: Case 01.

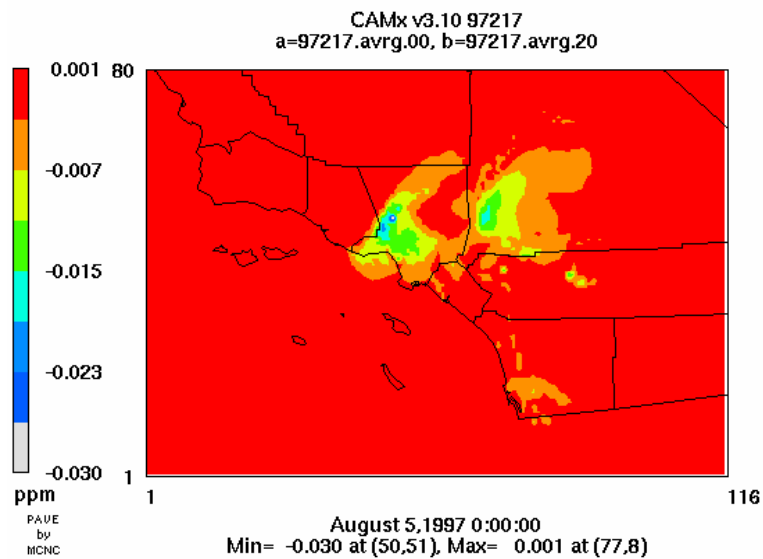
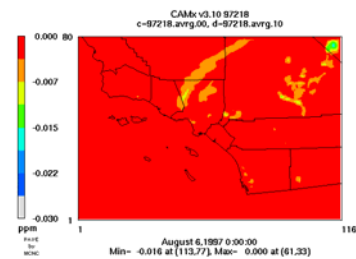


Above: Case 02.

Figure 33. Maximum hourly decrease in ozone concentration at each grid cell for several scenarios (Cases 01, 02, 10, 20, and 22). Left: Changes on August 5. Right: Changes on August 6.



Above: Case 10.



Above: Case 20.

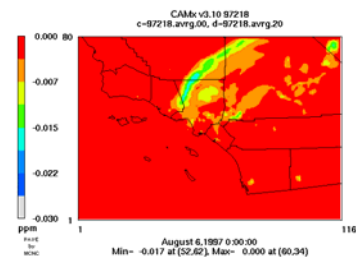
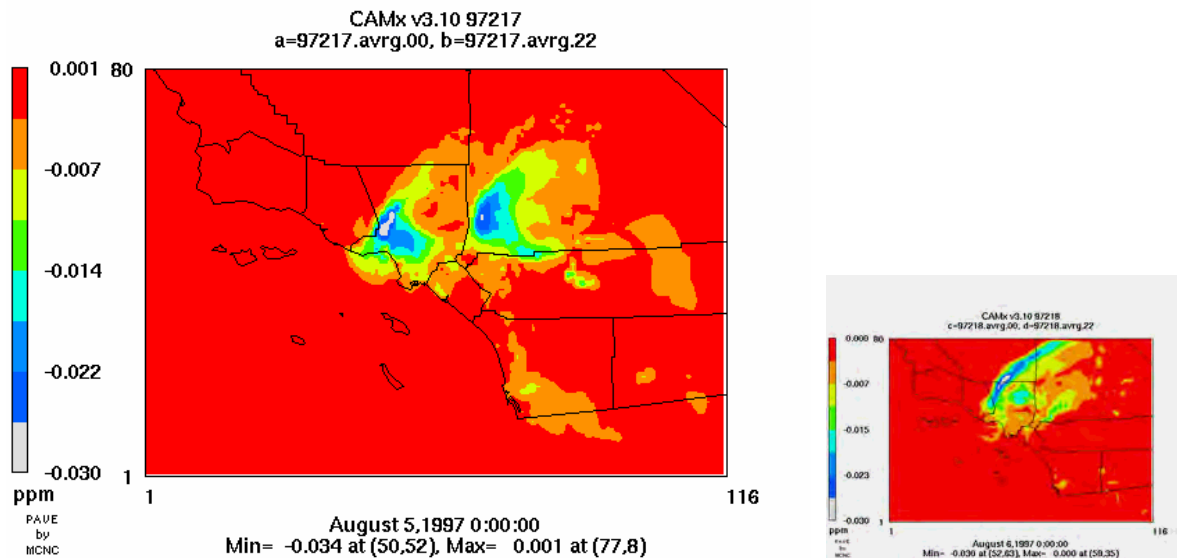


Figure 33. (continued).



Above: Case 22.

Figure 33. (continued).

To provide a relatively more quantitative analysis that also accounts for both positive and negative impacts on ozone concentrations, the 8-hour RRF is computed for monitors in each of the three zones of interest in Southern California. Those regions (zones 3, 4, and 5) were defined earlier in **Figure 18**.

In **Figure 34 (A–C)**, the 8-hour average RRF is computed in a standard manner, but is plotted as $(RRF-1)\%$ to make it easier to compare various scenarios. Shown is the primary day of the episode (August 5). The results suggest that the effectiveness of surface modification strategies is higher in Zone 3 where, for example, case 22 can produce a RRF of 91% (a reduction of up to 9%). The reductions in zones 4 and 5 are up to about 4% and 2%, respectively (for case 22). It is also evident that the larger increases in surface properties, e.g., going from cases 10 or 02 to case 22, can more than double the beneficial impacts, that is, decreasing ozone concentrations. Recall that Zone 3 is where some of the peaks on August 6 occur and Zone 4 is where the peak on August 5 occurs.

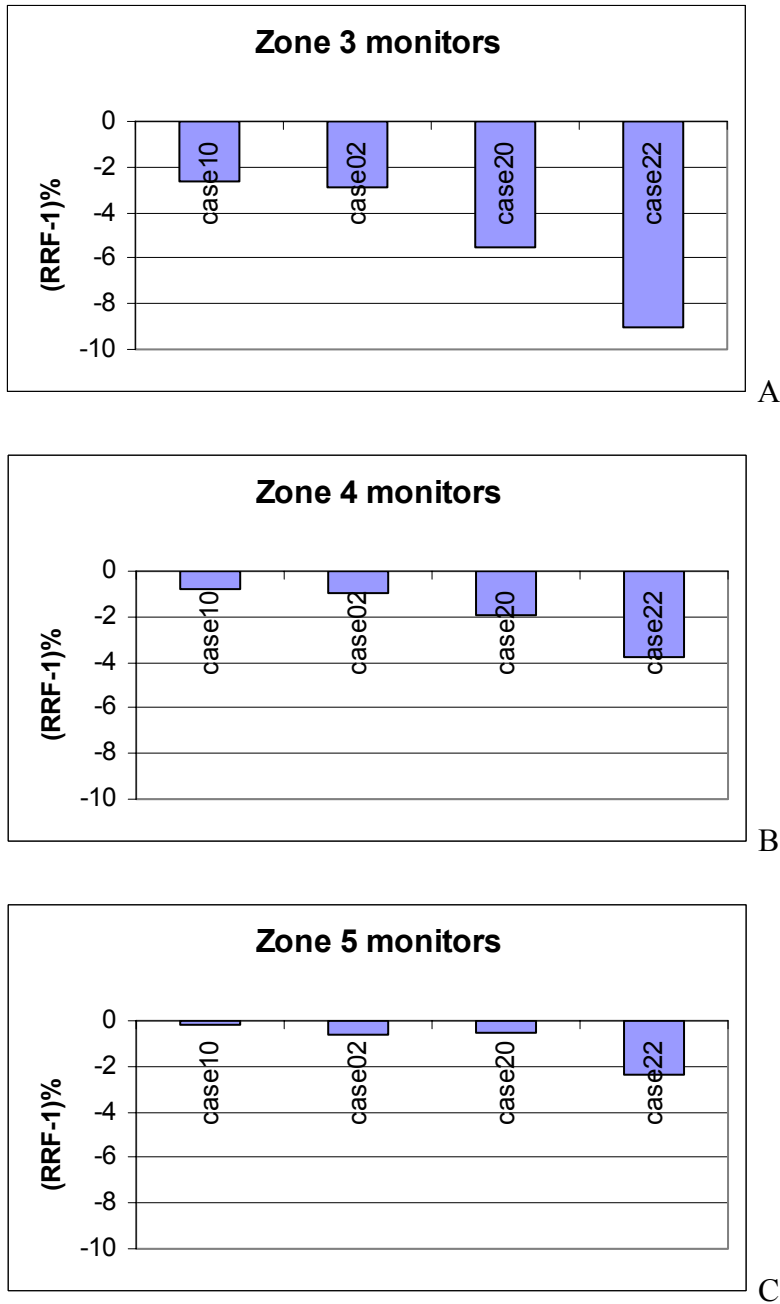


Figure 34. RRF (plotted as RRF-1) for four scenarios (cases 10, 02, 20, and 22) for Southern California (zones 3,4, and 5) on August 5

In terms of the 1-hour average peak concentrations, the effects of those strategies are relatively smaller, as seen in **Table 36**, and relatively more uniform across all scenarios (i.e., between a 2 and 3 ppb decrease in the peak. In this table, changes in 1-hour peak ozone are averaged over two days (August 5 and 6) to obtain more representative values (in some cases, the peak is unchanged and can even increase on August 5, but always decreases on August 6). These average values will be used in Section 16 to estimate equivalent changes in emissions.

Table 36. Changes in domain-wide unpaired peak (averaged over two days; August 5 and 6) for the Southern California Domain

Scenario →	01	02	10	20	22
Δ ppb →	-2	-2	-2.5	-3	-0.5

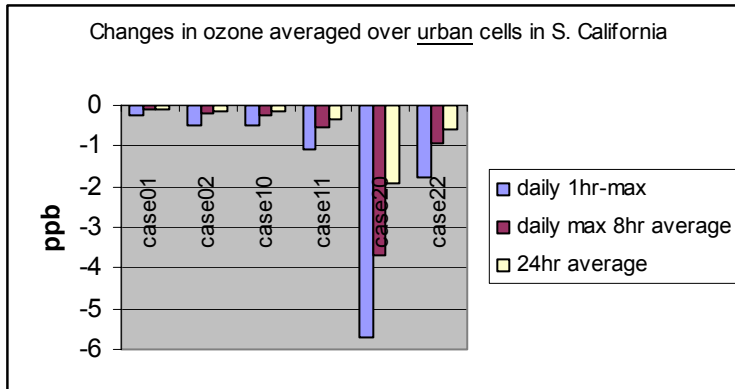
Of interest in Table 36 is that case 22 produces a relatively smaller impact on the 1-hour peak than do the other cases, despite their smaller surface modifications. Although it is not possible to pinpoint a single cause for this behavior, a potentially important factor is the change in the mixing height and wind speed as the level of surface modifications increases. The further decrease in the mixing height and reduction in wind speed (see again Figure 31 B, D, F, H), combined with an increase in surface modification can offset some of the decrease in ozone concentrations. This behavior will be seen again in the figures below as well. Here, two points need to be clarified:

- First, most monitors (e.g., in zones 3, 4, and 5) discussed above are in or near urbanized areas—that is, in locations where surface modifications are assumed to occur. Thus, as the level of surface modification increases, one expects to see larger impacts on ozone concentrations near those monitors. This is the case in Figure 34, where scenario 22 has larger impacts than case 20, since the changes in air quality accounted for in the RRF calculations are those occurring at the monitor locations (urbanized areas). However, when the peak concentrations (e.g., in Table 36) or other metrics such as the 1-hour and 8-hour averages (discussed below) are considered, other factors affect the way the effectiveness of control scenarios is evaluated. For example, the peaks (and their changes) do not typically occur near or within urbanized areas where surface modifications are the largest. Most peaks occur some distance downwind, so in most cases their changes do not correlate directly to the level of surface modifications. Thus case 22 can appear to be less effective than case 20 (in terms of peak reduction) because of this factor. In addition, when the 1-hour or 8-hour averages are calculated, a larger area (which includes both urbanized and non-urbanized regions) is used in computing these averages. As a result, some of the areas within this averaging domain can have increases, as well as decreases, in concentrations.
- As discussed above, case 22 can produce smaller ozone reductions than case 20 in some situations, despite the fact that the meteorological changes for case 22 are larger than those for case 20 (e.g., more cooling). There are a number of reasons for this, most notably: (1) the effects of further decreasing the mixing height and slowing the winds (as discussed above), and (2) the impacts on biogenic emission rates as temperature drops further. This is complicated by the nonlinear chemistry and space-varying NO_x/VOC concentrations, as well as by the fact that at relatively higher temperatures (e.g., 37°C–45°C (99°F–113°F), as simulated for this episode in some Southern California areas) decreasing temperatures can cause bidirectional impacts on biogenic emission rates.

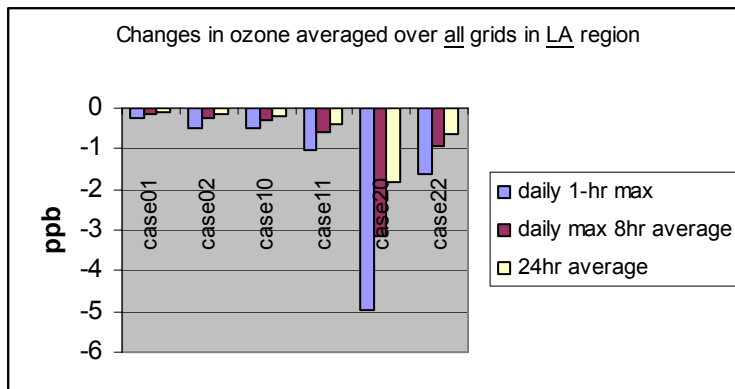
In **Figure 35**, a relatively more compact presentation of overall impacts on ozone is given. In Figure 35 A, only urbanized grid cells are considered (e.g., those 1291 cells defined earlier in Figure 26 for the Southern California domain). In Figure 35 B all grid cells in the South Coast Air Basin (whether urbanized or not urbanized) are considered. In Figure 35 C, all grid cells in the San Diego region are considered. For each of these three regions, three indices are given:

- Changes in average daily 1-hr max (ppb). This is the difference between the daily 1-hr maximum for a given case and the base case at each grid cell, which is then averaged over all the grid cells in regions of interest. Those grid cells are defined in the paragraph above.
- Changes in average daily 8-hr max (ppb). This is the difference between the daily maximum 8-hr average for a given case and the base case at each grid cell, which is then averaged over all the grid cells in each of the above-defined regions.
- Changes in averaged 24-hr changes (ppb). This is the difference between the 24-hr average for a given case and the base case, at each grid cell in the regions defined above, which is then averaged over all the grid cells in the region.

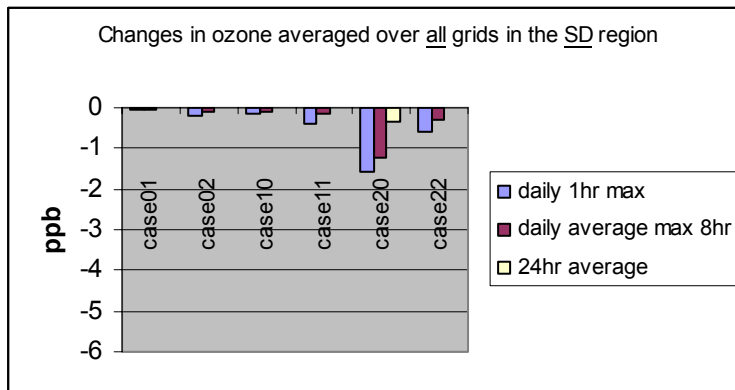
The results suggest that the most effective scenario under the episodic conditions and assumed surface modifications is case 20, followed by case 22, 11, 10, 02, and 01 in all three regions. Of course the magnitude of the changes is larger in the South Coast Air Basin than in San Diego because the latter has relatively smaller surface modifications than those in Los Angeles. Also noticeable is that all indices are affected more or less equally and that the sequence across the scenarios is relatively similar.



A



B



C

Figure 35. Changes in selected indices for the Southern California domain. A: All urban grid cells, B: All cells in the South Coast Air basin, C: All cells in the San Diego area.

15.2 Central California

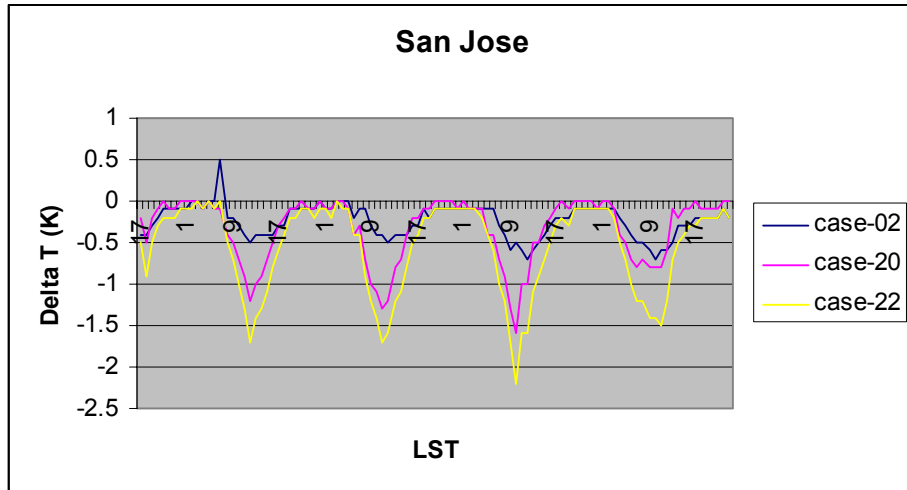
Following the same pattern of discussion of the Southern California results in Section 15.1, this section presents results obtained for Central California, and summarizes scenarios 02, 20, and 22 (as differences from the base case). The time series presented in **Figure 36 (A–H)** are for regions in: (1) San Jose, (2) Sacramento, (3) Fresno, and (4) Bakersfield. Of course other areas could also be selected for presentation, but here the purpose is to discuss a few regions while keeping

the presentation relatively compact. These are also regions with some of the larger meteorological (e.g., temperature) changes.

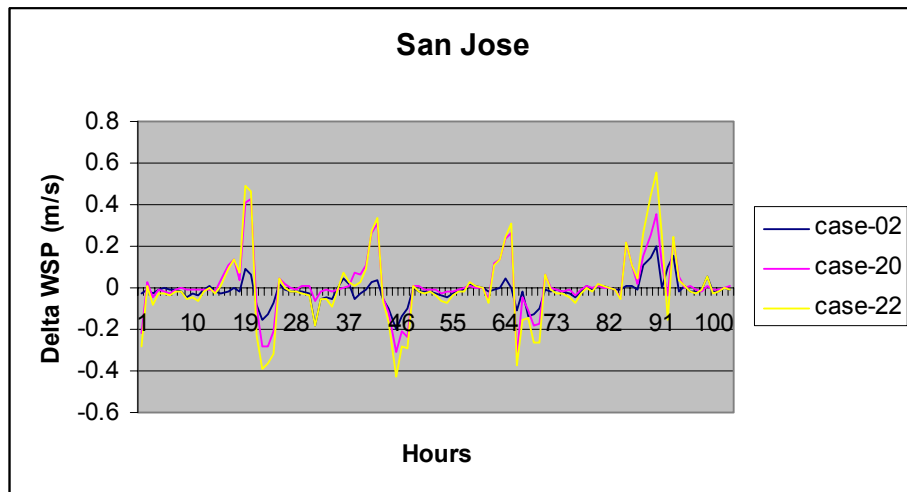
Figure 36 (A–H) summarizes changes in 2-m air temperature and 10-m wind speed for these four regions and the three scenarios identified above. The time-series are for four days (September 29, 30, 31, and August 1st, 2000). The last few hours of September 28 can also be seen at the left end of each figure. As with the Southern California results, a typical temperature change pattern in Central California (due to “implementation” of surface modification strategies) is seen as a decrease during the daytime hours and smaller (or near-zero) decreases during the night. Also as discussed earlier, the amount of temperature decrease gets larger as the level of surface modification increases. Overall, the effectiveness of these strategies at reducing air temperature is in the following order of scenarios: 02, 20, and 22.

In San Jose (Figure 36 A), the largest decreases in air temperature (e.g., those corresponding to case 22) are on the order of 1.5°C–2°C (2.7°F–3.6°F) and about 1°C–1.5°C (1.8°F–2.7°F) in case 20. The largest decreases in air temperature occur on July 31. In Sacramento (Figure 36 C), the same change pattern is evident but with slightly smaller magnitudes, e.g., about 1°C–1.5°C (1.8°F–2.7°F) in case 20. The effects of scenario 02 in both regions seem to be smaller; up to about 0.5°C in cooling. In Fresno (Figure 36 E), the effects are similar in magnitude to those in San Jose and across all three scenarios. Finally, in Bakersfield (Figure 36 G), the changes are smaller than in the other three regions. Here the largest decreases are in the order of 0.5°C–0.7°C (0.9°F–1.3°F) for cases 20 and 22. As pointed out earlier, this is a result of smaller surface modifications in this region. In all cases, the decrease in air temperature starts at about 0900 LST and tapers off around 1900 LST, but at different magnitudes.

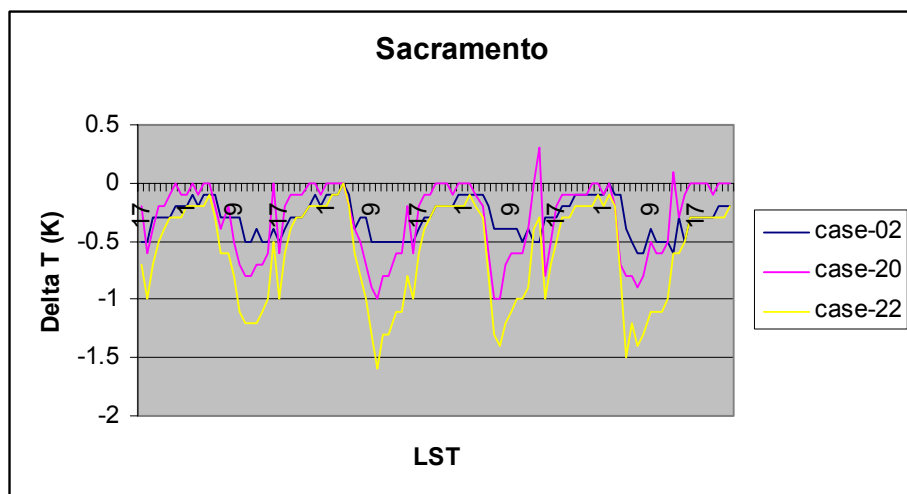
Wind speed changes are shown in **Figures 36 B, D, F, and H**, where a diurnal pattern is generally evident in all four regions. The changes in wind speed (whether reduction or increase) are generally proportional to the level of surface modification, i.e., in the sequence of cases 02 → 20 → 22. Most of the changes are in the range of about $\pm 0.4 \text{ m s}^{-1}$, except in Sacramento, where the decrease in wind speed can reach up to 1 m s^{-1} at certain times. Also, the reduction and increase in wind speeds are relatively equal, except in Sacramento, where the reduction in wind speed dominates (there is very little increase in wind speed).



A

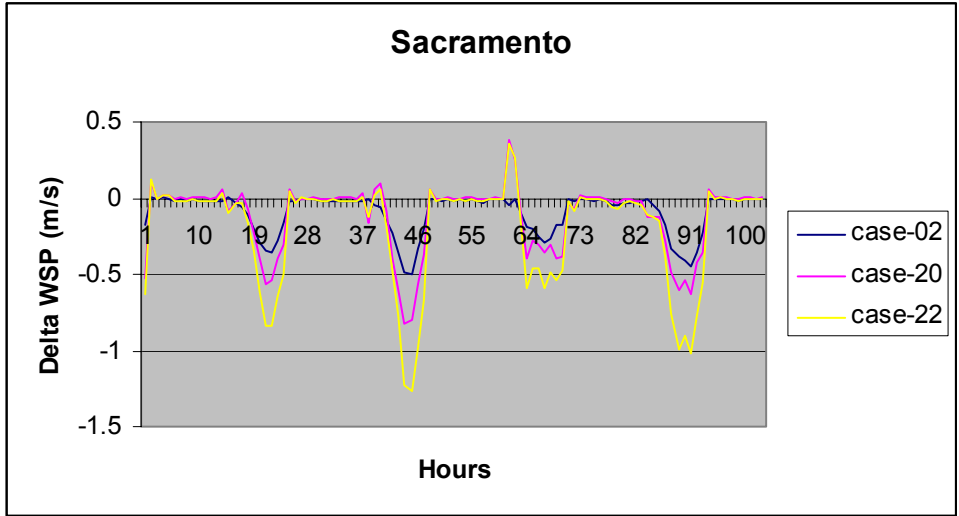


B

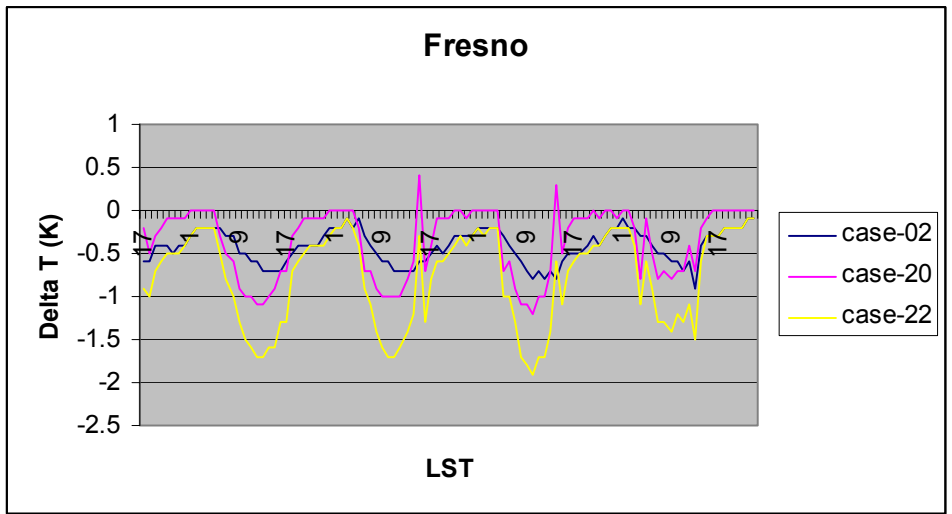


C

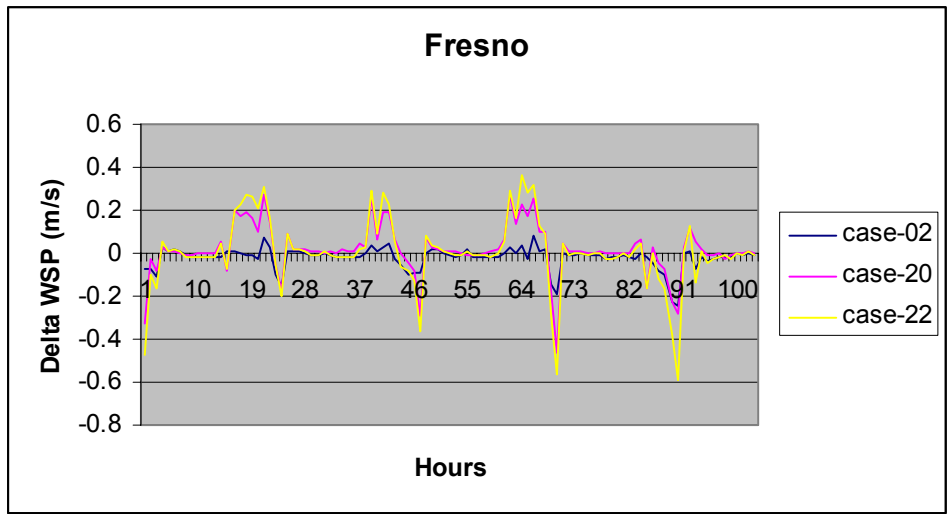
Figure 36. (A–H). Changes in 2 m air temperature and 10 m wind speed in four Central California regions and for three surface-modification scenarios. Data are from a representative grid cell in each defined region.



D



E



F

Figure 36. (continued).

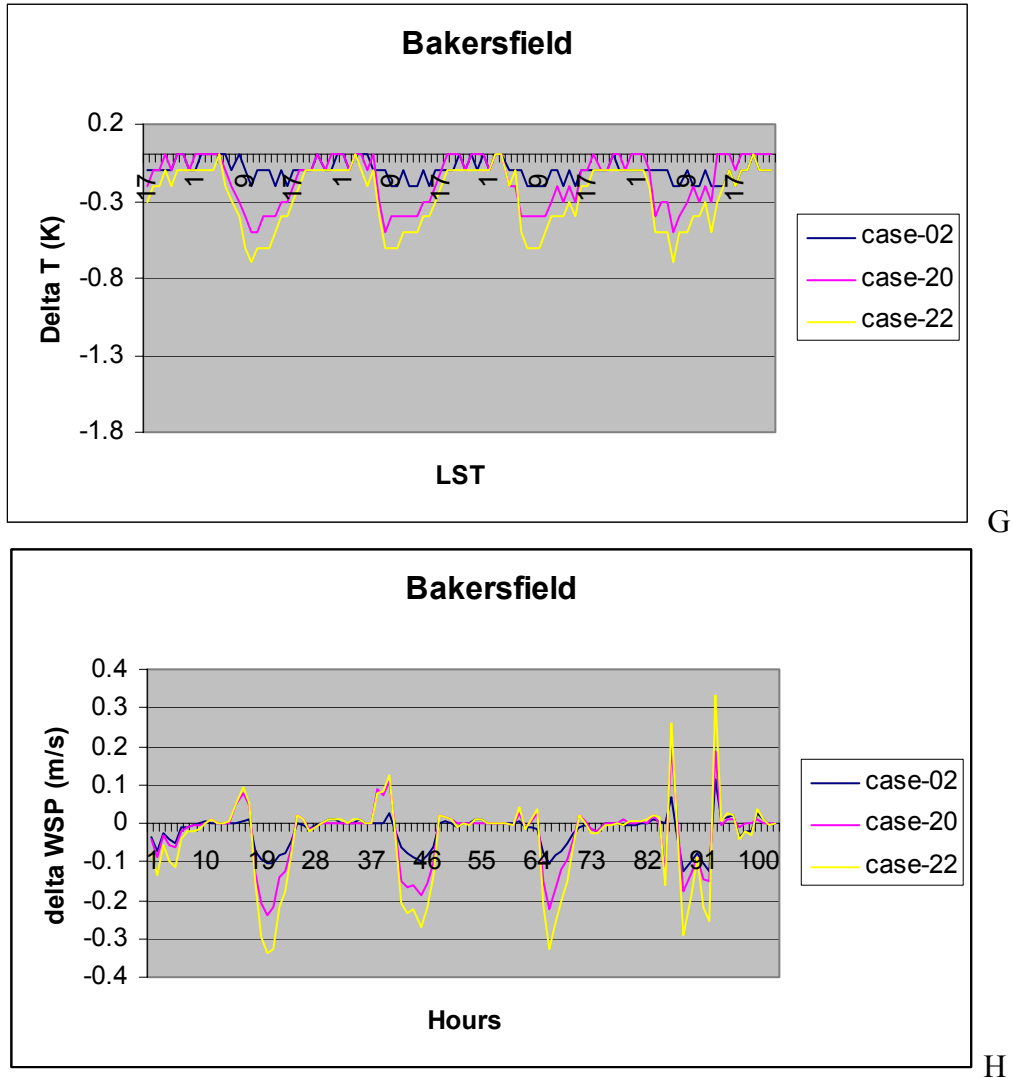
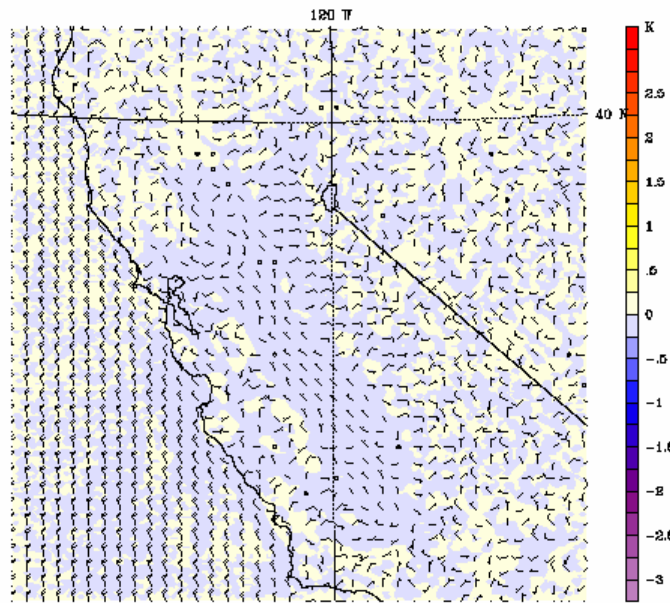


Figure 36. (continued).

Next, one scenario (case 20) is selected for two-dimensional graphical analysis in **Figure 37**. The figure shows the change in air temperature (case 20 minus case 00) superimposed on the base-case wind vector field of case 00. A number of hours (at two-hour intervals) are shown for July 31 from 0600 to 1600. As with the results for Southern California, the temperature difference evolution throughout the day, shown here for case 20, is typical across all other days and scenarios (not shown), but at different magnitudes. At night and through dawn, there is no difference in air temperature in all cases (as seen, for example, in Figure 37 A). The spatial distribution of temperature change matches very closely the distribution and level of surface modifications in the modifiable areas, e.g., compare **Figure 37d** (changes in air temperature) with **Figure 27** (potential for surface modifications in the Central California domain). As the area and potential for modification increase, so does the decrease in air temperature.

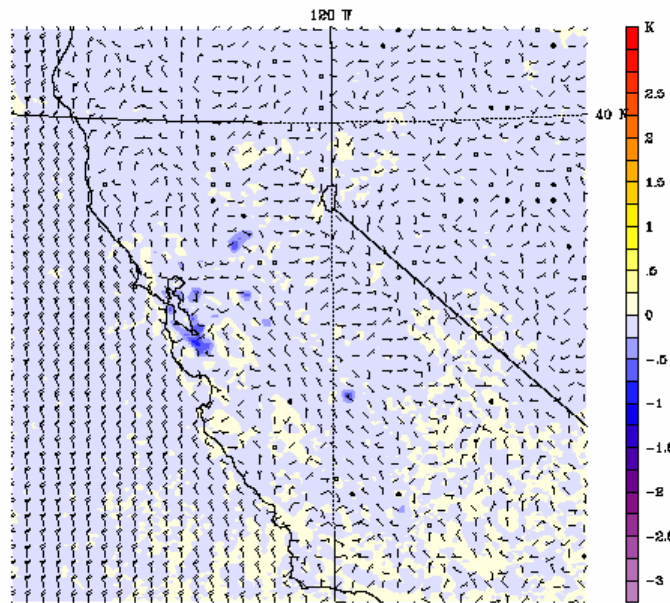
Dataset: case20 RIP: ripexecute.diff Init: 0100 UTC Mon 31 Jul 00
 Fcst: 12.00 Valid: 1300 UTC Mon 31 Jul 00 (0600 PDT Mon 31 Jul 00)
 Temperature at sigma = 0.999
 (diff. from case=case00, time= 12.00)
 Horizontal wind vectors at sigma = 0.999



Model Info: V3.6.1 No Cumulus KRF PBL Simple Ics 4 km, 28 levels, 6 sec

A

Dataset: case20 RIP: ripexecute.diff Init: 0100 UTC Mon 31 Jul 00
 Fcst: 14.00 Valid: 1500 UTC Mon 31 Jul 00 (0800 PDT Mon 31 Jul 00)
 Temperature at sigma = 0.999
 (diff. from case=case00, time= 14.00)
 Horizontal wind vectors at sigma = 0.999

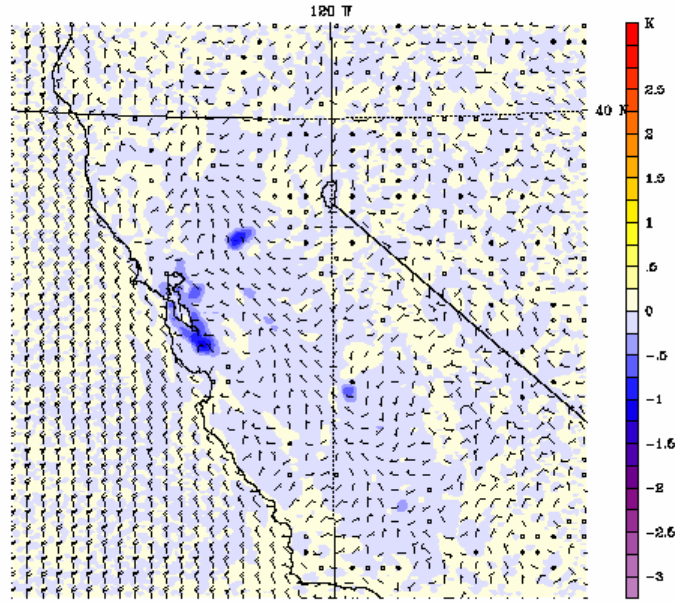


Model Info: V3.6.1 No Cumulus KRF PBL Simple Ics 4 km, 28 levels, 6 sec

B

Figure 37. (A–F). Air temperature difference (from base case) for case 20 in the CCOS modeling domain, overlaid on base case wind vector field.

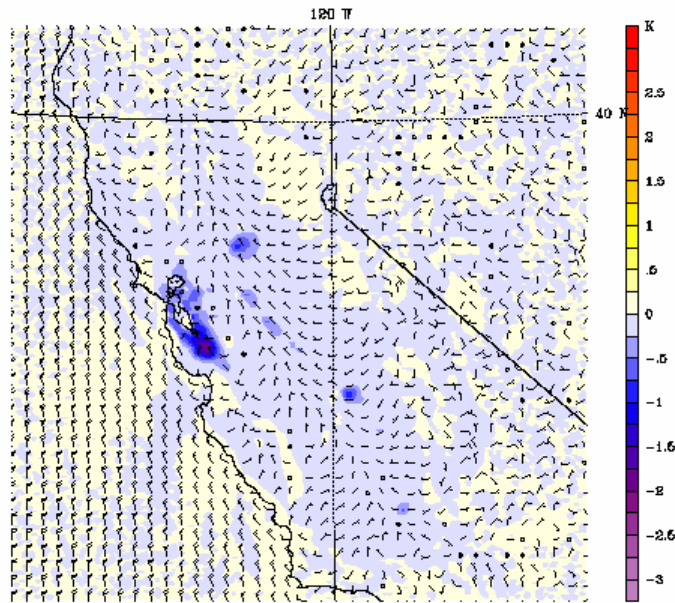
Dataset: case20 RIP: riperecute.diff Init: 0100 UTC Mon 31 Jul 00
 Fcst: 16.00 Valid: 1700 UTC Mon 31 Jul 00 (1000 PDT Mon 31 Jul 00)
 Temperature at sigma = 0.999
 (diff. from case=case00, time= 16.00)
 Horizontal wind vectors at sigma = 0.999



Model Info: V3.6.1 No Cumulus MRF PBL Simple Ice 4 km, 28 levels, 6 sec

C

Dataset: case20 RIP: riperecute.diff Init: 0100 UTC Mon 31 Jul 00
 Fcst: 16.00 Valid: 1900 UTC Mon 31 Jul 00 (1200 PDT Mon 31 Jul 00)
 Temperature at sigma = 0.999
 (diff. from case=case00, time= 16.00)
 Horizontal wind vectors at sigma = 0.999

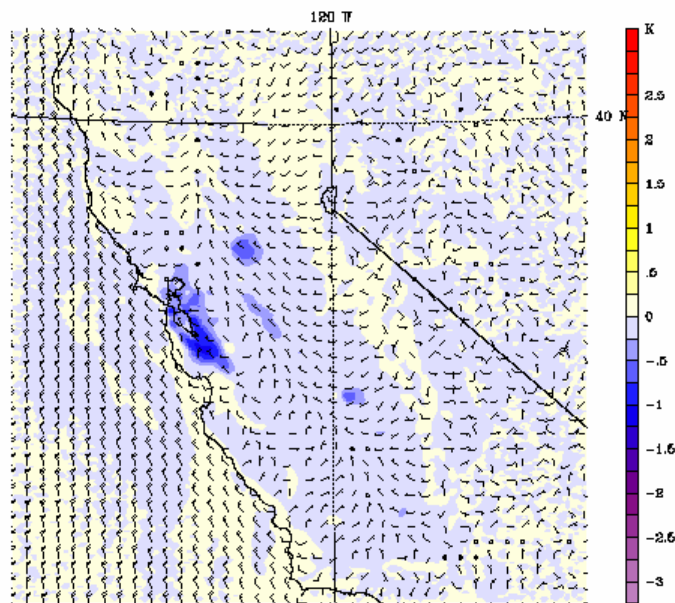


Model Info: V3.6.1 No Cumulus MRF PBL Simple Ice 4 km, 28 levels, 6 sec

D

Figure 37. (continued).

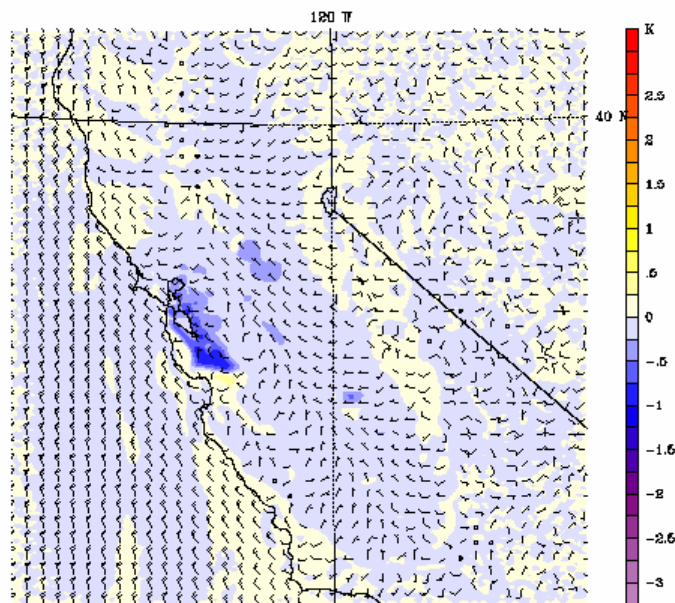
Dataset: case20 RIP: ripexecute.diff Init: 0100 UTC Mon 31 Jul 00
 Fcst: 20.00 Valid: 2100 UTC Mon 31 Jul 00 (1400 PDT Mon 31 Jul 00)
 Temperature at sigma = 0.999
 (diff. from case=case00, time= 20.00)
 Horizontal wind vectors at sigma = 0.999



Model Info: V3.6.1 No Cumulus KRF PBL Simple Ics 4 km, 28 levels, 6 sec

E

Dataset: case20 RIP: ripexecute.diff Init: 0100 UTC Mon 31 Jul 00
 Fcst: 22.00 Valid: 2300 UTC Mon 31 Jul 00 (1600 PDT Mon 31 Jul 00)
 Temperature at sigma = 0.999
 (diff. from case=case00, time= 22.00)
 Horizontal wind vectors at sigma = 0.999



Model Info: V3.6.1 No Cumulus KRF PBL Simple Ics 4 km, 28 levels, 6 sec

F

Figure 37. (continued).

The ozone air-quality implications of these meteorological changes are discussed next. A qualitative assessment is given first, followed by a more quantitative evaluation (e.g., specific metrics). **Figure 38 (A–F)** shows the ozone-concentration differences for case 20 (minus base case) at the same hours shown above for temperature differences. As seen in Figure 38 A, there are no differences in concentrations during early morning hours (e.g., 0600), except for some minor impact from earlier hours (e.g., ± 2 ppb in some areas). But in general there is no systematic change in concentrations at that hour. At 0800 (Figure 38 B), small differences begin to appear. In Sacramento there is a decrease of up to 4 ppb, and in the SFBA there is a decrease of up to 4 ppb, but they are still relatively small overall, especially in the remainder of the domain. By 1000, the reduction in ozone concentrations (signal) becomes clearer and covers a larger area in these regions where surface modifications occur. Decreases of up to 6–7 ppb are seen in the SFBA, Sacramento, and Fresno and decreases of up to 6 ppb in Bakersfield are also evident. Concentration decreases of some 3–5 ppb along the Highway 99 corridor (Lodi, Stockton, Manteca, Modesto, Turlock, and Merced) are also seen. There is also a very small area of increase in concentrations over the San Francisco Bay (three grid cells southeast of San Francisco), seen as a small area in red. From its location and extent, it likely is model noise, rather than a true signal.

At 1200, the signal is stronger, with decreases of up to 16 ppb in the SFBA and up to about 10 ppb in the Sacramento region. The decreases in Fresno and Bakersfield are up to 10 and 5 ppb respectively. In the Highway 99 corridor, decreases range from up to 4 to 7 ppb. It should be noted that there are no increases in concentrations (1 ppb in a few cells). The same spatial pattern exists at 1400, but now with relatively larger decreases. In the SFBA the decreases reach up to 23 ppb in a small area, but overall the region experiences decreases of 14–20 ppb at this hour. In Sacramento the decreases are up to 7 ppb. In Fresno, decreases of up to 6 ppb are seen, and in Bakersfield up to 3 ppb. For the last hour shown in this figure (1600), decreases of up to 24 ppb are seen in the SFBA (there is also a small area of increases of up to 3 ppb in the Morgan Hills area). In Sacramento, the decrease reaches up to 6 ppb, in Fresno up to 5 ppb, and in Bakersfield up to 3 ppb. In the Highway 99 corridor, the decreases reach up to 6 ppb. The time interval 1400 through 1600 is the period of ozone peaks in many regions throughout the domain and the above reductions in concentrations are significant during this period.

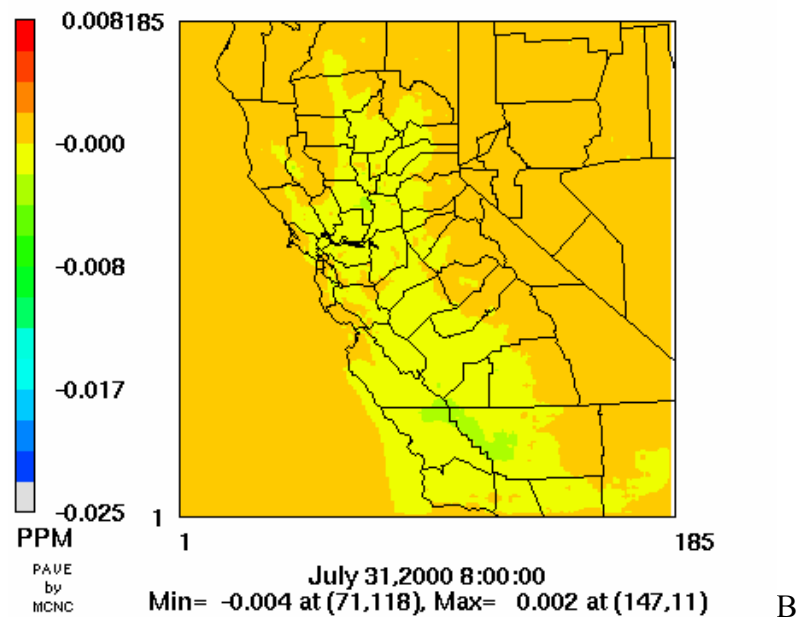
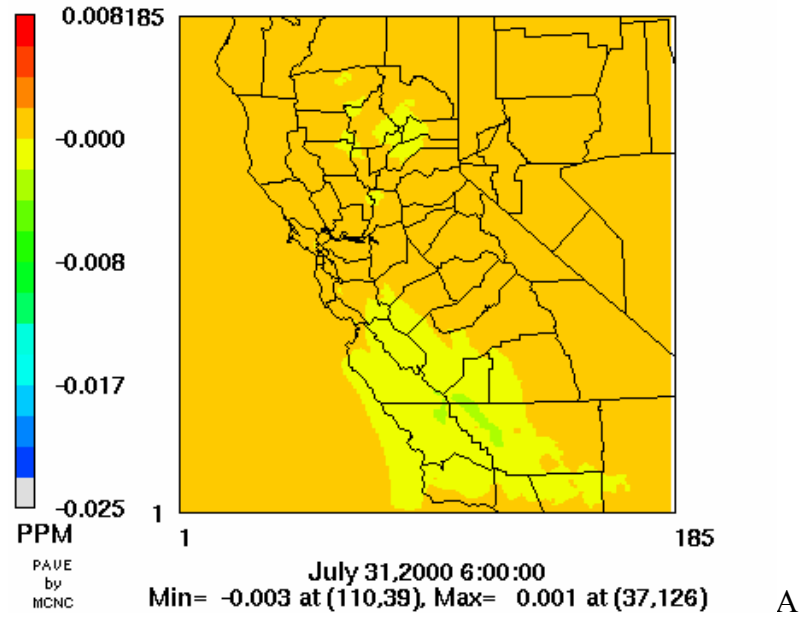
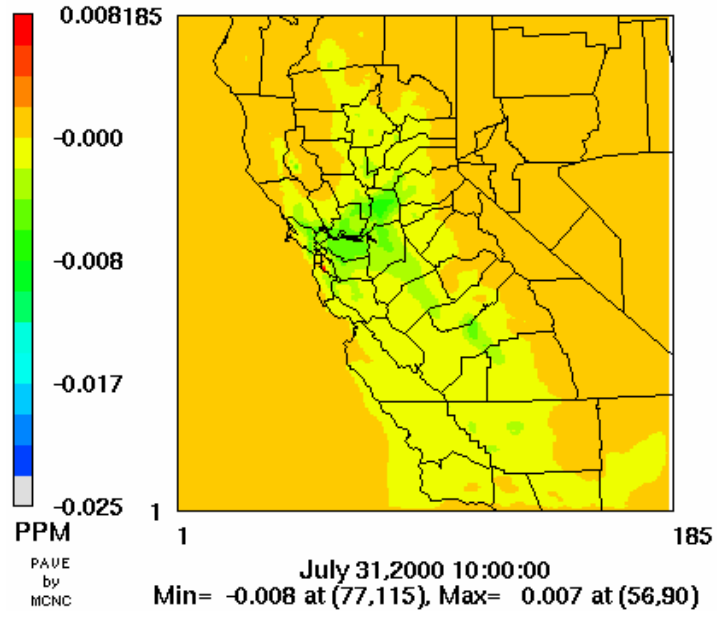
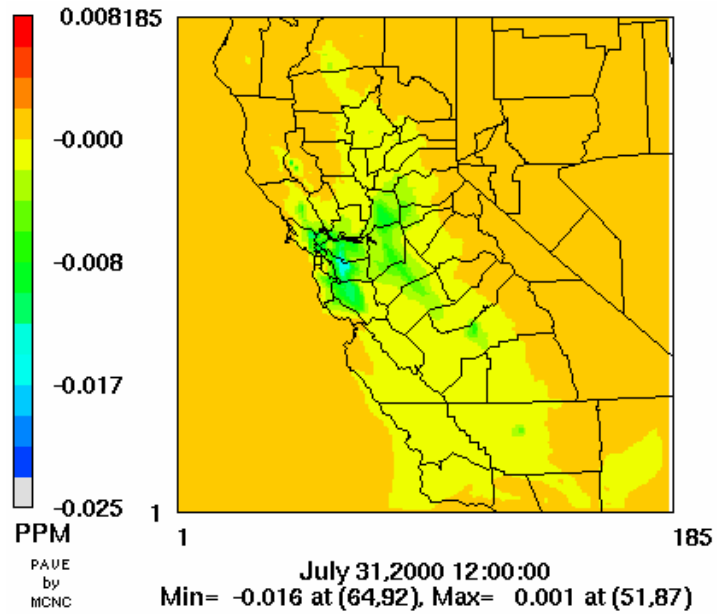


Figure 38. (A–F). Differences in ozone concentrations (case 20 minus base case) for July 31 and the hours corresponding to those in Figure 37.



C



D

Figure 38. (continued).

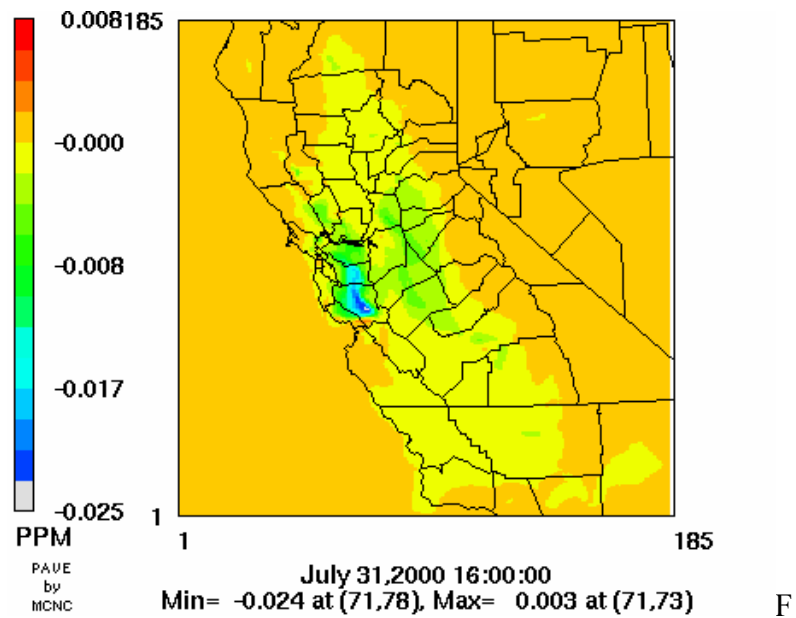
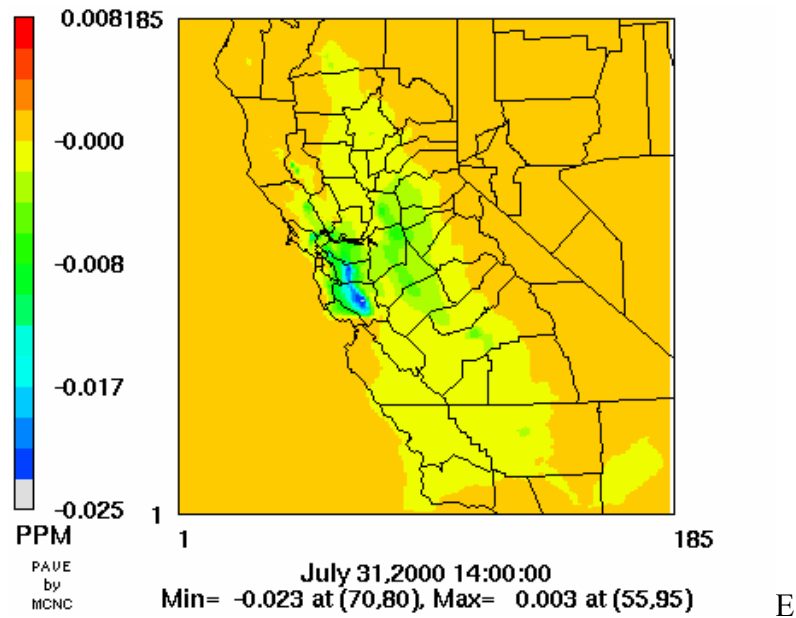


Figure 38. (continued)

In **Figure 39**, the largest 1-hour changes throughout the CCOS domain are shown for four scenarios and three days each (primary days of episode). This figure is similar in nature to Figure 33 for Southern California; it shows the largest *decrease* in concentration at each grid cell in the domain (i.e., the maximum decrease in 1-hour average). Again the purpose is simply to show where such reductions occur without any specific indication as to timing or how that reduction relates to the local peak. The results suggest that the magnitude of changes increases as the level of surface modifications becomes larger. It can be noted however, that many of the larger changes occur in areas close to the local peaks. The spatial distribution of the decreases is roughly similar in all scenarios, but the magnitude of the change differs from one to another. For example, the largest decreases on July 30 are 12, 12, 14, and 16 ppb for cases 02, 10, 20, and 22,

respectively. For these four cases (in the same order), the largest decreases on July 31 are 23, 24, 25, and 25 ppb respectively. Finally for August 1, the largest decreases are 26, 26, 28, and 30 ppb for these cases (in the same order).

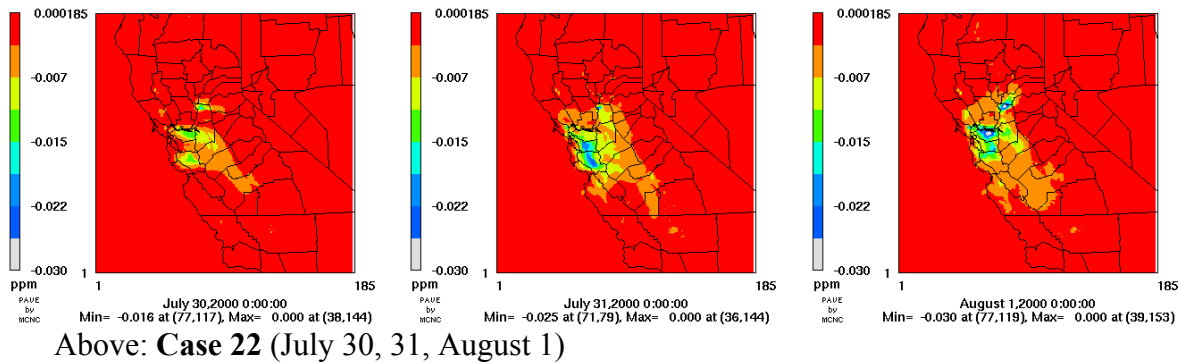
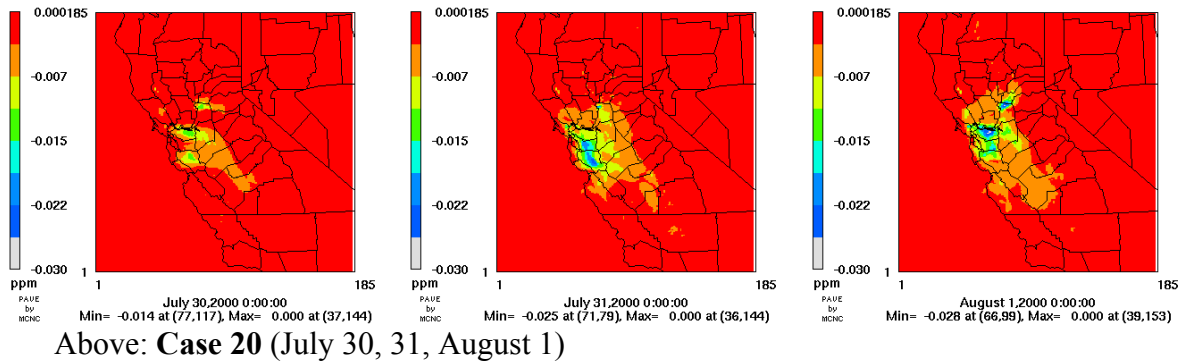
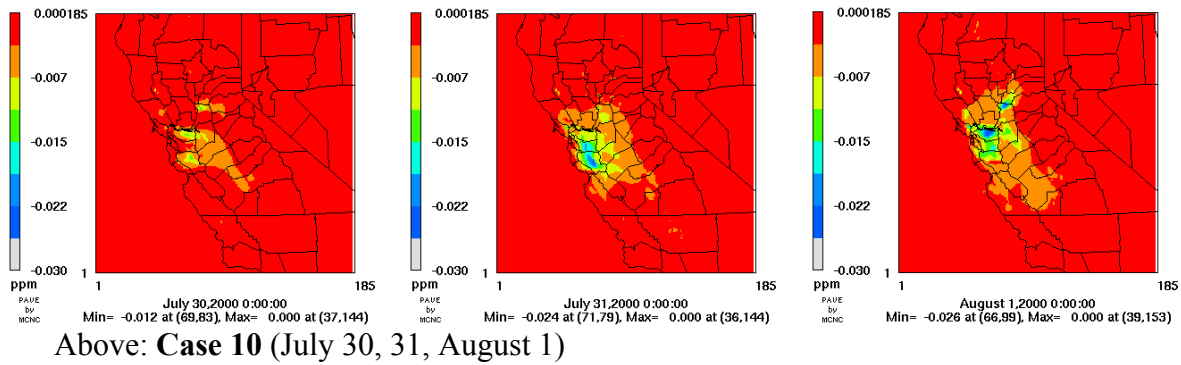
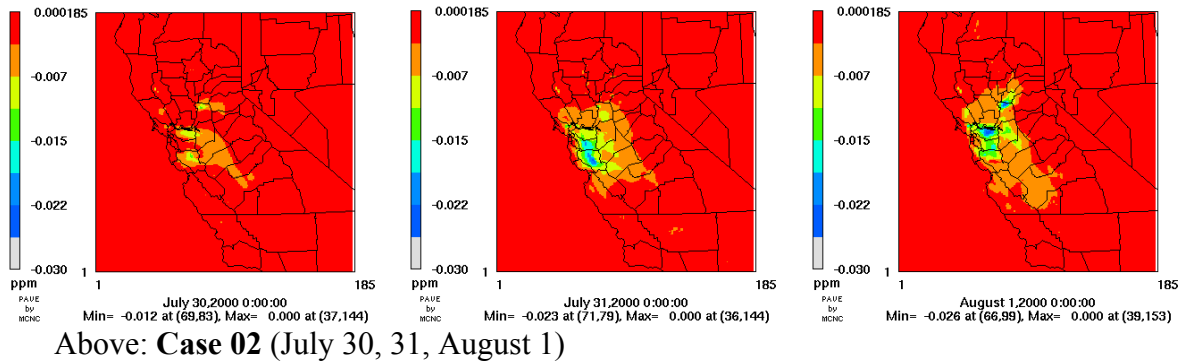


Figure 39. Maximum hourly decrease in ozone concentration at each grid cell for several scenarios

Finally, the changes in 1-hour peak concentrations are examined for the CCOS domain and for the above scenarios. In Figure 40, four regions are considered for this exercise: Sacramento Valley, San Francisco Bay Area, North San Joaquin Valley (Fresno), and South San Joaquin Valley (Bakersfield). For each region, the reduction in the peak 1-hour average concentration is shown for three days (August 30 and 31 and August 1). The top figure is for case 10 whereas the bottom is for case 20. The results suggest that, of the four regions selected for this analysis, Sacramento and the San Francisco Bay area would experience the largest reductions in the peaks under the episodic conditions simulated here.

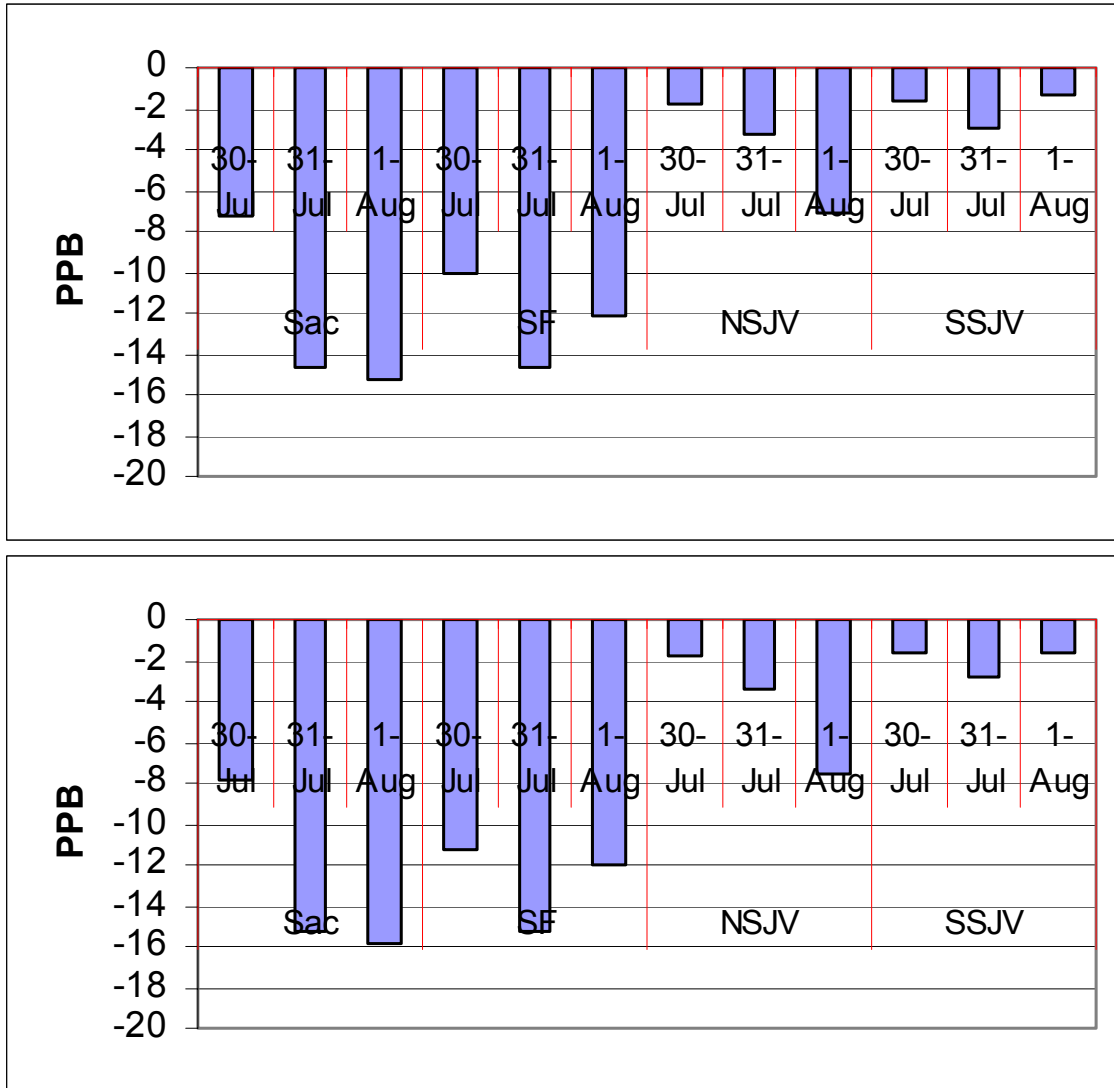


Figure 40. Changes in the 1-hour peak for case 10 (top) and case 20 (bottom) for four CCOS regions and three days. Sac=Sacramento; SF=San Francisco Bay Area; NSJV= North San Joaquin Valley; and SSJV=South San Joaquin Valley.

The simulations suggest that peak concentrations can be decreased by a range from 6 to 16 ppb in Sacramento, 10 to 16 ppb in the SFBA, 2 to 8 ppb in Fresno, and 1 to 3 ppb in Bakersfield (across both cases 10 and 20). In the Sacramento and SFBA regions, the largest decreases occur during those days with relatively higher local peaks (i.e., July 31 in SFBA and August 1 in Sacramento). The figure also shows that relative to case 10, case 20 does not decrease the peaks by an amount proportional to surface modification differences, as discussed earlier in this report.

Impacts on the peak ozone concentrations appear to be relatively larger in the Central California simulations than in the Southern California simulations for the respective episodes and domains. Possible reasons include:

- *Temperature range and impact on biogenic emissions:* in the Los Angeles area, absolute temperature as simulated here are as high as 45°C (113°F), whereas in the urban regions of the CCOS, they are up to about 38°C (100°F). As discussed in Section 14, temperature reductions around 41°C–45°C (106°F–113°F) can have little or no effect on (and sometimes can increase) biogenic emission rates, whereas a decrease in temperature at about 38°C (100°F) can significantly reduce emissions of biogenic hydrocarbons.
- *Geographical location of biogenic emission sources:* Large biogenic emission sources are located differently with respect to urbanized areas in the CCOS and SCOS regions. In the CCOS domain, sources of biogenic emissions are close to and often upwind of urban areas, whereas in the SCOS domain, the largest such sources are the forested areas on the mountain ranges and are often downwind of urban areas. That is not to say there are no biogenic emissions in and around urban areas in the SCOS domain, only that there are relatively less than those around urban areas in the CCOS domain.

Another summary of changes in the regional peaks (in the CCOS domain) is shown in **Table 37**. Here, the changes in region-averaged daily 1-hour maximum ozone concentration are given for July 31 (changes in 1-hour maximum ozone at each grid cell then averaged over region) for case 20 as an example. The base concentrations (ppb) in **Table 37** are also region-averaged 1-hour ozone maxima. As seen elsewhere in this report, the results in this table also suggest that the larger the area (the more surface modification is possible), the larger the impacts on ozone concentrations (e.g., decreases in the peaks and averages). Thus the largest effects are seen in the SFBA and the smallest in south San Joaquin Valley.

Table 37. Changes in region-averaged peaks (CCOS)

	Region-averaged base-case peak (ppb)	Region-averaged peak changes for case 20
Sacramento	80.67	-3.47
SF Bay Area	76.79	-5.79
NSJV	81.4	-2.2
SSJV	75.9	-0.8

16. Energy and Emission Equivalents

Energy and emission equivalents of the meteorological and ozone changes (respectively) are other interesting aspects related to the impacts of surface modification strategies. For example, (1) changes in temperature can be indirectly translated into equivalent reductions in peak demand for cooling electricity; whereas (2) changes in ozone concentrations can be indirectly translated into precursor-emission changes, such as NO_x and/or VOC equivalent emissions. This section explores some of these potential impacts and ideas. However, this is a relatively qualitative exercise, which will need to be further quantified in detail in future studies.

Ideally, this analysis would be performed for all affected regions and utility service territories in the state. Data was solicited for this purpose, but as of this writing, only partial information was made available to this study. As a result, only a limited and qualitative analysis was done for one region in the Southern California domain, as shown below. In the future, when similar information becomes available for other regions in California, it will be included in follow-up analysis. The preliminary analysis below focuses on the South Coast Air Basin (for emission equivalence) and on the City of Los Angeles (for energy/peak demand analysis). Specifically, the energy component focuses on the boundaries of the Los Angeles Department of Water and Power's service territory.

16.1 Energy Equivalents: Los Angeles Example

Daily peak demand data for five years (1999 through 2004) were obtained from the Los Angeles Department of Water and Power (LADWP). In addition, corresponding daily air temperature data were obtained from LADWP for four locations in the Basin: (1) LAX (airport), (2) Burbank, (3) Civic Center, and (4) Woodland Hills. Because the Los Angeles Civic Center is located closest to the central region of the LADWP service territory, temperature data from this location were used to develop a correlation with peak demand.

The maximum daily temperature readings for the last five years from Civic Center were first examined for a general trend and correlation with daily peak demand. The entire dataset is plotted in the top part of **Figure 41** (peak demand vs. maximum daily temperature at Civic Center) where it can be seen that below about 70°F (21°C) shown with a yellow vertical line (~ 21°C, or ~70°F) the peak demand is relatively independent of temperature, e.g., closely related to the base load. Above 21°C (70°F), the trend suggests some temperature dependence (and weather dependence in general). Thus in the bottom part of **Figure 41**, only those points with temperatures higher than 20°C (68°F) are plotted. A simple linear regression is then fitted. The regression has an R² value of 0.41 (relatively low) and a significance of ~ 0 (good). The linear fit suggests a slope of about 102 megawatts (MW)/C° for the range of temperature above 20°C (68°F).

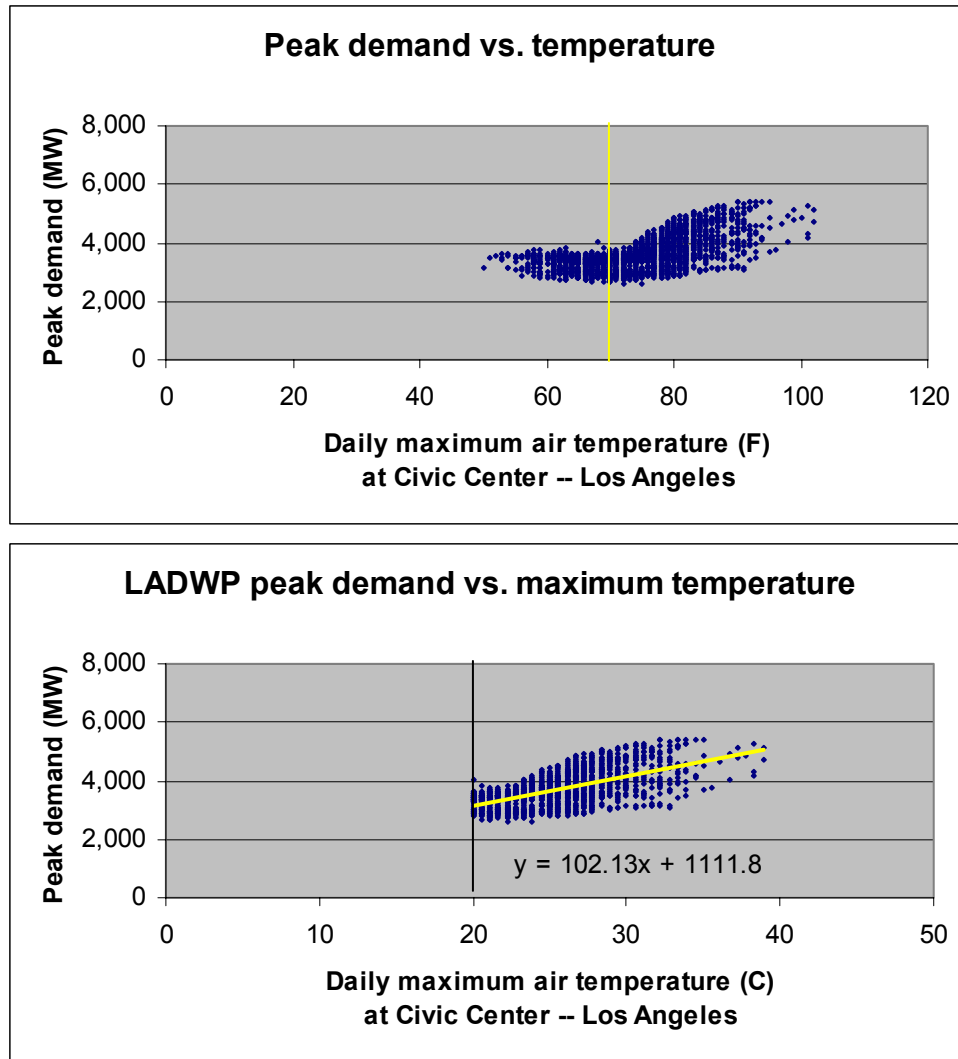


Figure 41. Daily peak load (LADWP) vs. daily maximum air temperature (1999–2004) in Los Angeles

To evaluate the potential reductions in peak demand, *representative* changes in simulated air temperature at the time of the maximum (time of peak temperature) in the LADWP service territory are used in the following calculations. Such temperature reductions (at time of maximum) were shown, for example, in **Figure 31A** (for Los Angeles). Using the regression coefficients from above, the following can be summarized for three scenarios, as in **Table 38**:

Table 38. Potential reduction in LADWP peak demand for three scenarios

	Representative decrease at time of maximum temperature (°C)	Equivalent reduction in peak demand (MW)
Case 02	1.0	100 (↓ 2.0%)
Case 20	1.8	184 (↓ 3.6%)
Case 22	3.0	300 (↓ 6.0%)

At the time of the maximum temperature, the simulated air temperature (discussed earlier) in the Civic Center area was in the neighborhood of 39°C (102°F), corresponding to a base-case peak demand of 5090 MW for LADWP. Thus, with respect to this baseline peak demand, the decreases in Table 38 correspond to 2%, 3.6%, and 6% of the peak demand, respectively, as shown in the right column of the table. A similar analysis can be done for other regions of interest to get an estimate of state-wide savings in peaks. When such information becomes available to this study, they will be incorporated in the future.

16.2 Emission Equivalents: South Coast Air Basin Example

As often done in regulatory modeling, converting certain aspects of changes in ozone concentrations into emission equivalents would rely on full sensitivity modeling and analysis of emission control scenarios and their impacts on ozone, e.g., peak concentrations or other indices. Another, simplified, approach that is also used to qualitatively estimate the emission equivalents of reductions in concentrations relies on Empirical Kinetic Modeling Approach (EKMA)-type modeling and analysis, where episode- and region-specific conditions and emission inventories are simulated for a number of control scenarios by incrementally cutting the emissions of NO_x and/or VOC and computing the resulting 1-hour ozone peaks (or other indices of interest, e.g., averages, 8-hour standard indices, etc). The results are often plotted as isopleths of peak concentrations (or other indices) to facilitate the graphical evaluation of effectiveness of various control strategies as function of emission reductions. Milford et al. (1989) performed such evaluations for South Coast Air Basin using the episode of August 30–31, 1982. Based on their results, Taha (2004) estimated that a change of 2 ppb in the basin peak is equivalent to changes of about 5% in emissions of NO_x and VOC (5% each). In addition, Taha (2003a) and Taha et al. (2000) used this method in estimating the efficiency of surface modification strategies in altering the atmospheric carrying capacity in several regions. For an episode in mid-July 1990 in Sacramento, Taha et al. (2000) estimate that a change of 2.5 ppb (around a peak of 139 ppb) is equivalent to a change of about 2.25 % in emissions of each of NO_x and VOC.

In this study, no new or additional photochemical sensitivity modeling was performed to assess the effectiveness of surface modification strategies in terms of their emission reduction equivalents. A simple and crude estimate is made here based on available information, e.g., based on sensitivity analysis performed by the SCAQMD (AQMP 2003, Chapter 5, Future Air Quality) for a number of emission scenarios. Here, a plot of peak ozone concentrations versus emission of NO_x and VOC is shown in **Figure 42** (based on AQMP data). The vertical axis shows domain peak ozone concentration (averaged over August 5 and 6) and the horizontal axes labeled VOC and NO_x show the equivalent reductions in emissions. Thus the point at 0,0 (meaning no reduction in emissions relative to the baseline scenario) produces a peak ozone concentration of 196 ppb (actually, this is an average between August 5 and 6). The figure also shows that, for example, to reduce peak ozone to 122 ppb (average of 5 and 6) at the bottom of the scale, reductions of 50% in NO_x and 60% in VOC emissions would be needed.

Using this crude correlation, shown in Figure 42, suggests that a reduction in peak 1-hour concentrations of 3 ppb (e.g., corresponding to case **20** in **Table 36**) around an absolute value of 160–170 ppb (as simulated in this study) the equivalent reductions in emissions would amount to about 4% in NO_x and VOC (4% each). This is generally similar in magnitude to the results of Taha (2004) above, based on Milford et al. (1989), as well as those of Taha et al. (2000). Of

course there are differences due to different episodic conditions, models, data, etc. Based on emission inventory information in **Table 3**, the total NO_x and VOC emissions for this episode are 1283 and 1262 TPD, respectively. Thus a reduction of up to 4% (from above) is roughly equivalent to reductions of 51 and 50 TDP in emissions of NO_x and VOC respectively. Of course the other scenarios will have smaller reductions than case **20**.

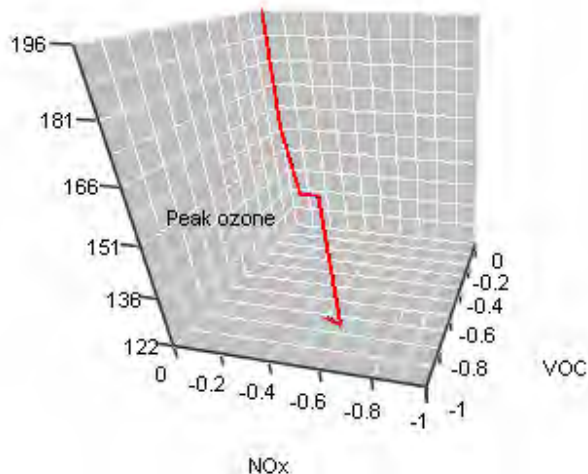


Figure 42. Domain-peak ozone concentration (averaged over August 5 and 6) plotted against NO_x and VOC emissions (%) for Southern California

Although the above exercise was not sufficiently robust or quantitative, its purpose was simply to demonstrate how a qualitative assessment of an “order of magnitude” of expected benefits can be derived for comparison purposes. In follow-up modeling studies, a detailed sensitivity analysis based on photochemical modeling will be done to develop more reliable estimates.

17. Conclusions

17.1 Recap

This numerical modeling study was undertaken to evaluate the potential meteorological and ozone air-quality impacts of surface modification strategies in California. The strategies of interest include urban albedo modifications, reforestation, and related morphological or physical changes in the urban environment. The impacts of surface modifications were simulated and quantified for a number of regions in the state, such as the Sacramento Valley, greater San Francisco Bay Area, North and South San Joaquin Valley (including the Highway 99 corridor, Fresno and Bakersfield), and Southern California (e.g., Los Angeles Basin, San Fernando Valley, Antelope Valley/Mojave, and San Diego). The overall goal of surface modification strategies is to cool urban areas, reduce the rate of precursor emissions, and lower the concentrations of ground-level ozone.

To be compatible with regulatory modeling work done in California, this study used two episodes (CCOS-2000 and SCOS-1997) to simulate relatively recent summer conditions and the potential impacts of the proposed strategies on ozone air quality. The study used two state-of-science models that have gained popularity in the regulatory and research environments, i.e., the PSU/NCAR MM5 meteorological model and the CAMx photochemical model. In addition, a suite of land-use and emission models, as well as study-specific pre- and post-processors were developed and used. The models were further modified as appropriate to accommodate the specific needs of this study and related sensitivity analysis.

Following an initial stage of modeling work and model performance evaluation, a base-case scenario was established for each of the domains in this study, i.e., Central and Southern California, and for each respective episode. Model performance was evaluated for both meteorological and photochemical simulations and deemed to be reasonable enough, within the time frame and scope of this study, to proceed in evaluating the potential impacts of surface modification strategies. Model performance was also compared with that demonstrated by the ARB, air districts, and their consultants in simulating these episodes for SIP modeling purposes.

Following the establishment of baseline model performance, a number of surface modification scenarios were constructed for albedo and vegetative cover changes in urban regions in California. These changes were used as a basis for establishing modified (perturbed) meteorological, emissions, and photochemical scenarios. The simulations of those scenarios indicate that increased albedo and vegetation cover in California's urban areas are effective in modifying air temperature near the surface and in the boundary layer and, as a result, modify emission rates of ozone precursors and related photochemical reaction rates. Because certain emission rates (e.g., for biogenic hydrocarbons) are meteorology-sensitive (temperature, solar radiation, moisture, CO₂)—as are the pathways for ozone production via thermal decomposition of PAN—the effects of surface modifications on temperature can have significant positive and negative impacts on the rates of production and accumulation of ozone in the polluted boundary layer. These strategies also impact other meteorological fields, such as mixing height and wind speed, thus further compounding their effects on air quality. In addition, the impacts vary significantly in space and time throughout the modeling domains and episodes.

In general, areas with the largest levels of surface modifications are also those that experience the largest benefits from decreases in air temperature and often the largest decreases in ozone concentrations as well. Changes in air temperature, and in ozone levels, typically follow the spatial distribution and area of changes in surface properties (modifiable areas). However, some impacts, both positive and negative, are also seen downwind of such modifications.

17.2 Results Summary

Results from coupled meteorological, emissions, and photochemical modeling in this study suggest that implementation of surface modification strategies in California would have a net beneficial effect in terms of ozone air quality. The main mechanism at work in these strategies is the reduction in air temperature, which results in a reduction in the rates of precursor emissions and the rates of photochemical production/accumulation of ground-level ozone. While all meteorological fields change as a result of surface modifications, the discussion in this report and Conclusion section focuses on changes in air temperature. Here, 2 m air temperature and 10 m winds are discussed for a number of scenarios. In the discussion below, as in the report, scenarios are identified as follows: **01** (small increases in vegetative cover), **02** (larger increases in vegetative cover), **10** (small increases in albedo), **20** (larger increases in albedo), and cases **11** and **22** (combinations).

17.2.1 Southern California

In general, surface modification scenarios cause a temperature change pattern consisting typically of a decrease during daylight hours and smaller or zero decrease during the night. The amount of temperature decrease becomes larger as the level of surface modification increases. For example in Los Angeles, cases 20 and 22 have the highest impacts with decreases in air temperature of as much as 3°C (5.4°F) and up to 3.5°C (6.3°F), respectively, during some hours. The other modification scenarios (with relatively smaller surface modifications), produce smaller impacts on air temperature, e.g., decreases of up to 1°C (1.8°F). Overall, the effectiveness of the strategies at reducing air temperature in the Los Angeles area is, in increasing order: 01, 10, 02, 20, and 22.

In other Southern California regions, the results point to a similar directionality in the changes. In Pomona, for example, the same difference pattern is seen but with slightly smaller magnitudes, e.g., smaller than in Los Angeles by about 0.5°C (0.9°F) in some cases and at certain times. But overall, the effect is about the same as in Los Angeles. In San Diego, where surface modifications are relatively smaller, the impacts on air temperature are likewise reduced. Although the sequence of strategies (effectiveness) is the same as in the other areas, the changes in temperature are about 1°C (1.8°F) smaller than in Los Angeles, overall. In the San Fernando Valley, the changes are of the same order of magnitude as in Los Angeles and Pomona, with a slight difference in the timing of the largest decrease (e.g., on the first two days of the simulated episode), which seems to occur later during the day rather than earlier, as in the other cases. In almost all scenarios, the onset of decrease in air temperature (relative to the base-case scenario) occurs at about 0900 LST and tapers off around 2100 LST, although at different magnitudes in each region. In all cases, the spatial distribution of temperature change matches very closely that of surface modifications. There is also a certain amount of temperature-difference advection downwind of the modified areas (at the end of the day), e.g., through the northern and eastern mountain passes of the basin and into the Mojave Desert.

In terms of wind speed changes, there is likewise a general diurnal pattern relative to the base case conditions. The decrease in wind speed is also generally proportional to the level of surface modification. In Los Angeles, for example, there is almost a diurnal cycle where the wind slows down (by up to about 0.7 to 1 m s⁻¹) between 1500 and 0300 LST. On two of the episode days, there is also a slight acceleration between 0800 and 1000 LST (of about 0.3 to 0.5 m s⁻¹). In Pomona, there is a cyclic reduction of up to about 0.6 m s⁻¹ between 1200 and 2000 LST, i.e., with onset slightly further delayed than in Los Angeles but also of a shorter duration. The increases in speed occur between 0700 and 1200 LST and of a magnitude of up to 0.4 m s⁻¹. In San Diego, the changes appear to be less systematic than in the Los Angeles and Pomona regions, but still display a pattern of decrease between 0900 and 2000 and then between 2200 and 0200 LST almost daily. The acceleration is somewhat more random. The changes are also relatively smaller, generally about up to 0.4 m s⁻¹. Finally, in the Burbank region and San Fernando Valley, the changes in wind speed appear to have a periodic decrease between 1000 to 1600 LST (of up to about 0.3 m s⁻¹).

In terms of ozone concentration changes, and as discussed in the report, the nonlinear nature of the photochemical reactions system producing ozone can cause both increases and decreases in concentrations as a result of surface modifications and attending meteorological perturbations. One of several indices presented in this study that capture the overall and net effects of such changes is the 8-hour RRF. The results suggest that the effectiveness of those strategies is different in different regions of Southern California. For example, the effects are larger in the northern part of the basin and San Fernando Valley where, for example, case 22 can produce a RRF of 91% (a reduction of up to 9%). The reductions in inland zones (further east) and in the coastal areas (west basin) are up to about 4% and 2%, respectively (for case 22). The larger increases in surface properties, e.g., going from cases 10 or 02 to case 22, can more than double these beneficial impacts—that is, decreasing ozone concentrations.

The effects of those strategies on the regional peak are relatively more uniform across all scenarios (i.e., between 2 and 3 ppb decrease, on the average). The domain peak on August 5 in Southern California can increase in some scenarios but always decreases on August 6 (in all scenarios). The numbers provided above are averages for both days. In terms of other indicators (e.g., maximum 8-hour average, 1-hour maximum, and 24-hour average ozone), the results suggest that the most effective case under the episodic conditions and assumed surface modification scenarios in this study is case 20, followed by cases 22, 11, 10, 02, and 01 in most urbanized regions in Southern California. The net decreases are generally significant even when averaged over a large area. For example, when averaged over all urbanized grid cells, the changes in daily 1-hour maximum ozone can be as much as 5.7 ppb (case 20), 3.8 ppb in daily maximum 8-hour average, and up to 2 ppb in 24-hour average (all numbers are for case 20, which is the most effective case). The simulations also suggest that the magnitude of the changes is larger in the South Coast Air Basin than in the San Diego region because the latter has relatively smaller surface modification potential, compared to that in Los Angeles.

17.2.2 Central California

As with Southern California, a typical temperature-change pattern in Central California (due to “implementation” of surface modification strategies) is a decrease during the daytime hours and smaller or non-existent decreases at night. As also discussed earlier, the amount of temperature change gets larger as the level of surface modification increases. Overall, the increasing effectiveness of these strategies at reducing air temperature in Central California is, in the following order of scenarios: 02, 20, and 22.

In San Jose, for example, the largest decreases in air temperature, e.g., those corresponding to case 22, are in the order of 1.5°C–2°C (2.7°F–3.6°F) and about 1°C–1.5°C (1.8°F–2.7°F) in case 20. The largest decreases in air temperature occur on July 31. In Sacramento, the same pattern is seen but with slightly smaller magnitudes, e.g., decreases of up to 1°C–1.5°C (1.8°F–2.7°F) in case 20. The effects of scenario 02 in both regions seem to be smaller; up to about 0.5°C (0.9°F) in cooling. In Fresno, the effects are similar in magnitude to those in San Jose and across all three scenarios. In Bakersfield, the changes are smaller than in these three regions. Here the largest decreases are in the order of 0.5°C–0.7°C (0.9°F–1.3°F) for cases 20 and 22. As discussed in the report, this is a result of smaller surface modifications in the Bakersfield region. In all cases, the decrease in air temperature starts at about 0900 LST and tapers off around 1900 LST, although at different magnitudes of course. As with Southern California, the spatial distribution of temperature change matches very closely the level of surface modifications and their distributions in the modifiable areas. As the area and potential for modification increase, so does the decrease in air temperature.

Wind speed changes also show a general diurnal pattern in all regions. The changes (whether reduction or increase) are generally proportional to the level of surface modification, i.e., in the sequence of scenarios 02 → 20 → 22. Most of the changes are in the range of about $\pm 0.4 \text{ m s}^{-1}$, except in Sacramento where the decrease in wind speed can reach up to 1 m s^{-1} at certain times. Also, the reduction and increase in wind speed are generally equal, except in Sacramento where the reduction in wind speed dominates.

The ozone air-quality implications of these meteorological changes are typically such that the impacts are seen during the daytime and there are no effects during the night or early morning hours. For example, at 0800, small differences in concentrations begin to appear, e.g., in Sacramento (up to 4 ppb decrease) and the San Francisco Bay Area (SFBA) (up to 4 ppb decrease) but are still relatively small overall, especially in the remainder of the CCOS domain. By 1000, the reduction in ozone concentrations (signal) becomes clearer and covers a larger area in these regions where surface modifications occur. Decreases of up to 6–7 ppb are seen in the SFBA, Sacramento, and Fresno and up to 6 ppb in Bakersfield. Concentration decreases of some 3–5 ppb along the Highway 99 corridor (Lodi, Stockton, Manteca, Modesto, Turlock, and Merced) are also seen. At 1200, the signal is stronger/clearer with decreases of up to 16 ppb in the SFBA and up to about 10 ppb in the Sacramento region. The decreases in Fresno and Bakersfield reach up to 10 and 5 ppb respectively. In the Highway 99 corridor, decreases range from up to 4 to 7 ppb. The same spatial pattern exists at 1400 but now with relatively larger decreases. In the SFBA the decreases reach up to 23 ppb in a small area, but overall, the urban region experiences decreases of 14–20 ppb at this hour. In Sacramento the decreases are up to 7 ppb and in Fresno and Bakersfield, up to 6 and 3 ppb, respectively. At 1600, decreases of up to

24 ppb are seen in the SFBA (there is also a small area of increases of up to 3 ppb in the Morgan Hills region). In Sacramento, the decrease reaches up to 6 ppb, in Fresno up to 5 ppb, and in Bakersfield up to 3 ppb. In the Highway 99 corridor the decreases reach up to 6 ppb.

The results suggest that changes in ozone concentrations become larger as surface modifications increase. It can also be noted that many of the larger changes occur in areas close to the local peaks. The spatial distribution of the decreases in each region is roughly similar in all scenarios, but the magnitude of the change differs from one to another. For example, the largest decreases on July 30 are 12, 12, 14, and 16 ppb for cases 02, 10, 20, and 22, respectively. For these four cases (in same order), the largest decreases on July 31 are 23, 24, 25, and 25 ppb respectively. Finally, for August 1, the largest decreases are 26, 26, 28, and 30 ppb for these cases (and in the same order). However, these changes on August 1 (despite being the largest) should not be considered, because model performance on that day was not as good as on the other days of the episode.

In terms of peak concentrations in the Sacramento Valley, San Francisco Bay Area, North San Joaquin Valley (Fresno) and South San Joaquin Valley (Bakersfield), the results suggest that, of the four regions selected for this analysis, Sacramento and the San Francisco Bay Area would experience the largest reductions in the peaks under the episodic conditions simulated here. The simulations suggest that the peaks could be decreased by a range from 6 to 16 ppb in Sacramento, 10 to 16 ppb in the SFBA, 2 to 8 ppb in Fresno, and 1 to 3 ppb in Bakersfield (across both cases 10 and 20). In the Sacramento and SFBA regions, the largest decreases occur during those days with relatively higher local peaks (i.e., July 31 in SFBA and August 1 in Sacramento). The figure also shows that relative to case 10, case 20 does not decrease the peaks by an amount proportional to surface modification differences.

17.3 Recap of Next/Future Steps and Research Needs

- Meteorological-photochemical model performance should be improved further and as much as possible within the constraints posed by this application. Although model performance in this study appears to be relatively reasonable for initial evaluation of the proposed strategies, it may not be sufficiently robust for the results to be used in basing policies for surface modification implementation and credits. Further improvements may also be needed if a recognition of these results by regulatory agencies in California is sought.
- Multi-episodic evaluations may be needed to assess the potential impacts of the proposed strategies under varying meteorological and emission conditions. A number of meteorological episodes could be generated and emissions updated for running a number of corresponding photochemical scenarios. The meteorological episodes can be generated with the meteorological model for a number of different synoptic conditions and regional scenarios for use in this type of analysis.
- Implementation-specific and city-specific modeling may also be needed to account for actual urbanization trends and growth plans. An evaluation of a larger number of combinations of surface modification strategies, in space and in level, may also be needed to obtain an overall range (ensemble) of possible impacts on local meteorology and air quality. Furthermore, implementation-specific modeling needs to be done that accounts specifically for the likely levels of saturation of such surface modification

strategy (in space and time), i.e., a progression sequence of implementation for each urban area/region of interest.

- Fine-resolution “urbanized” (urban canopy parameterization, or UCP) mesoscale modeling is needed to capture the smaller-scale, canopy-layer phenomena that strongly influence the emission, deposition, dispersion, and chemistry in the polluted boundary layer. For example, an urbanized version of the MM5 (EPA’s urbanized DA-SM2-U) is currently being used by Taha and others and is being further developed for similar applications in other regions. This version could be further developed and used in follow-up studies of surface modification strategies in California.
- Improve the characterization of land-use/land-cover distribution and classification system. Currently, most USGS-based LULC data are relatively outdated, and thus more recent and improved LULC classification schemes may be needed, e.g., based on more recent USGS or other data such as ISA (impervious surface area) information from National Oceanic and Atmospheric Administration (NOAA)/National Environmental Satellite, Data, and Information Service (NESDIS) or local agencies in California, such as SCAG (Southern California Association of Governments).
- Use the latest versions of mesoscale meteorological and photochemical models, e.g., version 3.6-7 of MM5 (possibly the last version before the model is “frozen”), Weather Research and Forecasting (WRF) model, as well as latest versions of the CAMx model (e.g., versions 4.10 and 4.11s) or CMAQ.
- Perform UCP modeling using fine-resolution morphology characterization (e.g., derived from Lidar products or other sources of fine-resolution remotely-sensed information such as aerial photography and satellite imagery).
- It may be of value to further narrow down the critical ranges or thresholds of surface modifications (beyond which net ozone benefits may begin to decrease) for each region and for varying meteorological conditions.
- Evaluate the impacts of the proposed strategies with future-year emission inventories in each region (this study has evaluated surface modification strategies using only historical emissions, i.e., 1997 for SCOS and 2000 for CCOS). Future-year controlled emissions should also be used in evaluating the effectiveness of these strategies under scenarios of near-attainment and significantly lower emissions. Such future-year scenarios can be based on AQMP projections or on hypothetical emission reductions that can be used in sensitivity simulations.
- Model modifications and improvements may be needed beyond what was achieved in this study to make the application more specific to certain regions and conditions.
- A number of assumptions and parameterization modifications made in this study may need to be re-examined and re-evaluated for acceptance, e.g., by regulatory modelers. For example, among others, these include such modifications as: (1) the scaling of vertical diffusivity profiles (to compensate for PBL-height over-prediction in the MRF scheme), (2) running the meteorological model in a standalone-grid (downscaled) fashion that might introduce a certain level of noise, and (3) warmer boundary conditions in Southern California simulations.
- City-specific surface-type-based modification levels need to be developed in follow-up studies.

18. References

- Akbari, H., R. Levinson, P. Berdahl, and L. Rainer. 2003. "A review of methods for the manufacture of residential roofing materials," Lawrence Berkeley National Laboratory Report No. 55574, LBNL Berkeley, California.
- Akbari, H., S. Rose, and H. Taha. 1999. *Characterizing the Fabric of the Urban Environment: A Case Study of Sacramento, California*. Lawrence Berkeley National Laboratory Report No. LBNL-44688, Berkeley, California.
- Anthes, R. A. 1977. "A cumulus parameterization scheme utilizing a one-dimensional cloud model." *Monthly Weather Review* 105:270–286.
- Atwater, M. A. 1984. Influence of meteorology on high ozone concentrations. In *Evaluating the scientific basis for ozone/oxidants standards: Proceeding of the international specialty conference*. Air Pollution Control Association. Houston, Texas.
- Berdahl, P., H. Akbari, and S. Rose. 2002. "Aging of reflective roofs: Soot deposition." *Applied Optics* 41 (12):2355. Also Lawrence Berkeley National Laboratory Report No. 45367.
- Berdahl, P., and S. Bretz. 1997. *Preliminary survey of the solar reflectance of cool roofing materials*. Lawrence Berkeley National Laboratory Report No. 41294.
- Betts, A. K., and M. J. Miller. 1986. "A new convective adjustment scheme. Part II: Single column tests using GATE wave, BOMEX, ATEX, and Arctic air mass data sets." *Quarterly Journal of the Royal Meteorological Society* 112:693–709.
- Bloch, L., and A. Winer. 1994. "Estimation of hydrocarbon emissions from trees using phylogenetic relationships". In *Analysis of Energy Efficiency and Air Quality in the SoCAB – Phase II*. H. Taha et al., editors. Chapter 9. Lawrence Berkeley National Laboratory Report No. 35728.
- Burian, S. J., W. S. Han, S. P. Velugubantla, and S. R. K. Maddula. 2003. *Development of gridded fields of urban canopy parameters for Models-3/CMAQ/MM5*. Department of Civil and Environmental Engineering, University of Utah.
- Burk, S. D., and W. T. Thompson. 1989. "A vertically nested regional numerical prediction model with second order closure physics." *Monthly Weather Review* 117:2305–2324.
- CARB. 1990. "Derivation of the EMFAC7E emission and correction factors for on-road motor vehicles." California Air Resources Board, Sacramento, California.
- CARB. 1996. "Methodology for estimating emissions from on-road motor vehicles." Volume I: Introduction and overview (Nov 1996). California Air Resources Board, Sacramento, California.
- CARB. 2000a. "Staff Report: Public meeting to consider approval of revisions to the State's on-road motor vehicle emission inventory." (May 2000). California Air Resources Board, Sacramento, California.
- CARB. 2000b. "EMFAC2000 Technical Support Documentation." (July 2000). California Air Resources Board, Sacramento, California.

- Cardelino, C. A., and W. L. Chameides. 1990. "Natural hydrocarbons, urbanization, and urban ozone." *Journal of Geophysical Research* 95 (D9):13971–13979. August.
- Cardelino, C. A., W. L. Chameides, W. L. Chang, and M. F. Chang. 1995. "The application of land use patterns to study the impacts of temperature, biogenic emissions, and land use pattern changes on ozone precursor emissions and ozone concentrations." Proceedings of the International Specialty Conference: *Regional Photochemical Measurement and Modeling Studies*. Volume 2. Air & Waste Management Association. 439–455.
- Clark, T. L., and T. R. Karl. 1982. "Application of prognostic meteorological variables to forecasts of daily maximum one-hour ozone concentrations on the northeastern United States." *Journal of Applied Meteorology* 21:1662–1671.
- Cooper, C. D., and F. C. Alley. 1994. *Air pollution control: A design approach*. Prospect Heights, Illinois: Waveland Press Inc. 694 pp.
- Cox, W. M., and S. H. Chu. 1993. "Meteorologically adjusted ozone trends in urban areas: A probabilistic approach." *Atmospheric Environment* 27B:425–434.
- DaMassa, J., P. Allen, T. McGuire, D. McNerny, A. Ranzieri, K. Wagner. 1992. "Technical Guidance Document: Photochemical Modeling." California Air Resources Board. Sacramento, California. April.
- Deuel, H. P., P. D. Guthrie, W. Moody, L. Deck, S. Lange, F. Hameed, J. Castle, L. and Mearns. 1999. "Potential impacts of climate change on air quality and human health." Air & Waste Management Association, 92nd Annual Meeting and Exhibition, June 20–24, 1999, St. Louis, Missouri.
- Dimitriades, B. 1989. "Photochemical oxidant formation: Overview of current knowledge and emerging issues." In *Atmospheric Ozone Research and its Policy Implications*. Amsterdam: Elsevier.
- Dudhia, J. 1993. "A non-hydrostatic version of the Penn State/NCAR mesoscale model: Validation tests and simulation of an Atlantic cyclone and cold front." *Monthly Weather Review* 121:1493–1513.
- Environ 2001. "Enhanced meteorological modeling and performance evaluation for two Texas ozone episodes." Report prepared for the Texas Natural Resources Conservation Commission, August 31, 2001.
- Environ 2002 (with ATMET LLC and Alpine Geophysics LLC). "Development of a photochemical modeling system to support the Bay Area Air Quality Management District's 2004 State Implementation Plan," Environ Corp., Air Sciences. Novato, California. December.
- EPA 1989. "The potential effects of global climate change on the United States: Report to Congress." Report EPA-230-05-89-058, Washington D.C.
- EPA 1991. "Guidelines for regulatory application of the Urban Airshed Model." U.S. Environmental Protection Agency Report EPA-450/4-91-013. Office of Air Quality Planning and Standards, RTP, NC 27711. May 1991.
- EPA 1996. "Air quality criteria for ozone and related photochemical oxidants." Volume-I, Report EPA-600-P93-004aF. U.S. EPA, Office of Research and Development, National Center for Environmental Assessment, Washington D.C.

EPA 2000. "National air pollutant emission trends: 1900–1998." EPA 454-R-00-002. EPA OAQPS, RTP, North Carolina.

Flaum, J. B., S. T. Rao, and I. G. Zurbenko. 1996. "Moderating the influence of meteorological conditions on ambient ozone concentrations." *Journal of the Air & Waste Management Association* 46:35–46.

Fuentes, J. D., M. Lerdau, R. Atkinson, D. Baldocchi, J. W. Bottenheim, P. Ciccioli, B. Lamb, G. Geron, L. Gu, A. Guenther, T. D. Sharkey, and W. Stockwell. 2000. "Biogenic hydrocarbons in the atmospheric boundary layer: A review." *Bulletin of the American Meteorological Society* 81 (7):1537–1575. July 2000.

Gabersek, S., and H. Taha. "Impacts of surface characteristics changes on urban heat island intensity." ICB 96, 14th International Congress of Biometeorology, September 1–8, 1996, Ljubljana, Slovenia.

Gery, M. W., G. Z. Whitten, J. P. Killus. 1988. *Development and testing of the CBM-IV for urban and regional modeling*. Report EPA-600/3-88-012, U.S. EPA, Research Triangle Park, North Carolina.

Gery, M. W., R. D. Edmond, and G. Z. Whitten. 1987. *Tropospheric ultraviolet radiation: Assessment of existing data and effect on ozone formation*. EPA-600-3-87-047, US EPA, RTP, North Carolina.

Grell, G. A., Y. H. Kuo, and R. Pasch. 1991. "Semi prognostic test of cumulus parameterization schemes in the middle latitudes." *Monthly Weather Review* 119:5–31.

Grell, G. A., J. Dudhia, and D. R. Stauffer. 1994. "A description of the fifth generation PSU/NCAR mesoscale modeling system (MM5)." Technical Note NCAR/TN—379+STR, NCAR.

Guenther, A., P. Zimmerman, P. Harley, R. Monson, and R. Fall. 1993. "Isoprene and monoterpene emission rate variability: Model evaluations and sensitivity analysis." *Journal of Geophysical Research* 98:12609–12617.

Guenther, A., B. Baugh, G. Brasseur, J. Greenberg, P. Harley, L. Klinger, D. Sereca, and L. Vierlang. 1999. "Isoprene emission estimates and uncertainties for the Central African EXPRESSO study domain." *Journal of Geophysical Research* 104:30625–30639.

Guenther A. B., R. Fall, P. R. Zimmerman, P. C. Harley, and R. K. Monson. 1993. "Isoprene and monoterpene emission rate variability: Model evaluations and sensitivity analyses." *J. Geophys. Res.* 98 (D7):12,609–12,617.

Harrison, R. M. 1990. "Important air pollutants and their chemical analysis." In *Pollution: Causes, Effects, and Control*. Harrison R.M. (ed.), 2nd edition, Royal Society of Chemistry.

Hogo, H., and M. W. Gery. 1988. "User's guide for executing OZIPM4 with CBM-IV or optional mechanisms." EPA report 600/8-88/-82. US EPA, RTP, North Carolina.

Hong, S. H., and H. L. Pan. 1996. "Nonlocal boundary layer vertical diffusion in a medium-range forecast model." *Monthly Weather Review* 124:2322–2339.

Hsie, E. Y., and R. A. Anthes. 1984. "Simulations of frontogenesis in a moist atmosphere using alternative parameterizations of condensation and precipitation." *Journal of Atmospheric Science* 41:2701–2716.

Jeffries, H. E., K. G. Sexton, J. R. Arnold, and T. L. Kole. 1989. "Validation testing of new mechanisms with outdoor chamber data." Volume 4: Appendices to photochemical reaction photolysis rates in the University of North Carolina outdoor chamber. EPA-600-389-010d. U.S. EPA, Research Triangle Park, North Carolina.

Jones, K., L. Militana, J. Martini. 1989. "Ozone trend analysis for selected urban areas in the continental U.S." Presented at the 82nd annual meeting and exhibition of the A&WMA. Anaheim, California. June 1989.

Kain, J. S., and J. M. Fritsch. 1993. "Convective parameterization for mesoscale models: The Kain-Fritsch scheme." In *The Representation of Cumulus Convection in Numerical Models*. Meteorological Monographs, K. A. Emmanuel and D. J. Raymond, eds. 46:165–170. American Meteorological Society.

Kelly, N. A., and R. F. Gunst. 1990. "Response of ozone to changes in hydrocarbon and nitrogen oxide concentrations in outdoor smog chambers filled with Los Angeles air." *Atmospheric Environment Part A*, 24:2991–2005.

Kuntasal, G., and T. Y. Chang. 1987. "Trends and relationships of O₃, NO_x, and HC in the south coast air basin of California." *JAPCA* 37:1158–1163.

Lehrman, D., B. Knuth, and D. Fairley. 2001. *Characterization of the CCOS 2000 measurement period*. Technical report, California Air Resource Board, Sacramento, California.

Liu, S.C., and M. Trainer. 1988. "Response of the tropospheric ozone and odd hydrogen radicals to column ozone change." *Journal of Atmospheric Chemistry* 6:221–233.

McNider, R. T., W. B. Norris, and J. A. Song. 1995. "Regional meteorological characteristics during ozone episodes in the Southeastern United States." Proceedings of the International Specialty Conference: *Regional Photochemical Measurement and Modeling Studies*. TR-24, pp. 832–846. Air & Waste Management Association.

Milford, J. B., G. A. Russell, G. J. McRae. 1989. "A new approach to photochemical pollution control: Implications of spatial patterns in pollutant responses to reductions in nitrogen oxides and reactive organic gas emissions." *Environmental Science & Technology* 23:1290–1301. October.

Morris, R., M. Gery, M. Liu, G. Moore, C. Daly, and S. Greenfield. 1989. "Sensitivity of a regional oxidant model to variations in climate parameters." In *The potential effects of global climate changes on the United States. Appendix F: Air Quality*. U.S. EPA. Washington D.C.

Morris, R., G. Z. Whitten, and S. M. Greenfield. 1991. "Preliminary assessment of the effects of global climate change on tropospheric ozone concentrations." Proceedings of the Specialty Conference: Tropospheric Ozone and the Environment II. Air & Waste management Association, pp. 5–30, Pittsburgh, Pennsylvania.

O'Brien, J. J. 1970. "A note on the vertical structure of the eddy exchange coefficient in the planetary boundary layer." *Journal of the Atmospheric Sciences* 27:1213–1215.

Olerud, D. T., T. E. Pierce, K. L. Schere, A. F. Hanna. 1995. "Sensitivity of the Regional Oxidant Model to meteorological parameters." In *Proceedings of the International Specialty Conference: Regional Photochemical Measurement and Modeling Studies*. 2:832–846. Air & Waste Management Association.

- Pan, H. L., and L. Mahrt. 1987. "Interaction between soil hydrology and boundary-layer development," *Boundary Layer Meteorology* 38:185–202.
- Penner, J., P. Connell, D. Wuebbles, and C. Covey. 1989. "Climate change and its interactions with air chemistry: Perspectives and research needs." In *The potential effects of global climate changes on the United States, Appendix F: Air Quality*. U.S. EPA. Washington D.C.
- Pielke, R. A. 2002. *Mesoscale Meteorological Modeling*. International Geophysics Series, Volume 78. 2nd Edition, Academic Press Inc., San Diego.
- Pielke, R. A. 1984. *Mesoscale Meteorological Modeling*. Academic Press Inc, San Diego.
- Reisner, J., R. J. Rasmussen, R. T. Bruintjes. 1998. "Explicit forecasting of supercooled liquid water in winter storms using the MM5 mesoscale model," *Quarterly Journal of the Royal Meteorological Society* 124B:1071–1107.
- Rose, S., H. Akbari, and H. Taha. 2003. "Characterizing the fabric of the urban environment: A case study of Greater Houston, Texas." Lawrence Berkeley National Laboratory, Report No. LBNL-51448, Berkeley, California.
- Sailor, D. 1993. "Role of surface characteristics in urban meteorology and air quality." Ph.D. dissertation. University of California, Berkeley.
- Samson, P. 1988. "Linkages between global climate warming and ambient air quality." A paper presented at the Global Climate Linkages Conference, Washington D.C. November.
- Schultz, P. 1995. "An explicit cloud physics parameterization for operational numerical weather prediction." *Monthly Weather Review* 123:3331–3343.
- Seaman, N. L. et al. 1997. "The use of the San Joaquin Valley meteorological model in preparation of a field program in the South Coast Air Basin and surrounding regions of Southern California. Volume II: Numerical modeling studies for the development and application of a guidance technique to support the design of the 1997 Southern California Ozone Study field program." Prepared for the California Air Resources Board, Department of Meteorology, Pennsylvania State University, University Park, Pennsylvania.
- Seaman, N. L., and D. R. Stauffer. 1996. "SARMAP meteorological model final report." Prepared for the San Joaquin Valleywide Air Pollution Study Agency, Department of Meteorology, Pennsylvania State University, University Park, Pennsylvania.
- Seinfeld, J. 1975. *Air Pollution – Physical and Chemical Fundamentals*. New York: McGraw-Hill.
- Seinfeld, J. H. 1988. "Ozone air quality models: A critical review." *Journal of the Air Pollution Control Association* 38:616–641.
- Seinfeld, J., and S. N. Pandis. 1998. *Atmospheric Chemistry and Physics: From air pollution to climate change*, New York: Wiley Interscience. 1326.
- Sillman, S., and Samson, P. 1995. "Impact of temperature on oxidant photochemistry in urban, polluted rural, and remote environments." *Journal of Geophysical Research* 100:11497–11508.

- Sillman, S., J. A. Logan, and S. C. Wofsy. 1990. "The sensitivity of ozone to nitrogen oxides and hydrocarbons in regional ozone episodes." *J. Geophys. Res.* 95:1837–1851.
- Smith, J. B., and D. A. Tirpak, editors. 1989. "The potential effects of global climate change on the United States." Report to Congress, U.S. EPA, EPA-230-05-89-050, Washington D.C. 409 pp.
- Stauffer, D. R., and N. L. Seaman. 1990. "Use of four-dimensional data assimilation in a limited area mesoscale model. Part I: Experiments with synoptic-scale data." *Monthly Weather Review* 118:1250–1277.
- Stern, A. C., R. W. Boubel, D. B. Tuner, and D. L. Fox, 1984. *Fundamentals of Air Pollution*. Academic Press, Inc. 530 pp.
- Stockwell, W. R., P. Middleton, and J. S. Chang. 1990. "The second generation regional acid deposition model chemical mechanism for regional air-quality modeling." *Journal of Geophysical Research*. 95:16343–16367.
- Taha, H. 1996. "Modeling the Impacts of Increased Urban Vegetation on the Ozone Air Quality in the South Coast Air Basin." *Atmospheric Environment* 30 (20):3423–3430.
- Taha, H. 1997a. "Urban climates and heat islands: Albedo, evapotranspiration, and anthropogenic heat." *Energy and Buildings* 27 (1007):99–103.
- Taha, H. 1997b. "Modeling the Impacts of Large-Scale Albedo Changes on Ozone Air Quality in the South Coast Air Basin." *Atmospheric Environment* 31 (11):1667–1676.
- Taha, H. 1999. "Modifying a Mesoscale Meteorological Model to Better Incorporate Urban Heat Storage: A Bulk-Parameterization Approach." *Journal of Applied Meteorology* 38 (4):466–473.
- Taha, H., S. Konopacki, and S. Gabersek. 1999. "Impacts of large-scale surface modifications on meteorological conditions and energy use: A 10-region modeling study." *Theoretical and Applied Climatology* 62 (3-4):175–185.
- Taha, H., S. C. Chang, and H. Akbari. 2000. "Meteorological and air-quality impacts of heat island mitigation in three U.S. cities." LBNL Report No. 44222. April.
- Taha, H., H. Hammer, and H. Akbari. 2002. "Meteorological and air quality impacts of increased urban surface albedo and vegetative cover in the Greater Toronto Area, Canada." LBNL Report No. 49210. April 2002.
- Taha, H. 2003a. "Mesoscale meteorological and air quality modeling of heat island reduction strategies (HIRS)." Technical Note, Lawrence Berkeley National Laboratory, Berkeley, California. April 2003. 53 pp. Available from H. Taha, Altostratus Inc., haider@altostratus.com.
- Taha, H. 2003b. "Multi-regional modeling assessment of the potential meteorological impacts of heat island reduction." Technical Note, Lawrence Berkeley National Laboratory, Berkeley, California. April 2003. 46 pp. Available from H. Taha, Altostratus Inc., haider@altostratus.com.

Taha, H. 2003c. "Potential meteorological and air-quality implications of heat-island reduction strategies in the Houston-Galveston TX region." Technical Note HIG-12-2002-01, Lawrence Berkeley National Laboratory, Berkeley, California. 143 pp. Available from H. Taha, Altostratus Inc., haider@altostratus.com.

Taha, H. 2004 (Draft in progress). "Improved modeling of meteorological and ozone air-quality impacts of urban surface modifications in California." Report prepared for the California Energy Commission, for Contract 500-02-013. Report 04-B, Altostratus Inc. Will be published by the Energy Commission in fall 2005.

Tao, W. K., and J. Simpson. 1993. "Goddard cumulus ensemble model. Part I: Model description." *Terrestrial, Atmospheric, and Oceanic Science*. 4: 35–72.

Tesche, T. W., D. E. McNally, C. A. Emery, and E. Tai. 2001. "Evaluation of the MM5 model over the Midwestern U.S. for three 8-hour oxidant episodes." Prepared for the Kansas City Ozone Technical Workgroup. Alpine Geophysics LLC and Environ Corp.

Tesche, T. W. 1988. "Accuracy of ozone air-quality models." *Journal of Environmental Engineering* 114 (4):739–752.

Thompson, A. M. 1992. "The oxidizing capacity of the Earth's atmosphere: Probable past and future changes." *Science* 256:1157–1165.

Wackter, D. J. and Bayly, P. V. 1988. "The effectiveness of emission controls on reducing ozone levels in Connecticut from 1976 through 1987. In Wolff, Hanish, and Schere (eds.). *The scientific and technical issues facing post-1987 ozone control strategies*. Transactions of the APCA international specialty conference, Hartford, Connecticut.

Wakim, P. G. 1989. "Temperature adjusted ozone trends for Houston, New York, and Washington D.C. 1981–1987." Presented at the 82nd annual meeting and exhibition of the A&WMA, Anaheim, California, June 1989. A&WMA, Pittsburgh, Pennsylvania.

Walcek, C. J., and H. H. Yuan. 1994. "The sensitivity of oxidant formation rates to uncertainties on temperature, water vapor, and cloud cover." Section 4.9 (pp. 184–185), American Meteorological Society, 8th Joint conference on applications of air pollution meteorology with the AWMA, January 23–28, 1994, Nashville, Tennessee.

Wunderli, S., and R. Gehrig. 1991. "Influence of temperature on formation and stability of surface PAN and ozone: A two-year field study in Switzerland." *Atmospheric Environment Part A*. 25:1599–1608.

Yarwood, G., R. E. Morris, M. A. Yocke, H. Hogo, and T. Chico. 1996. "Development of a methodology for source apportionment of ozone concentration estimates from a photochemical grid model," 89th AWMA Annual Meeting, Nashville, Tennessee. June.

Zhang, D. L., and R. A. Anthes. 1982. "A high resolution model of the planetary boundary layer – Sensitivity tests and comparisons with SESAME 79 data." *Journal of Applied Meteorology* 21:1594–1609.

Zhang, J., S. T. Rao, and S. M. Daggupaty. 1998. "Meteorological processes and ozone exceedances in the Northeastern United States during the 12–16 July 1995 episode." *Journal of Applied Meteorology* 37:776–789.

Glossary

AGL	Above ground level
AQMD	Air Quality Management District
AQMP	Air Quality Management Plan
AVHRR	Advanced Very High Resolution Radiometer
AVIRIS	NASA Airborne Visible Infra-Red Imaging Spectrometer
BAAQMD	Bay Area Air Quality Management District
BEIS	Biogenic Emissions Inventory System model
CAA	Clean Air Act
CAAQS	California Ambient Air Quality Standards
CALGRID	ARB's Photochemical Grid Model
CAMx	Comprehensive Air quality Model with extensions
CB-IV	Carbon bond mechanism
CCOS	Central California Ozone Study
CDD	Cooling degree-days
CMAQ	Community Multiscale Air Quality model
DOE	U.S. Department of Energy
DTIM	Direct Travel Impact Model
EKMA	Empirical Kinetic Modeling Approach
EMFAC	Emissions model (pollutants emission from motor vehicles)
EPA	U.S. Environmental Protection Agency
FDDA	Four-Dimensional Data Assimilation
GDAS	Global Data Assimilation System
GPS	Global positioning system
HDD	Heating degree-days
ISA	Impervious surface area
LADWP	Los Angeles Department of Water and Power
LULC	Land use and land cover
mb	Millibar
MIR	Mid-infrared
MM5	PSU/NCAR mesoscale model, fifth generation
MRE	Mean relative error
MRF	Medium range forecast
MURE	Mean unbiased relative error
NCAR	National Center for Atmospheric Research
NCEP	National Centers for Environmental Protection
NDVI	Normalized Difference Vegetation Index
NESDIS	National Environmental Satellite, Data, and Information Service
NESTDOWN	A computer program that interpolates data from a coarse grid to a fine grid.
NIR	Near infrared
NNRP	NCAR NCEP Reanalysis Project
NOAA	National Oceanic and Atmospheric Administration
PAN	Peroxyacetyl nitrate
PAR	Photosynthetically active radiation
PBL	Planetary Boundary Layer
PPB	parts per billion
PM	particulate matter

PSU	Pennsylvania State University
ROG	reactive organic gases
RRF	relative reduction factor
SAPRC(99)	Statewide Air Pollution Research Center (chemical mechanism)
SAR	surface-to-area ratio
SCAG	Southern California Association of Governments
SCAQMD	South Coast Air Quality Management District
SCOS	Southern California Ozone Study
SIP	State implementation plan
SMAQMD	Sacramento Metropolitan Air Quality Management District
SVF	Sky-view factor
TKE	Turbulent kinetic Energy
TPD	tons per day
UAM-IV; UAM-V	Urban Airshed Model (versions)
UCP	urban canopy parameterization
UHI	Urban heat island
UHIPP	Urban Heat Island Pilot Project
VOC	Volatile Organic Compounds
WRF	Weather Research and Forecasting

APPENDIX A

Brief Aspects of Meteorology and Photochemistry and Relevance to California

All meteorological variables exert an influence, directly or indirectly and in varying degrees, on the production of photochemical smog, the distribution of air pollutants and precursors, and the resulting ozone concentrations. The impacts can be positive or negative and vary significantly with atmospheric and geophysical conditions. In the following discussion some meteorological parameters of interest are presented separately in describing their potential roles in or impacts on ozone formation and concentrations. Obviously, all meteorological fields are tightly coupled and their complex feedback may make it difficult in reality to isolate the effects of one parameter from those of another. In the sections below, the discussion relates to aspects of meteorology that have direct relevance to ozone air quality, but because of the interest in temperature in this study, there is relatively more focus on the role of this variable.

That ozone formation is as a strong function of complex interactions between meteorology and pollutant/precursor emissions is well known. Stern et al. (1984) for example, attempted to put this complex dependency into a simple qualitative relation, such as the proportionality:

$$c \propto \frac{(ROG)(NO_x)(S)(T)}{(U)(Z_i)} \quad (1)$$

where c is ozone concentration, ROG (reactive organic gases) and NO_x are precursors concentrations (and emissions) both biogenic and anthropogenic, S and T are solar radiation (actinic flux) and temperature, U is wind speed, and Z_i is inversion or mixing height (depth of the mixed boundary layer). Concentrations of NO_2 are important in the photochemical production of tropospheric ozone as NO_2 photolysis (absorption of a photon) produces NO and O (atomic oxygen). The latter reacts with atmospheric O_2 to produce ozone, as will be seen later (equations 16, 17, and 18). This process is the only pathway generating *tropospheric* ozone, e.g., in the polluted boundary layer.

The dependence of tropospheric ozone on one or more of these parameters is easy to observe. Conditions of high emissions, temperature, solar radiation and low wind speed and mixing have been well documented (e.g., Cox and Chu 1993) and correlated with high ozone concentrations. For example in summer of 1988, prevailing meteorological conditions conducive to ozone formation caused ozone levels in 76 U.S. cities to exceed the NAAQS by at least 25% (EPA 1989). It should be noted however that relation (1) is only a general directionality and that at times, one or more of these parameters can cause the opposite effect depending on ambient environmental conditions and mix of chemical species in the atmosphere.

Ozone formation and destruction are continuous processes in the atmosphere, sometimes leading to a photo-stationary state in which no net ozone changes occur. Ozone concentrations can increase when certain processes allow it to accumulate in an air mass. In addition, ambient VOC, NO_x , and radicals have significant impacts on ozone formation and accumulation, as will be explained later in this discussion. At regional scales, factors of importance to tropospheric ozone formation are (EPA 1989):

1. Changes in air temperature and their spatiotemporal distributions
2. Changes in stratospheric ozone and corresponding changes in UV downwelling to the troposphere (impacts on photolysis)
3. Changes in solar radiation and cloud cover affecting actinic flux, as well as temperature
4. Changes in the pattern and persistence of high pressure systems (e.g., the Pacific high, for California) and related changes in temperature, vertical mixing, and wind fields
5. Changes in emission rates of ozone precursors as a function of temperature, solar radiation, water vapor, and CO₂
6. Changes in dry and wet deposition rates (affecting ozone and its precursors)
7. Changes in regional and planetary albedo as a result of sulfates, soot, and other aerosols

Temperature

It was stated elsewhere in this report that temperature is often directly or indirectly correlated with ozone levels. While there is a physical basis for making temperature a popular air-quality “index” or “predictor”, it must be emphasized that higher temperature results from—and is often a surrogate for—other meteorological conditions that are conducive to accelerated tropospheric ozone formation and accumulation. For example, higher temperatures usually are (but not always) associated with larger solar radiation flux, UV flux, less cloudiness, higher pressure, stagnation, increased emissions of precursors, etc.

For those photochemical reactions that are temperature sensitive, the functional dependency is of the form:

$$k = ae^{-\frac{E}{RT}} \quad (2)$$

where the reaction rate constant (k) depends on activation energy (E) and temperature (T). “R” is the gas constant and “a” is a frequency factor that is roughly constant across a range of gas-phase reactions (Stern et al. 1984). The overall effect of temperature change on the most influential reactions in forming tropospheric ozone (e.g., breakdown of PAN in the polluted boundary layer) tends to be a positive correlation. The effect of higher temperatures on PAN chemistry is to produce a significant amount of NO₂ (among other emissions) and as a result, increased O₃. This process is highly temperature-sensitive, with an E/R ratio of 13500 to 140000, whereby increased temperature accelerates the thermal decomposition of PAN, increasing the available pool of reactive nitrogen and increasing ozone (Cardelino and Chameides 1990). Seinfeld and Pandis (1998) also show that the temperature-O₃ relationship is driven mainly by PAN chemistry.

While the relationship between temperature and ozone formation in a controlled environment (e.g., smog chamber) can be explained in a relatively straightforward manner, the correlation between observed ozone concentrations and temperature in the atmosphere may not always be easy to verify. This may occur because air temperature is often a proxy for other meteorological fields, as discussed above, which can incorporate a range of conditions that may or may not be conducive to ozone buildup. But in general, as temperature rises, ozone concentrations increase (as an overall effect) even though some components of the photochemical smog-production

system may be responding differently to increased temperature or attending meteorological fields.

Some studies have shown that temperature change has little or no direct effect on ozone formation in the free troposphere (Sillman and Samson 1995), but that the impact of temperature on ozone is significant in the polluted boundary layer (Sillman et al.1990), which is where the T-O₃ correlation is strongest. Furthermore, Sillman and Samson (1995) show that the bulk of this correlation is due to photochemistry rather than to precursor emissions, water vapor, solar radiation, or other meteorological impacts of increased temperatures. In this case, the temperature effect is mostly associated with the removal rate for PAN which is a reservoir of reactive nitrogen (PAN is an increased sink for NO_x and free radicals at low temperatures) and which provides a pool of NO₂ and odd hydrogen. As temperature increases, PAN breakdown provides the needed NO₂ to start the cycle of ozone formation and, if conditions are right, its accumulation. Sillman and Samson (1995) further suggest that the correlation (based on observational aerometric data) may be actually stronger than some photochemical models predict it to be.

The strength of the temperature-ozone (T-O₃) correlation also depends on the range of absolute temperatures. For example, if air temperature rises, crudely in the range of 25°C to 35°C (77°F to 95°F), smog formation usually accelerates (good correlation), but if the temperature keeps increasing beyond that range, increased mixing and a breakup in the inversion layer can allow pollutants to vent into the free troposphere. The venting effect is to reduce the apparent concentrations of pollutants, e.g., ozone. In addition, and as discussed elsewhere in this report, it has been observed that below certain thresholds, higher temperature results in little or no impact on peak ozone concentrations, whereas above that threshold, the T-O₃ relationship generally strengthens. Some reasons behind this behavior are (EPA 1996):

- Increase in photolysis rates under meteorological conditions associated with high air temperatures
- Increase in water vapor content at higher temperatures
- Increase in rates of PAN thermal decomposition at higher temperatures
- Increased temperature-dependent emissions of anthropogenic and biogenic hydrocarbon (HC) and/or NO_x

The fact that temperature is only one of many parameters affecting ozone formation explains why there exists a wide range (scatter) of ozone concentrations at each given temperature. The upper bound of the O₃-T envelope is where maximum ozone concentrations (at a given temperature) can be achieved under the most favorable conditions. In smog chambers, on the other hand, the correlation with temperature is linear with minimal scatter because of absence of real-atmosphere complicating factors. Thus in summary, higher temperature typically results in higher ozone concentrations (above certain temperature thresholds) but under conditions when there are not enough precursors to sustain ozone formation, the increase in temperature actually accelerates ozone formation (higher rates) but the total amount produced may not be larger and can actually be smaller in some cases.

Increased water vapor content as a result of higher temperatures can have an important role in ozone formation. However, it is not straightforward to establish the directionality of this effect with some conditions of increased water vapor (and consequently OH) conducive to increased ozone (EPA 1996) and other conditions conducive to decreased ozone concentrations (Seinfeld and Pandis 1998).

Solar radiation/cloudiness

The general effect of increased cloudiness, beyond scattered clouds, is to reduce solar radiation (e.g., actinic/UV flux in the boundary layer) and as a result, slow ozone formation. Using an outdoor smog chamber, Jeffries et al. (1989) showed that a partial cloud cover could decrease the UV flux by up to 14%. Clouds can also modify the spectral characteristics of the solar radiation flux. In addition, the timing of cloudiness can be as important as its amount, e.g., afternoon or nighttime clouds have generally smaller impacts relative to morning clouds.

Increased solar radiation can have several direct and indirect effects that can impact ozone formation, such as: (1) increased surface and air temperatures, (2) increased biogenic hydrocarbon emissions that are sensitive to solar radiation (and photosynthetically active radiation, or PAR), (3) accelerated photochemical reactions that are sunlight-dependent, and (4) increased UV radiation flux (e.g., resulting from depletion of stratospheric ozone). The latter increases the photolysis rates for a number of active species, e.g., NO₂ and O₃.

Water vapor

Impacts of changes in water vapor content can be examined in two manners: (1) as a meteorological variable (physical), and (2) as a chemical species (chemical). As a result, it is difficult to predict the overall role of water vapor in ozone production because of its dependence on conditions that can vary significantly in space and time.

1. Water vapor as a meteorological parameter (physical effect)

An increase in water vapor can act to increase wet scavenging of pollutants (both ozone itself and its precursors), thus ultimately reducing ozone formation. In addition, as temperature changes, evaporation rates follow and changes in atmospheric water vapor content can potentially lead to impacts on local cloud cover, precipitation, and solar radiation at the surface. Urban heat islands, for example, can increase the rate of cumulus cloud formation downwind of urban centers where the heat-moisture plume is advected. In sensitivity studies, and assuming that cloud cover and precipitation are unchanged as a result of water vapor increase, Penner et al. (1989) show that a temperature increase of 2°C (3.6°F) causes an increase in water vapor content of 10% to 30%. But in general, there is high uncertainty in predicting spatiotemporal distributions of clouds, which makes it difficult to develop future-year scenarios corresponding to surface modifications or other control strategies.

2. Water vapor as a chemical species (chemical effect)

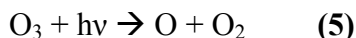
The role of water vapor as a chemical species in atmospheric production of ozone is complex. It is known, for example, that water vapor participates in producing radicals and hydrogen peroxide and that it can enhance ozone formation. Thus another indirect impact of temperature increase may be that of increasing atmospheric water vapor content and thus increasing the concentrations of those radicals, accelerating ozone formation (Penner et al. 1989). Water vapor is one source of hydroxide (OH), and the primary one in the background troposphere (Harrison 1990), producing this radical via photolysis of ozone. Thus changes in water vapor could have a direct impact on the abundance of OH. Changes in vegetative cover or other sources/sinks of water vapor, such as anthropogenic and combustion sources can also alter the net amount of OH produced. Seinfeld and Pandis (1998) suggest that keeping all else constant, an increase of 2°C (3.6°F) in air temperature can cause an increase of 10%–30% in water vapor content, which causes an increase of some few percents in OH and HO₂. The reaction of HO₂ with ozone cycles back to OH, thus replenishing the latter's concentrations via (3) (Seinfeld and Pandis 1998):



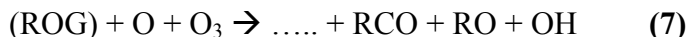
The OH radical is an important tropospheric reactive species. It reacts with several trace species and is constantly regenerated via cyclic reactions, e.g., reaction (3). As mentioned above, one important pathway for production of OH is the photolysis of ozone to atomic oxygen, O, and then via reaction (4):



This pathway is temperature dependent, with increased OH formation at higher temperatures. How this affects ozone production and concentrations in the end is not straightforward, but it can be mentioned here that this will strongly depend on concentrations of other species, e.g., NO_x and VOC. The other pathway for H₂O→OH mentioned above (as a primary source of OH in the background troposphere) is via photolysis of ozone (Harrison 1990):



This partially explains why increased atmospheric humidity (H₂O) and sunshine (hν) can generally result in an increase in OH content in the troposphere. This in turn, can enhance ozone formations under the right conditions. Of course there are a number of other pathways for formation of OH that do not include water vapor as a reactant. Such pathways can be more important in the polluted boundary layer relative to the above pathways for background tropospheric formation of OH. An example of such pathway (Cooper and Alley 1994) is:



where, according to common terminology, “R” is any organic group.

It is to be noted that reactions (5) and (6) can also provide a pathway for the removal (sink) of ozone which could accelerate with increased water vapor concentrations (thus a counter effect to the above). This will depend on the state of the atomic oxygen produced by (5) and the rate constants for the various reactions involved. In the end some 10% of O(¹D) can react with H₂O via (6) generating OH (Seinfeld and Pandis 1998). The presence of OH is also important in increasing ozone concentrations by allowing it to accumulate (which also depends on VOC/NO_x ratio discussed later). Thus from this perspective, the increases in water vapor can provide a basis for increased accumulation of ozone.

Wind and mixing

In California, the Pacific High pressure system is a dominant feature in the summer—that is, times of typically high ozone levels. This high-pressure system has an important impact on the region's wind field and thus on transport and dilution of ozone and its precursors. The stronger or more persistent this pressure system becomes (and smaller the local gradients), the lower the wind speed will be, and thus stagnant conditions and decreased mixing can be expected. Coupled with relatively stronger capping subsidence inversions, such conditions are conducive for development of high ozone episodes in California, especially in the Los Angeles Basin. High pressure systems also inhibit cloud formation and thus relatively more solar radiation/UV can reach the troposphere and the polluted boundary layer. And, due to stagnant conditions, more precursor emissions can enter the slow-moving air masses and react to produce more smog. Conversely, low-pressure systems and associated higher wind speed and mixing help reduce stagnation and increase dilution of pollutants, thus lowering the apparent ozone concentrations.

The general impact of mixing height changes (i.e., the dilution or venting effect) is to increase or decrease the concentrations of pollutants in the boundary layer when the mixing height decreases or increases respectively. However, the direction of final impacts on ozone concentrations can change sometimes with variations in the VOC/NO_x ratio. For example, titration of O₃ by NO can increase with decreased mixing height, thus reducing its concentrations via (8):



An increase in temperature can also increase the mixing height and thus indirectly reduce the apparent O₃ concentrations or the rate of ozone formation because of the lower concentrations of the precursors (VOC and NO_x). However, there is a significant amount of feedback that can further complicate this process. And while most observations may suggest the type of correlations discussed above, some studies (e.g., McNider et al. 1995) have shown that the opposite can be true; that is, ozone concentrations can peak where the maximum mixing height is, which also is the location of highest temperatures.

Biogenic hydrocarbon emissions

The changes in meteorology, e.g., temperature, solar radiation, and water vapor mixing ratios (as well as CO₂ concentrations) have an impact on the rates of biogenic hydrocarbon emissions (isoprene and monoterpenes) from existing vegetation, as well as from newly introduced forest (if it is of the emitting type). The impacts of these parameters on isoprene and terpene emissions have been studied and quantified by Guenther et al. (1993) and Guenther (1999). For temperature correction of biogenic hydrocarbon emission rates, the functional form is:

$$C_T = \left\{ \exp \frac{\gamma(T - T_s)}{RT_s T} \right\} / \left\{ 1 + \exp \frac{\eta(T - T_m)}{RT_s T} \right\} \quad (9)$$

$$M_T = M_s \exp[\theta(T - T_s)] \quad (10)$$

where C_T is the *correction factor* for the effect of temperature on emission rate of isoprene at temperature T , and M_T is the monoterpene *emission rate* at temperature T . In the two equations above, γ , η , and θ are constants, T is actual air temperature (at which the emission rate is being calculated), T_s is standard air temperature, R is the gas constant, T_m is a constant (314K), and M_s is the emission at standard air temperature. Of course the relative amount of change depends not only on the change in temperature but also on absolute temperature and other factors.

On a regional scale, the impacts of a few degrees change in air temperature can be significant in terms of biogenic hydrocarbon emissions. For example, Fuentes et al. (2000) show that biogenic emissions from forests can increase by a factor of three if temperature increased from 20°C to 30°C (68°F to 86°F). EPA (2000) also shows that an increase of 10°C 18°F can cause over a two-fold increase in biogenic VOC and NO emissions. However, if absolute temperatures are already high, e.g., in the neighborhood of 37°C (99°F), an increase in air temperature may not cause much of an increase, and sometimes a decrease, in biogenic emissions. Such situations were simulated for the Southern California domain and episodic conditions in this study.

Anthropogenic emissions

Anthropogenic emission sources of interest in this application that are sensitive temperature changes include: (1) motor vehicles, (2) fugitive emissions from storage tanks and refueling operations, and (3) power plants (cooling electricity needs). While the actual regional impacts of meteorological changes (e.g., surface modifications) on emissions from such sources may require comprehensive regional modeling to estimate (e.g., EMFAC, DTIM, BEIS, and other models), the dependence of these emissions on temperature is provided in a qualitative manner below for the sake of illustration. Each correlation is valid only within a narrow range of environmental conditions (temperature, humidity, solar radiation, level of activity, etc.) and these are discussed in detail elsewhere, e.g., CARB (1990,1996,2000a,2000b).

To get an assessment of the sensitivity of emission rates to changes in temperature, partial derivatives of the correction factors, such as those used in EMFAC, were computed here to provide a very qualitative example. Thus the following changes in emissions (per change of 1°C (1.8°F) in air temperature) are obtained:

$$\frac{\partial RLC}{\partial T} \cong 2.4 \frac{\%}{^{\circ}C} \quad \frac{\partial RLi}{\partial T} \cong 4.1 \frac{\%}{^{\circ}C} \quad (11)$$

$$\frac{\partial HSc}{\partial T} \cong 1.9 \frac{\%}{^{\circ}C} \quad \frac{\partial HSi}{\partial T} \cong 8.8 \frac{\%}{^{\circ}C} \quad (12)$$

$$\frac{\partial DRL}{\partial T} \cong 1.5 \frac{\%}{^{\circ}C} \quad (13)$$

$$\frac{\partial ATime}{\partial T} \cong 2.2 \frac{\%}{^{\circ}C} \quad (14)$$

$$\frac{\partial EXhc}{\partial T} \cong 0.3 \frac{\%}{^{\circ}C} \quad \frac{\partial EXnox}{\partial T} \cong 0.4 \frac{\%}{^{\circ}C} \quad (15)$$

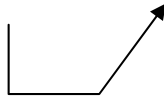
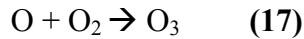
Above, *RLc* and *RLi* are running losses for carbureted and fuel-injected engines respectively, *HSc* and *HSi* are the hot-soak losses for carbureted and fuel-injected vehicles respectively, *DRL* is diurnal/resting losses, *ACtime* is the “on” time of the vehicle’s air conditioner, and *EXhc* and *EXnox* are the running exhaust emissions of hydrocarbons and NO_x, respectively. T is air temperature. Relations (11) through (15) are valid only within specific ranges of absolute air temperature, Reid vapor pressure, and other environmental conditions. For temperature, the range is typically between 25°C (77°F) and 35°C (95°F) but is different for each emission source or pathway (CARB 2000a,b).

The purpose of the above relations is to get a qualitative idea of the order of magnitude of change and (11) through (15) should by no means be regarded as specific or exact correlations. Such estimates have been performed for other regions as well. For example, Cardelino and Chameiedes (1990) used the EPA’s MOBILE 4 program to calculate that if air temperature in Atlanta, Georgia, was increased from 22°C to 29°C (72°F to 84°F), car emissions would increase by 47% and that hydrocarbon emissions from mobile sources would increase by about 5% per °C.

On the role of ROG and OH

The roles of reactive organic gases (ROG) and OH in ozone formation and accumulation are touched upon very briefly here. It was discussed earlier that while the impact of temperature on ozone formation depends on the ambient ROG/NO_x ratio, the general effect of increased temperature is to increase ozone formation by accelerating the photochemical reactions and rates of production of the hydroxyl radical. In general, however, when the ratio of ROG to NO_x is low, ozone formation does not necessarily increase with temperature.

The production of tropospheric ozone (e.g., in the NO_x-rich urban polluted boundary layer) depends initially on the photolysis of NO₂ and the cyclic photo-stationary reactions:



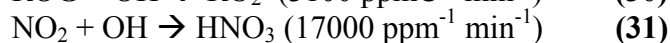
As such, the creation and destruction of ozone are roughly balanced and in steady state, and there is no net change in ozone. For its concentrations to increase, ozone must be allowed to accumulate by providing an alternate path for $\text{NO} \rightarrow \text{NO}_2$ conversion in (18) without consuming ozone. Under this scenario, the rate of ozone scavenging by NO is reduced and O_3 begins to accumulate. That alternate path (to allow accumulation of ozone) is indicated with the arrow, bypassing ozone. This path depends on presence of ROG and the OH radical, but a full description of related reactions and pathways is beyond the scope this report (this is another pathway through which water vapor, a parent of OH, can affect ozone concentrations, i.e., via accumulation). ROG react with the hydroxyl radical to produce peroxy radicals (RO_2) which then react with NO to produce NO_2 (Cooper and Alley 1994). Thus in simple terms, the alternate $\text{NO} \rightarrow \text{NO}_2$ path is:



Reactions (19) and (20) provide partial explanation for why a warmer and more humid weather (e.g., increased evaporation caused by higher temperatures) can be conducive to ozone formation if the extra water vapor is not flushed out of the system via precipitation and does not cause a reduction in solar radiation (and temperatures) via increased cloud cover. It is obvious that there is uncertainty regarding which way water vapor will affect ozone formation, but it is believed that the OH-ROG oxidation cycle is one mechanism for generally increasing ozone production (Seinfeld and Pandis 1998). In summary, the very important role of ROG in allowing ozone to accumulate is its impact on the $\text{NO} \rightarrow \text{NO}_2$ conversion process, and that depends on the actual ratio of ROG/NO_x in the atmosphere.

This issue is important because the limitation of the system (e.g., NO_x - or VOC-limited regimes) can change in space and time within a region depending on the mix of precursors in the atmosphere, for example, upwind or downwind of an urban area. Generally, reductions in ROG emissions and concentrations are beneficial or in the worst-case scenario have minimal impact on ozone concentrations, but reductions in NO_x emissions can cause both positive and negative impacts on ozone air-quality (e.g., increasing or decreasing peak ozone concentrations) depending on the local ROG/NO_x ratio among other factors. This has been shown to occur in urban areas (increase in urban ozone as a result of decreased NO emissions), e.g., Dimitriadis (1989). This topic is complex and beyond the scope of this analysis but it is possible to qualitatively and very briefly describe it as follows.

Seinfeld (1988) and Seinfeld and Pandis (1998) show that the rate constants for reactions involving competition between ROG and NO_x for the hydroxyl radical are about $3100 \text{ ppmC}^{-1} \text{ min}^{-1}$ (carbon atom basis) and $17000 \text{ ppm}^{-1} \text{ min}^{-1}$, respectively:



The ratio is 17000/3100 or about ~5.5 and represents an average because the actual values depend on the mix of ROGs present, since the OH rate constants differ with respect to one ROG than another (Seinfeld and Pandis 1998). Thus if an “average” ROG mix is assumed, then:

- At ROG/NO_x ratios larger than 5.5 (which constitutes an ROG-rich regime with little NO_x available for oxidation to NO₂ and thus is an environment where the production of ozone is controlled by the amount of available NO_x) decreasing NO_x causes a reduction in peak ozone concentrations. At high ROG/NO_x ratios, a decrease in NO_x retards ozone formation because peroxy-peroxy reactions become dominant and scavenge the free radicals.
- For ROG/NO_x ratios smaller than 5.5 the reaction of NO₂ with OH dominates and removes OH from the ROG oxidation cycle, thus less ozone is generally produced in this regime (smaller ROG content and thus the formation of ozone depends on controlling ROG). In this regime, NO can scavenge ozone relatively quickly, and thus decreasing NO_x can lead to accumulation of O₃ and increased peak concentrations. Low ROG/NO_x ratios typically occur in urban cores and their downwind plumes, such that NO_x control doesn't always result in the desired effect, unless reduced by a large amount.

This qualitative discussion sheds some light on why controlling NO_x emissions in urban areas can sometimes lead to the opposite effect, i.e., increased peak ozone. However, this process and its pathways are much more complex than implied above and the reader is referred to atmospheric chemistry texts (e.g., Seinfeld and Pandis 1998), for a rigorous discussion of this subject.

APPENDIX B
Observational Meteorological and Air Quality Monitors
in Southern and Central California

The tables below list observational meteorological and air quality monitors in Southern and Central California. Given are the stations' four-letter identifiers and their corresponding longitude/latitude coordinates. As discussed in the report, not all monitors or stations were used in model performance evaluation in this study.

Southern California Domain

MOBY -120.777 35.381	CLEM -118.488 32.924	WILS -118.060 34.238
PTAR -120.628 34.579	CATA -118.496 33.451	LALM -118.017 33.794
VBPP -120.611 34.596	RSDA -118.516 34.195	LSAL -118.017 33.794
SLMO -120.644 35.281	CLAR -118.532 34.395	WHTR -118.017 33.928
SLOM -120.644 35.297	STCL -118.516 34.395	PICO -118.050 34.011
ATAS -120.661 35.498	SCLR -118.533 34.400	WCOV -118.017 34.078
PSRB -120.678 35.632	VALA -118.449 34.061	LHAB -117.950 33.928
VBWT -120.595 34.780	CSUN -118.491 34.227	CMHB -117.917 33.660
GCTY -120.611 35.130	NEWH -118.482 34.429	CMMV -117.917 33.677
SLPL -120.611 35.214	CATI -118.415 33.414	CTMP -117.917 33.660
ARGR -120.561 35.047	LAWW -118.416 34.044	ANAH -117.900 33.827
NIPO -120.561 35.030	FCBH -118.399 34.111	AZSA -117.917 34.145
NPMO -120.561 35.047	TEHA -118.424 35.147	PINH -117.901 34.235
PTCL -120.445 34.462	PVSP -118.335 33.757	SANA -117.867 33.677
JALA -120.478 34.512	HAWH -118.366 33.928	GLDR -117.850 34.145
LPSH -120.445 34.646	LENX -118.366 33.928	DBAR -117.834 33.961
LOMP -120.462 34.713	WLA -118.382 34.061	SNDM -117.817 34.145
NPSW -120.495 35.047	TEHP -118.378 35.127	GDLO -117.834 34.145
LPHS -120.412 34.729	AVLN -118.316 33.343	POMA -117.751 34.078
LPHP -120.427 34.732	LANH -118.283 34.078	ELTR -117.684 33.627
SMSB -120.428 34.947	BRBK -118.299 34.178	CHNO -117.684 34.011
SMBB -120.395 34.930	LANM -118.233 34.078	CLRM -117.684 34.128
ROSA -120.233 34.019	SDLI -117.152 32.708	CINO -117.634 33.978
GAVE -120.195 34.479	SD12 -117.152 32.708	ONTA -117.651 34.078
gAVW -120.195 34.479	SDIS -117.152 32.724	SNBO -117.667 34.095
GTCA -120.212 34.479	SDUN -117.152 32.724	ULDS -117.651 34.095
gTCC -120.179 34.479	SMPK -117.132 33.194	MBLD -117.622 34.251
ODOR -120.212 34.479	TCRC -117.135 33.493	NORC -117.568 33.928
VDMR -120.162 34.479	TCCC -117.163 33.537	PRAD -117.584 33.944
GAVW -120.206 34.490	RDDL -117.152 34.061	NRCO -117.551 33.928
GTCC -120.179 34.479	REDL -117.152 34.078	PHEL -117.551 34.429
GTCB -120.179 34.529	TIPL -117.117 32.521	RVRS -117.451 33.961
SYAP -120.062 34.612	NALF -117.118 32.574	FNTN -117.468 34.111
ECSP -120.012 34.462	SDCR -117.102 32.775	FONT -117.501 34.111
LFCC -120.029 34.479	SDOV -117.118 32.825	CAJC -117.448 34.361
LFC2 -120.012 34.479	BLKM -117.117 32.990	CAJB -117.449 34.387
LFC3 -120.029 34.479	TIRP -117.058 32.360	RIVM -117.401 33.944
LFC4 -120.029 34.479	CHVT -117.052 32.624	RUBI -117.418 34.011
LFC1 -120.029 34.496	ESCO -117.069 33.125	OCEA -117.368 33.209
UCSB -119.863 34.412	VCEN -117.026 33.242	PEND -117.397 33.226
GLWF -119.813 34.445	BARS -117.019 34.896	UCRS -117.368 33.961
GOLE -119.780 34.445	TIIL -116.979 32.505	OSCL -117.335 33.192
LOSP -119.780 34.546	TITT -116.987 32.532	LELS -117.335 33.677
SBHD -119.763 34.445	OTAY -116.936 32.591	UCDC -117.335 33.961
SBST -119.697 34.429	ECAJ -116.936 32.791	SNBD -117.285 34.111
SPDR -118.249 34.061	ECHL -116.952 32.791	HESP -117.285 34.429
WTLA -118.249 34.061	ELCJ -116.952 32.791	VCTV -117.318 34.512
NLGB -118.183 33.827	HEMT -116.952 33.744	VICT -117.320 34.513
LYNW -118.200 33.928	BANN -116.869 33.928	SOLM -117.252 32.849
LAMC -118.200 34.061	BANH -116.869 33.928	DMMC -117.252 32.958
PASA -118.116 34.128	DBPR -116.786 34.863	PERR -117.235 33.794
PDEV -118.116 34.161	ALPM -116.810 32.873	SANB -117.268 34.111
PSDA -118.116 34.145	ALPN -116.753 32.825	SBE3 -117.268 34.111
LANC -118.116 34.696	WSPR -116.687 33.332	LGRE -117.268 34.245
MOJP -118.133 35.063	PALM -116.536 33.861	REDM -117.192 33.410
PDSW -118.100 34.095	JOSH -116.387 34.078	RDLN -117.185 34.061

TPLC -118.066 34.111	IDIO -116.220 33.710	LKAR -117.202 34.228
SBWC -119.697 34.429	INDO -116.204 33.710	APV -117.185 34.579
SNI -119.569 33.269	29PM -116.054 34.145	MEXI -115.403 32.627
CPGB -119.447 34.412	TNPM -116.054 34.145	CLXE -115.396 32.682
THOS -119.397 34.395	WEST -115.621 33.025	BKGS -118.998 35.398
MRCP -119.397 35.063	EC9S -115.555 32.791	OLDL -118.998 35.448
EMMA -119.314 34.295	CALE -115.472 32.674	TOMP -118.865 34.211
VENT -119.289 34.292	CLXC -115.505 32.674	EDSN -118.848 35.347
OJAI -119.264 34.445	MEXU -115.452 32.637	PRTG -118.815 34.395
SHFT -119.264 35.514	MEXA -115.432 32.666	ARED -118.765 35.214
PMGU -119.120 34.132	LAGP -119.063 34.120	ARVN -118.782 35.214
ELRO -119.131 34.262	BLFC -119.031 35.364	SVAL -118.682 34.278
MEXT -115.355 32.578		CALB -118.611 34.159

Central California Domain

Inland Central California	K87Q 35.670 -121.280	North Sacramento Valley
K3A6 34.370 -118.570	San Francisco Bay Area	KCIC 39.800 -121.850
KBIH 37.370 -118.370	KAPC 38.220 -122.280	KOVE 39.500 -121.620
KBLU 39.280 -120.720	KCCR 37.980 -122.050	KRBL 40.150 -122.250
KDAG 34.850 -116.780	KHWD 37.670 -122.040	KRDD 40.500 -122.300
KEDW 34.900 -117.880	KLVK 37.700 -121.820	Sacramento
KLOL 40.070 -118.570	KNUQ 37.420 -122.050	KMCC 38.670 -121.400
KMHV 35.070 -118.150	KOAK 37.730 -122.220	KBAB 39.130 -121.430
KMMH 37.620 -118.830	KPAO 37.470 -122.120	KMOD 37.630 -120.950
KNFL 39.420 -118.700	KRHV 37.330 -121.820	KMYV 39.100 -121.570
KNID 35.680 -117.680	KSFO 37.620 -122.380	KSAC 38.520 -121.500
KPMD 34.630 -118.080	KSJC 37.370 -121.920	KSCK 37.900 -121.250
KRNO 39.500 -119.780	KSQL 37.520 -122.250	KSMF 38.700 -121.580
KTPH 38.050 -117.080		KSUU 38.270 -121.930
KTRK 39.320 -120.130	Central San Joaquin Valley	KVCB 38.380 -121.960
KTVL 38.900 -120.000	KFAT 36.770 -119.720	
KWJF 34.730 -118.220	KHJO 36.320 -119.630	
KWMC 40.900 -117.800	KMAE 36.980 -120.120	
KEDW 34.900 -117.880	KMCE 37.280 -120.500	
KIYK 35.670 -117.830	KNLC 36.330 -119.950	
North Coast	KVIS 36.320 -119.400	
KACV 40.980 -124.100	Southern San Joaquin Valley	
KSTS 38.500 -122.820	KBFL 35.430 -119.050	
KUKI 39.130 -123.200	KPTV 36.030 -119.070	

APPENDIX C
Highlights of Selected Meteorological Models (Pielke 2002, Taha 2003a)

	HOTMAC	RAMS	MM5	URBMET/TVM
Equations	Hydrostatic and non-hydrostatic	Non-hydrostatic	Hydrostatic and non-hydrostatic	Non-hydrostatic, vorticity mode
Dimensionality	1, 2, 3-D	2-D, 3-D	3-D	1, 2, 3-D
Grid	Limits	Arakawa C	Arakawa B	Arakawa C
Finest horizontal resolution (~order)	4 m (depends on mode)	No minimum	~200m	~500m
Vertical resolution (~order)	1 m (variable)	No minimum	Variable	No limit
Domain	Limit	Multiple nests, no limits on size	Multiple nests, movable nests, no limit on size	Mesoscale
Initialization	Homogenous and FDDA	Single-sounding interpolation, objective analysis of observations	Integrated divergence removal	Single-sounding interpolation
Solution	2D and 3D ADI	Leap frog, forward time differencing, time splitting	Time: leapfrog (time splitting) Space: 2 nd order	Third order PPM, FTCS, stream function solved by gradient method
Coordinate system	Sigma	Sigma	Sigma	Sigma
Lateral b.c.	Vertical equations and smoothing using interior values	Relaxation, zero gradient, cyclic	Relaxation	Zero gradient
Top b.c.	Rigid	Lid, relaxation	Rigid or radiative	Zero vorticity and geostrophic wind
Surface	Energy budget and soil layer	Similarity theory, LULC	Similarity theory, LULC	Similarity theory, LULC
PBL schemes (sub-grid mixing)	Mellor and Yamada	Mellor and Yamada, Deardorff, Smagorinsky-Lilly	Bulk, Blackadar, MRF, Mellor and Yamada	TKE and 1.5 order closure, or E-ε parameterization, or 3-D parameterization
Cumulus parameterization	Mellor	Kuo	Various	None
Radiation parameterization	Sasamori	Various	Broadband	Various
Precipitation	Water vapor and rain	Warm rain, ice, graupel, hail (detailed)	Warm rain, ice, graupel,	Warm rain, ice, graupel, snow
Land surface models	None	Hydrology, vegetation	Several	None
FDDA	Yes	Yes	Analysis and observational	-

APPENDIX D
Highlights of Selected Photochemical Models (based on Environ 2001, 2003)

	CAMx	CMAQ	MAQSIP	UAM-IV	UAM-V
Horizontal advection	PPM, Bott, Smolarkiewicz	PPM, Bott	Bott, Smolarkiewicz	Smolarkiewicz	Smolarkiewicz
Horizontal diffusion	K-theory with varying K	K-theory with constant K	K-theory with constant K	K-theory with constant K	K-theory with varying K
Vertical diffusion	K theory (K is input)	K theory (internal K)	K theory (internal K)	K theory (internal K)	K theory (K is input)
Nesting	2-way, 1-way	1-way	1-way	1-way	2-way, 1-way
Deposition	Dry and wet	Dry and wet	Dry and wet	Dry only	Dry and wet
Chemistry	CB-4 and SAPRC97/99	CB-4 and RADM	CB-4 and RADM	CB-4	CB-4
Plume-in-grid	Yes	Yes	No	No	Yes
Process Analysis	Yes	Yes	Yes	No	Yes
Source apportionment	Yes	No	No	No	No

APPENDIX E

Some Surface Characterization Data Sources

Because the concept of improving air quality through urban surface modification requires making certain assumptions on surface properties and their changes, the characterization of the surface in this type of modeling becomes relatively more important than in other meso meteorological and air-quality studies. Thus, an improved characterization is needed for surface physical and geometrical properties, aerodynamic characteristics, land use/land cover (LULC), topography, water/land distribution, and certain properties such as albedo, thermal inertia, soil moisture content, and roughness length. Certain characterization methods can be relatively more accurate but costlier than others (e.g., fine-resolution remote sensed data) but sometimes cannot provide the entire spectrum of needed information. On the other hand, relatively inexpensive data usually tend to be limited in area and/or resolution. Thus the right combination of data for this type of modeling application should be decided upon based on the project and budget at hand. This should also include an evaluation of expected costs and effort versus needed accuracy and resolution of the data. Note, for example, that for planning, incentives, and neighborhood-by-neighborhood characterization and implementation-planning purposes, fine resolution data is essential (e.g., at a resolution of about 5m), but that for mesoscale modeling purposes, even if “urbanized”, a resolution of 0.25-0.50 km may be the optimal situation.

An optimal approach will involve a combination of data sources, whereby high-resolution information is used in areas of interest (e.g., modifiable regions) and default, coarser resolution data used in areas that are relatively more remote from the modifiable regions. In this approach, the mesoscale model’s coarse-grid characterization of the surface could be based on schemes such as the 38-category USGS land-use and land cover system or other locally improved LULC data, whereas in the fine grids and near the modifiable urban areas, information from finer-resolution sources (e.g., morphological data) can be used to develop accurate physical surface characterization and override the standard/conventional input to mesoscale models.

Fine-resolution morphology/Lidar data

Fine-resolution morphology/Lidar data is appropriate for and especially useful in “urbanized” meteorological modeling, whereby mesoscale models have been modified to explicitly incorporate urban canopy parameterizations (UCP) (Taha 2004). Although such characterization can be derived from any combination of sources, useful and accurate morphology information is typically obtained from Lidar data, e.g., Burian et al. (2003).

Lidar data are better than 1-m in resolution and are taken from aboard specially fitted aircraft. The data can be ordered from a third party (e.g., TerraPoint) and provided to a project in a format specified by the contractor. The data can help identify and geo-reference fine-resolution urban morphology (geometry) features such as buildings, trees, and other elements, as well as related characteristics like street orientations, canyon height-to-width ratios, building footprint information, frontal area density, etc. The cost of such data, from over-flight to delivery, is about \$200–300/km², depending on aerial coverage, and the timeframe for post-processing is about 2–3 months for an area like Los Angeles. Thus, depending on budget considerations, a study may elect to characterize only a small area of interest within a larger study domain. In any event,

Lidar data must be supplemented with other information, e.g., LULC, so as to be used in deriving future year scenarios. And, if there is cost restriction, LULC can be used in extrapolation of Lidar-based surface characterization to larger domains, as will be explained in the following sections.

Digital aerial photography

Because of its relatively high resolution, digital aerial photography can be quite useful in developing surface-type inventories. The source of aerial photographs is usually a digital camera and global positioning system (GPS) mounted on a low-altitude (e.g., single-engine) aircraft flying at about 2000–5000 feet above ground level (AGL) or higher, depending on airspace restrictions. The aircraft is equipped with the GPS for easy georeferencing of the photographs. Digital aerial photography products can have resolutions as fine as 30 cm to 1m, which is very useful for visual identification of objects, surface types, land use, and other characteristics (e.g., old vs. newer structures, high vs. low density built-up zones, public vs. privately owned land). Most aerial photography data come in only one band (visible; combined RGB) but some have an additional band in the near infrared. With only two bands at the most, it is not possible to develop a thermophysical characterization of the area of interest, nor derive useful properties such as albedo, Normalized Difference Vegetation Index (NDVI), or skin temperature based solely on this data source. It is also not possible to fully automate the process of surface-type recognition and, thus, the identification of surface type has to be performed visually.

This type of digital photography is useful in developing a percentage-wise distribution of surface types and cover types (e.g., vegetation, structures), and to visually discriminate any surface down to small objects if needed. However, this level of detail is not directly useful in mesoscale modeling applications, unless the information is converted into physical parameters that the model would understand, for example: density, soil moisture content, albedo, roughness length, thermal inertia, etc., which is typically difficult to infer accurately from such photographs. Of course, satellite data (see below) can provide this type of resolution and more information, but at a relatively greater cost. Also, for typical mesoscale grid resolutions of about 3–5 km (i.e., typical for current regulatory air quality modeling), using 1-m data entails so much averaging that much detail is lost. Even if the mesoscale/photochemical models were run at a grid spacing of 500 m or better, there will still be an averaging of some 250,000 times per grid.

Although the cost per “scene” of aerial photographs may be in the order of \$200–\$300/km², the cost of analyzing the data can be higher because identifying LULC from such photographs cannot be fully automated and must be done manually. In addition, because there likely is a cost limitation in such studies (i.e., limitation on the spatial coverage of the data that a project can afford), the characterization of several selected “representative” areas must be extrapolated from sampled scenes to region-wide basis if a regional-scale analysis is desired. Thus another type of data, such as satellite data at lower resolution or USGS LULC, is needed for the extrapolation. This step introduces additional costs and potential sources of errors as well.

Because of the cost and time it would take to analyze the photographs, it is necessary to extrapolate the small-scale data to regional scale. One method relies on using the USGS LULC (e.g., 200-m data) as a basis or template for such extrapolations. USGS LULC data classify the surface at 200-meter resolution into many different urban and non-urban categories. Urban

USGS LULC includes the following categories: residential, commercial and service, industrial, transportation and communications, industrial/commercial, mixed urban or built-up land, and other mixed urban and built-up land. These subcategories are usually sufficient for detailed characterization of the surface for mesoscale meteorological modeling purposes. However, there can be a mismatch between the aerial photos (typically more recent) and the USGS LULC that is typically older. This must be kept in mind during spatial extrapolation and interpolation of the aerial photography data in areas where substantial urbanization has occurred during the past 10 years or so.

AVIRIS

The NASA Airborne Visible Infra-Red Imaging Spectrometer (AVIRIS) can provide both data and digital aerial photos at a spatial resolution of 4 to 20 m in 224 bands (spanning 0.4–2.5 μm), i.e., at a spectral resolution of about 10 nanometers (nm). For practical purposes, this spectral coverage (at this resolution) can be considered continuous in the visible, near IR, and middle-IR ranges. AVIRIS is typically flown on NASA ER-2 aircraft. Cost information is not always available but it is expected that AVIRIS costs more, per unit area, than aerial photographs. Analysis of the data is expected to be expensive as well, at least initially, i.e., until some automation of the spectral analysis can be put in place for a particular intended use and application of the data. Since AVIRIS has fine resolution (both spectral and spatial), it will be very suitable for deriving spectral/thermal signatures of various surface types and possibly help automate the process of LULC recognition, fabric analysis, and derivation of gridded thermophysical properties. Cost is obviously a main concern, but if sample scenes are carefully selected, the dollar amount may be reasonable.

AVHRR

The Advanced Very High Resolution Radiometer (AVHRR) has a resolution in the order of 1km and in 5 bands (visible, NIR, and 3 in the thermal range). It offers a relatively more cost-effective data source than other sensors and the lower resolution (spatial and spectral) means larger coverage for the same cost. However, AVHRR may not be useful for all types of applications and is of limited use in LULC classification because of its coarse resolution. However, it is relatively useful in directly deriving and developing thermophysical properties for modeling purposes (providing lower boundary conditions for met models) and its resolution and coverage are similar to those of mesoscale models. Ideally, data from AVHRR would be used in characterizing the coarser-grid domains in areas that are not modifiable. AVHRR allows the derivation of broadband albedo, NDVI, and skin temperature, among other parameters, at the relatively low resolution of 5 bands. The cost for a scene of several tens of thousands of km^2 may be in the order of \$10,000. Analysis of the data is relatively more straightforward than the other types but cannot be automated except for large and uniform surface types, e.g., water bodies, forests.

ATLAS

While more expensive than AVHRR, ATLAS data provide relatively better resolution in space (e.g., 10 to 20 m) and spectrum (15 bands; roughly half in and near the visible range and half in the near-infrared (NIR) and mid-infrared (MIR). ATLAS is typically flown on board NASA ER-2 or Learjet aircraft at altitudes of 10,000–20,000 feet. Because they can be customized, the flyovers can capture areas of interest at desired dates and times. If finer resolution is needed, the

aircraft can also adjust its altitude for this purpose. Because of its 15 bands, ATLAS data can be characterized and classified semi-automatically and can be used in deriving spectral signatures and certain thermophysical properties, such as albedo, NDVI, temperature, etc. In areas with small-scale features, e.g., residential neighborhoods, ATLAS data cannot provide visual discrimination of land use or surface types, thus may be of limited use in LULC identification in such areas. However, in larger and more uniform areas, e.g., agriculture, forest, large buildings, water bodies, large parking lots, etc., the data can be helpful in visual interpretation as well. In addition, some ground truthing may be needed to validate and calibrate the properties derived from remotely sensed data, e.g., the spectral signatures of various surface types.

Landsat TM/ETM+

Landsat Thematic Mapper (TM) and ETM+ (enhanced thematic mapper plus) are satellite-based sensors that provide multispectral (8 bands) data in the visible, near-infrared, and thermal portions of the electromagnetic spectrum. Most bands have a resolution of 30 m, for example as follows: (1) 0.45–0.52 μm , 30 m; (2) 0.52–0.60 μm , 30 m; (3) 0.63–0.69 μm , 30 m; (4) 0.76–0.90 μm , 30 m; (5) 1.55–1.75 μm , 30 m; (6) 10.4–12.5 μm , 60 m; (7) 2.08–2.35 μm , 30 m; (8) 0.50–0.90 μm , 15 m. Thus, Landsat data can be used for derivation of thermophysical properties, but, while better than AVHRR, are less useful than ATLAS or AVIRIS. The data analysis process can be automated and the cost of TM data is in the same order of AVHRR's. Because the resolution is about 30 m, Landsat data cannot be used to visually interpret and classify small-scale features, such as residential buildings, roadways, etc.

LULC (e.g., USGS)

For meteorological and air quality modeling purposes, LULC data is necessary for developing both base line conditions and future surface-modification scenarios, regardless of availability of any other type of data, e.g., morphology, fine-resolution remotely-sensed data, and aerial photography. This is because the strategies of urban surface modification are inherently land use-based. In most cases, the source of remotely sensed data cannot provide LULC information and thus must be supplemented by using LULC data. In addition, the LULC data can sometimes provide a template for extrapolation of expensive fine-resolution remotely sensed data to cover much larger regions of interest, as discussed above in Lidar and AVIRIS data. The most suitable source of LULC for mesoscale modeling is the USGS, e.g., 200-m LULC, and a significant amount of data can be obtained at no cost. Where available, more recent and finer-resolution *local* LULC data can be used to complement or improve upon those from the USGS, especially if more up-to-date and more resolved (e.g., have a larger number of urban sub-categories or others). Local surveys and planning agencies can also offer more up-to-date information than USGS LULC can (although perhaps more limited in scope or coverage) that should be assimilated in any input to this type of meteorological and air quality modeling.